



HAL
open science

Evaporation in microfluidic systems: From radially evolving capillary structures to phyllotaxic spirals

Chen Chen

► **To cite this version:**

Chen Chen. Evaporation in microfluidic systems: From radially evolving capillary structures to phyllotaxic spirals. Construction durable. INSA de Toulouse, 2016. English. NNT : 2016ISAT0020 . tel-01553833

HAL Id: tel-01553833

<https://theses.hal.science/tel-01553833>

Submitted on 3 Jul 2017

HAL is a multi-disciplinary open access archive for the deposit and dissemination of scientific research documents, whether they are published or not. The documents may come from teaching and research institutions in France or abroad, or from public or private research centers.

L'archive ouverte pluridisciplinaire **HAL**, est destinée au dépôt et à la diffusion de documents scientifiques de niveau recherche, publiés ou non, émanant des établissements d'enseignement et de recherche français ou étrangers, des laboratoires publics ou privés.



Université
de Toulouse

THÈSE

En vue de l'obtention du

DOCTORAT DE L'UNIVERSITÉ DE TOULOUSE

Délivré par : *l'Institut National des Sciences Appliquées de Toulouse (INSA de Toulouse)*

Spécialité : *Dynamique des Fluides*

Présentée et soutenue le *23/03/2016* par :

Chen CHEN

Titre: Evaporation au sein de systèmes microfluidiques: des structures capillaires à gradient d'ouverture aux spirales phyllotaxiques

JURY

B. SCHEID	Professeur, Université Libre de Bruxelles	Rapporteur
H. BODIGUEL	Professeur, Université de Grenoble	Rapporteur
P. DURU	Maître de Conférences, Université de Toulouse	Co-encadrant
M. PRAT	Directeur de recherche, CNRS	Co-encadrant
S. GEOFFROY	Professeur, Université de Toulouse	Directeur
P. JOSEPH	Chargé de Recherche, CNRS	Co-directeur
L. TADRIST	Professeur, Université d'Aix-Marseille	Examineur

École doctorale et spécialité :

MEGEP : Énergétique et transferts

Unité de Recherche :

Laboratoire Matériaux et Durabilité des Constructions de Toulouse (EA 3027)

Directeur(s) de Thèse :

Sandrine GEOFFROY et Pierre JOSEPH

Rapporteurs :

Hugues BODIGUEL et Benoît SCHEID

Remerciements

...

Résumé

Les effets capillaires sont très courant dans la Nature. Dans le contexte du séchage de milieux poreux dont la taille de pore est dans la gamme micromètre-millimètre, ils jouent un effet dominant en contrôlant la répartition des phases (liquide-vapeur) dans l'espace poral, au fur et à mesure que le séchage se produit. L'idée du présent travail est d'étudier le séchage d'un fluide pur et mouillant dans des micromodèles, c'est-à-dire des milieux poreux modèles quasi-2D et micro-fabriqués. Nous présentons des résultats obtenus pour différentes géométries. Typiquement, les micromodèles utilisés sont constitués de réseaux de cylindres pris en sandwich entre deux plaques. La distribution des phases et le taux d'évaporation dans de tels micromodèles peuvent être aisément mesurés par visualisation directe puis traitement d'images.

En jouant sur l'arrangement spatial des cylindres, on obtient dans un premier temps des micromodèles pour lesquels le taux de séchage est quasi-constant, depuis le début de l'expérience de séchage jusqu'à l'évaporation totale du liquide saturant initialement le système. Typiquement, cette situation est obtenue quand la taille des pores décroît en allant du centre du micromodèle vers sa périphérie (les micromodèles sont axisymétriques). Au contraire, quand la taille des pores croît du centre vers la périphérie, l'invasion d'un front de séchage stable est observée, d'où un temps de séchage total bien supérieur.

Nous avons aussi réalisé un autre type de microsystèmes, au sein duquel les cylindres sont arrangés en spirale de Fibonacci, en nous inspirant de motifs observés en phyllotaxie. Dans de tels systèmes, des films liquides épais se développent le long des spirales, au cours du séchage, et jouent un rôle crucial dans la cinétique d'évaporation. Cette situation rappelle celle déjà étudiée par Chauvet dans des tubes capillaires de section carrée [10]. Cependant, elle est plus complexe, de par la nature poreuse du micromodèle (alors qu'un tube capillaire, tel qu'étudié par Chauvet, peut être vu comme un pore unique) et parce que les films liquides y ont une forme plus complexe. Pour de tels systèmes, nous présentons des résultats expérimentaux quantifiant l'effet des films liquides sur la cinétique de séchage, en lien avec des prédictions théoriques issues d'un modèle de séchage visco-capillaire. Un tel modèle nécessite l'utilisation du logiciel Surface Evolver pour modéliser la forme des films liquides, couplée avec des simulations directes de l'écoulement de Stokes dans les films liquides, pour y calculer la résistance visqueuse à l'écoulement induit par l'évaporation.

Enfin, dans un dernier chapitre, plusieurs expériences d'évaporation sont conduites sur des micromodèles déformables. Des effets élasto-capillaires peuvent en effet induire des changements de géométrie de l'espace poral en cours d'évaporation,

ce qui, comme vu précédemment, peut affecter la distribution des phases et la cinétique de séchage.

Mots clés: Milieux Poreux, Séchage, Evaporation, Films liquides, Elasto-capillarité, Micro-fabrication, Micomodèle, Traitement d'images.

Abstract

Capillarity is a common phenomenon encountered in Nature. In the context of the drying of porous media with pore size in the micrometer-millimeter size range, capillary effects play a dominant role in controlling the phases (liquid or vapor) distribution in the pore space as drying occurs. The basic idea of the present work is to study the drying of pure, wetting fluids in micro-fabricated, quasi-2D, model porous media (hereafter called micromodels). We present results obtained for different micromodel geometries. Typically, the micromodels used consist of arrangements of cylinders sandwiched between a top and bottom plate. Phases distribution and evaporation rates in such micromodels can easily be measured by direct visualizations and subsequent image processing.

By tuning the cylinders pattern, one can first obtain micromodels for which the drying rate is almost constant, from the beginning of the drying experiment to the total evaporation of the liquid initially filling the system. Typically, this situation is obtained when the pores size decreases from the micromodel center to the periphery (the micromodels are axisymmetric). On the contrary, when the pores size increases from the center to the periphery, invasion of a stable drying front is observed, resulting in a much longer total drying time.

We also designed another type of micromodel where the cylinders are arranged in a Fibonacci spiral pattern, a design inspired by phyllotaxic structure. In such systems, thick liquid films develop along the spirals during drying and play a key role in the drying kinetics. This situation is reminiscent of that already studied by Chauvet in capillary tubes with square cross-sections [10]. However, it is more complex because of the porous nature of the micromodel (whereas a single capillary tube, as studied by Chauvet, can be viewed as a unique pore), and because of the much more complex liquid films shapes. For such systems, we present some experimental results on the liquid films effects on the drying kinetics, together with theoretical prediction, based on a visco-capillary drying model. Such a modelling requires the use of the Surface Evolver software to model the film shape, coupled with DNS simulations of the Stokes flow within the liquid films to compute the viscous resistance to the evaporation-induced flow.

Finally, as a last part of this thesis, several evaporation experiments performed on deformable micromodels are presented. This preliminary work aims at reaching a situation where elasto-capillary effects modify the pore space geometry during evaporation. This, as seen above, should in turn alter the phase distribution during evaporation and the drying kinetics.

Key words: Porous media, Drying, Evaporation, Liquid films, Elasto-capillarity,

Micro-fabrication, Micromodel, Image Processing.

Contents

Résumé	ii
Abstract	v
1 Research background and bibliography	2
1.1 Research background	2
1.1.1 Capillarity	2
1.1.2 Evaporation in porous media	3
1.1.3 The role of liquid films	4
1.1.4 Drying of a capillary tube with a square-cross section.	6
1.2 Research objective and manuscript organization	8
2 Materials and methods	11
2.1 Global design strategy	11
2.1.1 Pattern with radial gradient in cylinders spacing	11
2.1.2 Fibonacci spiral pattern	13
2.1.3 Micro-fabrication protocol	15
2.1.4 Characterization of the micromodels	18
2.2 Experimental setup and techniques	20
2.2.1 Equipmental setup, protocol and working fluids	20
2.2.2 Mass drop recording by balance	23
2.2.3 Image processing	24
3 Numerical techniques	30
3.1 Surface Evolver: presentation and a first test case	30
3.1.1 Achieving a stable interface in SE	30
3.1.2 Reliability of the results obtained from SE	33
3.2 Presentation of the different cases studied with Surface Evolver	34
3.2.1 Liquid rings around cylinders	35
3.2.2 Liquid bridges on spirals	37
3.2.3 Receding front between two spirals	41
3.3 Direct numerical simulations (DNS) of the flow within a liquid bridge	43
3.3.1 Model explanation	43
3.3.2 Viscous flow simulations	43

4	Controlled evaporation by capillary structure	50
4.1	Introduction	50
4.2	Experimental set-up	51
4.3	Evaporation in radial gradients capillary structures	53
4.3.1	Phase distributions during drying	53
4.3.2	Drying kinetics	59
4.4	Some modelling considerations (stable case)	61
4.5	Phyllotaxy inspired capillary structures	67
4.5.1	Motivation	67
4.5.2	Phase distribution during drying	70
4.5.3	Drying kinetics	72
4.6	Conclusions	75
5	Spiral system: experimental results and modelling	77
5.1	First qualitative observations	77
5.1.1	Small micromodels (50 μm thickness)	77
5.1.2	Large micromodels (500 μm thickness)	79
5.1.3	Fibonacci spirals as a model porous medium	79
5.2	Quantitative description of a drying experiment	82
5.2.1	Description of the interfaces displacement	82
5.2.2	Reproducibility	84
5.3	Experimental results	85
5.4	Theoretical approach	87
5.4.1	A capillary theory for the drying of spiral micromodel	88
5.4.2	Viscous effects	98
5.5	Conclusions	103
6	Elasto-capillary devices	105
6.1	Introduction to elasto-capillarity	105
6.1.1	Mechanism of elasto-capillarity	105
6.1.2	Device design objectives	109
6.2	Elasto-capillary spring	109
6.2.1	Device design and fabrication	109
6.2.2	Experiments and results	110
6.2.3	Preliminary conclusion	111
6.3	Drying in deformable cylinder array	111
6.3.1	Deformable cylinder array design and fabrication	112
6.3.2	Experimental results: drying of non-confined arrays	113
6.3.3	Experimental results : drying of confined arrays	113
6.4	Conclusion	116
7	Conclusion and perspectives	120
	Bibliography	122
A	Algorithm used to generate the Fibonacci spiral pattern	127

B	Surface Evolver simulation of a receding front, in a Fibonacci spiral pattern	129
C	Flow resistance of liquid bridge	133
D	Vapor concentration field in a Fibonacci spiral micromodel, during the CRP	141

introduction

Chapter 1

Research background and bibliography

In this chapter, we introduce some basic notions and research background that are relevant for the present study. They include the concept of capillarity, evaporation in porous media and the effects of liquid films, with the case of the drying of a square capillary tube reviewed as an example. Finally, the objectives and organization of the present PhD manuscript are given.

1.1 Research background

1.1.1 Capillarity

Capillarity is one of most common phenomenon one can encountered in daily life, commonly at millimeter and sub-millimeter scale. Figure 1.1a illustrates a typical example of capillary rise in small tubes. This a classical experiment in school class where the liquid rise in tubes is seen to be more important in thinner tubes, compared to thicker ones. Capillary effects have a molecular origin and result from the competition between liquid-solid intermolecular forces (adhesive force) and liquid-liquid intermolecular forces (cohesive force). Regarding capillary rise in glass tubes, if one dig deeper to molecular scale, one need to consider that water molecule has a polarized structure, between which hydrogen bond dominates, while the composition of quartz glass surface is $(SiO_2)_n$ (overall chemical formula). Since Si-O bond is more polarized comparing with H-O bond in water, the water molecule prefers adhering to the glass surface (still by means of hydrogen bond), so the capillary rise and also a meniscus shape seen at the tube diameter scale, as shown in Figure 1.1b.

When the meniscus shape is at steady state, a pressure difference is sustained across the liquid-gas interface, which is famously expressed by the Young-Laplace equation:

$$\Delta P = P_g - P_l = \gamma C = \gamma \left(\frac{1}{R_1} + \frac{1}{R_2} \right). \quad (1.1)$$

In equation 1.1, ΔP is the difference in pressure difference across the liquid-gas interface (P_g is the pressure in the gas phase, P_l in the liquid), γ is the surface

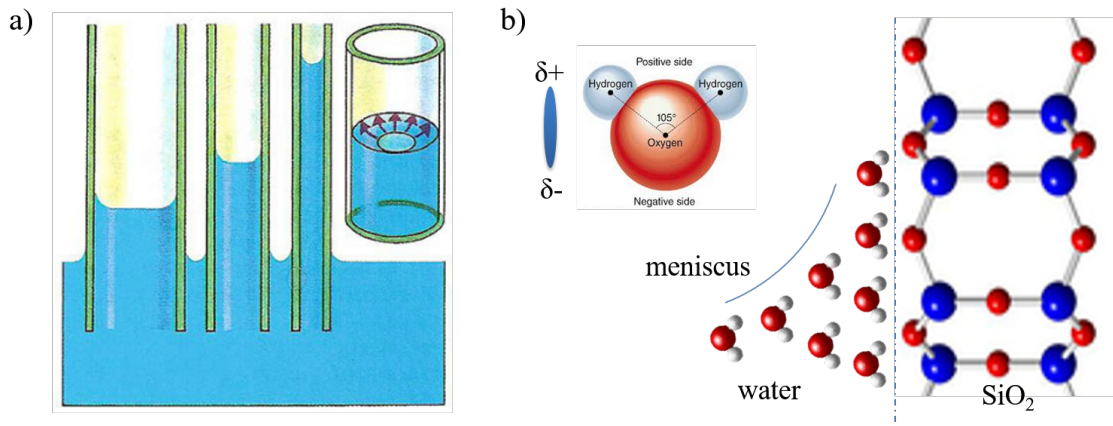


Figure 1.1: a) Capillary rise in glass tubes. b) Molecular mechanism of capillarity: owing to higher polarized Si-O bond in solid surface, water molecular prefers to “adhere” on solid surface through hydrogen bond. Inset illustrate the water molecular structure. Red, blue and gray spheres represent oxygen, hydrogen and silicon atoms respectively. Figures taken from internet.

tension, and C is the interface mean curvature with R_1 and R_2 the principal radii of curvature of the interface. The Young-Laplace equation describes the normal stress balance for a static interface between two non-miscible fluids.

Capillary effects dominate over gravity effects at millimeter scale and below. This is why they are very important in many problems involving porous media. Most of the materials encountered in daily life have a porous structure, i.e. contain a tremendous number of “voids”, called pores: for instance, soil, textiles, pharmaceuticals and masonry materials (stone/brick/mortar/concrete block), etc. If the pore size is small enough, capillarity can trap some water in the pore space without assistance of an external force. Also, if for some reasons the curvature of the menisci encountered in a wet porous media changes from one point to another in the liquid cluster, the Young-Laplace law tells us that some difference in liquid pressure appears, inducing a flow in the liquid (this effect is called capillary pumping).

1.1.2 Evaporation in porous media

Evaporation or drying of porous media wet by a liquid is an important topic in many natural and industrial processes. Let’s cite for instance the drying of soil [34, 56], of foodstuff [24] and of pharmaceutical products.

Drying is considered as one of the most complex phenomenon in engineering since the drying process associates various mass and energy transfers occurring simultaneously, such as molecular diffusion and convection in gas and liquid phases, phase-change at interfaces and heat transfer on both phases. It’s worth to mention that many pore-scale mechanisms are also involved, such as menisci displacements, transfers between liquid clusters through thick films. And these problems are all the more complicated to describe because they occur in the very complex geometry of the pore space.

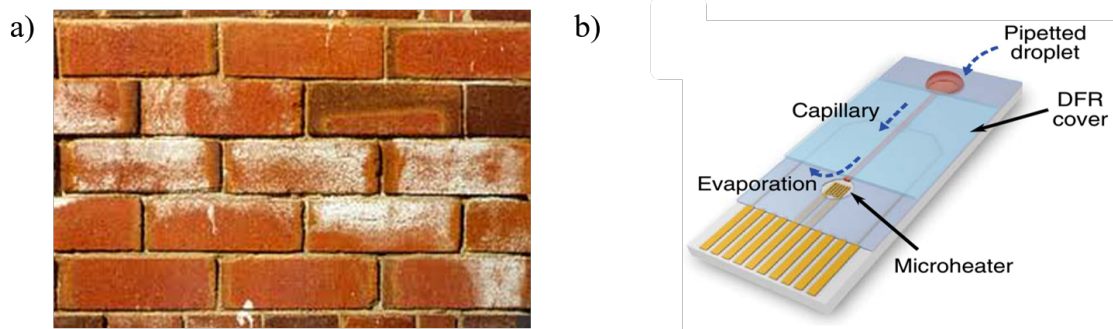


Figure 1.2: a) Efflorescence at the surface of building bricks. b) A microfluidic chip involving an evaporation stage controlled by capillary pumping [51]. Here, capillary pumping occurs in a somewhat simplified geometry (the microchannels of the chip), compared to real porous media applications.

A very common phenomenon associated with the drying of porous media is the formation of efflorescences, as shown in Figure 1.2a). Efflorescences result from the crystallization of salts initially present in a liquid saturating the porous media and can cause severe damages to buildings [44, 54]. Their formation results from the coupling between the drying of the saline solution wetting the porous media and the associated transport of salt in the porous structure (the salt accumulates close to the evaporation surface until crystallisation occurs). Another interesting application of evaporation in porous-like structure is found in microsystems called micro-caloducs or in more conventional microfluidics chips [32, 62], see Figure 1.2b).

In recent decades, much progress have been made in the field of porous media drying, using for instance concepts from invasion percolation (IP) theory [35] and pore network methods (PNMs) [28, 29]. Invasion percolation [31, 59] is an algorithm that describes the slow displacement (drainage) of a wetting fluid by a non-wetting fluid in a porous medium. This happens progressively, pore by pore. The invasion preferentially takes place at the largest pores, that have the smallest capillary pressure threshold. Drying in porous media is often a very slow process associated with very low capillary number, so that it follows the main feature of IP, where the gas phase is considered as the invasive non-wetting phase, and the liquid phase is the drained wetting phase [35, 36]. PNMs is a well-established technique that models the pores in a given porous medium as a network of interconnected pores (sites) and bonds (throats), as shown in Figure 1.3. Nowadays, the pore network can be constructed from direct imaging, for example, micro-X-ray computerized tomography. Therefore, PNMs are considered as a good method for investigating the drying, taking into account of information from the *real* microstructure such as pore size distribution and 3D shapes. Researches on drying based on PNMs have been recently reviewed by Prat [37].

1.1.3 The role of liquid films

Recent researches have exposed that the liquid films trapped in corners or crevices in pore scale due to capillarity have a great influence on the drying rate. The first

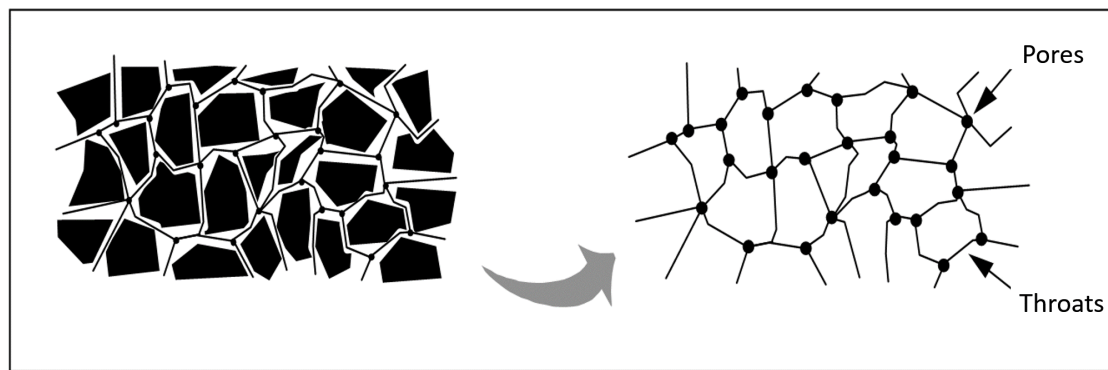


Figure 1.3: Illustration of pore networks models in 2D model. The voids space in porous media is represented by a network of pores that are connected by throats [37].

article mentioning a liquid film effect in the context of drying of porous media is Shaw’s experimental study on drying of a beads packing confined in a Hele-Shaw cell [47]. Shaw found that the drying front observed in the porous bead packing moved one order of magnitude faster than the drying front observed when evaporation of liquid in the Hele-Shaw cell without beads was studied, under comparable external conditions. He attributed this effect to the flow in the intricate network of thick liquid films formed around contact points between the beads¹. The flow in the films is in opposite direction compared to the liquid-gas interface displacement direction. It transports the fluid towards the evaporative surface and helps to maintain a high evaporation rate.

Figure 1.4 explains this film effect in more details. Here, the porous media is hydrophilic and initially saturated with liquid (say, water), and exposed at its top surface to a complete dry atmosphere (where the water vapor concentration is close to zero). Since a water vapor concentration gradient exists between the liquid-gas interface and the external air, evaporation occurs. As a result, the gas phase begins to penetrate into the pore space. However, thick liquid films remain trapped in the pore space (more precisely in corners and contact regions between solid grains, cracks, etc) and form a connected liquid network, shown as the light-gray region in Figure 1.4,left. There is a liquid flow within the liquid films, induced by capillary pumping, from the receding front (below which the porous media is saturated with liquid) to the drying front. This transport is far more efficient when compared to the transport by mass diffusion that would take place without films, which explains the larger evaporation rate when films are present. In this situation, the main resistance to mass transfer comes from diffusion across a mass boundary layer, of thickness ζ , on top of the evaporative surface. At one point, the films “depin” from the top of the porous media and a completely dry region appears, see Figure 1.4,right. Then, the drying rate decreases as the main resistance to mass transfer

¹The term “thick” -i.e. micrometer scale- is usually attributed to the liquid films we deal with, to make a distinction with the nanometer-scale films that may remain on the solid surface due to adsorption forces. These latter films have a negligible hydraulic conductivity and thus do not intervene in the liquid mass transfer [20].

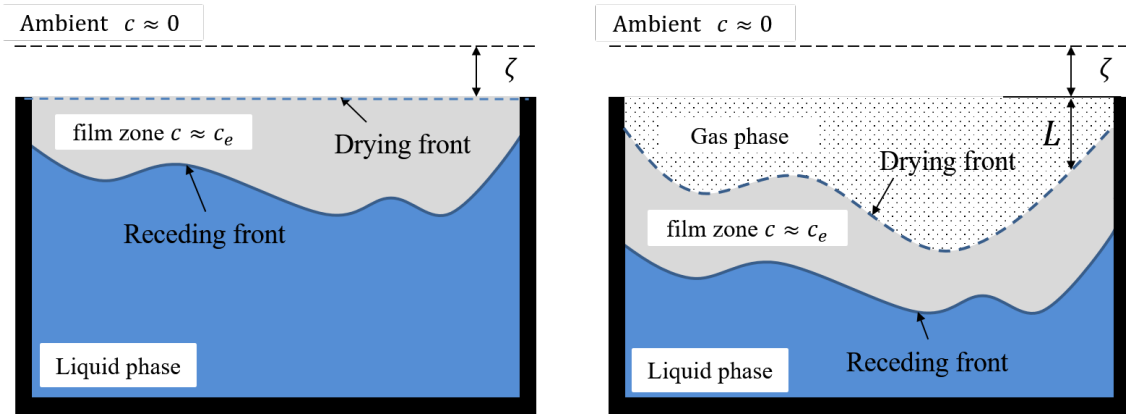


Figure 1.4: Drying of a porous medium with liquid film effects. Left: during a first drying stage, there is an hydraulic pathway for the liquid from the receding front to the drying front due to the liquid films. The gas in the films zone is saturated with vapor, the vapor concentration c is equal to the saturation value c_e . The main resistance to mass transfer comes from diffusion across a mass boundary layer, of thickness ζ , on top of the evaporative surface. In the surrounding dry air, $c \approx 0$. Right: at one point, a completely dry region forms on top of the porous media. Then, the drying rate decreases as the main resistance to mass transfer comes from diffusion across a larger distance $L + \zeta$, where L is the height of the dry region.

comes from diffusion across a larger distance $L + \zeta$, where L is the height of the dry region (and L is increasing with time as evaporation proceeds).

Following Shaw’s pioneering experiments, Laurindo & Prat [29] compared the drying rate experimentally measured in 2D etched-glass micromodels with pore-network simulation results which did not take into account liquid films. The experimental drying rates were found to be about sixfold higher than the numerical drying rates demonstrated the strong liquid films effect. Such an important effect was also observed and quantified on beads packing by Yiotis *et al.* [60]. Recently, Chauvet *et al.* studied the drying of straight capillary tube with a square cross-section [10]. We give some details on their study in the next subsection as the ideas and framework of this previous work will be used throughout this manuscript.

1.1.4 Drying of a capillary tube with a square-cross section.

Qualitative description of the drying kinetic

Let’s consider a square-cross section capillary tube initially filled with a wetting fluid. When evaporation occurs, liquid films remain trapped in the four tube corners as a bulk meniscus recedes into the tube, see Figure 1.5.

Owing to the transport of the liquid within the films, a first drying phase is observed where the drying rate is almost constant. The bulk meniscus recedes but the four liquid films remain “attached” at the opened end of the tube. Then, it is found that the liquid film “depin” from the tube entrance which marks the beginning of a rapid decrease of the drying rate. From top to bottom, one ends up with having a dry region in the top part of the tube, then a region with the liquid

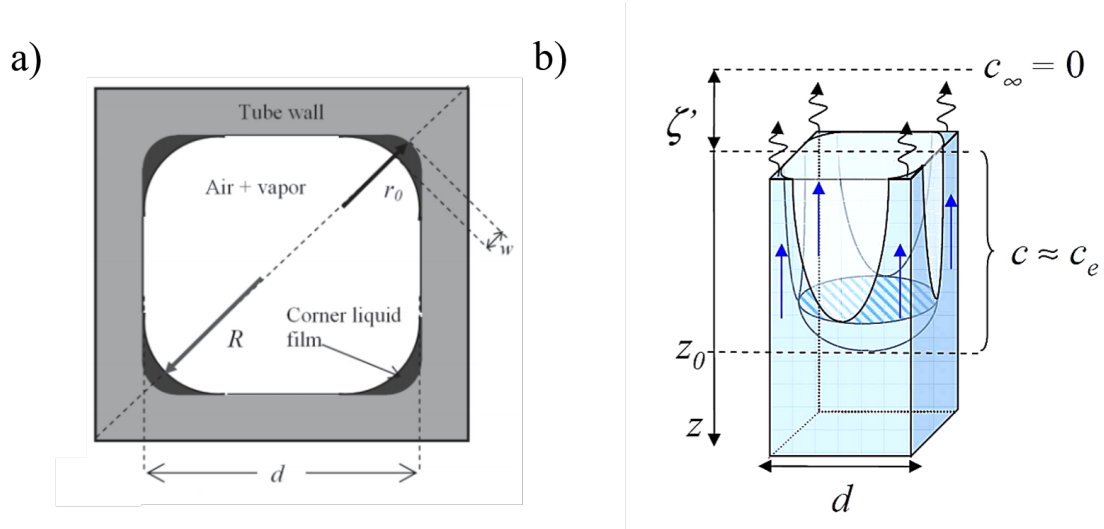


Figure 1.5: Evaporation in a square cross-section capillary tube. a) Cross-section view of the tube, with the four liquid films in black; b) Overall view, from Chauvet [10].

films and then the bulk meniscus. This situation is very close to the one described above for porous media, see Figure 1.4. Consequently, the drying kinetic of the tube displays the distinctive 3 periods classically observed in porous media drying (see, e.g. [18]): a constant drying rate period (called CRP), then a falling rate period (FRP) and finally a receding front period (RFP). This is studied in details in [10] and shows that the square tube geometry contains a relevant physic as far as drying is concerned, the liquid films effect. In other words, the square tube geometry can be viewed as a very simplified model of a porous medium, a “single pore” porous medium, displaying film effects.

Modelling of the liquid film effect

To model the situation depicted above, focusing on the liquid films effects, the starting point is the use of a Poiseuille-like law to model the flow in the liquid corners [39]. The total flow rate, in the 4 corners, is then written:

$$q_{liq}(z) = -\rho_l \frac{A_c R^2}{\beta \mu_l} \left(\frac{dP_l}{dz} - \rho_l g \right)$$

where A_c is the films cross-section ($A_c = (4 - \pi)R^2$ for a square capillary tube and a perfectly wetting fluid). The flow resistance β is a function of the contact angle and of the film transverse curvature R . Combining this equation to the Young-Laplace equation written neglecting the longitudinal curvature of the films, $P_l = P_a - \gamma/R$, one obtains :

$$q_{liq}(z) = -\rho_l \frac{A_c R^2}{\beta \mu_l} \left(\frac{\gamma}{R^2} \frac{dR}{dz} - \rho_l g \right).$$

The total mass flow of the evaporating fluid is the sum of the flow rate in the films and of the flow rate in the gas phase. The latter can be related to the evolution

of the vapor concentration along the capillary tube (using a 1D model) and it can be shown that assuming that the gas is saturated in vapor in the tube is a good approximation [11]. Therefore, the flow rate in the films $q_{liq}(z)$ is constant along z and equals the evaporation rate E (which is measured experimentally). The equation above can be made dimensionless by dividing the length R and z by R_{mp} , the transverse curvature at the bulk meniscus and introducing $E^* = E/(R_{mp}Dc_e)$ (D is the molecular diffusion coefficient of vapor in air):

$$\frac{dR^*}{dz^*} = \frac{Ca}{2\pi} E^* \beta(R/R_{mp}) \frac{1}{R^{*2}} + BoR^{*2} \quad (1.2)$$

where $\beta(R/R_{mp})$ can be found in Zhou *et al.* [61] and where the Bond number Bo and capillary number Ca are defined as:

$$Bo = \rho_l g R_{mp}^2 / \gamma \quad , \quad Ca = \frac{2\pi \mu_l D c_e}{(4 - \pi) \rho_l \gamma R_{mp}}$$

The Bond number compares the effects of capillarity versus gravity whereas the Capillary number compares the viscous effects to the capillary effects.

Equation 1.2 can be used to predict the film length at depinning and was compared to experimental results in [11]. It contains the essential ingredients needed to describe the film effects and the way gravity and viscous effects act against capillarity to limit the maximal film extent. Note that in Chauvet's work [11], the tubes were held vertically so that gravity was the major mechanism which limited the film vertical extent.

1.2 Research objective and manuscript organization

The basic idea of the present work is to study the drying of pure, wetting fluids in micro-fabricated, quasi-2D, model porous media (hereafter called micromodels). In particular, we show how "tuning" the capillary forces at play in a micromodel, through the design of the pore space geometry, can result in controlling the drying rate of a liquid initially filling the pore space. This idea is demonstrated using different model porous media which are micro-fabricated, resulting in a very good control of the geometry of the pore space. Typically, the micromodels used consist of arrangements of cylinders sandwiched between a top and bottom plate. The evaporation rate and phases (liquid-vapor) distribution in experiments are measured by image processing. These results are compared to numerical and theoretical predictions. Thus, this work is a natural follow-up to Chauvet's study [10]. The main difference is that the model of porous media used are more "realistic", compared to Chauvet's capillary tubes.

First, in Chapter 2, we present the Materials and Methods used for the experimental part of our work. The design and microfabrication of the micromodels are detailed, along with the experimental techniques (mostly based upon image processing). Then, in Chapter 3, the numerical tools that proved to be necessary for

our work are presented. First, the Surface Evolver software, which allows one to obtain the equilibrium shape for a liquid-shape interface and that we used to study the capillary shape of the liquid films trapped by capillary forces in the pore space of our micromodels. Interfacial shapes obtained from Surface Evolver were exported to Comsol so that the flow of liquid in the films could be computed, allowing us to take into account the impact of the evaporation-induced flow in the liquid films on the drying process.

Results are presented in two separate Chapters (each of which will be the basis for a scientific paper, in preparation at the time of writing). In Chapter 4, we relate the experimentally-studied drying kinetic of our micromodels to the characteristic of their pore space spatial arrangement. By tuning the cylinders pattern, one can first obtain micromodels for which the drying rate is almost constant, from the beginning of the drying experiment to the total evaporation of the liquid initially filling the system. Typically, this situation is obtained when the pore size decreases from the micromodel center to the periphery (the micromodels are axisymmetric). On the contrary, when the pores size increases from the center to the periphery, invasion of a stable drying front is observed, resulting in a much longer total drying time.

In Chapter 5, we present the results obtained with another type of micromodel where the cylinders are arranged in a “spiraling” pattern, a design inspired by phyllotaxic structure. In such systems, thick liquid films develop along the spirals during drying and play a key role in the drying kinetics. This situation is reminiscent of that already studied by Chauvet in capillary tubes with square cross-sections [10]. However, it is more complex because of the porous nature of the micromodel (whereas a single capillary tube, as studied by Chauvet, can be viewed as a unique pore), and because of the much more complex liquid films shapes. In such system, we present some experimental results on the liquid films effects on the drying kinetics, together with theoretical prediction, based on a visco-capillary drying model. Such a modeling requires the use of the Surface Evolver software to model the film shape, coupled with DNS simulations of the Stokes flow within the liquid films to compute the viscous resistance to the evaporation-induced flow.

Finally, as a last part of this thesis, several evaporation experiments performed on deformable micromodels are presented in Chapter 6. Elasto-capillary effects can indeed change the pore space geometry during the course of evaporation which in turn, as seen in the previous parts, affects the phases distribution within the pore space and the drying kinetic.

Chapter 2

Materials and methods

In this chapter, the experimental techniques are presented. Firstly, we detail the design strategy and microfabrication process of the micromodels used. Then, we turn to the various experimental techniques that were developed.

2.1 Global design strategy

Our goal is to conceive micromodels which will be in between the square cross-section, straight capillary tube and the 3D packing of beads in term of complexity of the pore space. We used micromodels consisting of 2D axisymmetric patterns of cylindrical pillars (called cylinders in the following) sandwiched in between 2 parallel plates. Different micromodels were realized, with different spatial arrangement of the cylinders: with a positive or a negative gradient in cylinders spacing in the radial direction and with a Fibonacci spiral arrangement

2.1.1 Pattern with radial gradient in cylinders spacing

Two designs were considered. In Figure 2.1a, the spacing between the pillar decreases from the micromodel center to its periphery, whereas the opposite is true for the second case, see Figure 2.1b). From the side view, it can be seen that the circular bottom plate has a slightly larger diameter than the top plate. The micromodel thickness is denoted h .

Since the design method is similar in both cases, we detail below only the case of the pattern shown in Figure 2.1a. On this design, the cylinders are positioned around concentric circles. Each circle is marked out by an integer number n and has a radius R_n . One starts with the outermost circle of radius R_1 (which also determines the whole size of device). The spacing S_1 between the cylinders located around this circle is chosen ($S_1 = 620 \mu\text{m}$) and therefore the number of pillars on the outermost circle is obtained. The radius R_2 of the second circle is $R_2 = R_1 - S_1$ and the cylinder spacing on this circle is $S_2 = S_1 + (\alpha 2^3 + \beta)$ with $\alpha = 0.0086$ and $\beta = 5$ (for the case shown in Figure 2.1a). Then, this procedure is repeated for the third circle and so on. To sum up, the pillar spacing on a circle $n + 1$, S_{n+1} , is set to be $S_n + (\alpha n^3 + \beta)$ and $R_{n+1} - R_n = S_n$, see the close-up in Figure 2.2. The

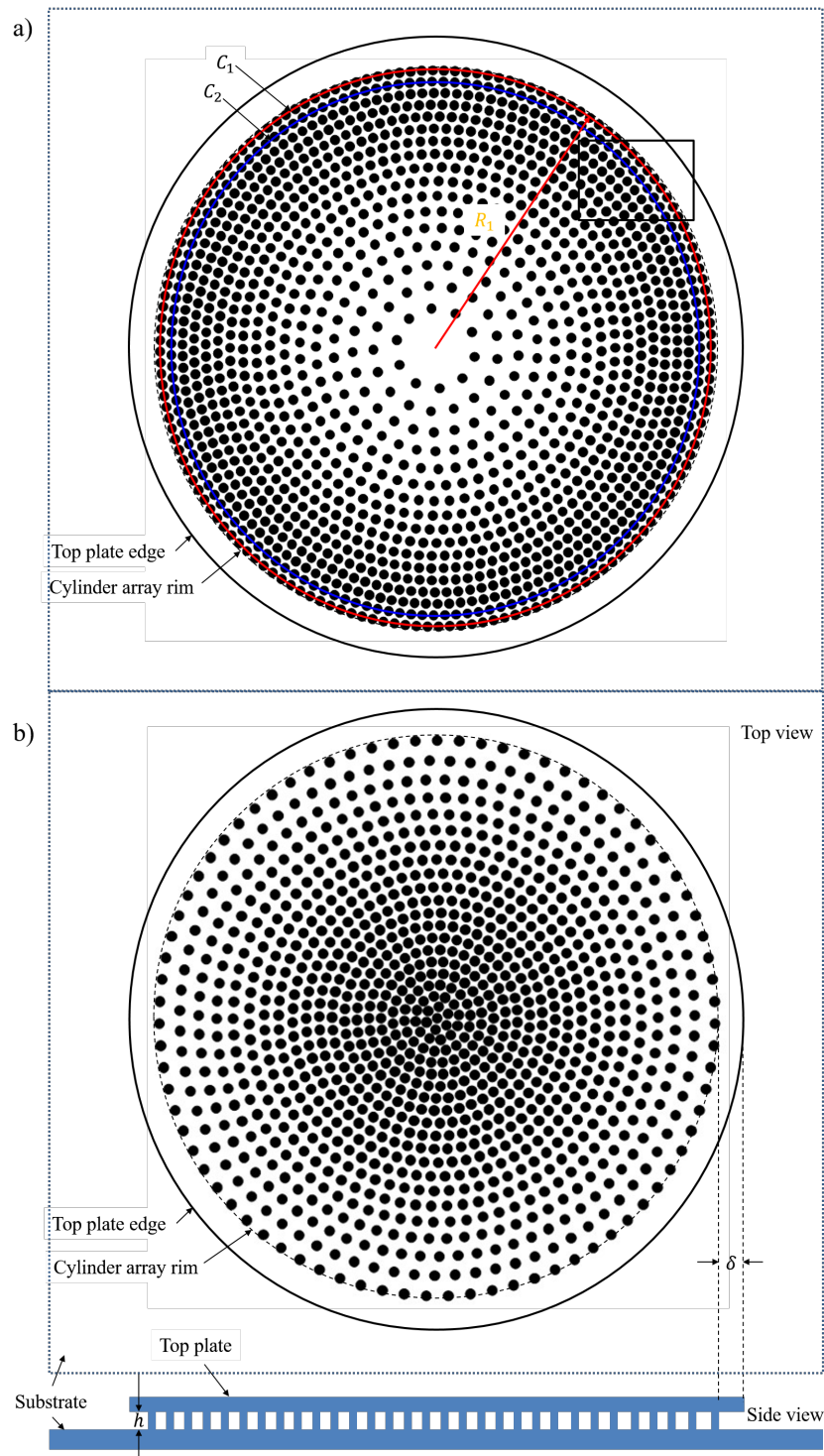


Figure 2.1: Micromodel with a radial pattern with decreasing (a) or increasing (b) spacing between the cylinders from center to periphery. The micromodel thickness is denoted h and δ is the distance between the circular top plate and the rim of the cylinders pattern.

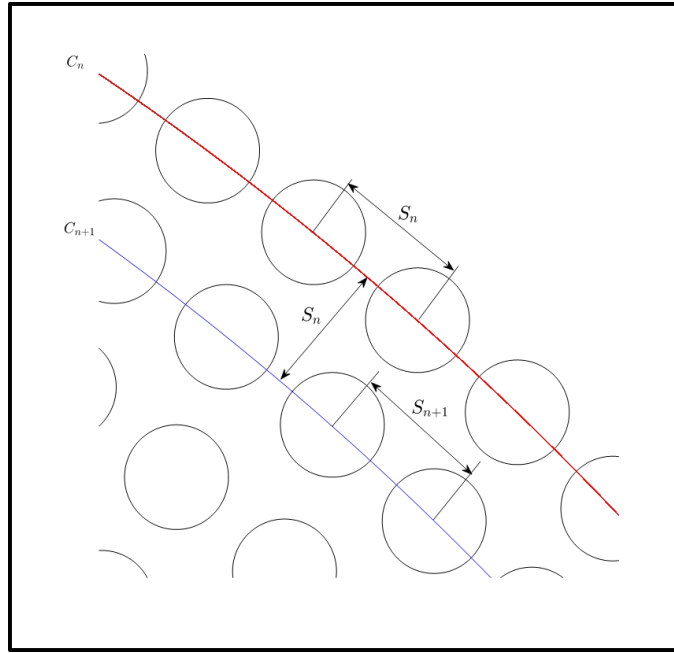


Figure 2.2: Zoom on the micromodel with a radial pattern, with decreasing spacing between the cylinders from center to periphery. The outer circle C_n ($n = 1$ for the outermost circle on the micromodel) is colored in red. Along this circle, the spacing between two neighboring cylinder is S_n . S_n is also the difference between the radius of circles n and $n + 1$: $S_n = R_n - R_{n+1}$.

radial position of the first cylinder to be positioned along a given circle is chosen randomly. That's why the cylinders are not aligned in the radial direction.

2.1.2 Fibonacci spiral pattern

Fibonacci spirals can be found in Nature, such as pinecones or sunflowers for instance, see Figure 2.4. Inspired by this design, we designed a network of cylinders with such a phyllotaxic pattern, as shown in Figure 2.3. There are 661 cylinders in the pattern for 28 spirals, each consisting of 23 or 24 cylinders. The algorithm used to generate such pattern is given in Appendix A.

This design was chosen because we intuitively felt that liquid films could be maintained along each spiral during evaporation, which proved to be correct in the following. Also Fibonacci spirals are a nice way to “pack” the cylinders while keeping a quasi-axisymmetry.

Figure 2.5a is a zoom on the region of interest marked out by a rectangle in the top of Figure 2.3. We introduce the center-to-center spacing between neighboring cylinders along each spiral direction, w_{\parallel} , and the center-to-center spacing between two side-to-side cylinders, belonging to two adjacent spirals, w_{\perp} . The values for w_{\perp} and w_{\parallel} are shown in Figure 2.5b, made dimensionless by dividing by $2d_c$ where d_c is the cylinder diameter.

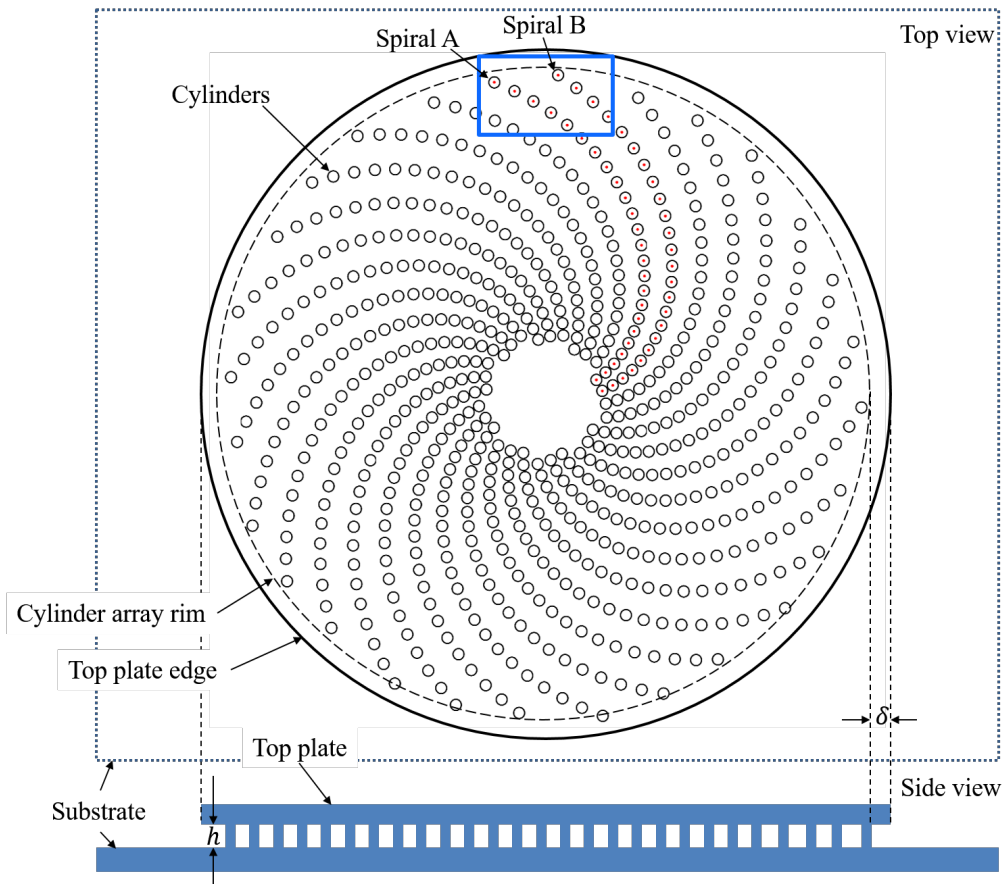


Figure 2.3: Fibonacci pattern. Two adjacent spirals (spiral A, B) are labelled with red dots at cylinders centers. The side view below show the thickness h and δ is the distance between the circular top plate and the rim of the cylinders pattern.

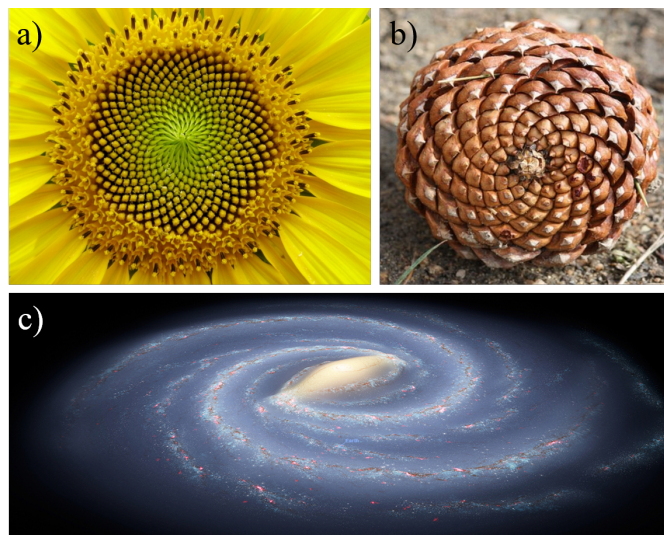


Figure 2.4: A sunflower (a), a pinecone (b) and also a spiral galaxy (c), all displaying a Fibonacci arrangement.

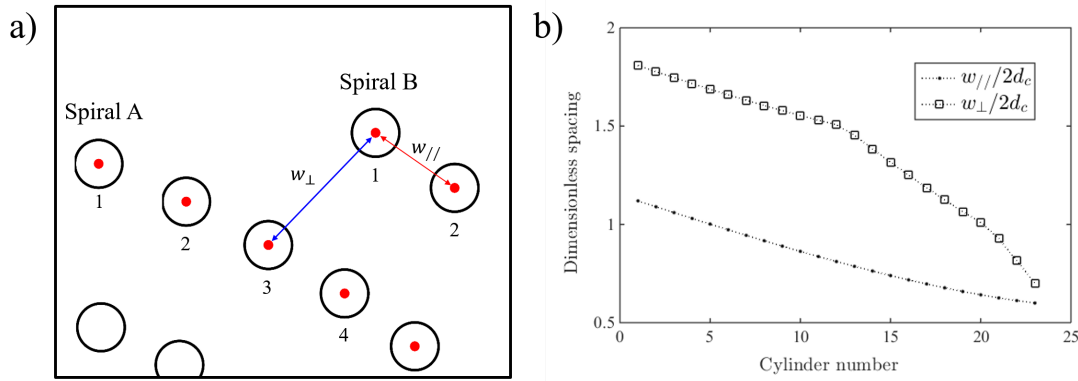


Figure 2.5: a) Zoom on the Fibonacci pattern: note the way the cylinders are numbered and the definition of w_{\parallel} and w_{\perp} . b) Values of the center to center spacing, w_{\parallel} and w_{\perp} , as a function of the cylinder number.

2.1.3 Micro-fabrication protocol

Photo-lithography technology was used to fabricate the micromodels with the design presented above. Photo-lithography is a mature micro-fabrication technology in the field of IC (integrated circuit) and MEMS (Micro electromechanical Systems), which uses light to transfer a geometric pattern from a photomask to light-sensitive chemical photoresist on the substrate. Two types of micromodels were fabricated: “large” devices with cylinder diameter d_c and height h equal to $500 \mu\text{m}$, and smaller ones scaled down to tenth, with $h = d_p = 50 \mu\text{m}$.

In this study, we use the photo-resist SU-8. It’s a commonly used epoxy-based (8 epoxy groups, see Figure 2.6a), negative resist. The part that is exposed to UV light cross-links, becomes insoluble to any photoresist developer so that one obtain the desired geometry after exposure to the developer. The transparency of SU-8 on visible spectrum is high enough, above a wavelength of 400 nm , the transmission is greater than 95%, see Figure 2.6b. Excellent optical transparency makes it suitable for optical measurement of the liquid overall saturation and spatial distribution in the micromodel, as described in Section 2.2 below. The Young’s modulus (E) for SU-8 hard-baked at 200°C is $E = 4.95 \pm 0.42 \text{ GPa}$ [50]. Such a high value prevents any unwanted deformation that may be induced by elasto-capillary effects. In addition to this, polymerized SU-8 is also considered to be chemically stable and resistant to most acids and solvents [17].

Microfabrication was done at LAAS-CNRS (Laboratoire d’Analyse et d’Architecture des Systèmes in Toulouse), by Pierre Joseph. The protocol is illustrated in Figure 2.7 and detailed below.

Micro-fabrication protocol

The micro-fabrication process of micromodels with a characteristic length of $500 \mu\text{m}$, for all designs, is described in the following. Note that the designed pattern was first drawn in the mask design software CleWin 4. The corresponding chromium photomask necessary for microfabrication were fabricated in LAAS. The successive

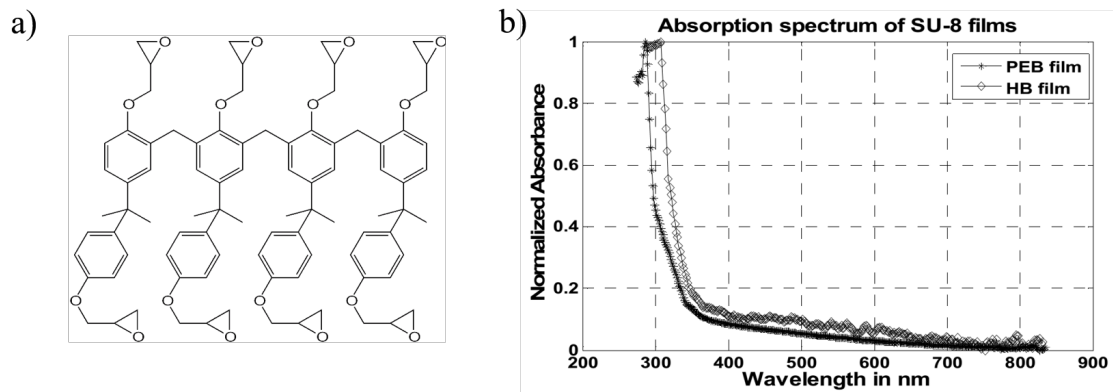


Figure 2.6: SU-8 photoresist molecular and its absorption spectra. a) Structural formula of SU-8 monomer, from wikipedia. b) Absorbance spectra of SU-8 for post exposure baked (PEB) and hard baked (HB) SU-8 films, refers to [6].

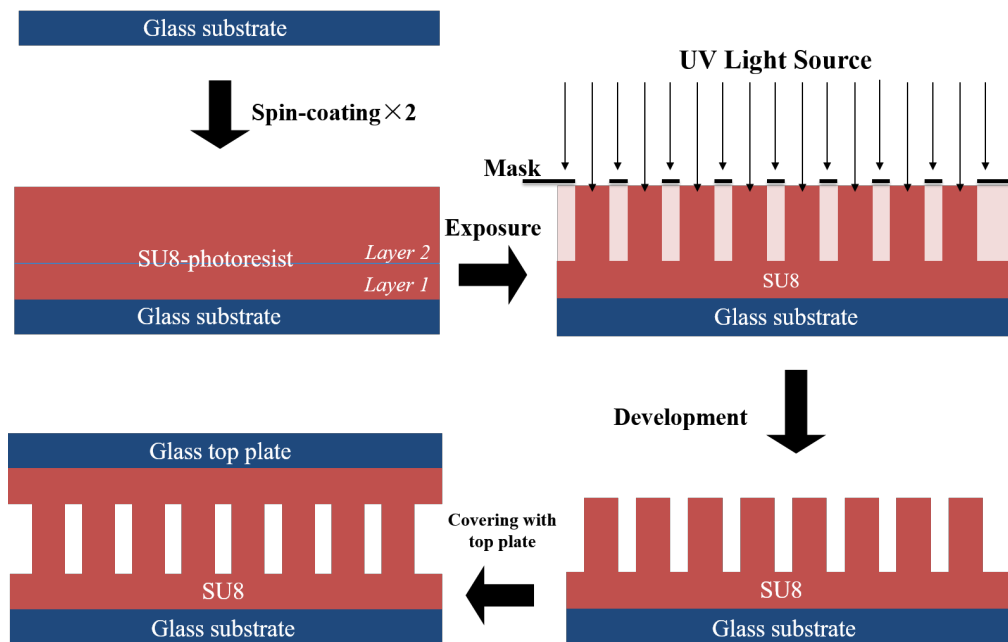


Figure 2.7: Microfabrication protocol using photo-lithography.

protocol steps are as follows:

1. Clean the bottom glass wafer (4 inch in diameter, 1 mm in thickness) by exposure to an oxygen plasma (1 min, 500 W, 1000 sccm oxygen flow rate). Plasma treatment will enhance the wetting/adhesion of bottom wafer.
2. A first 10 μm thick layer of SU-8 3005 is spin coated on the wafer (spinning speed: 3000-3500 rpm) and fully reticulated (soft Bake 3 min, 95°C, full exposure under a mask aligner, and post-exposure bake 3 min, 95°C), in order to get a homogeneous SU-8 bottom substrate.
3. SU-8 cylinders fabrication: two methods have been developed to realize the

500 μm -thick cylinders. The first approach relies on three cycles of spin-coating and curing of SU-8 3050 on an automated spin-coater (EVG120), since the designed cylinder height is quite important for microfabrication. Baking is realized (95°C) overnight for releasing stress. The second approach consists in simply pouring 5.2 mL on the wafer, followed by curing and exposure. For such thick patterns, a precise weighting enables to obtain the required pillars thickness.

4. Exposure is done on a mask aligner (MA6, Karl Suss), in hard contact mode to keep good resolution for such thick resist. The exposure time is set to 66 s, in order to reach the appropriate dose with a $16\text{ mW}/\text{cm}^2$ light power. A 365 nm wavelength filter, best suited for SU-8 resist, is used to enhance resolution.
5. Post-exposure bake (PEB) is realized to complete reticulation of the exposed zones, on a programmable heat plate, from 65°C to 95°C (7 min) with progressive temperature variations to limit stress. This process is not shown in Figure 2.7.
6. Development: the non-reticulated photoresist is removed by immersion in a solvent with agitation for about 30 min.
7. Hard-bake (HB): finally, a further cross linking of SU-8 is realized, to release mechanical constraints in SU-8 (not shown in figure 2.7).
8. Preparing the top plate wafer: we spincoat SU-8 3005 at 900 rpm on a glass wafer, to obtain SU-8 thickness about 10 μm . We soft bake for 7 min at 95°C to evaporate solvents. In order to keep the resist sticky, post-exposure bake is omitted here.
9. Assembly (bonding top and bottom substrates) is achieved on a wafer bonder machine (AML WB4), by applying a controlled force (500 N) upon heating ($\sim 75^\circ\text{C}$) for a few minutes. After assembling the top plate and bottom plate, the whole device is exposed on MA6 for 30 s, and then PEB on SU-8 heater with ramp 3 min at 95°C , Hard Bake 1 min at 110°C . These final steps permits SU-8 reticulation and definitive sealing of the device.

For the smaller systems, the typical dimension of which is one tenth that of large scale device, the diameter of each micromodel is around 3.5 mm. Around 25 devices, located on 1.5 cm grid, can be put on a 4 inch wafer. The protocol is given below:

1. Bottom wafer (4 inch glass, AF32[®], 500 μm in thickness) was cleaned under oxygen plasma for 15 min, power 800 W, 1000 sscm.
2. Cylinder array realization: spin-coating SU-8 3005 on glass wafer with 50 μm thick (spinning speed: 3500 rpm), then soft bake for 3 min at 95°C . Exposure full wafer with mask 1 on mask aligner (MA150, Suss Microtech), with filter 365nm. Exposure time is set to 18.6 s in order to obtain the appropriate dose with a lamp power of $10.5\text{ mW}/\text{cm}^2$). PEB for 3 min 30 s at 95°C to achieve exposed resist reticulation, followed by standard development for 12 min.

3. Top plate realization: in order to have a precise alignment of the top plate, the method to realize the chip enclosure was changed. The top plate on small scale device are coated with a negative dry film photoresist (DF1020), with thickness of 20 μm . Because this dry film is also epoxy-based, it has same wetting property as SU-8. The top plate is added on top of pillar by lamination, followed by photo-lithography, which permits aligning pillar pattern with the circular shape of the top plate, thanks to mask aligner. Two masks were thus needed, one is with cylinder arrangement pattern (mask 1), the other is with top plate pattern (mask 2).
4. Laminating the drying epoxy film (DF1020, 20 μm thick) on Shipley system (60°C, pressure 2 Bars, velocity 1 m/min). Exposure for 25 s on MA150 system (no filter, hard contact) after alignment, with mask 2. PEB on SU-8 hotplate with ramp (1 min at 65°C, up at 10 °C/min, 7 min at 100°C, down at 5 °C/min to 25°C.) Development in cyclohexanone for 6 min. Hard-bake for 1 hour at 175°C.

2.1.4 Characterization of the micromodels

Large micromodels

Images of the large micromodels are shown in Figure 2.8. Owing to the thin thickness of SU-8 layers and the use of glass as supporting bottom and top plate, the device exhibit great transparency, as shown in Figure 2.8b,c and d, an important characteristic for measurements based upon image processing.

Measurements were done after micro-fabrication to check its quality. Note that this was done prior to the bonding of the top plate. The average thickness of each large scale device was measured by an optical profilometer at several locations on the wafer. Averaging over a dozen of different locations, a first wafer was found to be $525 \pm 2 \mu\text{m}$ in thickness. This is very close to the desired 500 μm and remarkably homogeneous. A second one was found to be less good with a thickness of $515 \pm 35 \mu\text{m}$, the non-uniform thickness being probably due to a non-horizontality of the hotplate when the several hours soft bake was performed (step 3 of the protocol). The first wafer was used in the experiment for the Fibonacci spiral pattern and the radial pattern with decreasing center-to-center spacing from the center to the edge of the micromodel. The third pattern (radial pattern with increasing center-to-center spacing from the center to the edge) was obtained on a third wafer which was found to have a much smaller thickness, $360 \pm 20 \mu\text{m}$.

The bonding of the top plate was a tricky operation and we suspect that it may have resulted in a slight crushing of some of the external cylinders. Also, it was found by inspection that the top plates were not perfectly centered onto the pattern.

The dimension of the whole device shown in Figure 2.8b is 35 mm; this diameter is determined by its top plate diameter. The spacing between the pillar array edge (red circle in Figure 2.8b) and the top plate edge (blue circle in Figure 2.8b), δ , is not uniform along the micromodel periphery. This defect is caused by the fact that the top plate is positioned manually prior to the bonding stage. To quantify

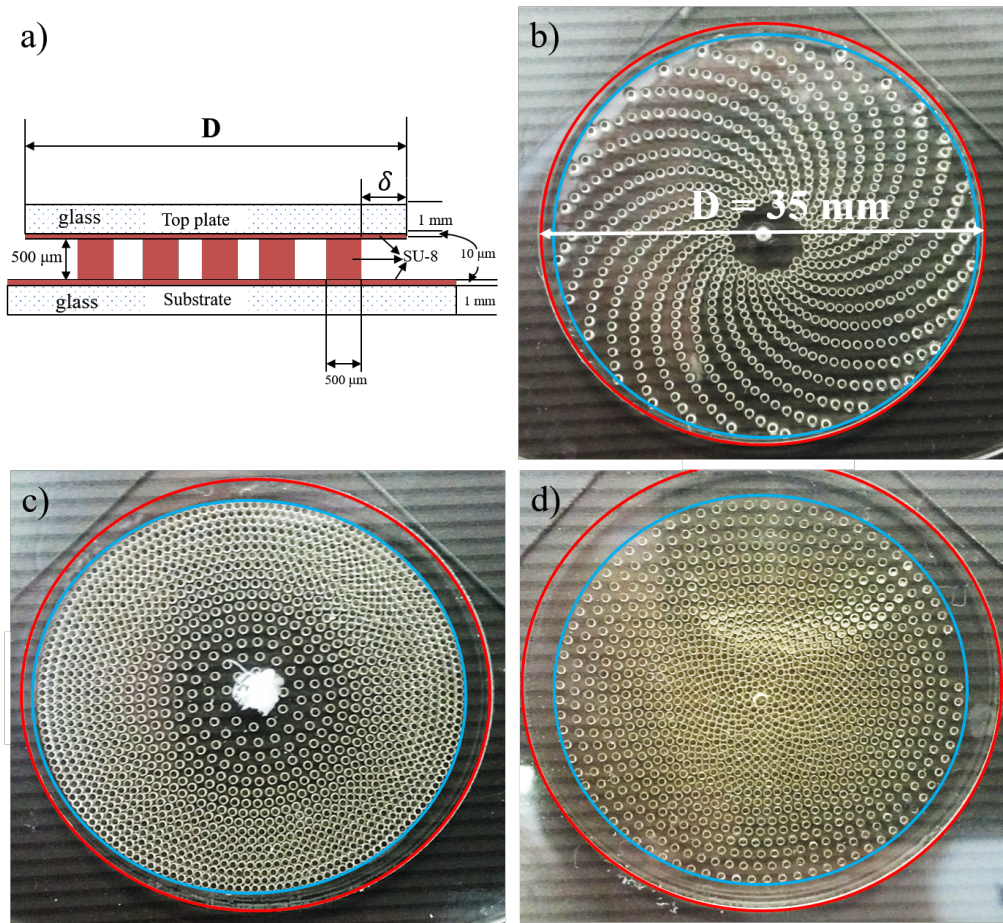


Figure 2.8: Large micromodels. a) Schematic of the sectional side of the pillar array. b) to d) The three kinds of design micro-fabricated. The top plate diameter is 35 mm, red and blue circles represent the edge of top plate and edge of cylinders array respectively.

it, we measured δ for the three micromodels as a function of a radial position along each micromodel periphery, see Figure 2.9. The value of δ is in the range $[0.4 - 1.4]$ mm for the Fibonacci spiral micromodel, $[0.9 - 2]$ mm for the radial array with decreasing spacing between cylinders from center to periphery and $[2 - 3.1]$ mm for the third design.

Small micromodels

The small micromodels were designed to be ten times smaller than the larger systems, that is with a thickness h and cylinders diameter d_c reduced to $50 \mu\text{m}$. Before bonding of the top plate by lamination, they were characterized with an optical profiler system (Veeco WyKo NT) and SEM. Some typical results are shown in Figure 2.10.

The center of a small micromodel, where the spacing between the cylinders is the smallest is shown in Figure 2.10a. We can see that the cylinders are well-defined, without collapse and that the height keeps good uniformity (see the homogeneity of

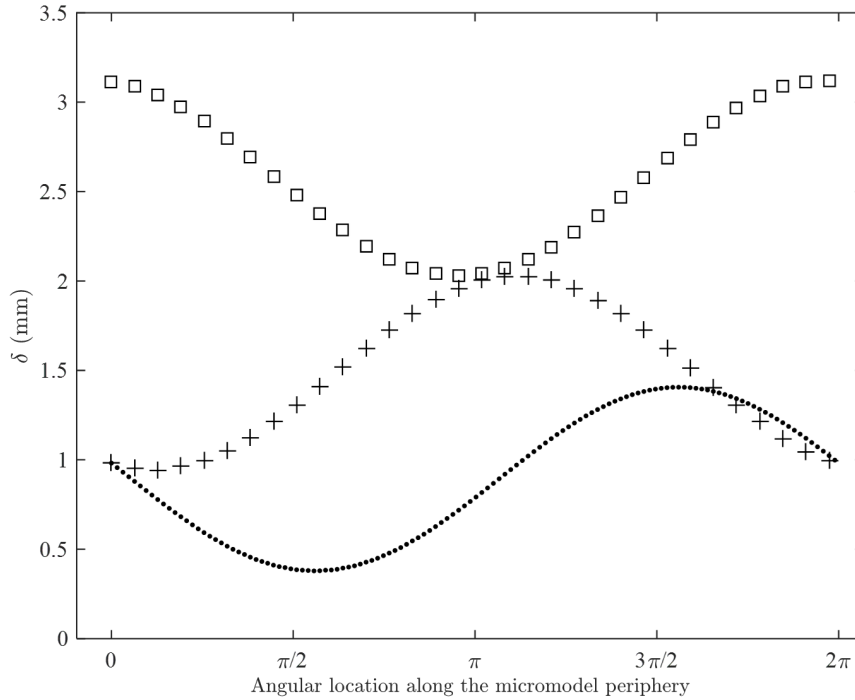


Figure 2.9: Margin spacing variation range in large scale array. Dots: Fibonacci spiral pattern; Squares: radial pattern with increasing spacing from center to periphery; Crosses: radial pattern with decreasing spacing from center to periphery.

the red intensity, which represents the height). The intervals between the cylinders are clean (no unexpected impurities). The averaged thickness is $h = 54 \mu\text{m}$, with a few microns as a maximum difference between different locations.

After the top film was laminated on the device, the thickness measurement was repeated, see Figure 2.10b) for a radial pattern for instance. In this case, the center region is a little bit lower than the region closer to edge, probably due to deformation of the soft film during lamination. Also, having less cylinders in the center imply less mechanical support for the top film. The opposite is observed for the radial pattern with opposite radial gradient in pillar spacing. Contrary to what was observed with the large micromodels, the top circular film is well-centered on the patterned region. The spacing δ is constant and equals to the designed $100 \mu\text{m}$.

2.2 Experimental setup and techniques

2.2.1 Equipmental setup, protocol and working fluids

Equipmental setup

A sketch of the experimental setup is shown in Figure 2.11. The micromodel under study is placed on a balance and direct visualization are made from the top by a CCD camera. The frame acquisition rate and other camera settings (exposure time,

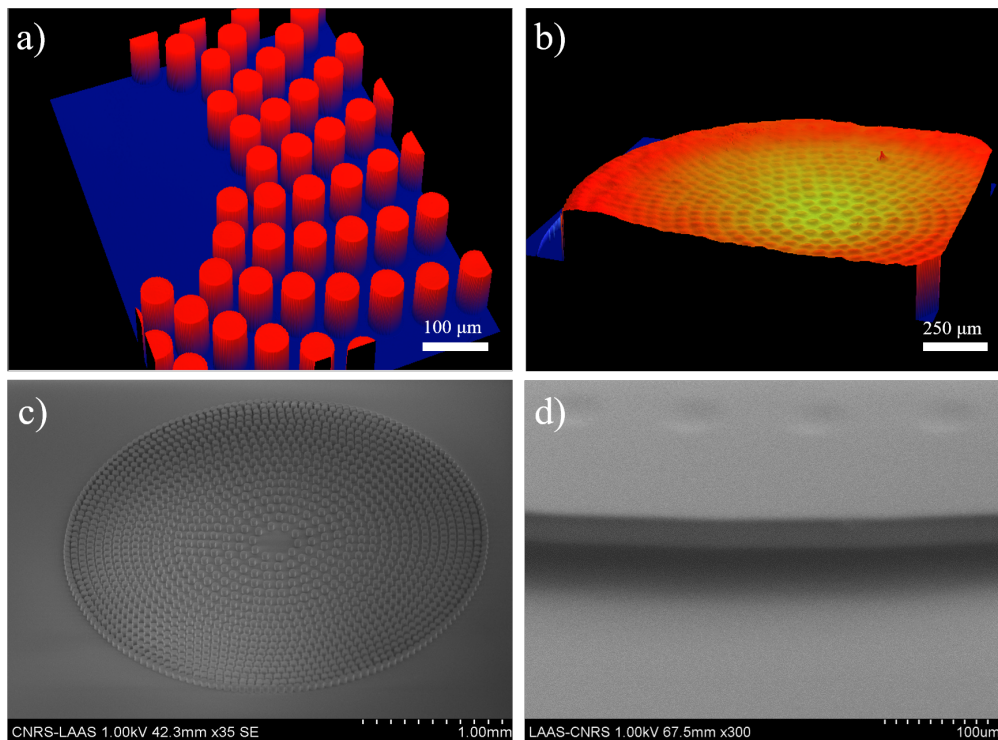


Figure 2.10: Post-microfabrication characterization of the small systems. a) Partial view of a Fibonacci spiral array by optical profilometry. b) Thickness measurement after covering with the top plate film, for a radial pattern. The height at the periphery of the micromodel is slightly higher than in the center region, the difference is less than $3\ \mu\text{m}$. c) SEM image of a radial array before covering with top plate film. d) SEM image of a radial array after laminating the top plate film. The most external pillars go a bit through the film, but the margin region remains open.

etc.) are controlled by the CamWare software. The camera used has a 2048×2048 pixels CCD sensor. With an appropriate lens, one can ensure to acquire images with a nice spatial resolution (down to 1.8 microns per pixel).

In order to increase the contrast of the images, a plane LED light source (PHLOX LedW-BL) that offers a homogeneous plane light (Uniformity 97%) is placed below the micromodel, on the balance. Because the evaporation process is sensitive to ambient temperature, the close distance between the LED panel and the micromodel may be a problem. To decrease any heating due to the LEDs, a transparent board with height of 10 mm is used to avoid the direct contact between device and light source. Second, the light source is triggered by an external source and synchronized with image acquisition. Therefore, between two images, the light is off and the micromodel does not receive the heat radiation of light source.

As illustrated in Figure 2.11, the LED light source is connected to its electronic controller. During the experiments, we found that the connecting wire has a great influence on the balance data recording. Our micromodels are so small (liquid mass below 0.3 g) that even a slight vibration from the wire can perturb the balance recording. That's why we finally ran the image and mass acquisition as two distinct experiments: when the mass is acquired, the micromodel is directly put on the scale

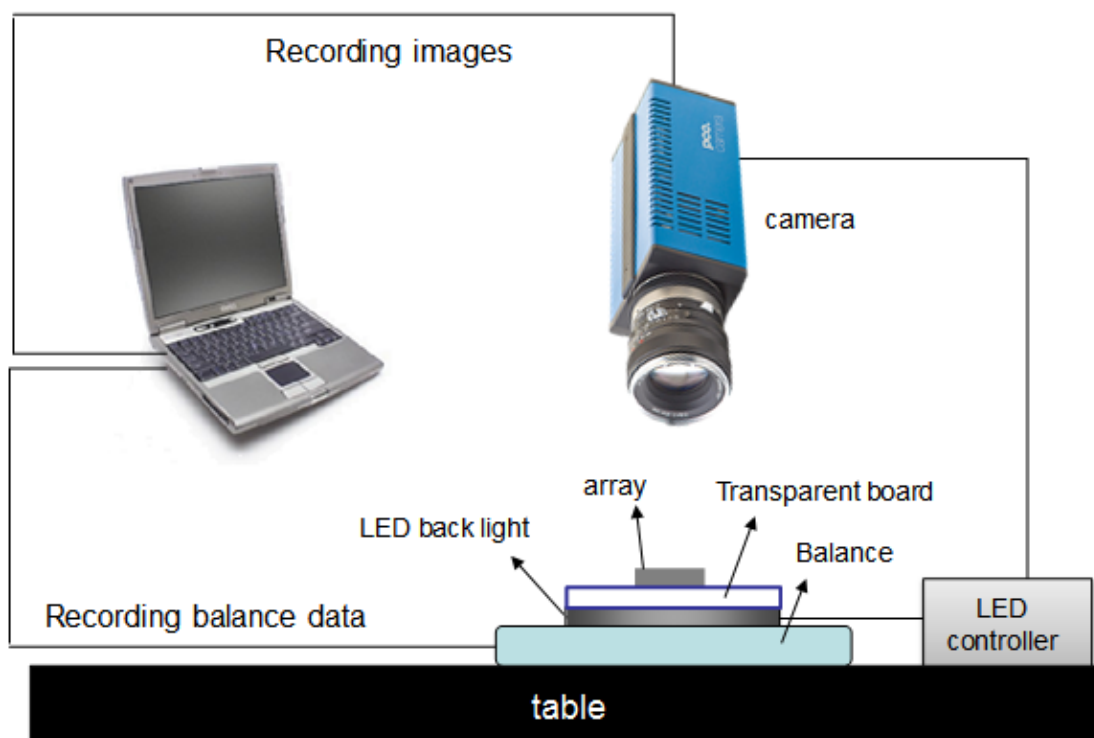


Figure 2.11: Sketch of the experimental setup.

and when images are recorded, no balance is used.

Protocol for drying experiments

Firstly, the camera and computer are set up on the working table and lighted up 2 hours before starting recording. If needed, the lens and camera sensor should be cleaned by an air blower to remove any dust. The glass bottles used for carrying the liquid are cleaned with detergent, water and ethanol successively, then dry off in oven and rinsed three times using the volatile liquid used in the subsequent experiments. Before filling the micromodels, the liquid used in the experiment is placed in the lab room at least one hour, so that it can reach the ambient difference (the chemicals in our lab are stored in a specific lab room, which is slightly cooler than the lab room where the experiments were performed).

The working table and camera are carefully adjusted horizontally with a level. This operation is not trivial since departing from the vertical axis can deteriorate the image quality, because the camera focusing plane do not overlap with the thin micromodel median plane (because we typically zoom a lot on the micromodel, the depth of focus of the camera lens is very small).

We used disposable pipette to transfer the liquid to the micromodels. The liquid is released at the edge of cells, and then fully fills the cell by capillary suction. Water was used for a couple of tests. As it is non-wetting on SU-8, the filling procedure was different: the micromodel was immersed under water in a petri dish, and put under vacuum during 10 min which proved to be enough for water to fully saturate

Index	$\rho_l(\text{g cm}^{-3})$	$\lambda(\text{mN m}^{-1})$	$\mu_l(\text{mPa s})$	$D(\text{mm}^2 \text{s}^{-1})$
Ethanol	0.789	22.27	1.201	12.1
2-Propanol	0.781	23.00	2.040	9.8
Pentane	0.626	15.48	0.240	15.5
Hexane	0.661	17.89	0.300	8.1
Heptane	0.679	19.66	0.387	7.2
Octane	0.703	21.62	0.537	2.1
Nonane	0.718	22.85	0.727	1.6
Decane	0.730	23.80	0.920	1.3
Dodecane	0.750	25.35	1.340	0.8

Table 2.1: Working liquid properties at 25 °C: ρ_l , λ , μ_l , D correspond to liquid mass density, surface tension, dynamic viscosity and diffusion coefficient for liquid vapor in air, respectively.

the micromodel, without trapping air bubbles. Once the micromodel is filled, the optics is carefully focused in order to get a sharp contrast between air and liquid-filled region of the micromodel and the drying experiment starts.

Working fluids

In this study, we use several kinds of volatile liquids and deionized water as working fluids. The volatile liquid used are ethanol, isopropanol, pentane, hexane and heptane. Their basic physical and chemical properties at room temperature are presented in Table 2.1. All the volatile liquid are from Sigma-Aldrich with purity of chemical analysis level, which is at least 99%. Besides, the volatile liquid used here is chemically stable with respect to SU-8, no dissolution or swelling phenomena were observed during experiments. These liquids exhibit different volatility and viscosity in normal condition, so different drying rates and liquid film effects are expected.

The contact angle of all these working liquids on SU-8 was estimated by a Drop Shape Analyzer (DSA100, KRÜSS) with a room temperature equals to 22°C. This is a very tricky measurement as the small-volume, sessile droplets that are deposited by the system on a SU-8 substrate evaporate very quickly. It is nonetheless possible to see how they spread easily on the surface while evaporating. Consequently, we consider that the contact angle θ is close to zero in the following, for all the volatile fluids used. Note that the contact angle of deionized water on SU-8 equals to $70 \pm 1^\circ$. It was also measured by the Drop Shape Analyzer as deionized water was used in a couple of test experiments.

2.2.2 Mass drop recording by balance

The first obvious way to obtain the drying rate is to record the mass of the micromodel during the drying experiment. To that end, we used a Mettler Toledo balance with a ± 0.001 g accuracy. The data acquisition is controlled by a PC and a mass recording is typically done each second. Note that the data obtained with the

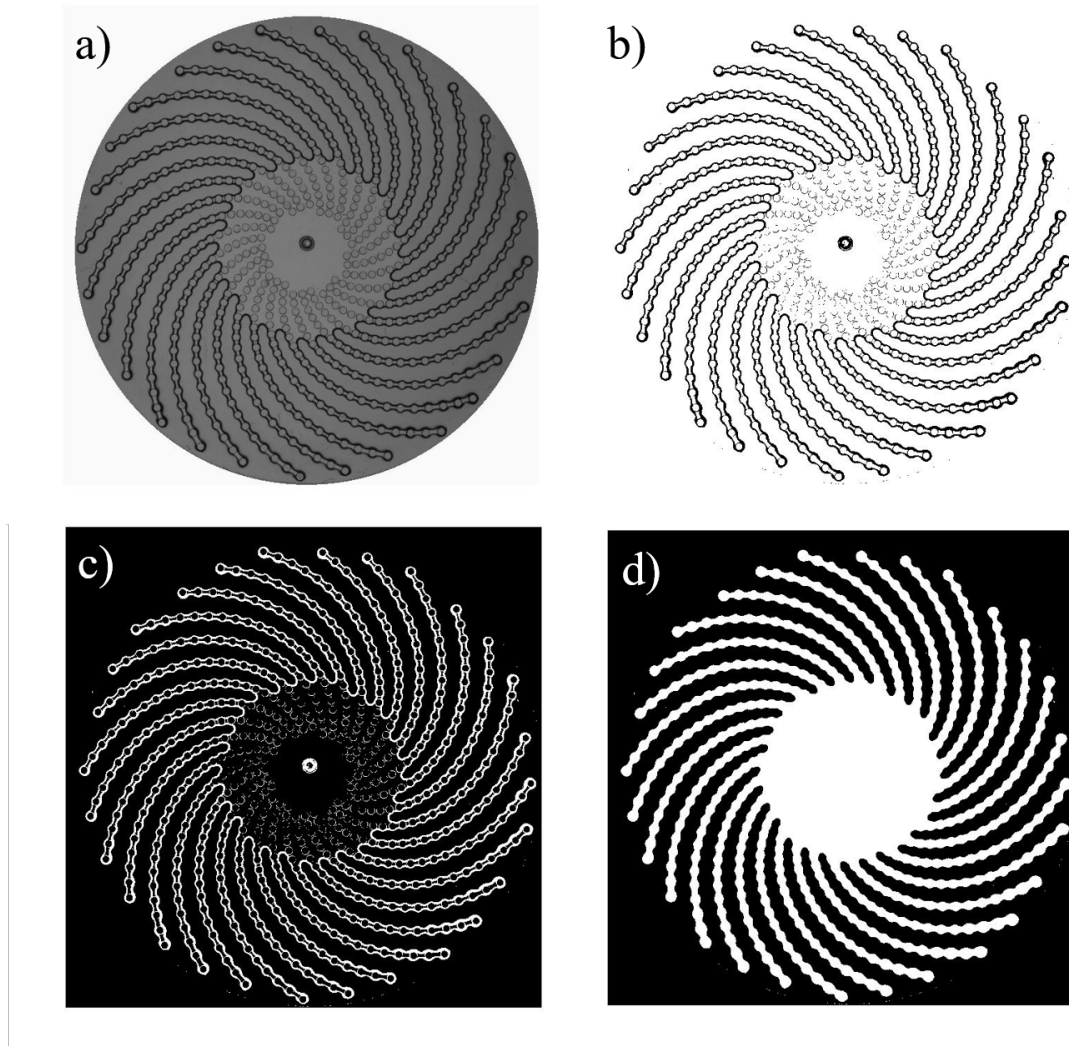


Figure 2.12: Image processing procedure for the Fibonacci spiral array. a) Original tiff image, after removing the region outside the top plate; b) Binarized image; c) Inverse binarized image; d) Image after filling the enclosed region of c).

balance recording, $m(t)$ are quite noisy and must be filtered out before calculating the drying rate dm/dt . A Savitzky-Golay filter implemented in Matlab was used to that end.

The micromodel weight measurement is only possible with the large micromodel as the total amount of fluid in the small micromodel is too small to be weighted with a sufficient accuracy. This is why we also developed a measurement technique based on image processing, that does not depend on the micromodel size.

2.2.3 Image processing

In this subsection, we explain the principle of image processing method used for predicting the mass drop in drying experiments. First, one has to mention that this technique is made possible because the transparent nature of the micromodels.

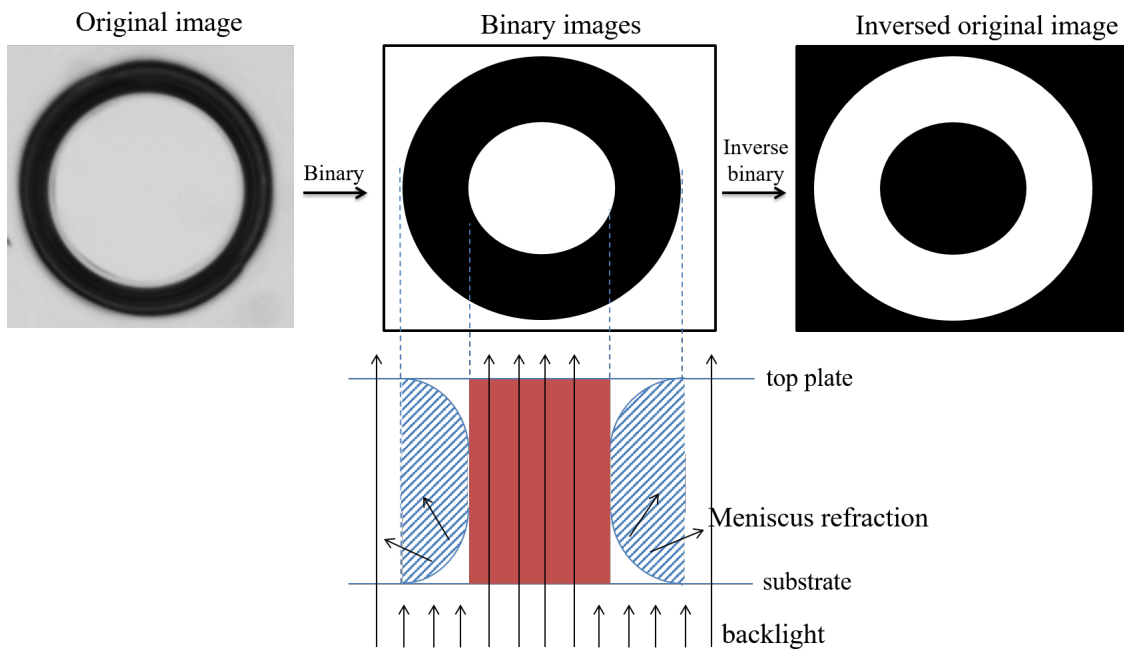


Figure 2.13: Light deviation by a meniscus. Here the case of a liquid ring located around a cylinder is shown as an example. The quasi-parallel light rays from the LED backlight are refracted when encountering the liquid meniscus interface. Binarization (and subsequent inversion of the gray levels) is therefore straightforward.

Also, the ombroscopy configuration used, with the micromodel positioned between the LED panel (which provides an almost parallel light) and the camera is the preferred one when it comes to detecting liquid-gas interfaces.

A typical image obtained with the CCD camera is shown in Figure 2.12a) (the images are saved in a 16-bit tiff format). On such an image, the menisci appear as the darkest regions. In fact, the curved menisci deviate the almost parallel light coming from the backlight, see Figure 2.13. The contrast between the dark menisci region and the bulk fluid region (liquid or air) is large enough so that applying a binarization operation is easy, leading to the image shown in Figure 2.12b, which is then inverted and filled, Figure 2.12c and d (inversion is necessary for the built-in Matlab function *imfill* to work).

Before explaining how to obtain the mass of liquid in the micromodel using such images, it must be mentioned that the very good spatial resolution allows us to perform precise measurements at the scale of the cylinders. Figure 2.14a shows a close-up on a liquid film that does not extent over all the cylinders of a spiral. Figure 2.14b shows the gray value profiles obtained along line 1 and 2 highlighted in Figure 2.14a. Such profiles show that the contrast is very good: a wide range of binarization threshold can be chosen to isolate the meniscus region. Also, quantitative information, on the width of the liquid bridges for instance, could be obtained from such images.

We now turn to the measurement of the liquid volume contained within the micromodel. The starting point is a binarized, filled image as the one shown in

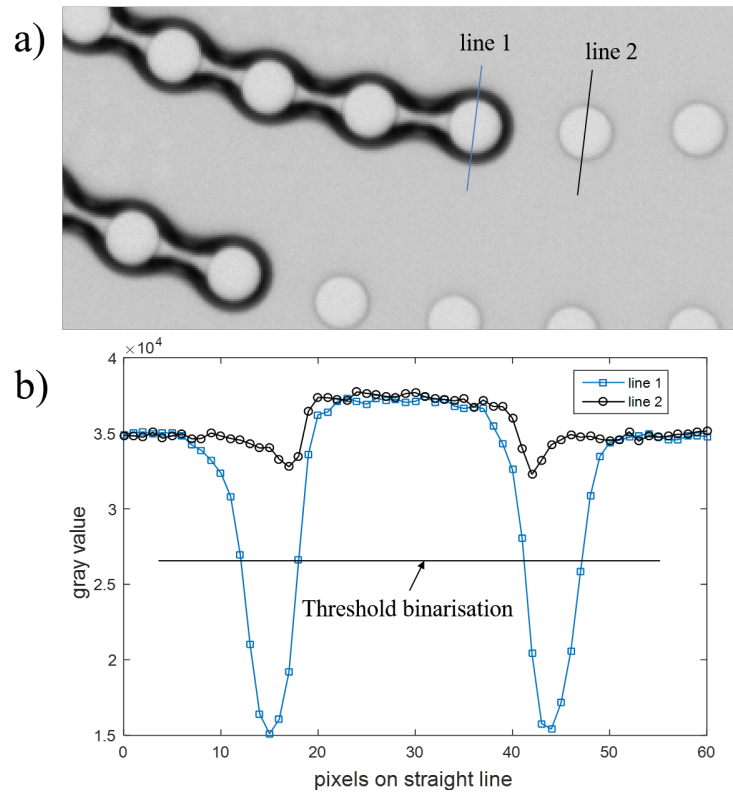


Figure 2.14: a) Zoom on a liquid bridge; b) Light intensity profile along line 1 (in blue) and line 2 (in black).

Figure 2.12d. The total area of the white region, A , can be readily obtained by image processing (using the Matlab *regionprops* built-in function). The same algorithm can be used to detect any cylinder that is no longer wet by the fluid and thus appear as an isolated circle. Knowing the total number of cylinders in the pattern (661 in the case of the Fibonacci pattern), one can have a first estimate of the liquid volume in the micromodel: $V = A \times h - N_w \times V_p$ where N_w is the measured number of cylinders embedded in the liquid cluster and $V_p = \pi h d_c^2 / 4$ the volume of a cylinder. Then, one has to note that the white region of area A seen in Figure 2.12d contains the total projected area of the menisci. This total projected menisci area, A_m , can be obtained from the image shown in Figure 2.12c (before the filling operation). In the menisci region, the fluid is not present over the full height h of the micromodel and this has to be taken into account. In fact, the formula above giving V over-estimates the liquid volume, whereas the alternate expression $V = (A - A_m) \times h - N_w \times V_p$ would underestimate it.

To estimate the amount of liquid in the menisci region, we used the software Surface Evolver to simulate the capillary shape of a liquid bridge located in between two cylinders. Surface Evolver and the way we used it will be presented in the following Chapter. For the moment, let us just consider a typical liquid bridge shape as shown in Figure 2.15, top and two particular outlines of this shape, Figure 2.15, bottom.

The total volume of liquid in the liquid bridge is a control parameter for the

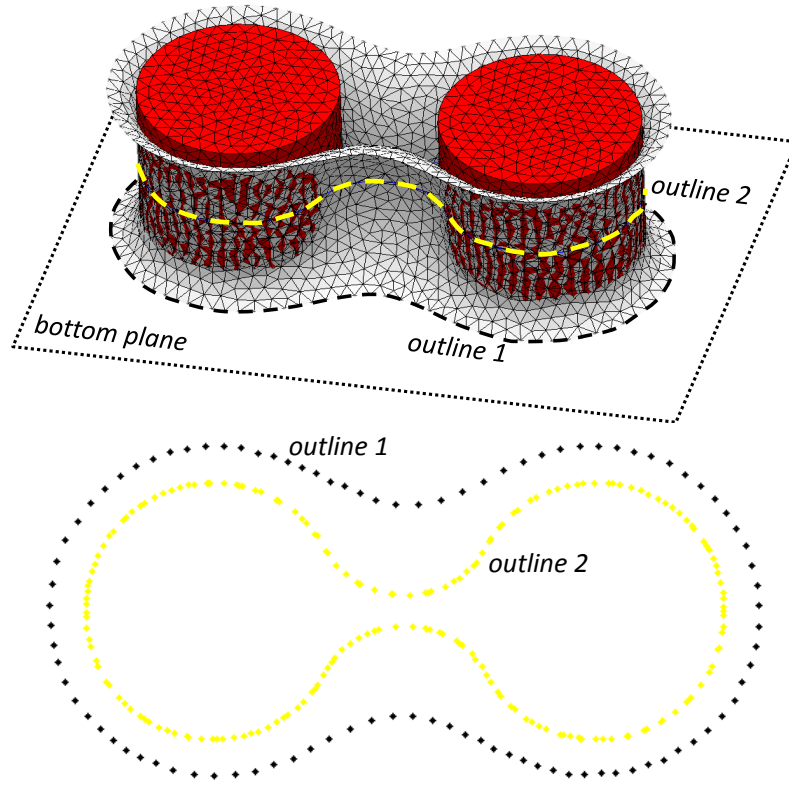


Figure 2.15: Top: typical liquid bridge capillary shape obtained from Surface Evolver (see next Chapter for details). The liquid bridge is trapped between two cylinders that appear in red and the liquid-gas interface appears as meshed with triangular elements. Bottom : two outlines of the capillary shape, at $z = 0$ (in black, bottom plane) and $z = h/2$ (mid-plane, in yellow).

Surface Evolver simulation; let's denote it V_{SE} . Let's also introduce A_1 and A_2 , the areas enclosed by the outlines 1 and 2 shown in Figure 2.15, bottom (minus the projected areas of the two cylinders). Following the image processing procedure explained above, the two above-mentioned formulas to compute V would come down to measure a liquid volume $A_1 \times h$ (over-estimation) or $A_2 \times h$ (under-estimation). The volume of gas in the meniscus region is $A_1 \times h - V_{SE}$ and the volume of the region between the two outline is $(A_1 - A_2) \times h$. Consequently, the liquid content in the meniscus region is $1 - \lambda$ where $\lambda = (A_1 h - V_{SE}) / (h(A_1 - A_2))$. The value λ can be computed from Surface Evolver simulation of the liquid bridge shape and post-processing of the obtained shape (to get A_1 and A_2). It depends on the spacing w_{\parallel} between the cylinders, the liquid volume trapped in the liquid bridge and on the contact angle, as seen in Figure 2.16. Finally, in the general case introduced above, the volume of liquid V in the cluster is estimated to be $A \times h - (1 - \lambda) A_m \times h - N_w \times V_p$, taking λ equals to a single average value of 0.16.

This technique for measuring the liquid content in the micromodel was validated against mass measurements performed with the balance. In Figure 2.17, the balance data are compared to data obtained from image processing with and without the

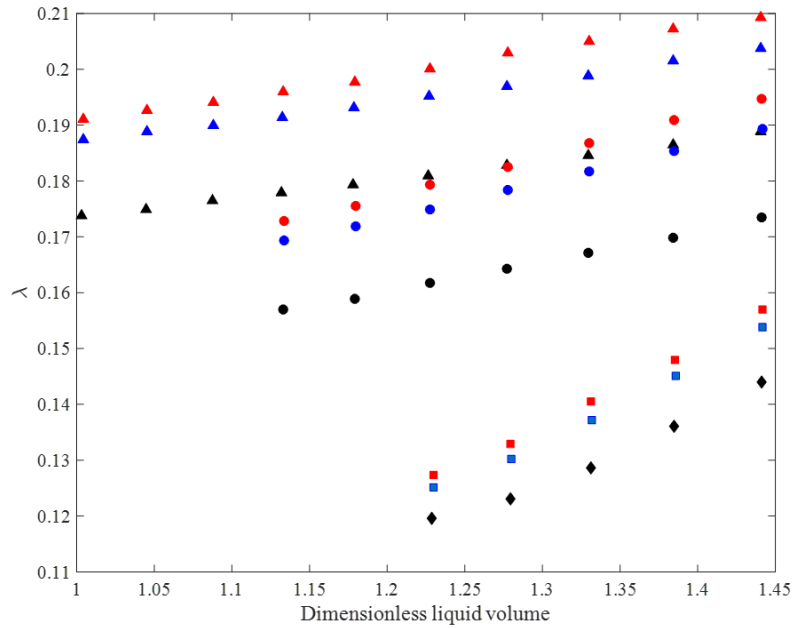


Figure 2.16: λ values as a function of the liquid bridge volume used in Surface Evolver, for 3 different center-to-center spacing $w_{//}$ between the cylinders (made dimensionless with $2d_c$): 0.7, 0.9 and 1.1 (marked with triangles, circles and squares respectively) and for different contact angle, $\theta = 0, 10, 20$ (red, blue and black symbols respectively). Note the liquid volume is made dimensionless by dividing by $d_p \times h \times w_{//}$.

specific correction for the menisci region discussed above. If the latter is taking into account, data from the balance and from image processing are similar. Note that two different experiments were performed for this validation test: one with balance only and a second one with the backlight but no weighting, as already explained. Note that in the following, evaporation rate measurement from image processing will be mostly used for the experiments performed with the small Fibonacci spiral pattern.

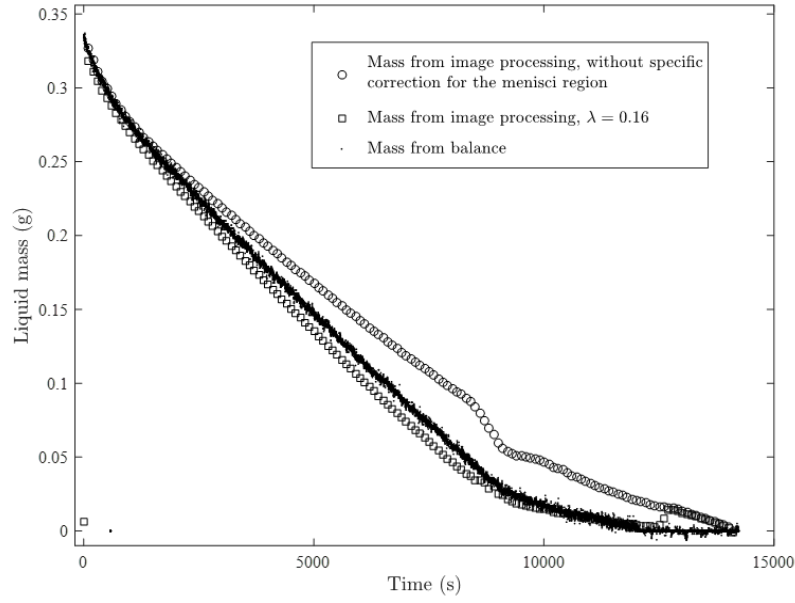


Figure 2.17: Evolution versus time of the mass of ethanol in a large Fibonacci pattern micro-model. Dots: data from the balance. Circles and squares: data from image processing. Circles do not take into account the menisci region correction ($\rho_l(A \times h - N_w \times \pi h d_c^2/4)$) whereas squares do ($\rho_l(A \times h - (1 - \lambda)A_m \times h - N_w \times \pi h d_c^2/4)$) with $\lambda = 0.16$.

Chapter 3

Numerical techniques

In this chapter, we present the two numerical tools that were used in the present work. First, we deal with the energy minimization software called Surface Evolver. We used it to simulate liquid-gas interface shapes obtained in several situations of interest in the present study, such as the case of a liquid ring around a cylinder, a liquid bridge located between two cylinders, a chain of liquid bridges, etc... For liquid bridges, the equilibrium interface shape obtained in Surface Evolver was then exported and used in COMSOL Multiphysics to compute the Stokes within the liquid and get access to the viscous flow resistance β .

3.1 Surface Evolver: presentation and a first test case

Surface Evolver (SE), created by Kenneth A. Brakke¹, is an open source interactive computer program that minimizes a surface energy when subject to specific constraints [5]. The initial surface shape is described as consisting of vertices, directive edges and facets. The surface energy can be linked to surface tension, gravity and other user-defined energies. Some constraints can be imposed: geometrical constraints on vertex position or integrated quantities such as target volumes or pressures. The minimization process is implemented by evolving the surface with an energy gradient descent method.

In this section we first examine the case of the computation of a sessile droplet shape by SE. This simple example will help us to explain how SE works, by recovering some basic results on the droplet mean interface curvature. More example and pieces of information can be found in the Surface Evolver user manual².

3.1.1 Achieving a stable interface in SE

We consider a small sessile droplet resting on a perfect substrate. The substrate area is kept constant and is denoted A_s . The system (substrate + droplet) is isothermal

¹<http://www.susqu.edu/brakke>

²<http://facstaff.susqu.edu/brakke/evolver/html/tutorial.htm>

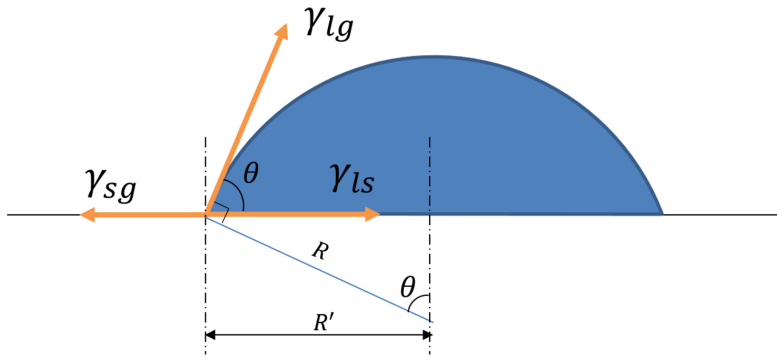


Figure 3.1: Side view of a sessile droplet at equilibrium on a smooth substrate. The contact angle is θ and γ_{sg} , γ_{ls} , γ_{lg} are the surface tensions of solid-gas, liquid-solid and liquid-gas interfaces respectively.

and there is no external forces. Gravity effects are thus neglected. The free energy of the system can reduce to:

$$G = \gamma_{sg}A_{sg} + \gamma_{ls}A_{ls} + \gamma_{lg}A_{lg} \quad (3.1)$$

where γ_{sg} , γ_{ls} , γ_{lg} and A_{sg} , A_{ls} , A_{lg} are the surface tensions and areas of solid-gas, liquid-solid and liquid-gas interfaces. Young equation expresses the forces equilibrium at triple line and reads:

$$\gamma_{sg} = \gamma_{lg}\cos\theta + \gamma_{ls} \quad (3.2)$$

where θ is the droplet contact angle. The free energy G to be minimized can then written as (ignoring the constant terms):

$$G = \gamma_{lg}A_{lg} - \gamma_{lg}A_{ls}\cos\theta \quad (3.3)$$

G is the sum of two terms. Once the liquid-gas interface is meshed, the first term is calculated by SE (the interfacial energy γ_{lg} can be user-defined but by default, SE takes $\gamma_{lg} = 1$). The second term is computed by using Green's theorem to convert the surface integral to a contact line integral. In fact, this term comes from the liquid-solid interface. We denote it E_{ls} and

$$E_{ls} = \gamma_{lg}\cos\theta \iint_A \vec{n} \cdot \vec{d}A = \oint_L \vec{w}dl, \quad (3.4)$$

where L is liquid-gas contact line, \vec{n} is contact interface normal vector. Solving $\text{curl}\vec{w} = \gamma_{lg}\cos\theta \cdot \vec{n}$, for liquid-solid interface on the $z = 0$ plane, one finds that $\vec{w} = -\gamma_{lg}\cos\theta y\vec{i}$ or $\vec{w} = -\gamma_{lg}\cos\theta x\vec{j}$, This term is also computed by SE and the total free energy can be minimized by considering successive shapes, in a iterative process.

For the other two constraints that used in our system, such as constraint on top

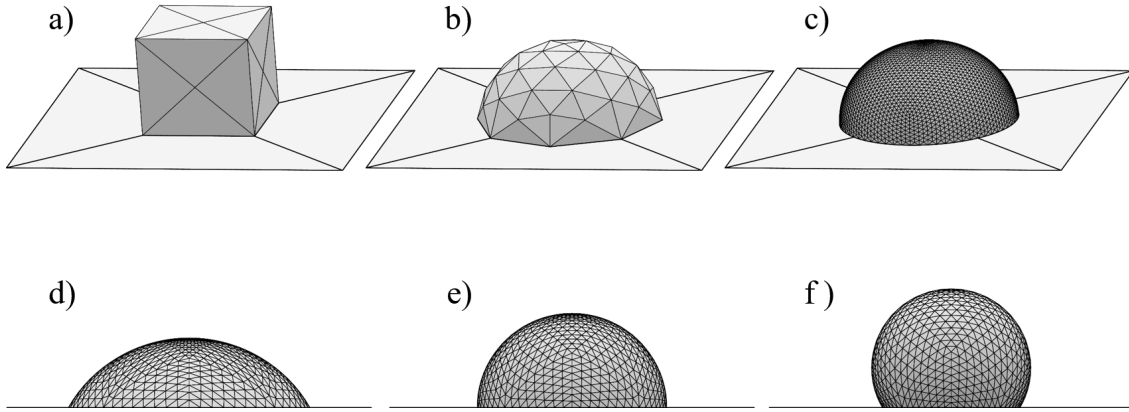


Figure 3.2: Shape of a sessile droplet computed by Surface Evolver. a), b) and c) are three successive shapes found in SE, from the initial one to the converged one ($\theta = 90^\circ$). d), e) and f) are three converged shapes for θ equals to 60° , 90° , 120° , respectively.

plate ($z = h$) and on cylinders ($(x - m)^2 + (y - n)^2 = R^2$, with m, n, R the cylinder coordinates on x-y plane and radius respectively), the edge integrand vector field \vec{w} of former is the same format with substrate case but with opposite symbol, \vec{w} for contact line on cylinder is $\vec{w} = \gamma_{lg} \cos \theta \frac{z}{R} ((y - m)\vec{i} - (x - n)\vec{j})$.

Since Evolver only deal with facets, the finite volume constraint is implemented by using divergence theorem:

$$\iiint_V \text{div} \vec{F} \cdot d\vec{V} = \oiint_S \vec{F} \cdot d\vec{S} \quad (3.5)$$

where \vec{F} is a vector field satisfying $\text{div} \vec{F} = 1$. Then the volume is $\iiint_V dV$. In SE, the default facet integral is $\vec{F} = z\vec{d}$. That is, intuitively speaking, the volume of a body is contributed by all the facet that oriented with normal outward from a body, by means of adding the volume of the vertical prism between the facet and the $z = 0$ plane.

Another useful constraints in Evolver that encountered in our cases is one-sided constraint, meaning that the vertex subjected to such a constraint must stay in that part of the domain where a level-set function (defined by the user) must remain non-negative or non-positive for instance. For instance, in our case, all the vertex are set with such constraint to prevent the vertex penetrate inside of cylinders during mesh evolution.

The evolution of sessile droplet in SE is shown in Figure 3.2a to c. Figure 3.2a corresponds to the initial, starting shape defined in SE, and is detailed in Figure 3.3. Vertexes are marked with the numbered circles, edges are defined from vertex, facets are constructed by directional edges then turn to elements of body definition. Facet attached to substrate (composed of edge 1-4) is exempt from meshing, since it can be indirectly obtained from meshed interfaces (the other five facets of cubic here), as described above.

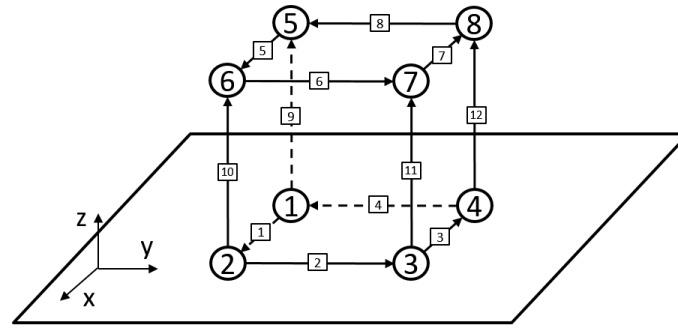


Figure 3.3: Initial framework for the sessile droplet case in Surface Evolver. Vertices and edges are marked with circles and square boxes. Facets constructed by edges are defined in script but absent here. Square facets are automatically transformed into triangular mesh, as shown in Figure 3.2a.

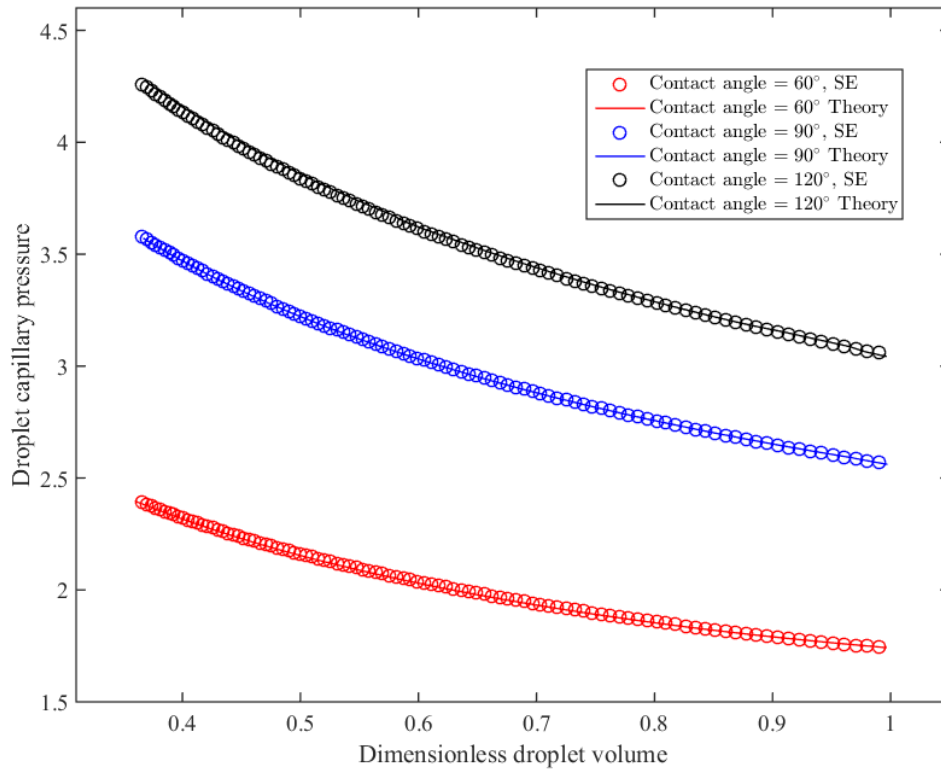


Figure 3.4: Comparing of pressure/curvature obtained in SE (circle markers) and theoretical calculation results (cross markers) in the case of sessile droplet on perfect substrate. Three contact angles (60° , 9° , 120°) are colored with red, blue and black, respectively. Droplet volume is dimensionless in SE.

3.1.2 Reliability of the results obtained from SE

By default, and for simplification, the liquid-gas surface tension, is set to $\gamma_{lg} = 1$ and the effect of gravity is ignored in our case. Based on the assumptions above,

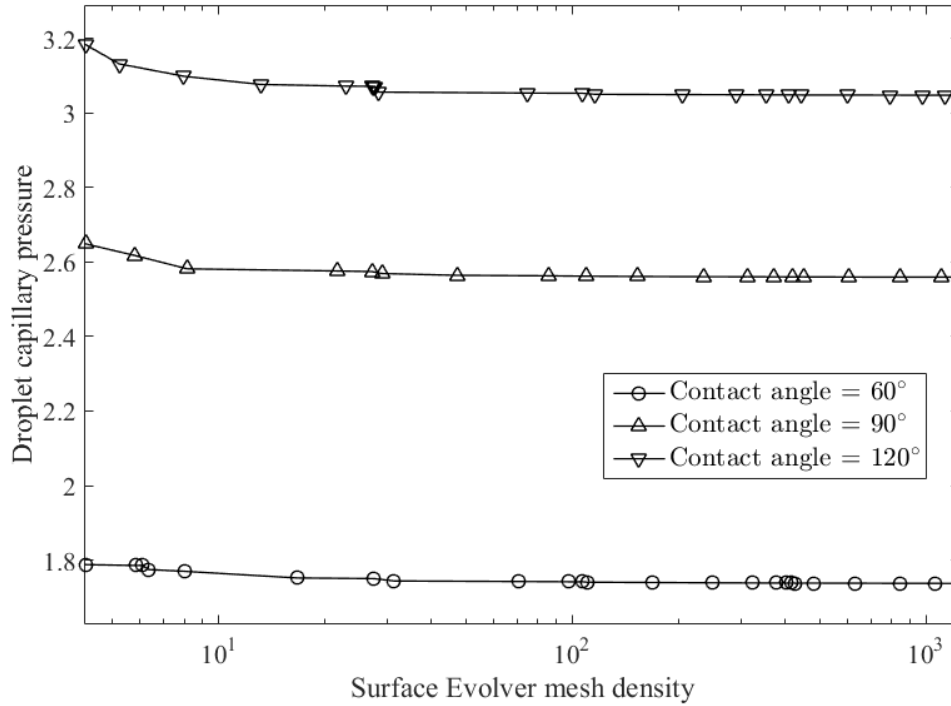


Figure 3.5: Capillary pressure of a sessile drop as a function of mesh density.

the equilibrium shape of sessile droplet on a flat substrate is a spherical cap. SE returns the droplet surface energy and capillary pressure.

Figure 3.4a compares the droplet capillary pressures obtained in SE (colored circles) and the theoretical values (solid lines) for three different contact angles cases ($\theta = 60^\circ$, 90° and 120°) and different fluid volumes. The difference between the SE results and the theoretical value is less than 0.6%, demonstrating the accuracy of SE. The corresponding droplet equilibrium shapes for the three contact angles are shown in Figure 3.1d to f. We also investigated the impact of mesh density on the SE results regarding capillary pressure results. As shown in Figure 3.5, the capillary pressure converges very rapidly towards its theoretical value when the mesh density is increased. The mesh density is defined as the total number of triangular meshes used by SE to describe the interface divided by the interfacial area. For the three contact angle used here ($\theta = 60^\circ$, 90° and 120°), the capillary pressure value has converged as soon as the mesh density is larger than 30.

3.2 Presentation of the different cases studied with Surface Evolver

In this section, we present the different cases studied with Surface Evolver in the present work, mostly inspired from the liquid films shapes expected in the Fibonacci spiral micromodel.

3.2.1 Liquid rings around cylinders

A liquid ring around one cylinder

The simplest liquid film geometry in our system is the meniscus ring that may be observed in the corner between a cylinder and the top or bottom plate. When dealing with the experimental results in the next Chapters, we'll see that this film geometry is mostly encountered in micromodel with a radial gradient in cylinder spacing, where liquid rings at equilibrium with their vapor can be observed. It is also seen in the Fibonacci spiral system but in this case, the liquid rings are located close to the drying front and quickly evaporates.

Figure 3.6a is the initial meniscus ring shape defined in the SE script, including 12 vertex (in numbered circles) and 12 edges (in numbered squares). The bottom plate is not shown for sake of clarity. Vertex 1-4 and edges 1-4 represent the triple line on the bottom plate. Vertex 9-12 and edge 9-12 represent the triple line on the cylinder. Every edge owns a pair of tail and head vertices. Oriented edges in counter-clockwise direction compose the facet data, the facets labels are omitted in Figure 3.6a. The constraints used on vertices, edges and facets in this case are listed in Table 3.1. Figure 3.6b shows a typical converged liquid ring shape obtained using Surface Evolver (the cylinder and bottom plate are not displayed). Inset in Figure 3.6b is the top view of a meniscus ring observed in a large micromodel, as seen on images recorded with the CCD camera. As already said, the dark circular ring around the cylinder is due to the backlight refraction at the curved meniscus interface.

Liquid film between two cylinders

We now turn to the case where a liquid ring is found to connect two neighboring cylinders. It is more complex to simulate than the previous case and we made use of an innovative re-settle volume method in Surface Evolver to study that case. Figure 3.7 displays the initial and converged shape. The modelling strategy is similar to the previous case, we simply add a second cylinder in the y -direction. The cylinder spacing $w_{//}$ in this case equals to cylinder diameter d_c . The constraints for each element in initial framework are listed in Table 3.2. Next, we investigate the evolution of this shape when the liquid volume is decreased.

Transition from a single liquid film to two isolated liquid rings In SE, the fluid volume can also be viewed as a constraint when it is given a target value. Once a target volume is defined, SE will automatically obtain the meshed interface

Index	Constraints	Vertices	Edges	Faces
1	$z=0$	1,2,3,4	1,2,3,4	
2	$x^2 + y^2 = R^2$	9,10,11,12	9,10,11,12	
3	$x^2 + y^2 > R^2$	5,6,7,8	5,6,7,8	1,2,3,4,5,6,7,8

Table 3.1: Constraints used in SE for the liquid ring case.

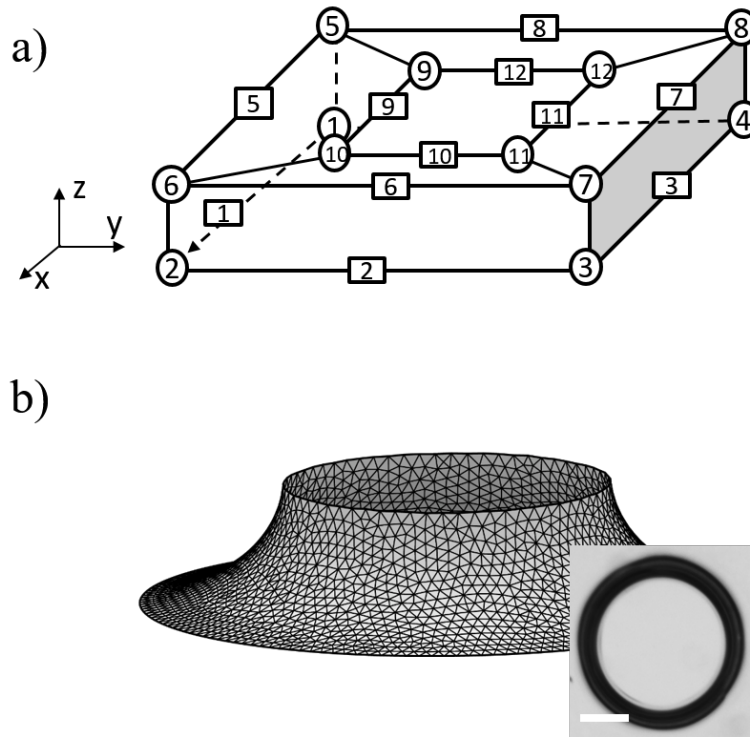


Figure 3.6: Surface Evolver simulation of liquid ring around a cylinder. a) Initial framework for SE: vertices are in numbered circles, edges are in numbered squares, facets are omitted here. b) Final converged shape. The contact angle on the bottom plate and cylinder surface is taken to be 10° . The cylinder and bottom plate are not displayed. Inset is the top view of a meniscus ring from experimental data (scale bar is $200 \mu\text{m}$).

Index	Constraints	Vertices	Edges	Faces
1	$z=0$	1,2,3,4	1,2,3,4	
2	$x^2 + y^2 = R^2$	9,10,11,12	9,10,11,12	
3	$x^2 + (y - d)^2 = R^2$	13,14,15,16	13,14,15,16	
4	$x^2 + y^2 > R^2$	1,2,5,6	1,5	ALL
5	$x^2 + (y - d)^2 > R^2$	3,4,7,8	3,7	ALL

Table 3.2: Constraints used in SE for the case of a liquid ring connecting two cylinders.

shape with its energy descent method. Based on this, a iteration that gradually decreases the target volume once a converged shape has been obtained can be set into place. The work flow of this re-settle volume method (VRM) is shown in Figure 3.8. A first example using the VRM is the study of the geometry transition from a single liquid “ring” connecting the two cylinders to two isolated liquid rings. The initial is the same with the one shown in Figure 3.7a. During the VRM iteration, a conditional statement judging if the liquid film has collapsed is applied. In our system, we consider that a film thickness less than 10^{-6} m indicates that the liquid film has broken-up.

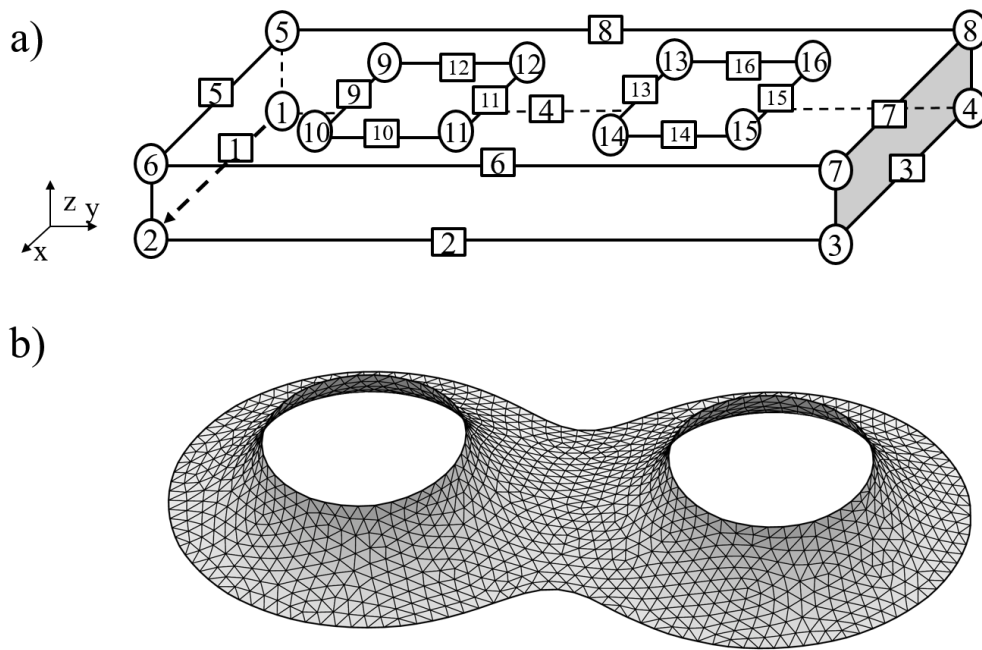


Figure 3.7: Surface Evolver simulation of a liquid “ring” connecting two cylinders. a) Initial framework: vertices are labelled in numbered circles, edges in numbered squares and the two cylinders are omitted. b) Final film shape obtained in SE. The contact angle on the bottom plate and cylinders surface is 10° .

Figure 3.9 illustrates the transition from a single liquid ring to two isolated rings using VRM. Cylinders geometry and mesh grid line are omitted, as in previous similar pictures, and only the interface shape is shown. Figure 3.9a is a typical geometry of liquid film connecting two cylinders, as in Figure 3.7. With VRM, the liquid volume decreases until a critical point is reached, see Figure 3.9b. At this point, a “split” algorithm is applied, which makes the thin film collapse in its center and resets the constraints on the few disconnected mesh elements (vertex and edges). Figure 3.9c shows two isolated meniscus rings after the dis-connection.

3.2.2 Liquid bridges on spirals

Liquid bridge between two cylinders

A single liquid bridge trapped between two cylinders and the top and bottom plates can be considered as the building block of the elongated liquid films that will be found to form along spiral in the Fibonacci spiral micromodel. This is why this case will be studied thoroughly.

As previously, Figure 3.10a and b show the initial and converged shapes. On Figure 3.10a, vertices 1-4 and edges 1-4 represent the contact line on the bottom plate, vertices 5-8 and edges 5-8 represent the contact line on top plate. Triple lines on the two cylinders are predefined with two opening squares. The left opening is represented by vertices and edges 13-16, and the right one by vertices and edges 17-20. Figure 3.10b is a typical liquid bridge equilibrium shape with contact an-

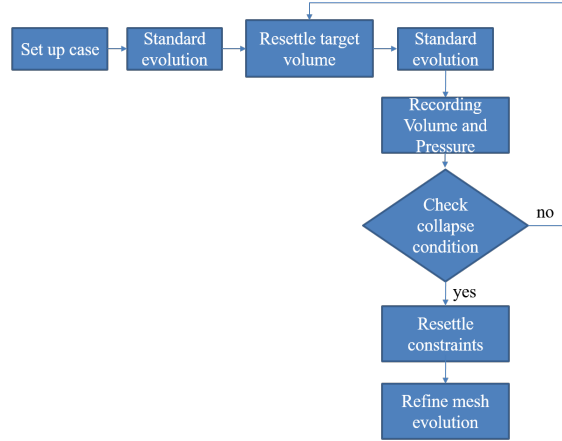


Figure 3.8: Work flow of the re-settle volume method in Evolver. Standard evolution involves combination actions of gradient descent step, equiangularization and vertex averaging (represent as $\{u; V; g\}$ respectively in SE single letter command, more details refer to SE manual.)

Index	Constraints	Vertices	Edges	Faces
1	$z=0$	1,2,3,4	1,2,3,4	
2	$z=h$	5,6,7,8	5,6,7,8	
3	$x^2 + y^2 > R^2$		9,10	ALL
4	$x^2 + (y - h)^2 > R^2$		11,12	ALL
5	$x^2 + y^2 = R^2$	13,14,15,16	13,14,15,16	
5	$x^2 + (y - h)^2 = R^2$	17,18,19,20	17,18,19,20	

Table 3.3: Constraints used in SE for the case of a liquid bridge.

gle equals to 0° , both on top/bottom plates and cylinders. Inset is the top view of an isolated liquid bridge from ethanol drying experiment images. Table 3.2.2 lists the constraints for the elements introduced in the initial framework in Figure 3.10a. The VRM strategy can be applied to this case, to study the capillary bridge shape for various liquid volumes. Then, the volume decrease step is $\Delta V = V_{ini}/200$, where V_{ini} is the liquid bridge initial volume for each iteration. Determination of ΔV value here is empirical, too large value of ΔV will make the mesh more unstable, while too small value is good for mesh stabilization but time consuming. Of course, for each shape computed during the VRM, one can export the liquid bridge capillary pressure, and also the liquid bridge geometrical characteristics (thickness for instance).

Transition from a single liquid bridge to four isolated liquid rings Similarly to the case of a liquid film between two cylinders, where a transition to two isolated liquid rings is observed for small liquid volumes, a transition is also expected to occur for a liquid bridge. Using the VRM, as the liquid volume decreases, a situation is reached where the two liquid-gas interfaces, on each side of the liquid bridge, touches. If the liquid bridge volume is still decreased, one obtain the un-

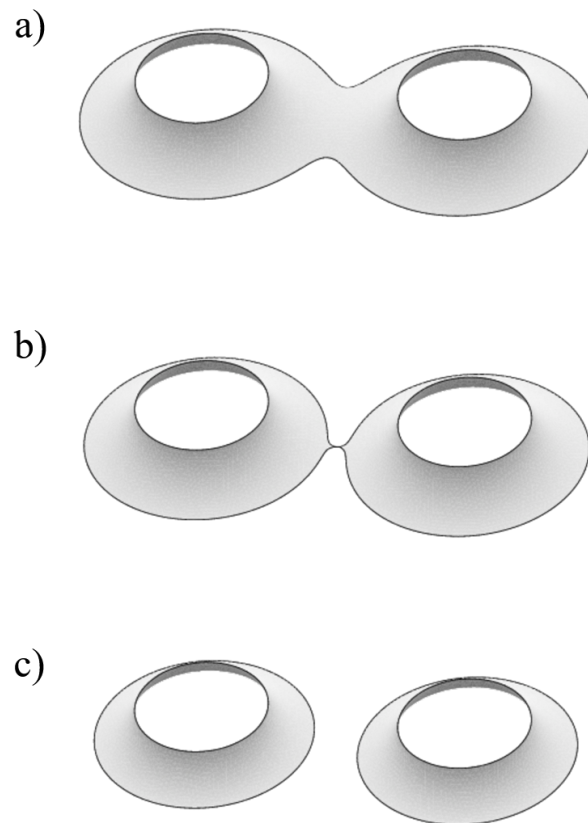


Figure 3.9: Transition from a single liquid cluster to two isolated liquid rings using the VRM method. a) Typical unique liquid film shape. b) Critical point at which the liquid film collapses. c) Two isolated meniscus rings are formed after a “split” step. The corresponding relative volume on these three successive images are 0.90, 0.70 and 0.45, made dimensionless by dividing by half the volume of a single cylinder. Contact angle on bottom plate and cylinder is 10° and $w_{\parallel} = 2d_c$.

physical situation where the two interfaces crosses one-another. We *assume* that the liquid bridge breakup occurs when the interfaces touch one another: in fact, we did not manage to dis-connect the liquid bridge using SE (as what was done in the liquid film case). After break-up, a re-organization of the liquid volume follows. Given the volume of liquid when this happens, and based in SE simulations of isolated liquid rings around the top or bottom of a cylinder, we know that the liquid shape after breakup must consist of 4 isolated liquid rings, as sketched in Figure 3.11. The critical pressure for a liquid bridge is the one obtained in SE “just before” the two liquid-gas interfaces collapses, i.e. when their spacing is less than $1 \mu\text{m}$.

Chain of liquid bridge along a spiral

In our drying experiment in Fibonacci spiral micromodel, liquid films are found along spirals and consists of several liquid bridges joining each other in a “head-

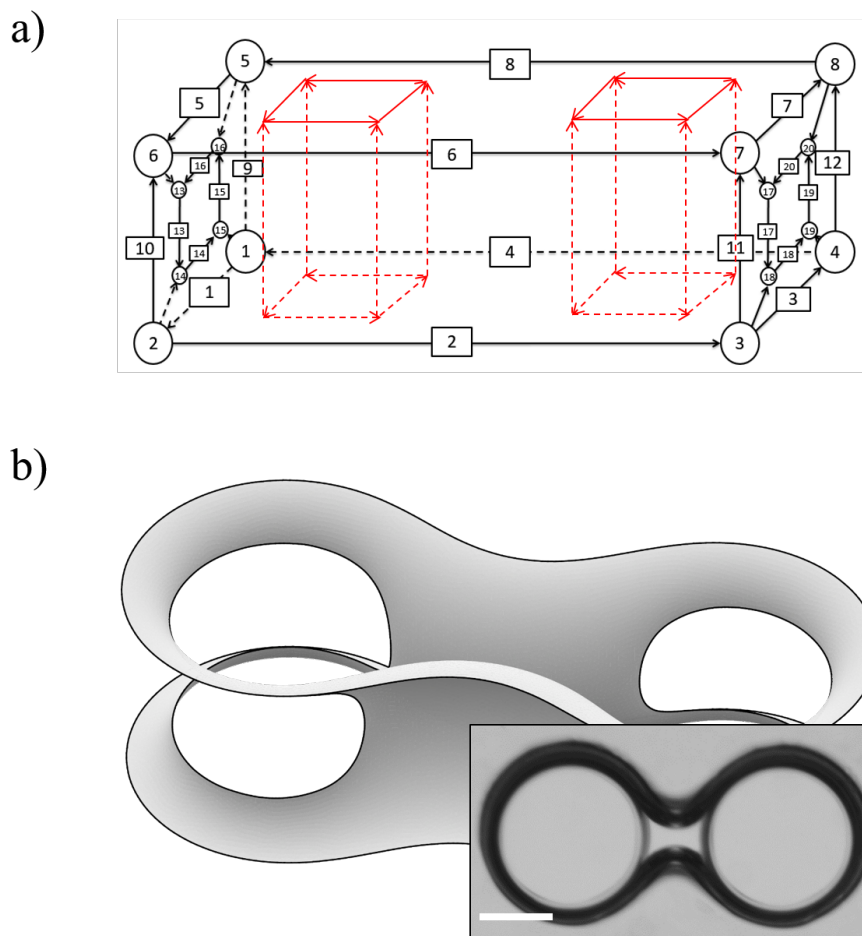


Figure 3.10: Surface Evolver simulation of a liquid bridge confined between two cylinders and top/bottom plates. a) Initial framework. Constraints on vertex and edges are listed in Table 3.2.2. (b) Final shape. Here, $w_{//} = 2d_c$, contact angle on both plates and on cylinder is 0° . Inset is the top view of a liquid bridge in ethanol experimental image with scale bar of $250 \mu\text{m}$.

tail” way. Simulating such interfacial shape is possible with SE but much more involved as the initial shape is built with a very large number of vertices, edges and facets. Dealing with the constraints on the surfaces of the cylinders is also really

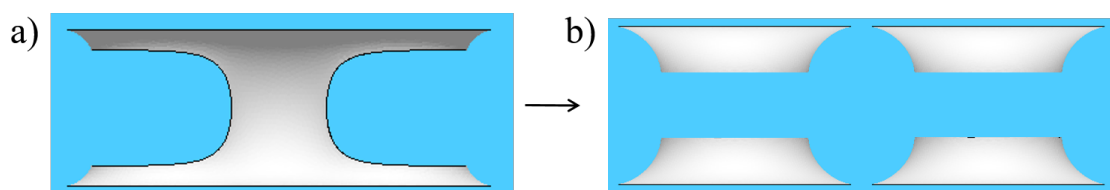


Figure 3.11: a) A typical liquid bridge shape obtained using Surface Evolver, side view. b) Four isolated liquid rings obtained after the break-up of the liquid bridge

cumbersome but choosing a zero contact angle on cylinders simplifies this point a lot. Two examples of liquid bridges chains are shown in Figure 3.12.

3.2.3 Receding front between two spirals

Finally, we tried to use VRM to simulate the progressive invasion of the liquid in between the pore space between two spirals, i.e. on roughly $1/28$ of the whole device. A typical result is shown in Figure 3.13. Seven successive locations for the interface are shown (numbered from 1 to 7). From the interface location, one can define a saturation as $S_l = (V_t - V_g)/V_t$ where V_t is the total volume confined in between the two spirals and V_g the gas volume that has penetrated between the two spirals. The liquid saturation for the 7 interfaces represented in Figure 3.13 are 1, 0.98, 0.93, 0.87, 0.76, 0.54 and 0.32 respectively. More details are given in Appendix B.

Index	Constraints	Vertices	Edges	Faces
1	$x=0$	1,4	4	
2	$x=h$	2,3	2	
3	$y=y1$	1,2	1	
4	$y=y2$	3,4	3	
5	$(x - m)^2 + (y - n)^2 > R^2$	ALL	ALL	ALL

Table 3.4: Constraints associated with the case depicted in Figure 3.13. h is the height of the cylinders, $y1$ and $y2$ are the y-coordinates of the two outermost cylinders; m and n are the coordinates of the cylinder array.

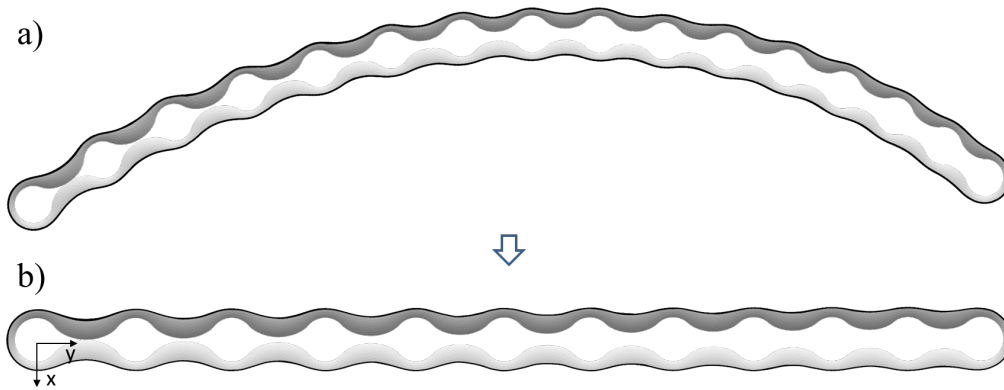


Figure 3.12: Top view of 2 chains of liquid bridges obtained with SE. a) Chain of liquid bridges with 16 cylinders arranged spatially as on the micromodel spiral. b) Chain of liquid bridges around 12 aligned cylinders. Contact angle on top/bottom plates and cylinders is 0.

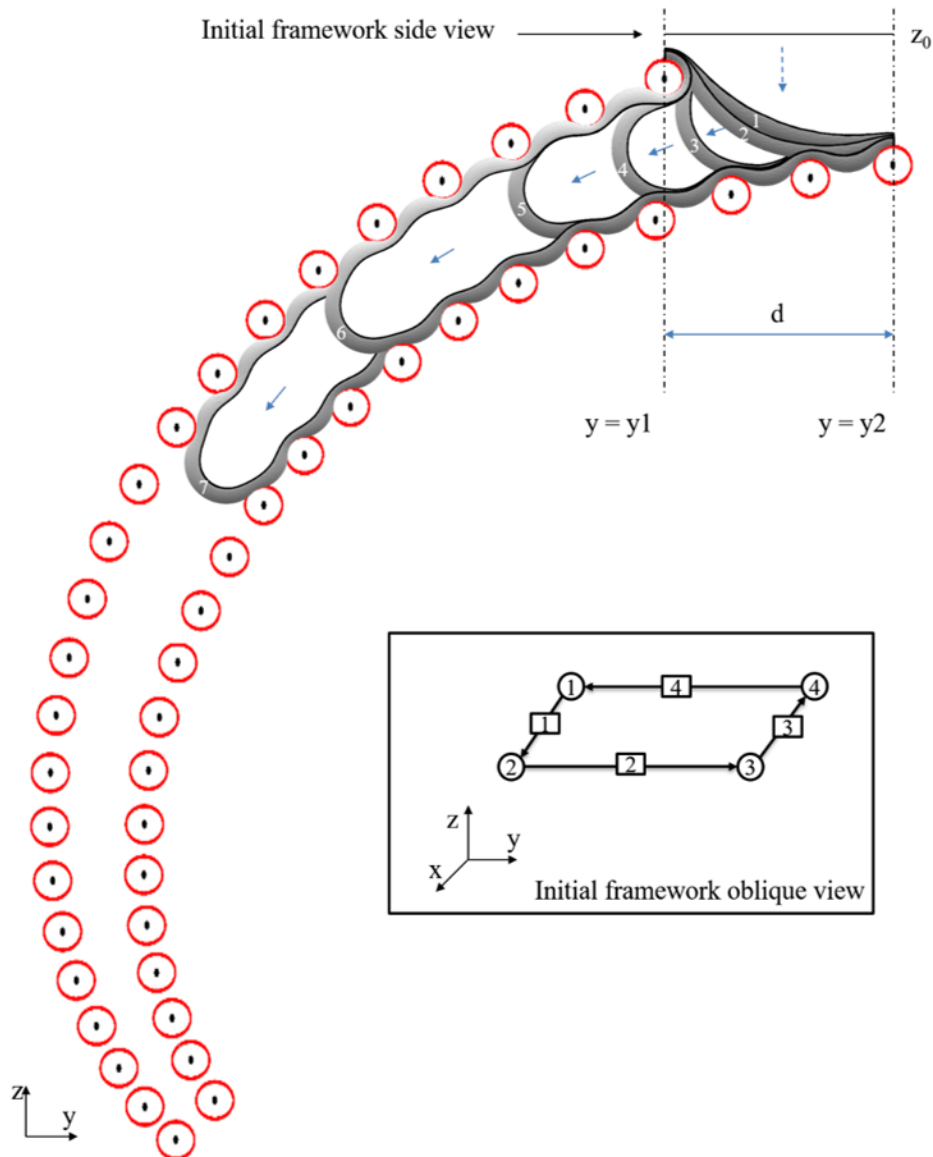


Figure 3.13: Successive interface locations between two neighboring spirals, obtained using VRM. The initial framework is a rectangle parallel with the x-y plane, as shown in inset. The red circles are the cylinders. The contact angle on the two plates is equal to 10° . The corresponding liquid saturation in between the two spirals from the first computed interface to the 7th are 1, 0.98, 0.93, 0.87, 0.76, 0.54 and 0.32 respectively. Blue solid arrows indicate the interface invasion pathway.

3.3 Direct numerical simulations (DNS) of the flow within a liquid bridge

As explained in the Introduction, the evaporation-induced flow in the thick liquid films is an important feature to take into account to study the drying kinetics of porous media. The liquid films seen in our micromodels are more complex than those seen in straight, square cross-section capillary tube but still much simpler than those that were observed in random packing of spherical particles, see for instance [42]. In this section, we will introduce the numerical method that we used to investigate the viscous resistance to the flow in our liquid bridge geometry. Following Chauvet' work [12], this viscous flow resistance is expected a crucial parameter to determine the spatial extent of the liquid films in the present micromodels and this will be the subject of Chapter 5.

3.3.1 Model explanation

We have shown in the previous section that simulating the capillary shape of a chain of connected liquid bridges is feasible with Surface Evolver. However this is really cumbersome and in the following we focus on a liquid bridge confined between 2 cylinders. The main objective is therefore to compute the viscous flow resistance in such a liquid bridge, as a function of the liquid volume contained in the liquid bridge and as a function of spacing $w_{//}$ between the cylinders. Such results will then be used to estimate the viscous flow resistance within a chain of liquid bridges.

A typical converged liquid bridge shape is shown in Figure 3.14. The surface of the pillars is displayed in red color. To ease the capillary surface visualization, the top and bottom plates are not displayed. The surface mesh display has also been turned off. We consider the case where the distance h between the two horizontal plates (i.e. the micromodel thickness or equivalently the cylinder height) is equal to the cylinder diameter d_c . The center-to center spacing between 2 cylinders is $w_{//}$. The unit-cell used for the DNS consists of the liquid bridge part that is confined between the $y = 0$ and $y = w_{//}$ planes on one hand and between the $z = 0$ and $z = h/2$ planes on the other hand, taking also $x > 0$, see Figure 3.14, and leading to the computational domain shown in Figure 3.15. The interface mesh is exported directly from SE (in IGES format) to Comsol for subsequent flow simulation. Mesh density is over 2000 in SE simulation.

3.3.2 Viscous flow simulations

Once the computational domain is obtained, the flow DNS can be set. The wetting fluid is supposed to be isothermal, incompressible and Newtonian with constant dynamic viscosity μ and constant density ρ . Gravity is neglected and due to small dimensions, the Reynolds number is far less than one. From these assumptions, the equations of motion reduce to Stokes equations. Continuity and momentum equations can thus be expressed as:

$$\nabla \cdot \mathbf{u} = 0 \tag{3.6}$$

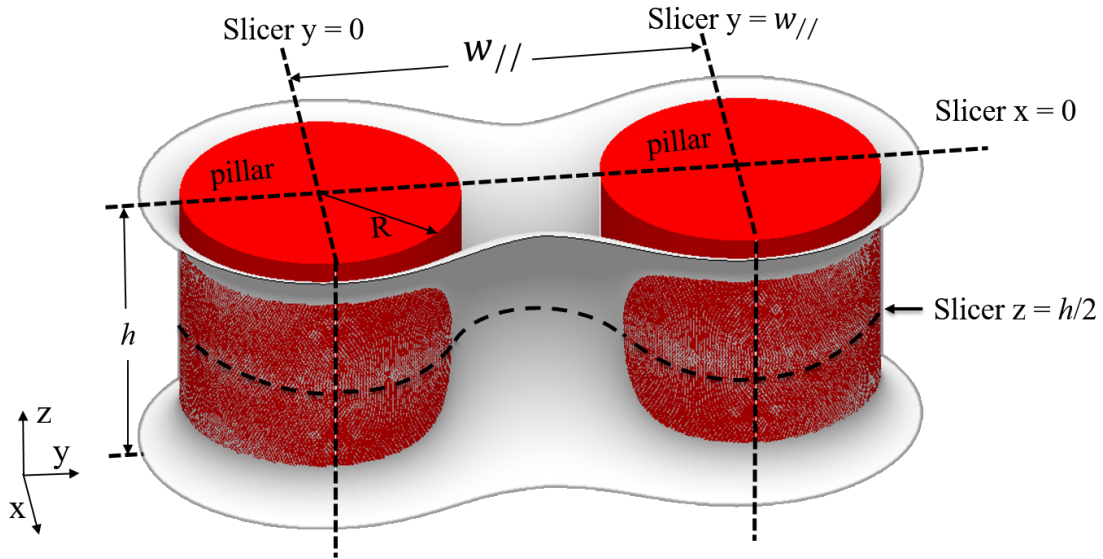


Figure 3.14: Liquid bridge connecting two cylinders and confined between two horizontal plates (not shown in this sketch). Here the dimensionless liquid bridge volume is 0.46 (the reference volume is the volume of a pillar).

$$\mu \nabla^2 \mathbf{u} - \nabla P_l = 0 \quad (3.7)$$

where \mathbf{u} is the liquid velocity and P_l the pressure in the liquid.

Equation 3.6 and 3.7 are solved numerically using the finite element based commercial software COMSOL Multiphysics in the liquid domain depicted in Figure 3.15. Free tetrahedral elements are used for meshing the liquid domain. A no-slip boundary condition is implemented on the liquid-pillar and liquid-bottom plate interfaces. No-viscous stress pressure boundaries are imposed at the computational inlet and outlet boundaries. Two different boundary conditions are used at the liquid-gas interface, namely a no-stress boundary condition or a no-slip boundary condition so as to simulate a perfectly clean interface or a rigidified interface due to surfactant for instance. The computational mesh is refined until obtaining results independent of meshing.

Validation of the numerical procedure

Before considering the case of liquid bridges, the numerical procedure combining Surface Evolver (SE) and Comsol computations was tested for a much simpler geometrical configuration, namely the flow in a liquid wedge trapped by capillarity in a right angle, straight corner, studied by Ransohoff & Radke (1988), see Figure ???. As in Ransohoff & Radke's paper, the viscous resistance within the liquid wedge is expressed by the dimensionless flow resistance β defined as:

$$\beta = \frac{-a^2}{\mu \langle \mathbf{u}_y \rangle} \times \frac{\Delta P}{L} \quad (3.8)$$

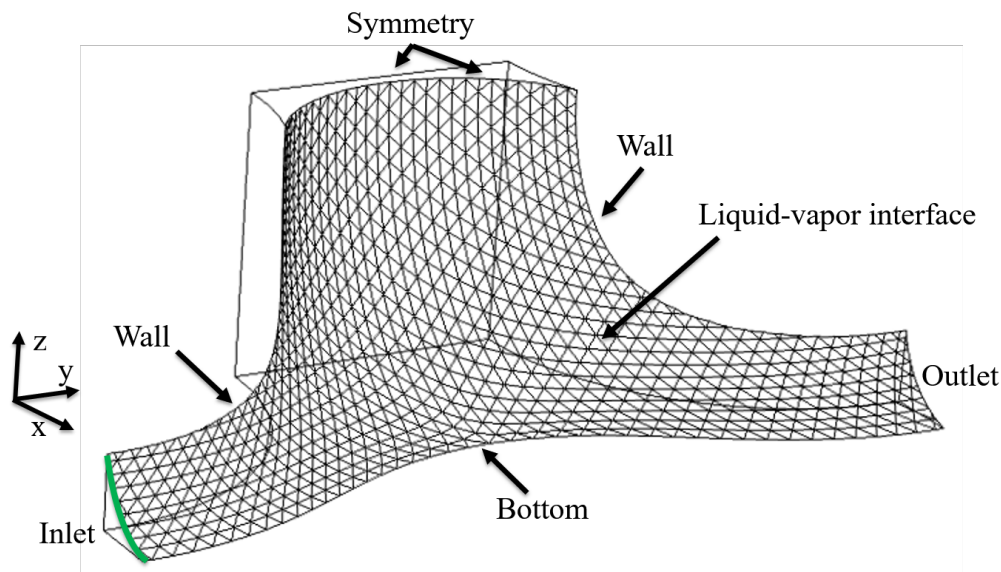


Figure 3.15: Computational domain and boundary conditions. The curvature radius of the green line highlighted at the inlet of the computational domain, in the (x-y) plane, will be denoted R_{in} in the following.

where $\langle \mathbf{u}_y \rangle$ is the average velocity in the wedge in the longitudinal direction, calculated by dividing the flow rate in the wedge by the liquid corner area, a is the interface curvature radius in the x-z plane in Figure ??a (the interface is flat in the y direction) and $-\Delta P/L$ is the pressure gradient driving the flow in the liquid wedge (L is the length of the liquid wedge along the y-axis).

The meniscus surface is first computed using SE in a right angle corner as illustrated in Figure ??a and varying the contact angle implemented on the y-z and x-y planes in Surface Evolver. The cross section profile of meniscus is then imported into Comsol and then the liquid wedge is rebuilt with an extrude tool available in Comsol to construct a mesh more adapted to the viscous flow computation. The vertical and bottom walls are set as no-slip boundary, the two cross-sections along the y-axis are set as inlet and outlet. A pressure difference ΔP_l is imposed between the inlet and the outlet. The no-viscous-stress or the no-slip boundary condition is imposed at the liquid-gas interface. After computation of the flow using Comsol, the viscous resistance is computed using Equation (3.8). The comparison between our computations and the results of Ransohoff & Radke ([39]) are shown in Figure ??(b). The red lines in Figure ??b corresponds to the flow resistance results obtained using our procedure whereas the blue ones are the ones from [39]. Black and blue lines correspond to no slip boundary and red and green lines correspond to no-stress boundary conditions at liquid-gas interface respectively. As can be seen, there is an almost perfect agreement between our results and the ones of Ransohoff & Radke.

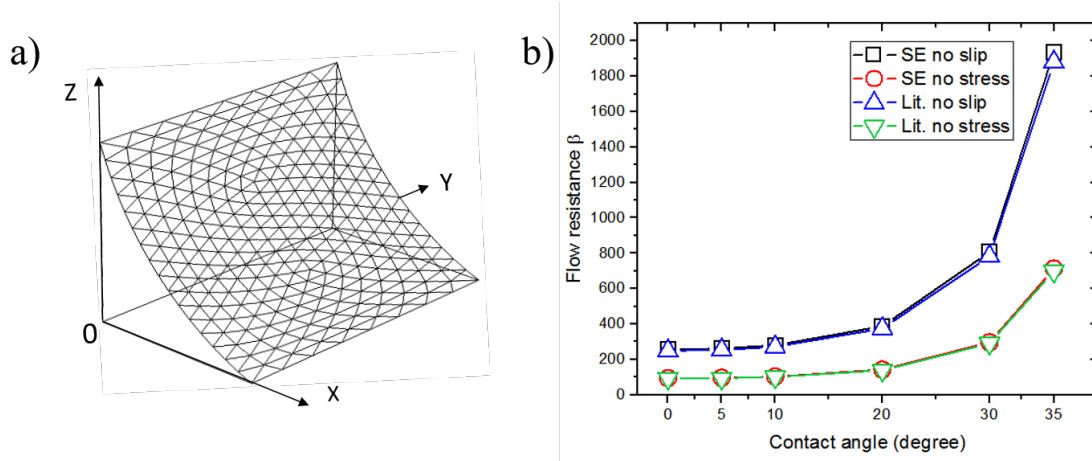


Figure 3.16: a) Liquid-gas interface in a right angle, straight corner computed using Surface Evolver. b) Variation of flow resistance β with the contact angle for the straight corner flow configuration. Comparison between the present computations (referred to as SE) and the results of (Ransohoff 1988)[39] (referred to as "Lit.").

Results for a liquid bridge

In the case of a liquid bridge, β is defined the following way:

$$\beta = \frac{-R_{in}^2}{\mu \langle \mathbf{u}_y \rangle} \times \frac{\Delta P_l}{w_{\parallel}} \quad (3.9)$$

where R_{in} is the interface curvature radius in the x-z plane, at the inlet of the computational domain, see the green outlined line in Figure 3.15. This curvature is obtained by fitting the interface profile with a circle.

Figure 3.17a shows a typical computed pressure field in the liquid. The pressure field is further illustrated in Figure 3.17b, which shows the pressure (blue line) and the pressure gradient along the bottom triple line outlined in Figure 3.17a. One can distinguish two main regions in the liquid bridge: the central region between the two pillars where the liquid bridge cross section areas in the x-z plane are relatively large and the constriction regions at the inlet and outlet of the unit cell where the liquid bridge is in contact with the pillars. As can be seen, the pressure gradient is concentrated in the inlet and outlet regions, i.e. the constriction regions of the bridge. The pressure variation is significantly weaker in the central region of the bridge between the pillars. The flow resistance in this example is thus mostly concentrated in the inlet and outlet regions of the liquid bridge.

Results for β as a function of the contact angle and liquid bridge geometry are given as Tables in Appendix C. Just to give an example, Figure 3.18 shows the evolution of β , made dimensionless by the value for a straight corner flow, as a function of R_{in}/w_{slash} , for various spacing w_{slash} between the cylinders and a fixed contact angle ($\theta = 10^\circ$). As expected, the bridge flow resistance varies with R_{in} (that is, equivalently, the liquid bridge volume) and can be greater or smaller than for the right angle straight corner case. The trend depicted in Figure 3.18 is consistent with the bridge shape variation with its volume, see insets. The liquid bridge is more

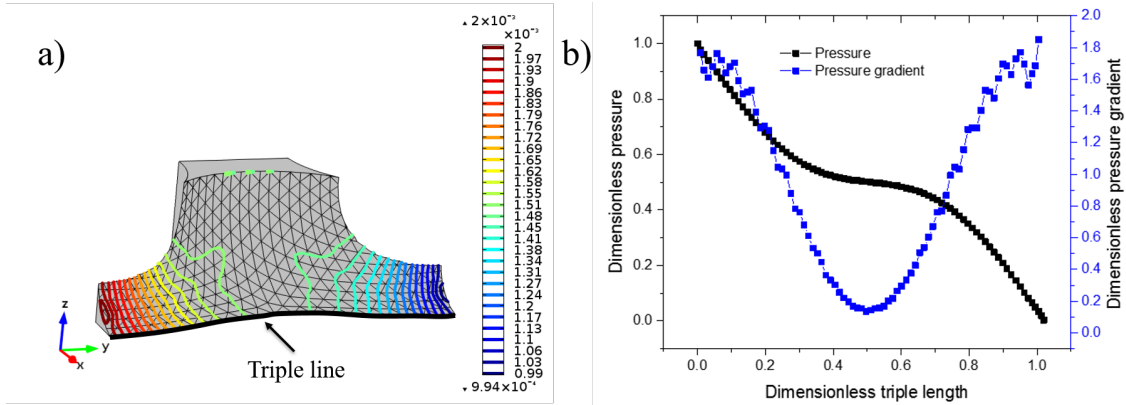


Figure 3.17: Typical results from Comsol. a) Computed pressure field in a liquid bridge with a no-stress boundary condition on the interface. Isobars on the liquid-gas interface are shown as colored lines; b) Dimensionless pressure (defined as $(P_l - P_{outlet})/\Delta P_l$) and pressure gradient in the liquid along the triple line outlined in a). The distance along the triple line is made dimensionless by dividing by w_{\parallel} and the dimensionless pressure gradient along the triple line is defined as $(dP_l/ds)/(\Delta P_l/w_{\parallel})$, where s is a curvilinear coordinate along the triple line.

“tortuous” for the smaller volumes, which is consistent with the increase of the flow resistance with decreasing bridge volume. For the largest volumes tested, the flow resistance is less than for a right angle straight corner. This is consistent with the fact that the shape is not tortuous anymore (see the shape on the right hand side in Figure 3.18) and less vertical wall is wetted comparatively with a straight corner of same length.

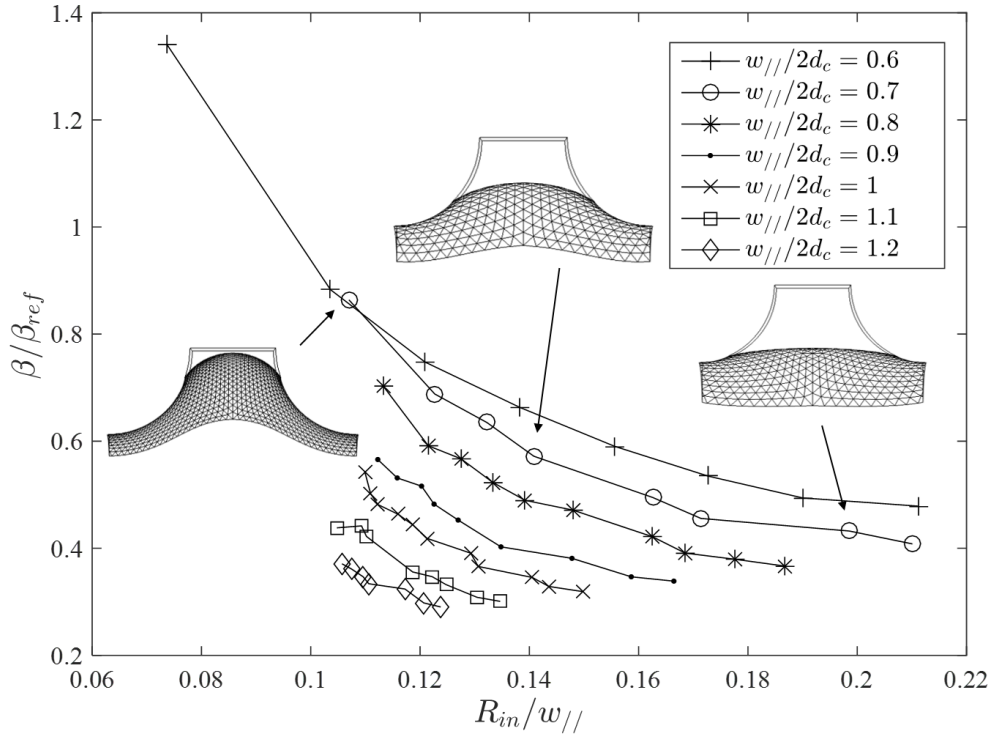


Figure 3.18: Liquid bridge flow resistance β/β_{ref} and liquid bridge shape variation as a function of $R_{in}/w_{||}$ (contact angle $\theta = 10^\circ$). Numerical results obtained with the no-viscous-stress boundary condition at the liquid-gas interface. The liquid bridge flow resistance is divided by the flow resistance for a right angle corner flow, β_{ref} documented in Ransohof & Radke (1988): $\beta_{ref} = 93.93$ for the no-viscous-stress boundary condition at $\theta = 10^\circ$. The symbols display the results obtained for various spacing between the two cylinders, see legend for details. The insets display top views of the liquid bridge, for selected cases.

Chapter 4

Controlled evaporation by capillary structure

In this chapter, we present some results on the drying kinetic observed in the micromodels used in the present work. Please note that this Chapter is self-consistent as it will be submitted soon as a research article. Its Introduction and Conclusion contain arguments also exposed in Chapter 1 and 7 of this manuscript and the short experimental setup section contains pieces of information that were already detailed in Chapter 2.

4.1 Introduction

Evaporation from capillary structures is encountered in many natural or technological systems or processes such as the evaporation from soils, e.g. Or *et al.* [34], the two-phase heat transport cooling devices used in the electronics cooling industry for hot-spot cooling and heat spreading [22], Garimella *et al.* [25], the porous coating formation, e.g. Velez & Gupta [53], the drying of porous media [45], as well as with the porous wicks used in several consumer products, such as air-fresheners and insect repellants, for dispensing volatile compounds into air. Evaporation is also used in microfluidic devices for the exploration of phase diagrams, e.g. Leng *et al.* [30], or the characterization of fluid properties, e.g. Clément & Leng [16]. Controlling evaporation is a mean in these devices to obtain concentrate solutions in a controlled way.

In most of these examples, an accurate control of the evaporation rate and of its variation over time is essential. Consider the convective drying of porous media, e.g. Scherer [45]. A simple method to control the drying speed is to play with the parameters of the environment such as the velocity, the temperature or the relative humidity in the surrounding gas mixture. However, it is well known that evaporation in this case is controlled by the external conditions only over a limited period of the drying process. The internal transfer mechanisms actually play a major role as regards the overall duration of the process. This suggests the possibility of controlling the evaporation process by playing with the structural properties of the medium, e.g. Vincent *et al.* [55], Cejas *et al.* [7]. A simple example is the control of evaporation of soil by playing with the properties of a superficial

upper layer e.g. Assouline *et al.* [1]. A still simpler example is the evaporation from a capillary tube, e.g. Chauvet *et al.* [10]. Making the tube of polygonal cross section can dramatically reduce the overall drying time compared to a circular tube owing to the trapping of liquid films by capillary effect along the tube internal corners. On the technological side, heat pipes and two-phase loops, e.g. Faghri [22], are examples of passive systems where a capillary structure controls the performances. Optimizing the capillary structure implies a sufficient understanding of the impact of capillary structure modifications on the evaporation process. Furthermore, the development of advanced technologies, such as 3D printing and other additive manufacturing techniques offer new possibilities for designing porous structures with properties tailored to specific applications. This reinforces the need of a better understanding of the impact of capillary microstructure geometry on the evaporation process so as to improving the effectiveness of capillary structures used in the applications.

In this context, we show how one can play with geometry in quasi - two-dimensional capillary structures to control the drying process. The work is based on one basic idea. Suppose that an evaporation front is located at a distance δ from the open surface inside a capillary structure. Then the evaporation flux j is inversely proportional to this distance, i.e. $j \propto D \frac{\Delta c}{\delta}$, where D is the molecular diffusion of the evaporating species in the gas phase and $\Delta c = c_e - c_\infty$ is the evaporating species concentration difference between the evaporation front, where the local thermodynamical equilibrium condition applies, and the far field, i.e. the external air. Controlling the drying process is thus controlling the distance δ and its variation over time. The control of $\delta(t)$ is sought in two ways: firstly, from the control of the liquid - gas distribution within the capillary structure during the drying process; secondly, from the control of capillary liquid films along the solid walls in the regions invaded by the gas phase. As we shall see the latter will be achieved from phyllotaxy inspired geometry (*phyllotaxy* refers to the arrangement of leaves on a plant).

4.2 Experimental set-up

The capillary structures investigated in this article consist in arrays of cylindrical pillars confined between two horizontal flat disks (see Figure 4.1). They are made in SU8. Vapor escapes from the outer perimeter of this sort of circular Hele-Shaw cell with pillars. The distance h between the two plates is equal to the diameter d of the pillars ($d_c = 500 \mu\text{m}$). All the pillars have the same diameter. Other details are given in the caption of Figure 4.1. The system is transparent. A Nikon D100 camera with a resolution of 3008 pixels \times 2000 pixels is set above the system. Images of the liquid-gas distribution within the system during the drying process are recorded using the acquisition software Nikon Capture Control with an image recording interval varying between 100 s and 2 min depending on the considered device. The evolution of the mass $m(t)$ of the system is measured using a Mettler-Toledo PM 6100 precision scale with an accuracy of 0.01 g. The device mass loss is measured with a time interval varying between 1 s and 15 s depending of the device with data automatically stored on a computer. All the experiments are performed

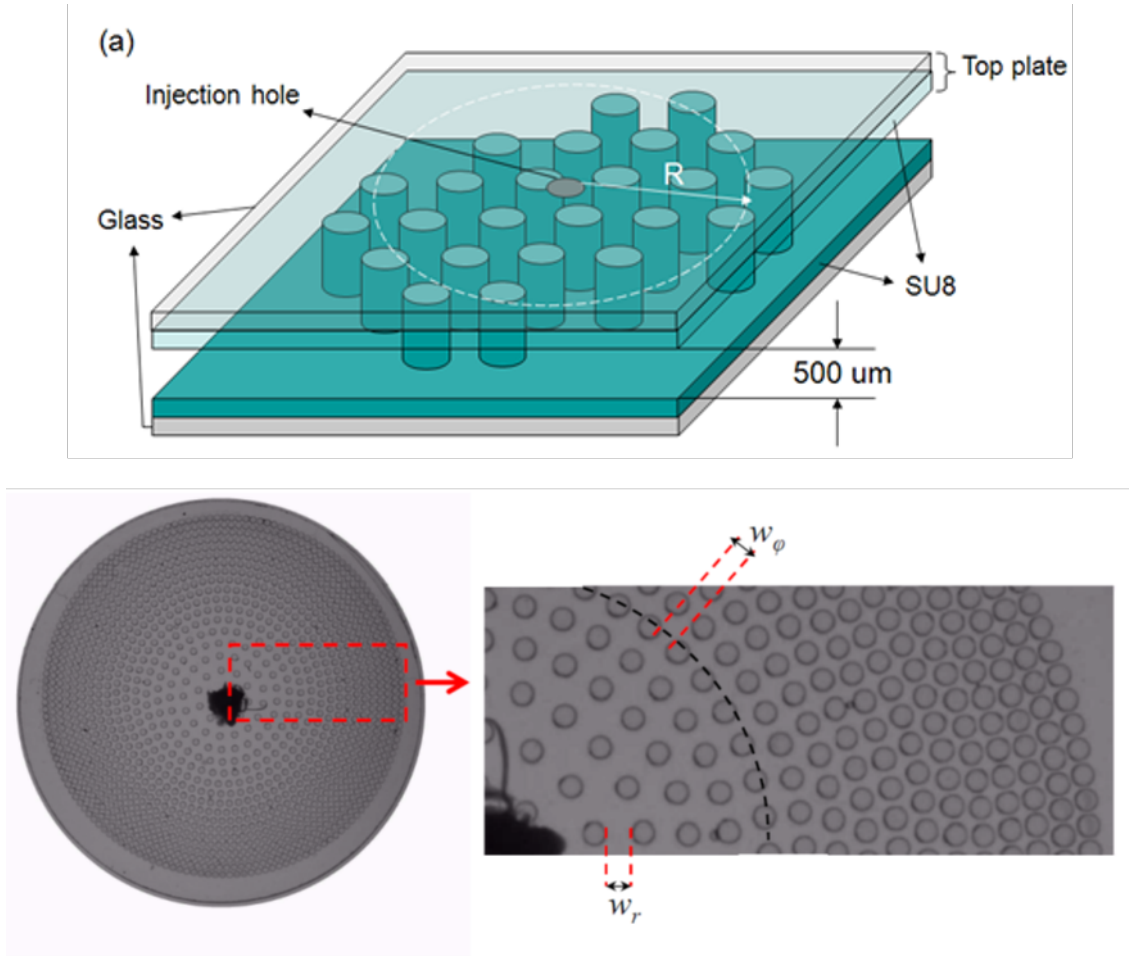


Figure 4.1: a) Sketch of studied capillary structures: An array of cylindrical pillars of identical diameter is confined between two transparent disks. This system is saturated by liquid initially. Vapor forming as a result of evaporation escapes from the outer perimeter of the device. The circle visible in the middle of the disk is used to fill the system with the liquid. It is sealed during a drying experiment. The pillar diameter d_c is equal to $500 \mu\text{m}$. The circular top plate radius is $R = 17.5 \text{ mm}$ whereas the radius of the region containing the pillars is $R_p = 15 \text{ mm}$ (distance to outermost pillar center); b) details (unstable case) with notations.

with ethanol (diffusion coefficient $D = 1.4 \times 10^{-5} \text{ m}^2/\text{s}$, dynamic viscosity $\mu = 1.2 \times 10^{-3} \text{ Pa}\cdot\text{s}$, density $\rho_l = 788 \text{ kg}/\text{m}^3$, surface tension $\gamma = 22 \times 10^{-3} \text{ N}/\text{m}$, contact angle $\theta = 0^\circ$ on SU-8). The experiment are performed under quasi-isothermal conditions in a room of controlled temperature ($T = 22^\circ\text{C}$). The equilibrium vapour concentration of ethanol at this temperature is $c_e = 0.122 \text{ kg}/\text{m}^3$. The ethanol vapour concentration in the surrounding air is $c_\infty = 0$.

System	m_0 (g)	Apparent overall porosity
stable	0.226	0.59
unstable	0.201	0.53
spiral	0.300	0.79

Table 4.1: Apparent overall porosity (deduced from the total evaporated mass, $R = 17.5$ mm and $h = 0.5$ mm) and initial mass m_0 of liquid at $t = 0$ in the three systems

4.3 Evaporation in radial gradients capillary structures

In this section as well as in the next section, we consider two situations where the pillars are organized in concentric circles. Figure 4.2 illustrates the phase distribution evolution for the case referred to as the stable case while Figure 4.3 show the unstable case. In the stable configuration, the gap w_φ between a pair of pillars along a concentric circle increases with an increasing distance from the system center (see Figure 4.1b) for an illustration of the definition of w_φ). The further the pair from the device center, the greater the gap. Hence $\frac{dw_\varphi}{dr} > 0$ in this case where r is the radial coordinate of a (r, φ) polar system with its pole at the center of the device. By contrast, $\frac{dw_\varphi}{dr} < 0$ in the unstable case (Figure 4.3), i.e. the closer the pair to the center, the larger the gap in this case. These systems are therefore referred to as pillar arrays in a gap radial gradient. Positive gradients correspond to the so-called stable case whereas negative gradients correspond to the unstable case. The stable and unstable names will be clear from the discussion on the evolution of the liquid gas phase distributions presented in what follows.

4.3.1 Phase distributions during drying

In the stable case (Figure 4.2), the evaporation front is concentric. As depicted in Figure 4.2, it progressively recedes into the system forming concentric circles corresponding to the outer perimeters of the succession of pillar concentric circles. By contrast, the evaporation front stays pinned over a long period along the outermost row of pillars at the periphery of the system in the unstable case (Figure 4.3). As illustrated in Figure 4.4, the gas invasion induced by the evaporation process is first characterized by the formation of an unstable and intermittent gas finger rapidly connecting the gas phase to the center of the system. As shown in Figure 4.3 and 4.4, quasi-concentric invasion front forms there while the evaporation front stays pinned at the system periphery. This invasion front outwardly moves within the pillar array until reaching the evaporation front, occasionally trapping some liquid clusters. The latter evaporate in the last phase of the process (Figure 4.6).

To understand the impact of gap gradient on invasion pattern, an invasion capillary pressure threshold P_c is associated with each constriction present in the void

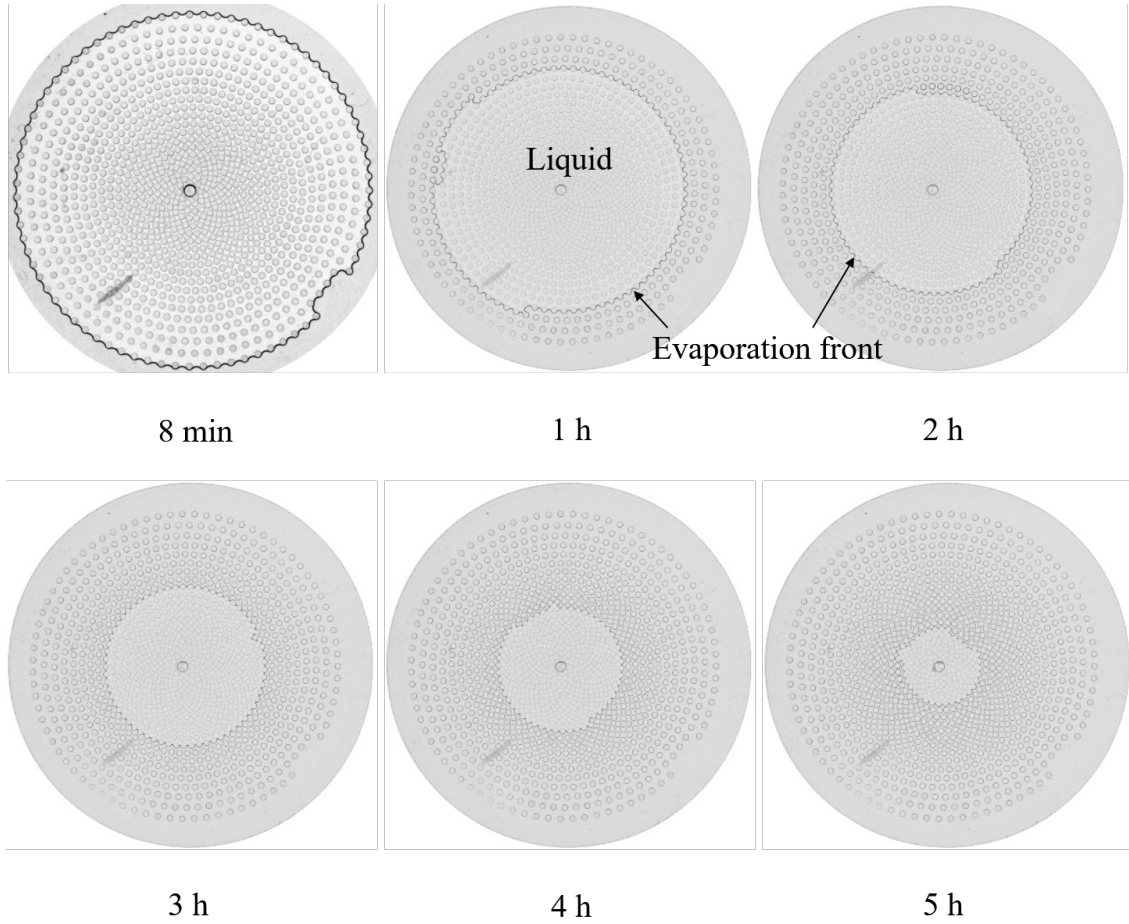


Figure 4.2: Images of liquid-gas phase distribution during drying in the stable case ($\frac{dw_\varphi}{dr} > 0$); Liquid phase (in light grey), gas phase (air + ethanol vapor) in darker grey

space. This threshold is the pressure difference between the gas and the liquid that must be overcome for a bulk meniscus to cross the constriction.

The constrictions refer to the narrowest passages between two cylinders. As illustrated in Figure 4.1, one can distinguish constrictions of width w_φ in approximately the radial directions (the cross-section plane of the constriction is approximately perpendicular to a radial direction) and constrictions of width w_r in azimuthal directions (the cross-section plane of the constriction is approximately perpendicular to a azimuthal direction, thus parallel to a radial direction). Approximations of p_c are given by

$$p_{cr} \approx \gamma \cos\theta \left(\frac{2}{h} + \frac{2}{w_\varphi} \right) \quad (4.1)$$

and

$$p_{c\varphi} \approx \gamma \cos\theta \left(\frac{2}{h} + \frac{2}{w_r} \right) \quad (4.2)$$

for constrictions in radial and azimuthal directions respectively. A more accurate

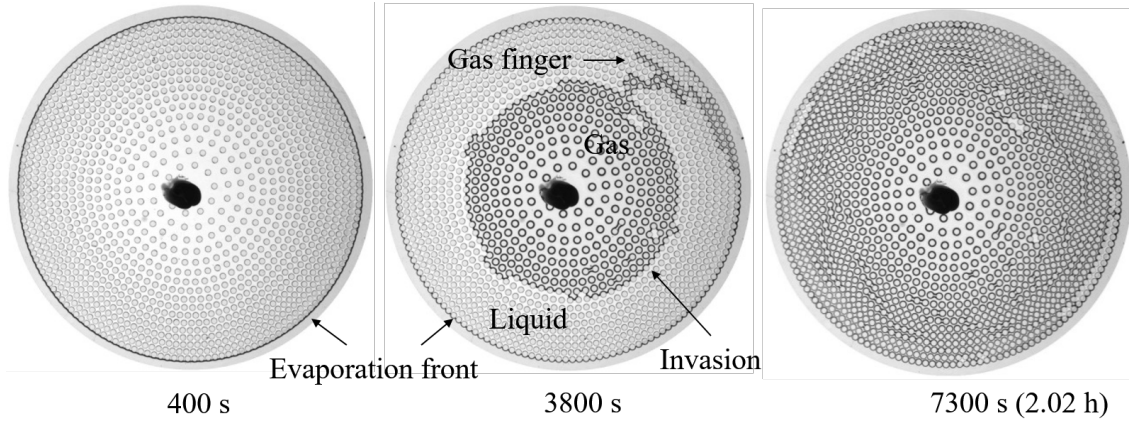


Figure 4.3: Images of main phase distribution patterns during drying in the unstable case ($\frac{dw_\varphi}{dr} < 0$): i) pinning of the evaporation front along the periphery of the outer row of cylinders, ii) formation of the unstable gas finger and gas zone developing outwardly from the centre, iii) last phase characterized by the evaporation of trapped liquid within the system at the end of the preceding phase. Liquid phase (in light grey), gas phase (air + ethanol vapor) in darker grey. The red circle shows a temporary trapped liquid cluster.

determination of the capillary pressure threshold requires the computation of the meniscus shape at its maximum total curvature within the constrictions. This will be presented in Chapter 5. The approximations considered here are sufficient for the present chapter. The evaporation process is slow and as a result it is considered that capillary effects control the pattern. The lower the capillary pressure threshold, the easier the local invasion, that is the displacement of the meniscus through the constriction.

The system is invaded by the gas phase by successive selection of the largest constriction available along the liquid-gas interface. As a result, all the azimuthal constrictions between two concentric circles of pillars are invaded before the gas phase can progress again toward the system center in the stable case since $\frac{dw_\varphi}{dr} > 0$ in this case. As illustrated in Figure 4.2, this leads to an invasion characterized by the successive pinning of the invasion front along each concentric row of cylinders. Since there is only little liquid temporarily trapped between the invasion front and the outer edge of the system, the invasion front practically coincides with the evaporation front in this case. Little variations in the geometry of the constrictions combined with local pressure variations due to the viscous flow induced in the liquid then decide for the constriction to be invaded when the front starts moving from one concentric row of cylinders to the next one.

In the unstable case ($\frac{dw_\varphi}{dr} < 0$), the gas phase mainly progresses directly toward the center in a first phase since the closer the constriction to the center, the lower its invasion capillary threshold.

As illustrated in Figure 4.4, this first phase is characterized by an interesting process of gas invasion by bursts. The process is as follows. A thin gas finger (see the

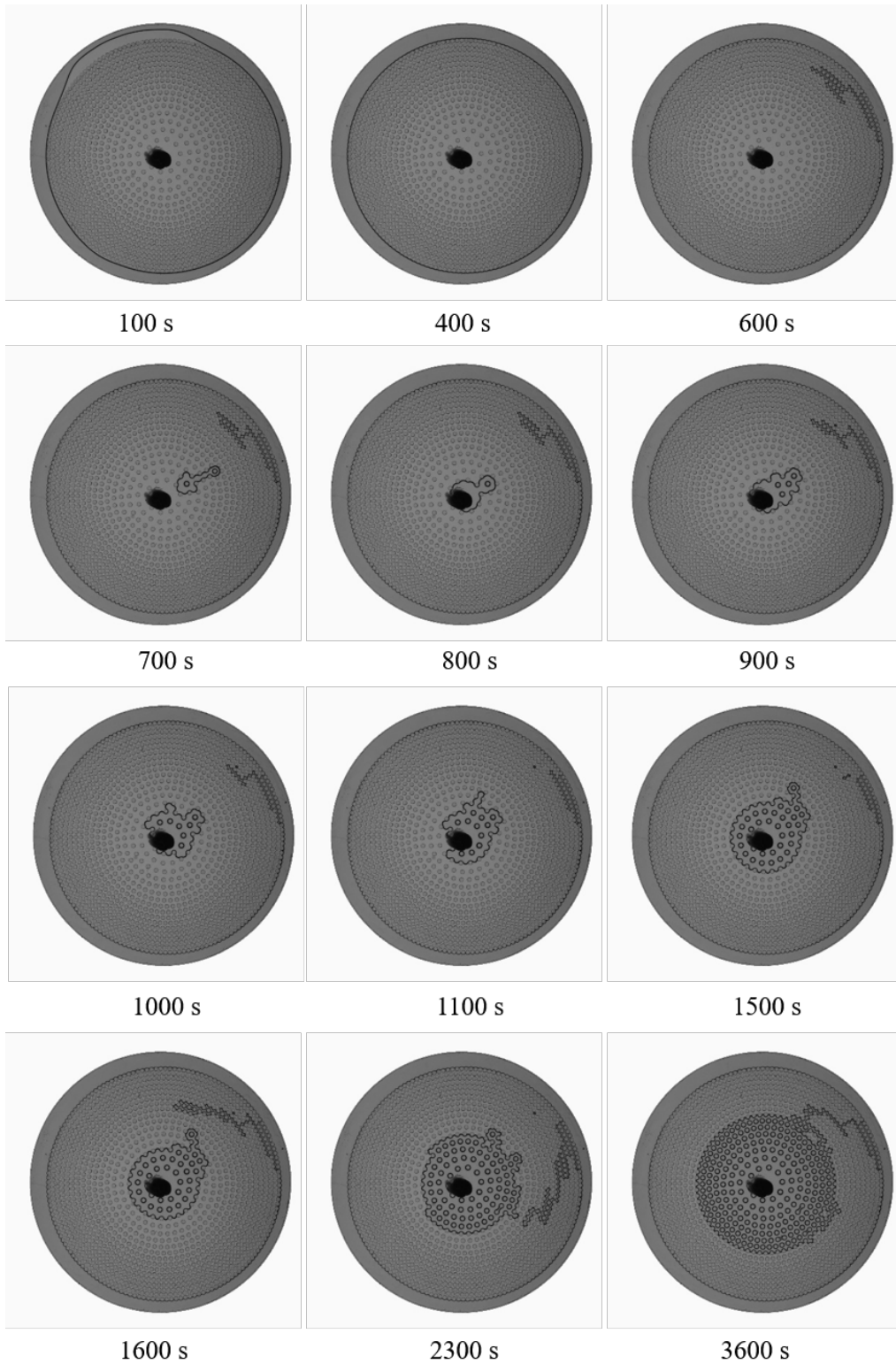


Figure 4.4: Phase 1 in the unstable case ($\frac{dw_\varphi}{dr} < 0$): formation of intermittent gas finger with the evaporation front pinned along the outer row of cylinders. Liquid phase (in light grey), gas phase (air + ethanol vapor) in darker grey.

images at time 1600 s or 2300 s in Figure 4.4) develops globally moving toward the center of the system since as discussed previously the constriction invasion capillary pressure thresholds decrease the closer the constriction to the center. However, Figure 4.4 clearly shows that the gas finger connected to the external gas is not stable. In fact, this finger repeatedly breaks up. A fraction of the gas contained in the gas finger right before the first break-up begins to form a gas cluster near the center of the system (see the image at $t = 700$ s in Figure 4.4) while the remaining shortened branch of the finger recedes toward the outer periphery of the system as a result of a capillary re-equilibrium process. Then the gas finger grows again until it reached the more central gas cluster. A new break-up then occurs resulting in the growth of the detached central gas cluster and in the receding of the shortened finger similarly as after the first break-up. This process repeats itself several times until the central gas cluster has sufficiently grown for the thin gas finger to stabilize (this corresponds to the image at $t = 3600$ s in Figure 4.4 where the gas finger forms a stable path between the growing central region and the external air). It can be also seen from Figure 4.4 that the path followed by the intermittent gas finger is not stable (compared the images at $t = 1600$ s and $t = 2300$ s in Figure 4.4). It is also important to note that the liquid gas front pinned along the outer concentric row of cylinders is not affected by the gas central invasion mechanism by bursts (see Figure 4.4, where it can be seen that the gas liquid distribution along the most peripheral cylinders does not change). The reason for the gas finger break-up is explained schematically in Figure 4.5. As in porous materials, e.g. Haines [26], the gas invasion is envisioned as succession of quasi-static capillary equilibria. The sudden and rapid event when the phases move from one capillary equilibrium configuration to another is referred to as a Haines jump. Thus this is during a Haines jump that the growing gas finger breaks up. The main point is to realize that the capillary equilibrium without constriction refilling (a phenomenon also referred to as snap-off) is not possible over a gas cluster developing over a too long series of cylinder rows (see Figure 4.5). As sketched in Figure 4.5, corner films form in the corners existing at the contact between the cylinders and the top and bottom plates of system as the gas finger advances inside the system. Consider only constrictions aligned with the azimuthal direction.

Under the condition of capillary equilibrium, we express that the capillary pressure in the corner film is about equal to the capillary pressure threshold necessary for the bulk meniscus to cross the constriction (at the finger tip):

$$\gamma \left(\frac{1}{R_1} + \frac{1}{R_2} \right) \approx \gamma \cos\theta \left(\frac{2}{h} + \frac{2}{w_\varphi} \right) \quad (4.3)$$

where R_1 and R_2 are the liquid corner main curvature radii. Neglecting the curvature radius in the in plane direction leads to

$$R_1 \approx \left[\cos\theta \left(\frac{2}{h} + \frac{2}{w_\varphi} \right) \right]^{-1} \quad (4.4)$$

Thus roughly,

$$R_1 \propto w_\varphi \quad (4.5)$$

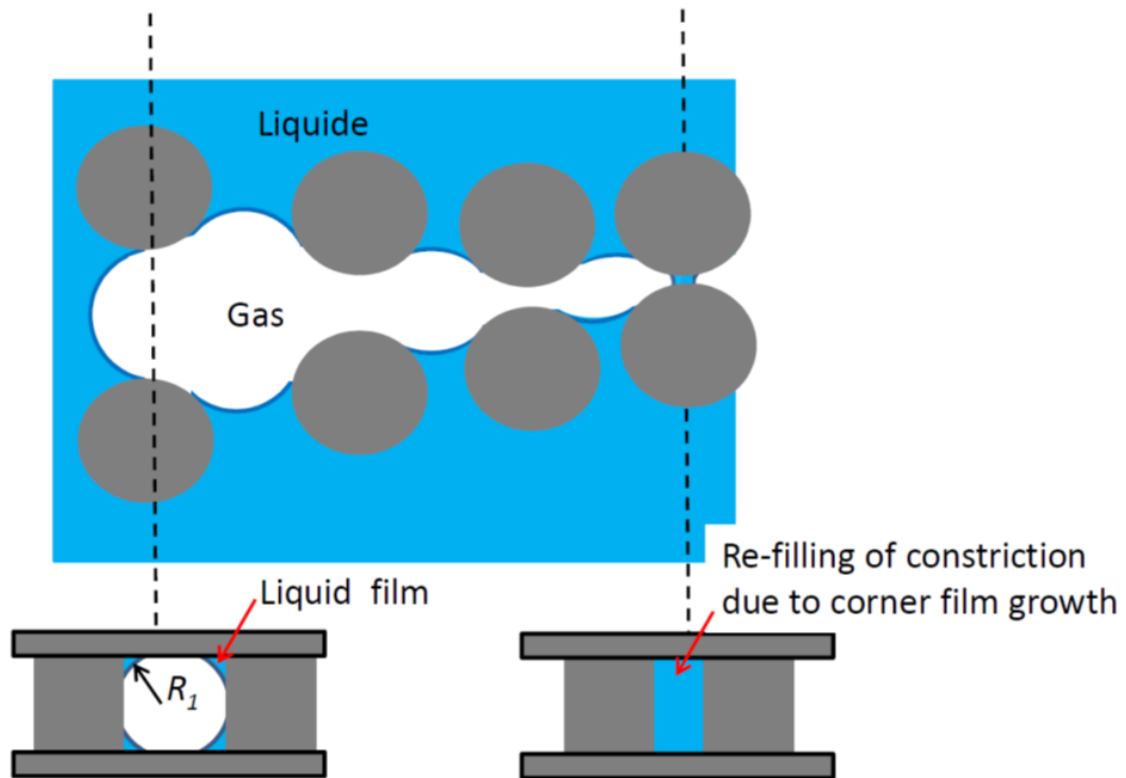


Figure 4.5: Schematic of break-up mechanism of the gas finger as the finger tip advances toward a region of locally lower local capillary pressure threshold.

The result is that the thickness of the corner liquid films (the greater R_1 , the thicker the film) increases as the gas finger advances in regions of wider constrictions. This increase takes place everywhere since the pressure is spatially quasi uniform in each phase under the condition of capillary equilibrium. Thus also within the constrictions along the gas finger located in the regions where the constrictions are narrower.

As the result of the film growth, the liquid corners eventually touch each other in narrower constrictions. Assuming a zero contact angle for simplicity, this must happen in constrictions such that $2R_1 \approx w_\varphi$. The “touch even”, e.g. Cieplack & Robbins [15], breaks the capillary equilibrium and leads to the gas finger break up via the refilling of at least one narrower constriction. Consistently with this scenario, the images in Figure 4.4 suggest that the break-up occurs in the regions of the gas finger of narrowest constrictions. This remains to be confirmed from images recorded at higher frame rates than the one (100 s) used to obtain the images shown in Figure 4.4. Note also that viscous effects and even inertial effects, Ferrari & Lunati [23], are not negligible during a Haines jump and contribute to decide where the refilling takes place.

Figure 4.6 shows the transition toward a second phase of drying where the evaporation rate is significantly lower (see next section for a more detailed discussion on the drying kinetics). The duration of the transition is short, about 1000 s (from $t = 6500$ s to $t = 7500$ s). It corresponds to the evaporation of the liquid trapped

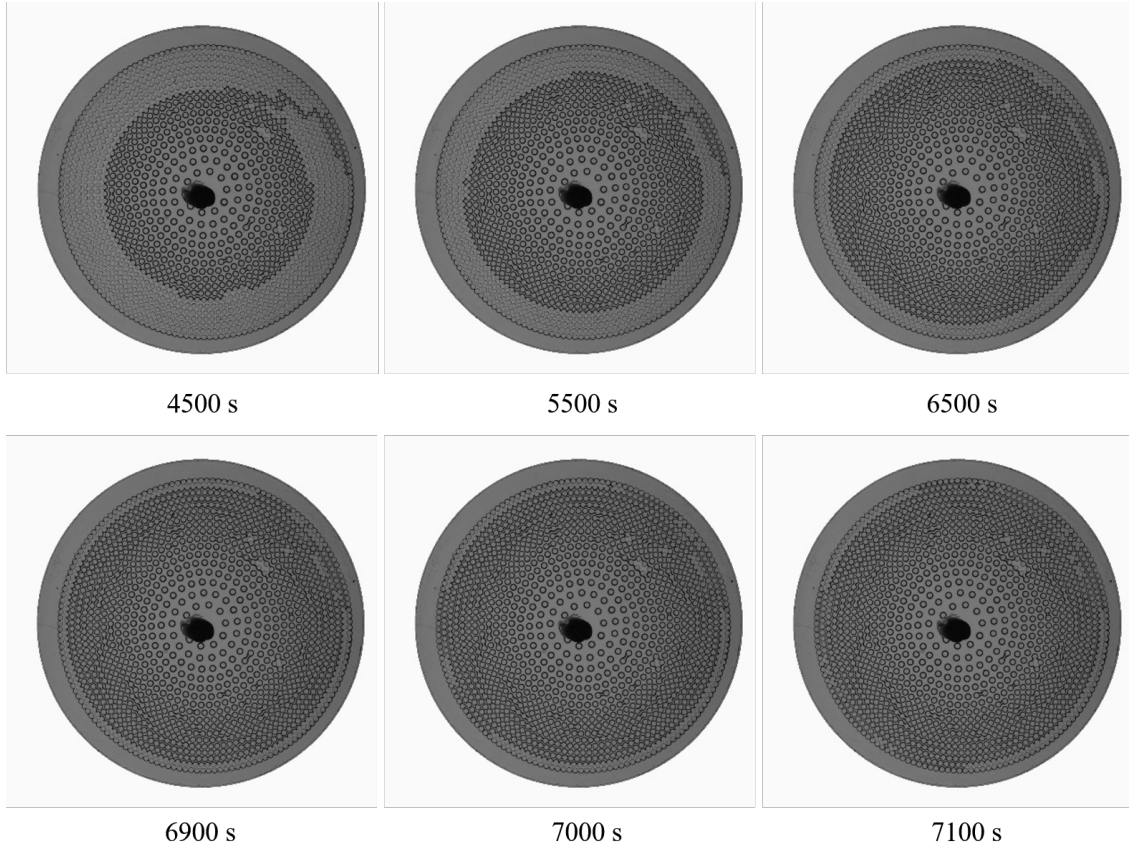


Figure 4.6: Details on the phase distribution evolution in the unstable case in the transition period (corresponding to point A in Fig 7a) between the drying period at high evaporation rate and the period when the drying rate sharply decreases.

along the most peripheral row of cylinders. As illustrated in Figure 4.6, the liquid region progressively thins out as the result of the growth of the central gas region until this region is only one cylinder diameter thick (image at $t = 6900$ s in Figure 4.6). Then this thin liquid region evaporates (as illustrated in Figure 4.6 by the images at time $t = 6900$ s, 7000 s and 7100 s).

At the end of the transition region, some liquid remains trapped within the capillary structure as illustrated in Figure 4.7. It corresponds to liquid bridges between pairs of cylinders and to liquid clusters attached to a few cylinders. A last and slow phase of drying corresponds to the evaporation of this residual liquid.

4.3.2 Drying kinetics

Based on the patterns discussed in the previous sub-section, major differences in the drying time are expected depending on the sign of $\frac{dw_\varphi}{dr}$. Since the evaporation front remains pinned at the system periphery over a long time in the unstable case, a much shorter overall drying time is expected in this case compared to the stable case. This is illustrated in Figure 4.8a, which shows the system mass loss $m(t)$ as a function of time for the two cases. The curve labelled Phyllotaxy will be discussed

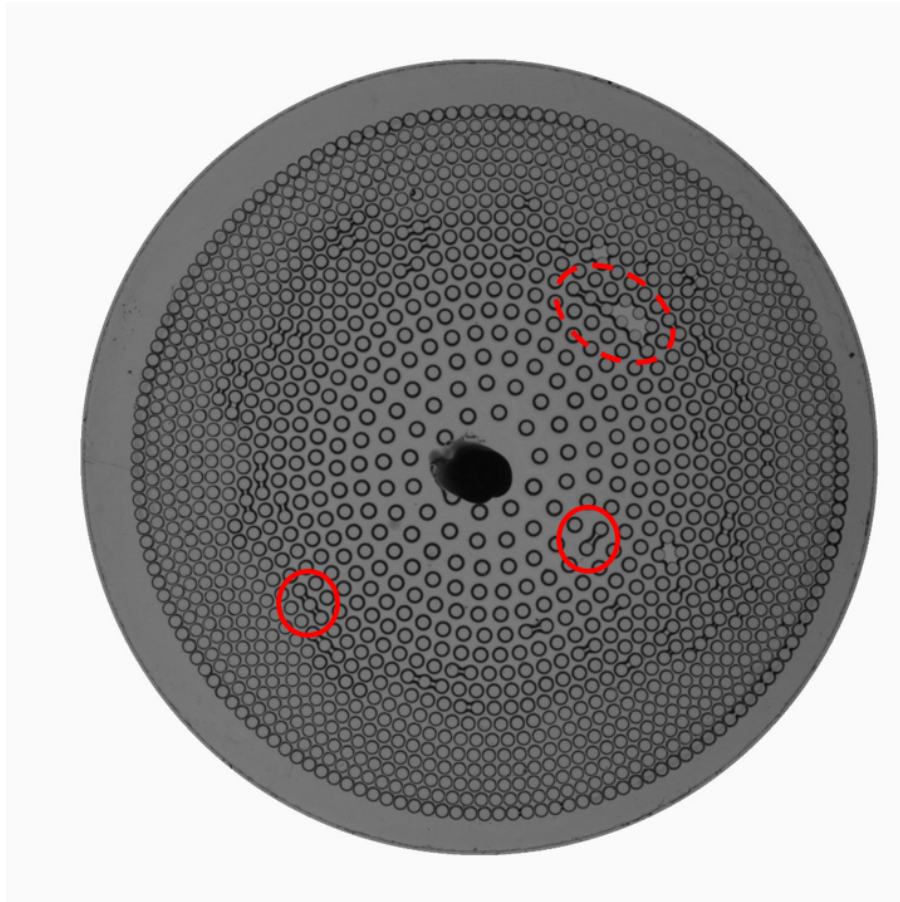


Figure 4.7: Example of phase distribution in the unstable case during the last and slow drying period (this is the phase distribution observed at $t = 7900$ s (2.19 h)). The red circles show example of liquid bridges between pairs of cylinders. The dashed red circle shows a liquid cluster between six cylinders attached to a liquid bridge and a chain of two liquid bridges.

in Section 5. The point A (kink in the curve $m(t)$ for the unstable case) is reached in about 2 hrs (7200 s) consistently with the time corresponding to the collapse of the peripheral liquid-gas front (Figure 4.6). To evaporate a similar mass in the stable case, it takes about 4 hrs. Thus, the unstable configuration reduces here the drying time by about a factor 2 (noting that that the mass in question represents about 85% and 93% of the initial mass of liquid for the stable and unstable cases respectively).

Figure 4.8b) shows the variation of the drying rate ($J = -\frac{dm}{dt}$) as a function of the saturation $S = m(t)/m_0$ where m_0 is the mass of water present in the considered system when the drying experiment starts. The drying rate $J_{ref} = 0.15$ g/h used in Figure 4.8b) as reference drying rate is representative of the evaporation rate when drying starts. In the drying literature, this type of curve is referred to as the drying kinetics, e.g. Van Brakel [52].

As can be seen from Figure 4.8b), the drying kinetics are, as expected, markedly different between the unstable and stable cases. This figure still more clearly shows

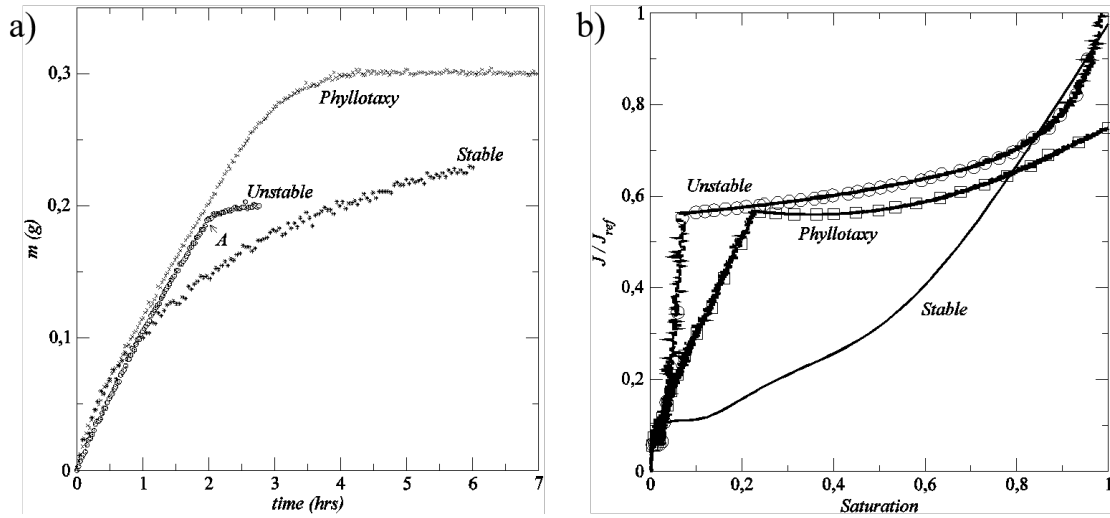


Figure 4.8: a) System mass loss as a function of time for the stable, unstable and phyllotaxy (spiral) cases, b) drying kinetics for the three cases. The reference evaporation rate is $J_{ref} = 0.15$ g/h. The saturation is defined as $m(t)/m_0$ where m_0 is the mass of water present in the considered system when the drying experiment starts.

that the evaporation rate stays high over most of the drying process in the unstable case. Consistently with the evolution of the phase distribution discussed in the previous section, we can distinguish three main phases drying kinetics in the unstable case. The first phase is a phase of rapid decrease in the evaporation rate. This corresponds to the evaporation of the liquid in the gap between the most external row of cylinders and the edge of the system. At the end of this phase, the front is pinned on the first row of cylinders. Then there is the formation of the gas finger penetrating toward the inside until it reaches the center and the gas phase continue to invade the inner part until it reaches back the most external cylinder row. This corresponds to phase 2. The variation of the evaporation rate is weak during this phase. Then there is phase 3 characterized by a rapid decrease in the evaporation rate. This last phase starts at a low liquid saturation and corresponds to the evaporation of the liquid trapped at the end of phase 2.

By contrast, there is no phase where the evaporation rate varies little in the stable case. The evaporation rate continuously decreases and becomes rapidly smaller that the evaporation rate in the stable case as the dry diffusive zone develops.

4.4 Some modelling considerations (stable case)

The stable case is characterized by a simple succession of concentric evaporation front shape. Although obviously questionable (see below), a simple approach is then to rely on the analytical solution proposed in (Clément & Leng [16]). This solution was developed for the case of the evaporation of a liquid confined between two disks (thus in the absence of cylinders in the gap between the two disks). By analogy with this solution for an homogeneous medium (system without pillars between the two

plates or with constant local porosity), i.e. (Clément & Leng [16]), the evaporation rate when the front is located at $r = r_f$ is expressed as

$$J = 2\pi D^* h \frac{\Delta c}{\left(\frac{\delta_{ext} D^*}{RD} + \ln(R/r_f) \right)} \quad (4.6)$$

where δ_{ext} represents an external mass transfer characteristic length, D^* is an effective diffusion coefficient taking into account the presence of the pillars, D is the vapour molecular diffusion coefficient in the gas mixture and $\Delta c = c_e - c_\infty$. For the reference evaporation rate ($J_{ref} = 0.15$ g/h), this gives $\delta_{ext} = 2.29$ mm. A simpler way of taking into account the external mass transfer resistance is to represent it in term of equivalent additional diffusive annulus at the periphery of the system. Accordingly, Equation (4.6) is expressed as

$$J = 2\pi D^* h \frac{\Delta c}{\ln(R^+/r_f)} \quad (4.7)$$

with $R^+ = 20.4$ mm (for $D^* = D$, see below) and $J_{ref} = 2\pi D^* h \frac{\Delta c}{\ln(R^+/R)}$. Then we express that the mass evaporated during the time dt correspond to a displacement dr_f of the evaporation front,

$$\rho_l 2\pi r_f h \varepsilon_g \frac{dr_f}{dt} \approx J \approx 2\pi D^* h \frac{\Delta c}{\ln(R^+/r_f)} \quad (4.8)$$

where ε_g is the porosity of the system (global porosity). The initial condition is $r_f = R$ at $t = 0$. As described in (Clément & Leng [16]), Equation (4.8) can easily be integrated to obtain

$$\alpha \ln \alpha - \alpha - \alpha_0 \ln \alpha_0 + \alpha_0 = \tau \quad (4.9)$$

where $\alpha = \left(\frac{r_f}{R^+} \right)^2$, $\tau = \frac{t}{t_{ref}}$ with $t_{ref} = (\rho_l \varepsilon_g (R^+)^2) / (4D^* \Delta c)$ and α_0 is the value of α at $t = 0$ ($\alpha_0 = (R/R^+)^2$). The liquid mass $m(t)$ is directly related to α : $m(t) = \rho_l \pi \varepsilon_g h (R^+)^2 \alpha$. The global porosity is specified as $\varepsilon_g = \frac{m_0}{\rho_l \pi R^2 h}$ where m_0 is the mass of liquid present in the system at $t = 0$. This gives $\varepsilon_g = 0.59$. Setting ε_g to this value ensures that the model leads to the same total evaporated mass as in the experiment. The only unknown parameter is then D^* . As illustrated in Figure 4.9, it is possible to set D^* so as to obtain a good agreement between this simple model (red curve in Figure 4.9) and the experiment. However the model must be (unphysically) superdiffusive with $D^* = D$. The conclusion is that the model is not predictive. It simply provides a convenient mathematical representation of the experimental data for the stable case.

Naturally, it was obvious from the beginning that the model was not consistent since the medium is strongly non homogeneous. This can be illustrated from the computation of the porosity of the dry zone (zone between $r = r_f$ and $r = R$). Suppose the front is located at $r = r_f$, the porosity of the dry zone is defined as

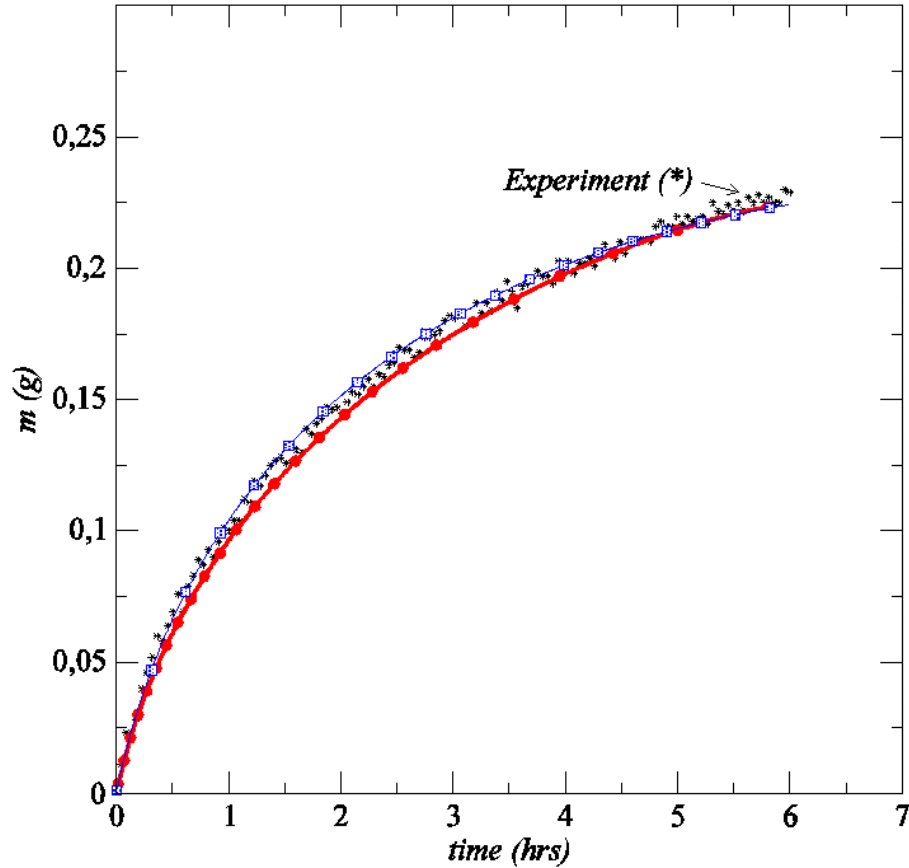


Figure 4.9: System mass loss as a function of time for the stable case. Comparison with homogeneous model (red disks; Equation 4.9) and heterogeneous model (blue squares; Equation 4.16).

$$\varepsilon_{dz}(r_f) = \frac{\pi(R^2 - r_f^2) - S_c}{\pi(R^2 - r_f^2)} \quad (4.10)$$

where S_c is the cross section area of cylinders located in the ring limited by the two circles $r = r_f$ and $r = R$. This leads to the results shown in the inset in Figure 4.10 indicating a significant decrease in the overall porosity of the dry zone as the position of front is located further inside the system.

As can be seen, the porosity variation is quasi-linear over a significant range of front positions. In this respect, this system is a simple example of medium with spatially evolving heterogeneities, e.g. Cushman & Gin [19]. It is well known that modelling transport phenomena in this type of system can lead to non-local transport equations (Cushman & Gin [19]). The non-local nature originates from the rapid spatial variation of the heterogeneity. However, diffusion tends to smooth out the impact of the variations in the heterogeneity. In brief the question arises as to whether a classical local approach leads to a good approximation provided that the medium heterogeneity is taken into account.

A simple approach is therefore to express the equation to be solved in the gas

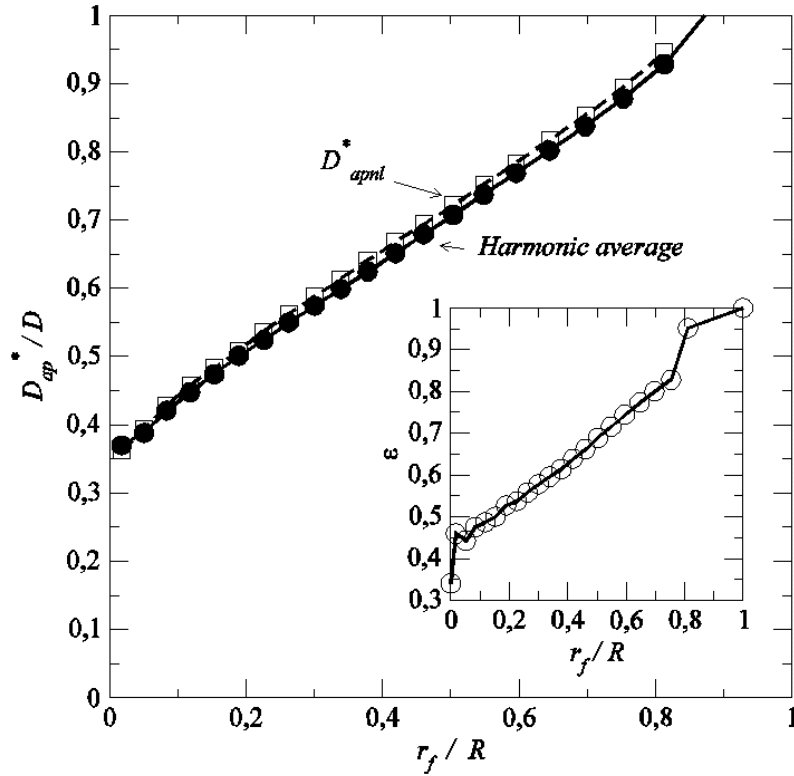


Figure 4.10: Variation of apparent diffusion coefficient D_{ap}^* of the dry zone as a function of evaporation front position for the stable configuration. The inset show the variation of the porosity of the dry zone (Equation 4.10) as a function of evaporation front position

phase as

$$\frac{d}{dr} \left(r D^* \frac{dc}{dr} \right) = 0 \quad (4.11)$$

with the boundary condition $c = c_e$ at $r = r_f$ and $c = 0$ at $r = R^+$. Note that here we slightly modify R^+ assuming that the diffusion coefficient is the molecular binary coefficient D within the extra annulus introduced to model the external mass transfer. This extra annulus is therefore considered as free of cylinders. This gives $R^+ = 19.95$ mm ($R^+/R = 1.14$). The essential difference compared to the previous solution (Equation 4.9) is then that D^* depends on r . To give a local value to D^* , the procedure was as follows. Considering the concentric annulus i containing the cylinder located at $r = r_c(i)$ ($r_c(i)$ is the cylinder centre position). The circles forming the boundary of this annulus are located at $r_{inf} = \frac{r_c(i-1) + r_c(i)}{2}$ and $r_{max} = \frac{r_c(i+1) + r_c(i)}{2}$ respectively. For a given concentration difference δc over the annulus the diffusion transfer rate can be expressed as

$$J = D^* \frac{2\pi h \delta c}{\ln(r_{max}/r_{min})}. \quad (4.12)$$

The diffusion problem can be solved at the scale of the cylinder concentric alley

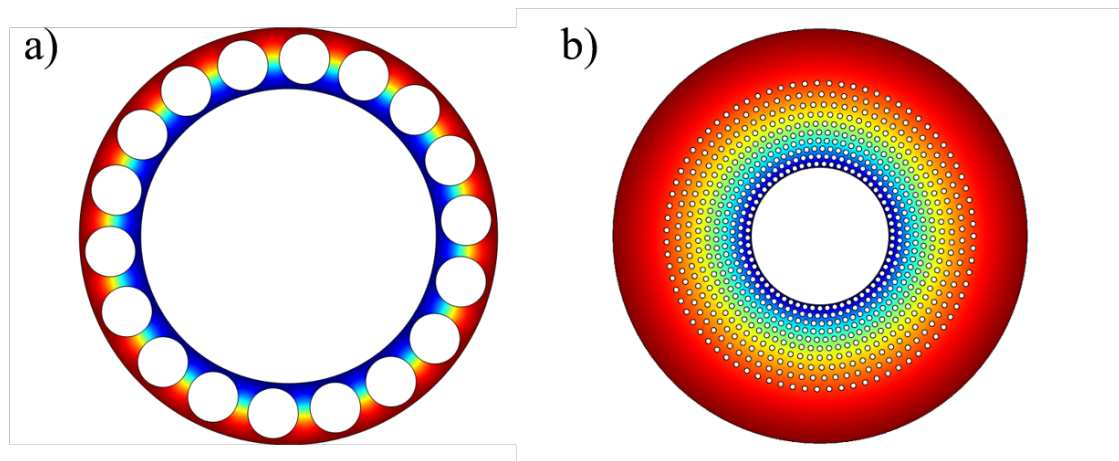


Figure 4.11: Examples of vapor concentration fields computed using Comsol Multiphysic: a) annulus with one row of cylinders, b) dry zone from $r = r_f$ (position of evaporation front) to $r = R^+$.

from the thickness averaged equation,

$$\nabla \cdot (hD\nabla c) = 0 \quad (4.13)$$

where the differential operators are 2D (in-plane). Equation (4.13) is solved using the commercial code Comsol Multiphysics with the same boundary conditions as above at $r = r_{min}$ and $r = r_{max}$ with in addition a zero flux condition at the cylinder boundary. This type of computation is illustrated in Figure 4.11. The diffusion transfer rate is then computed as

$$J_m = Dh r_{max} \int_0^{2\pi} \left. \frac{\partial c}{\partial r} \right|_{r=r_{max}} d\varphi \quad (4.14)$$

where φ is the azimuthal coordinate; D^* is then determined by expressing that $J = J_m$. This gives the results shown in Figure 4.12 where the local porosity is the void fraction is the considered annulus.

To compute the drying process, we express the mass balance similarly as before as

$$\rho_l 2\pi r_f h \varepsilon \frac{dr_f}{dt} \approx 2\pi r_f h D^* \left. \frac{dc}{dr} \right|_{r=r_f} \quad (4.15)$$

where ε and D^* are now local value. The diffusive transfer rate $J = 2\pi r_f h D^* \left. \frac{dc}{dr} \right|_{r=r_f}$ can be approximated from an harmonic average as

$$J = \frac{2\pi h \Delta c}{\sum_{i=1}^m \frac{1}{D_i^*} \ln \left(\frac{R_{i+1}}{R_i} \right)} \quad (4.16)$$

where $R_1 = r_f$ and R_i for $i > 1$ corresponds to the position of the boundary between two successive concentric rows of cylinders. Introducing the concept of apparent

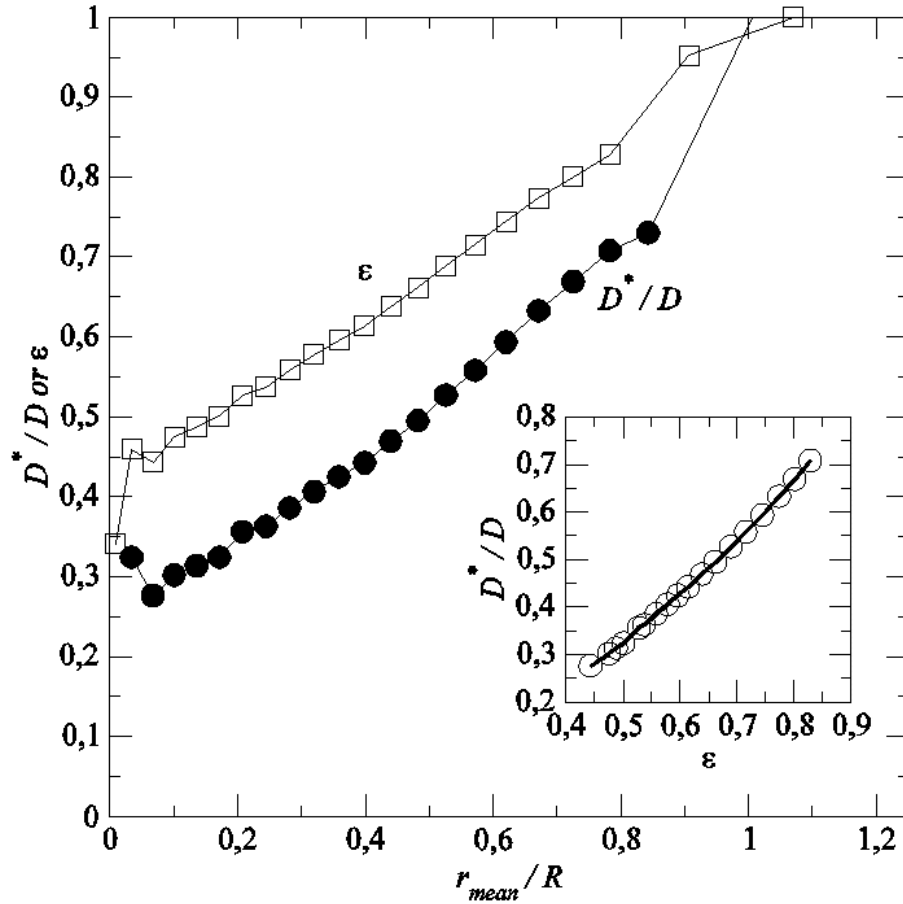


Figure 4.12: Variation of “local” D^* and “local” porosity as a function of radial position. The inset shows the variation of D^* as a function of the local porosity (excluding the first annulus from the centre).

diffusion coefficient of the whole dry zone D_{ap}^* , we deduce from the above a first estimate of D_{ap}^* given by Equation 4.17:

$$J = \frac{2\pi h \Delta c}{\sum_{i=1}^m \frac{1}{D_i^*} \ln\left(\frac{R_{i+1}}{R_i}\right)} = \frac{2\pi h D_{ap}^* \Delta c}{\ln\left(\frac{R^+}{r_f}\right)}. \quad (4.17)$$

That is,

$$D_{ap}^* = \frac{\ln\left(\frac{R^+}{r_f}\right)}{\sum_{i=1}^m \frac{1}{D_i^*} \ln\left(\frac{R_{i+1}}{R_i}\right)}. \quad (4.18)$$

This gives the variation of plotted in Figure 4.10 (labelled harmonic average in Figure 4.10). To evaluate the possible impact of the non-local nature of the problem, the apparent diffusion coefficient of the dry zone was also computed from the solution of Equation (4.13) over the whole dry zone for various positions of evaporation front r_f . Equation 4.13 was thus solved with the no flux boundary condition on the cylinders, $c = c_e$ at $r = r_f$ and $c = 0$ at $r = R^+$, then the diffusion transfer

rate was computed as $J_m = Dh r_f \int_0^{2\pi} \frac{\partial c}{\partial r} \Big|_{r=r_f} d\varphi$, from which the non-local apparent coefficient D_{apnl}^* was computed from $J_m = (2\pi h D_{apnl}^* \Delta c) / \ln(R^+/r_f)$. D_{apnl}^* so obtained is compared with D_{ap}^* in Figure 4.10. As can be seen from Figure 4.10 the difference with the harmonic average (Equation 4.18) is quite weak. Thus the rapid radial variation of the heterogeneity has actually here a quite weak impact (the difference in Figure 4.10 between the two sets of data is actually within the computational errors).

A simple numerical solution can then be expected from the mass balance,

$$\rho_l 2\pi r_f h \varepsilon(r_f) \frac{dr_f}{dt} = 2\pi D_{apnl}^* r_f h \frac{\Delta c}{\ln(R^+/r_f)} \quad (4.19)$$

where $\varepsilon(r_f)$ is the local porosity (porosity in the annulus of width dr_f). We actually took for $\varepsilon(r_f)$ the variation depicted in Figure 4.12 and computed from the consideration of annuli containing one circular row of cylinders.

Solving Equation (4.19) led to the results reported in Figure 4.9. The agreement with the experimental data looks quite good. This is actually misleading for the following reasons. First, we corrected the thickness h of the system to impose the same initial mass of liquid as in the experiment (there are 1444 cylinders in this system. This corresponds to a porosity of 0.78 whereas the porosity estimated from the total evaporated mass is only 0.59 !). Second we increased the molecular diffusion coefficient by a factor 1.4 ! to obtain the “good” agreement shown in Figure 4.9. It can be argued that the motion of the evaporation front is not continuous in the experiment since the front is repeatedly pinned on the successive circular rows of cylinders. Also the physical system is not perfectly axisymmetric. More work is needed to see if these elements can explain the somewhat poor predictions obtained from solving Equation (4.19).

4.5 Phyllotaxy inspired capillary structures

4.5.1 Motivation

Although playing with the radial gap gradient $\frac{dw_\varphi}{dr}$ is a simple way of controlling the drying process, another attractive possibility consists in playing with secondary capillary effects. Secondary capillary effects refer to liquid capillary trapping in the void space after the void space has been invaded in the bulk by the gas phase. The capillary thick films which can remain trapped along the corners of a capillary square tube are an archetypical example of capillary liquid structures due to secondary capillary effects, e.g. Chauvet *et al.* [10]. As discussed in 3.1, this type of corner liquid films are also present in our systems. The liquid bridges at the contact points between two particles in a random packing of particles (as illustrated in Figure 4.13) or the capillary rings in the microfluidic device discussed in Vorhauer *et al.* [57] are other examples of secondary capillary liquid structures.

In the case of arrays of pillars confined between two plates, the capillary elementary liquid structure that can form between two pillars is a liquid bridge. Such

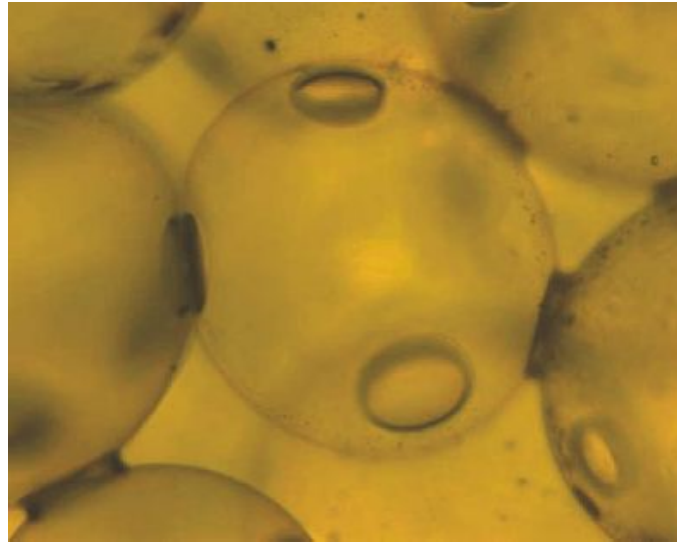


Figure 4.13: Closeup view into a model consisting of spherical glass beads (300 microns in diameter) and water as the wetting liquid. The latter is clearly seen to accumulate in little rings at the points of contact of adjacent grains. The space in between the spheres has been filled by an immersion liquid (mixture of toluene and di-iodomethane) in order to minimize refraction losses.

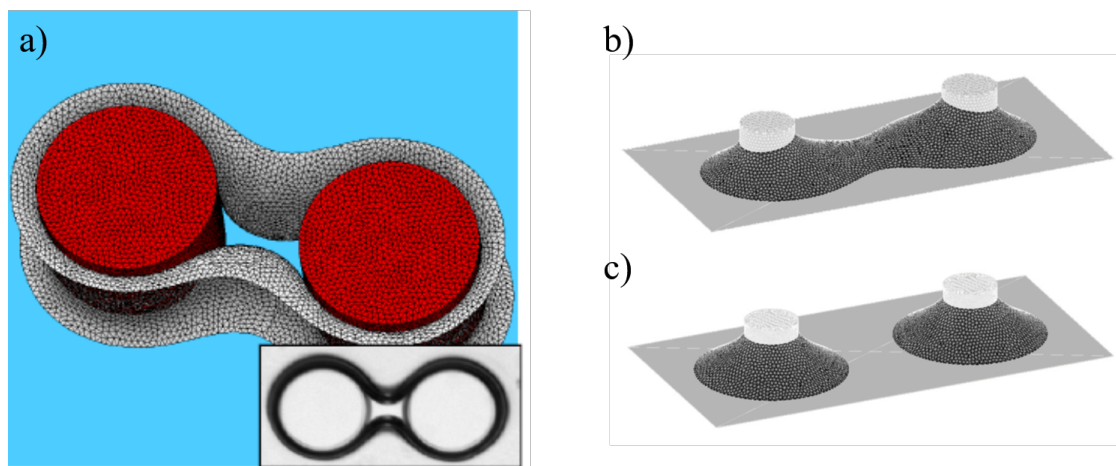


Figure 4.14: a) Liquid - gas interface of liquid bridge connecting two pillars computed using Surface Evolver [5]. The inset shows a top view of the liquid bridge in one of our experimental devices. The thick black contour corresponds to the projection of the liquid - gas interface onto a horizontal plane, b) c) Examples of computed equilibrium shape of liquid bridge for smaller liquid volumes than in Figure 4.14a (owing to symmetry only the lower part is shown).

an elementary object is shown in Figure 4.14 and is also visible in Figure 4.7

There are of course geometrical constraints for liquid bridges to form during the drying process. Consider an array of cylinders as depicted in Figure 4.15. We wish to approximately determine the total curvature within the bridge formed as a result of the displacement of the bulk meniscus in the radial direction through

the constrictions. The rationale is similar as in 3.1 (Eqs. (3-5)). Since the liquid bridge forms as the result of the crossing of the constriction by a bulk meniscus, we express that the capillary pressure in the liquid bridge is about equal to the capillary pressure threshold necessary for the bulk meniscus to cross one constriction:

$$\gamma \left(\frac{1}{R_1} + \frac{1}{R_2} \right) \approx \gamma \cos \theta \left(\frac{2}{h} + \frac{2}{w_\varphi} \right) \quad (4.20)$$

where R_1 and R_2 are the liquid bridge main curvature radii at the considered point of its surface. Suppose that the liquid bridge takes the form of four separated liquid bridges around the top and bottom regions of pillars (as depicted in Figure 4.14c) which only shows the bottom region owing to an obvious symmetry). We then consider the liquid bridge cross section sketched in Figure 4.15b (also in Figure 4.14c) and make the approximation $R_2 \gg R_1$. Assuming a perfectly wetting liquid, one therefore obtains $R_1 \approx \left(\frac{2}{h} + \frac{2}{w_\varphi} \right)^{-1}$. Now suppose we want the bridges to form a chain of interconnected bridges in the radial direction. The requirement is then simply $w_r < 2R_1$, i.e. $w_r < \left(\frac{1}{h} + \frac{1}{w_\varphi} \right)^{-1}$. For example for $h = w_\varphi = d$, this gives $w_r < d/2$. A more accurate constraint requires determining both the isolated bridge curvature as a function of its volume and the constriction invasion capillary pressure threshold. This can be done using Surface Evolver. The results will be presented in Chapter 5. Here we will make use of the approximate but quite simple estimates given above.

The question then is how to organize the pillars between the disks so as satisfy the geometrical constraint $w_r < \left(\frac{1}{h} + \frac{1}{w_\varphi} \right)^{-1}$. Furthermore we wish to make long chains of liquid bridges between pillars, possibly longer than a disk radius. Also we wish that the distance between two adjacent rows of pillars does not grow too much with the distance from the device center so that the pillar density (number of

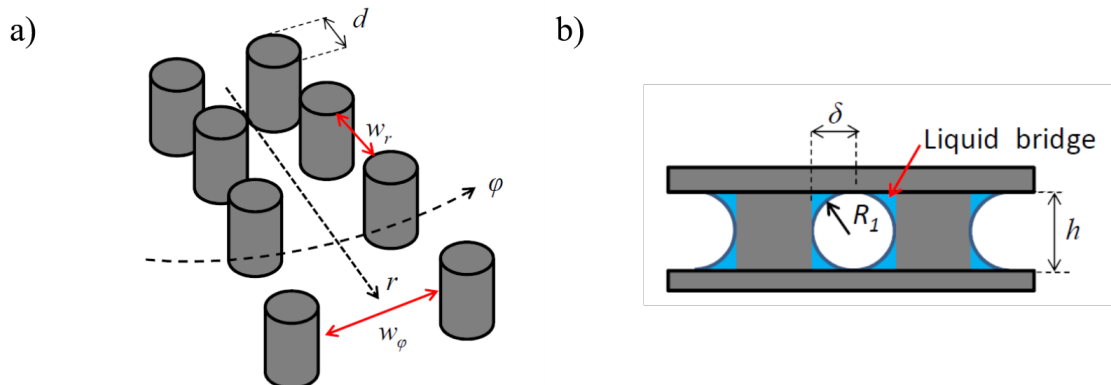


Figure 4.15: Sketch of pillar array with the used notations. Figure 4.18b shows a cross section of a liquid bridge in a vertical plane roughly corresponding to the median plane in Figure 4.18c.

pillars per unit length along the outer perimeter) at the periphery remains relatively high. This is important to maintain a high evaporation rate. A simple solution is a phyllotaxy inspired spatial organization of the pillars such as the one depicted in Figure 4.16c). This organisation allows having much more pillars within the system and a higher pillar density at the periphery compared to pillars simply aligned along radii of the system. Phyllotaxy e.g. (Rutishauser & Peisl [41]), is the mode of arrangement of leaves or scales with flowers. Of special interest are the arrangements in spiral as encountered in the central portion of sunflower for example (see Figure 4.16b)). The most common spiral phyllotactic patterns are called Fibonacci patterns because they involve consecutive Fibonacci numbers, e.g. (Douady & Couder [21]).

The pillar arrangement shown in Figure 4.16c) is actually constructed from Fibonacci spirals in such a way that the equivalent of the geometrical constraint $w_r < \left(\frac{1}{h} + \frac{1}{w_\varphi}\right)^{-1}$ is satisfied. Here this constraint can be expressed as $w_{//} < \left(\frac{1}{h} + \frac{1}{w_\perp}\right)^{-1}$ where $w_{//}$ and w_\perp are the local gaps between two neighbour pillars along a spiral and between two neighbour spirals respectively. As can be clearly seen from Figure 4.16c), $w_{//} < w_\perp$, i.e. the distance between a pair of pillars along a spiral is significantly less than the distance between two adjacent spirals in the vicinity of the considered pair of pillars. The geometrical details, such as the parameters of the spirals, the number of spirals, etc, are presented in Chapter 5.

4.5.2 Phase distribution during drying

The evolution of the phase distribution during drying in the phyllotaxy inspired device is illustrated in Figure 4.17. First, as expected since $\frac{dw_\perp}{ds} > 0$ where s is a curvilinear coordinate along a spiral with origin in the center of the system, the liquid-gas distribution during drying corresponds to a stable pattern. Similarly as in the device with the positive gradient in the gap discussed previously, the main liquid-gas front between the gas and liquid phases is almost concentric as a result of its pinning on almost concentric rows of cylinders. Owing to the organization in spirals the front is actually scalloped. As can be seen from Figure 4.17, the spatial period of the scallops corresponds to the distance between spirals in the azimuthal direction. This front advances toward the system center through a series of successive pinning along almost concentric alley of cylinders. This main liquid-gas front is referred to as the invasion front in what follows.

The novel and crucial aspect compared to the stable pattern discussed in 3 and depicted in Figure 4.2 is as expected the presence of a chain of liquid bridges along each spiral during a quite significant period of the drying process. These liquid bridge chains are clearly visible in Figure 4.17b and Figure 4.17c. As illustrated in Figure 4.17c, a liquid bridge chain ceases to develop over the whole spiral branch when the invasion front has sufficiently advanced inside the system. In other terms, the tips of the liquid bridge chains stay pinned at the most outer cylinder of each spiral for a while and then starts receding into the system. The mechanism leading to the tip depinning is briefly described in the next sub-section and is studied in

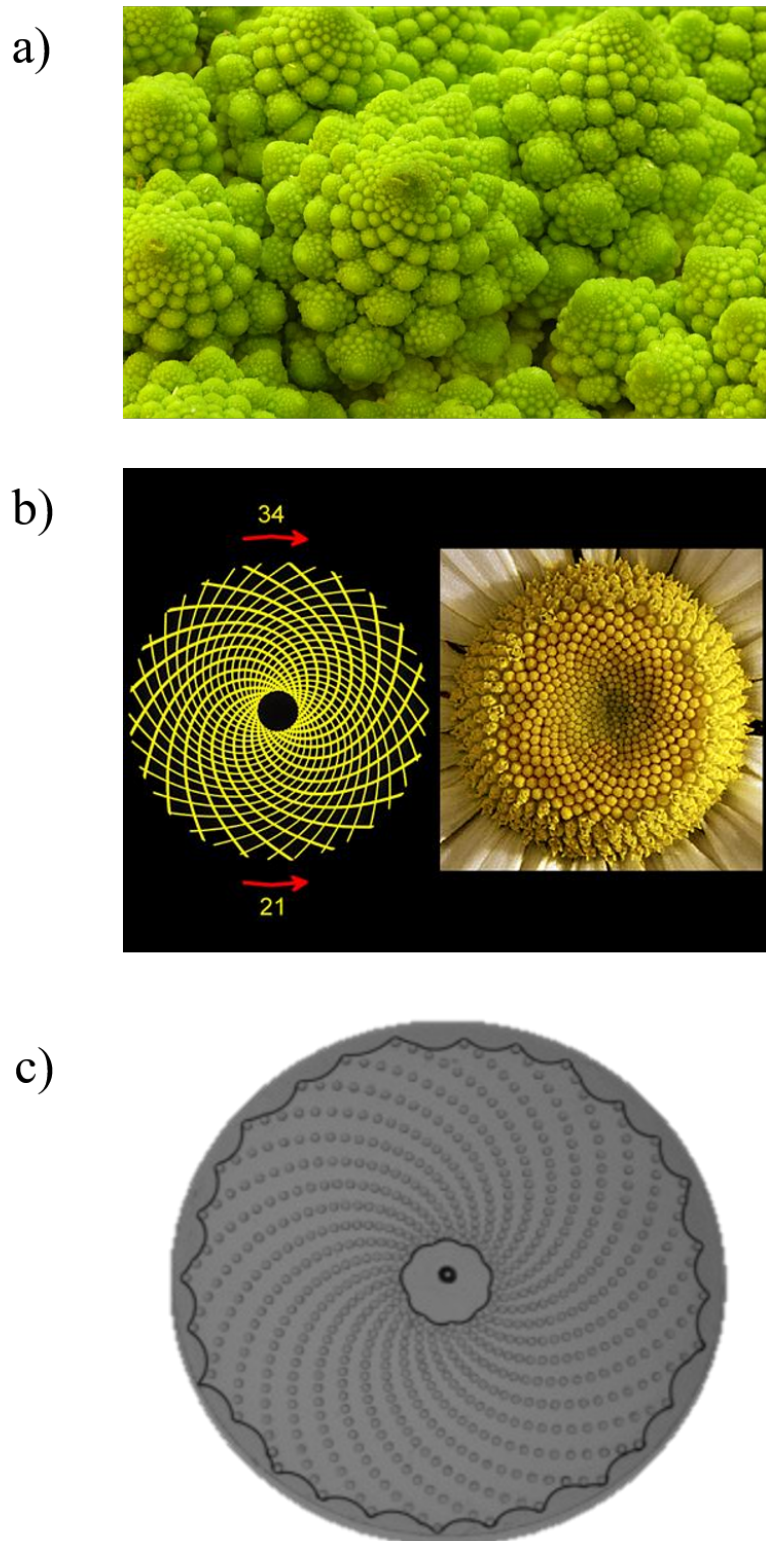


Figure 4.16: From phyllotaxy to a spiral capillary structure: a) romanesco cabbage, b) sunflower pistil, c) our phyllotaxy inspired capillary structure.

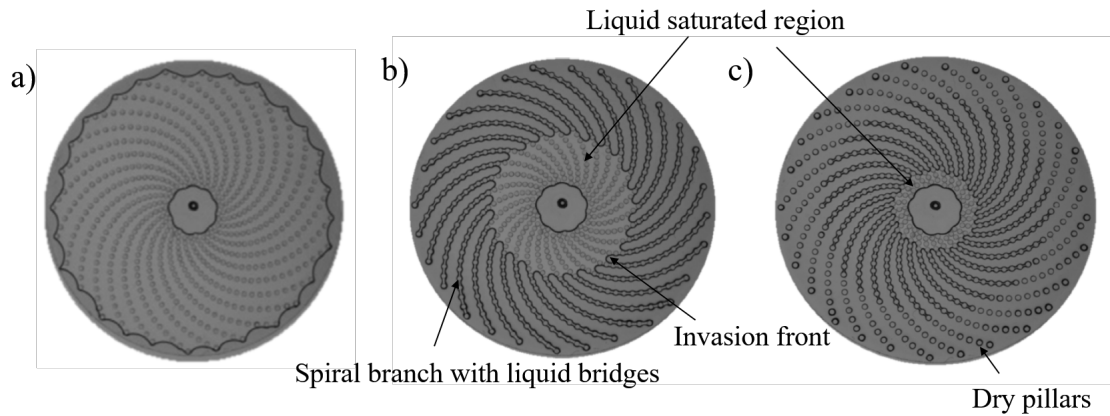


Figure 4.17: Liquid-gas phase distribution at different times during drying in the phyllotaxy-inspired pillar pattern: a) evaporation-invasion front pinned onto the outer edge of spirals, b) invasion front within the device with chains of interconnected liquid bridges covering all the portions of spirals located in the region invaded by the gas phase, c) the tips of the chains of liquid bridges along the spiral have receded within the system. Isolated pillars not interconnected by liquid bridges are clearly visible in the (dry) region adjacent to the outer edge of system. The circular top plate diameter is 37 mm whereas the diameter of the region containing the pillars is 32 mm.

more details in Chapter 5.

4.5.3 Drying kinetics

By analogy with evaporation in a capillary tube of square cross section, e.g. Chauvet *et al.* [10], where the impact of thick corner films is quite significant, it is expected that the evaporation front does not correspond to the invasion front, defined as the front between the fully liquid-saturated region in the system and the region invaded by the gas phase, but is located at the tips of the liquid bridge chains. Thus, the evaporation front is actually much closer to the system periphery than the invasion front. The physical picture is that the liquid is transported from the receding invasion front through the chains of liquid bridges up to the tip of each spiral where it evaporates. Since the liquid bridges long remain present at the tip of spirals, a quasi-constant evaporation rate period is expected. This is indeed what is found in the experiment as illustrated in Figure 4.3. As can be seen from Figure 4.3b, the evaporation rate in this period is comparable with the evaporation rate obtained with the unstable pattern. This clearly indicates that the fact that the liquid is only localized at the spiral tips and does not fill the gap between the spirals has a weak impact on the drying rate. This is a classical feature of diffusive evaporation from multiple discrete sources, when the density of sources is sufficiently high, e.g. Suzuki & Madea [48], Schlünder [46].

As pointed out in 5.2 and illustrated in Figure 4.17c, the liquid bridge chain tips recede into the system after a while. This leads to the progressive displacement of the evaporation front (located at the tip of the liquid bridge chains) toward

the centre of the device and therefore to the development of dry zone between the liquid bridge chain tips and the edge of the system. It is therefore expected that the evaporation rate decreases when the liquid bridge chain tips recede into the system. Consistently with this description, this is observed in Figure 4.3b, which shows that this falling evaporation rate period is observed when the saturation varies from approximately 0.2 to 0 (the saturation is the fraction of the void space in the system occupied by the liquid phase).

Therefore, the longer the chains of liquid bridges attached to the most outer pillar in each spiral, the longer the period of high evaporation rate.

It is therefore interesting to qualitatively discuss the mechanisms controlling the length of the liquid bridge chain. A quantitative analysis will be presented in Chapter 5. The rationale is somewhat similar to the one presented in 3.1 as regards the mechanisms leading to the break-up of the gas finger in the unstable case.

Consider the situation depicted in Figure 4.18. The invasion capillary pressure threshold in point A (bulk meniscus) for a perfectly wetting liquid is

$$p_{cr} \approx \gamma \left(\frac{2}{h} + \frac{2}{w_{\varphi A}} \right) \quad (4.21)$$

Then consider a liquid bridge along the chain of liquid bridge. We must have under quasi-static capillary equilibrium condition,

$$p_{cr} \approx \gamma \left(\frac{2}{h} + \frac{2}{w_{\varphi A}} \right) \approx \gamma \left(\frac{1}{R_1} + \frac{1}{R_2} \right) \quad (4.22)$$

where R_1 and R_2 are the in depth and in-plane curvature radii of the liquid bridge

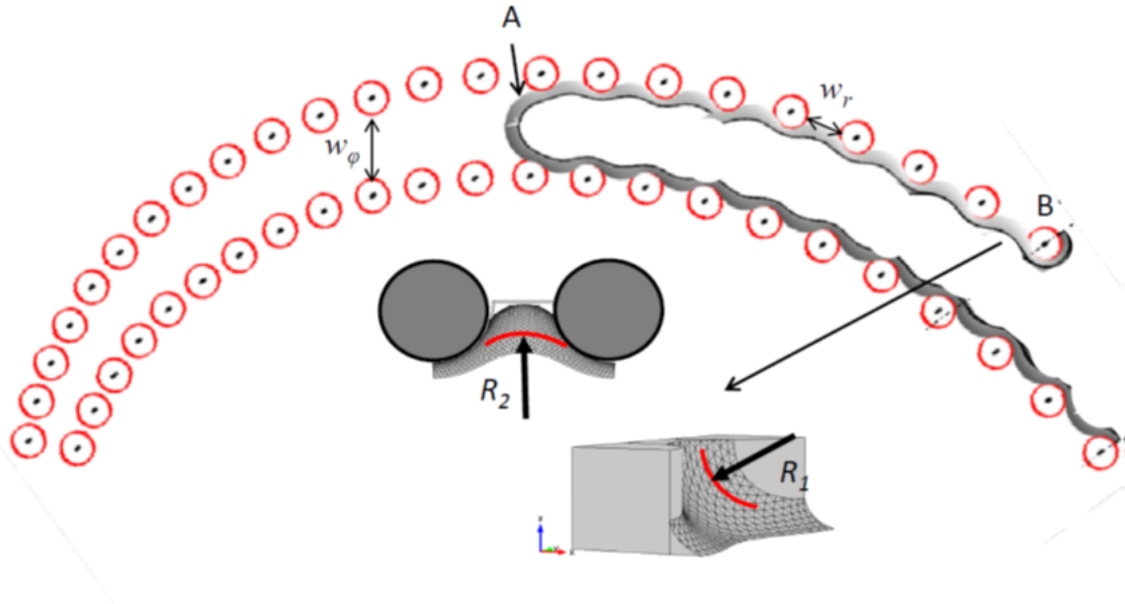


Figure 4.18: Chain of liquid bridges (computed using Surface Evolver) with bulk meniscus at point A. R_1 is the curvature radius of liquid bridge in the narrower region (constriction) of the liquid bridge.

(see Figure 4.18).

Since the distance between two adjacent spirals decreases as the bulk meniscus further moves inside the system, $w_{\varphi A}$ decreases as bulk meniscus A gets closer to the system center. The result is therefore that the invasion capillary threshold (Equation 4.21) increases as the main meniscus advances between the two spirals. Neglecting R_2 in Equation (4.22) in a first approximation, Equation (4.22) tells us that R_1 must decrease as the bulk meniscus advances in the system. Thus, the liquid bridges thin out as the main meniscus advances. If we still neglect the viscous effects and assume $R_2 \ll R_1$, then all the liquid bridges thin out the same way and thus we cannot explain why the liquid bridge chain breaks-up first at the tip. Now if we make the reasonable assumption that $R_2 \propto w_r$ (i.e. increases with the distance between the two pillars supporting the liquid bridge), we reach the conclusion that $R_1 \propto w_r^{-1}$ according to Equation (4.22). Therefore, the chain break-up must take place at the most outer liquid bridge along the chain from capillary equilibrium consideration only. An additional phenomenon, however, should contribute to the thinning of the liquid bridges.

The evaporation process at the liquid bridge chain tips induce a viscous flow within the liquid bridge chains since for a bulk meniscus to advance liquid must be transported from the bulk meniscus region to the liquid bridge chain tips where it evaporates. This viscous flow in the liquid bridge chains is therefore oriented from the bulk meniscus to the liquid bridge tips. It therefore induces a viscous pressure drop within the liquid bridge chains which can be expressed as

$$\Delta P_l \approx \frac{\mu}{\rho_l G(l_s)} \frac{J}{n} \gamma_s \quad (4.23)$$

where J is the evaporation rate μ is the liquid viscosity, ρ_l the liquid mass density, l_s the length of the considered bridge chain along the spiral, n the number of spiral, and G is the hydraulic conductance (m^4/s) of the bridge chain, Chen *et al.* [13] (see Chapter 5). As a result, Equation (4.22) must be reformulated as

$$\gamma \left(\frac{2}{h} + \frac{2}{w_{\varphi A}} \right) - \frac{\mu}{\rho_l G(\gamma_s)} \frac{J}{n} \gamma_s \approx \gamma \left(\frac{1}{R_1} + \frac{1}{R_2} \right) \quad (4.24)$$

which expresses that the viscous effect contribute to thin out further the liquid bridges located the further away from the bulk menisci. Equation (4.24) can be used to predict the maximum length of the liquid bridge chain as the bulk menisci recede into the system. However, in addition to the hydraulic conductance G , we also need to know the transition capillary pressure corresponding to the transition between the configurations shown in Figure 4.14b and Figure 4.14c, i.e. the capillary pressure when the bridge is about to break-up (for any further increase in the capillary pressure the liquid bridge would take the configuration shown in Figure 4.14). This question is also addressed in Chapter 5.

4.6 Conclusions

The objective of this chapter was to show that evaporation could be controlled from the geometry of capillary structures. One can distinguish two main control levers depending on which type of liquid-gas interface one is willing to control. The bulk interface can be controlled by playing with the gap gradient whereas the secondary capillary interface, corresponding to the liquid bridge chains considered in this chapter, is somewhat subtler to control. It requires a sufficient understanding of capillary invasion mechanisms so as to develop designs favouring the formation of thick capillary films or chains of liquid bridges. The system considered was relatively large to ease the visualizations and the determination of evaporation rates from weight measurements. The experiments were actually repeated with systems 10 times smaller and similar results as those discussed in this chapter were obtained. Weight measurements cannot be performed in this case because the initial mass of liquid in the system is too small but evaporation rates can be evaluated from the processing of phase distribution images (see chapter 5).

These results give a framework for the design of 3D systems with properties tailored to specific applications, e.g. microfluidic devices, porous materials, such as the porous component used in cooling devices, e.g. Faghri [22], as well as in many other technologies, e.g. fuel cells, coatings, textiles, diapers and wipes, etc. For example, the gradient in the gap should correspond to permeability gradient. The design of 3D systems favouring secondary capillary effects (films, liquid bridges) is of course much more challenging owing to the geometry complexity of the liquid gas interface in 3D. The formation of liquid bridges is common in porous media, e.g. Scheel *et al.* [43]. The consideration of the relatively simple bridge chains discussed here can be also seen as a step toward the significantly more complex arrangements of liquid bridges existing in porous media.

Chapter 5

Spiral system: experimental results and modelling

In this chapter, we first present the results of the experiments performed on the Fibonacci spiral microsystems. Then, we try to explain our experimental findings using some theoretical arguments, based on the numerical works presented on Chapter 3. Contrarily to what was done in the previous Chapter, where the emphasis was on the overall drying kinetic (at the scale of the whole micromodel), we focus here on the effects and dynamic of the liquid films that are observed along the spiral branches.

5.1 First qualitative observations

5.1.1 Small micromodels (50 μm thickness)

As mentioned in Chapter 2, the direct visualization of the phase distribution within the microsystem is quite easy. Figure 5.1 shows the liquid-gas distribution at four successive times, $t = 0$ (beginning of the experiment), $t = 18\text{ s}$, $t = 62\text{ s}$ and $t = 125\text{ s}$, for evaporation of heptane in the smallest of the two types of micromodel used. The experiment starting time, $t = 0$, is taken when the meniscus is fully positioned around the external end of the system, see Figure 5.1a. From $t = 0$ to $t = 18\text{ s}$ approximately, one can observe a progressive invasion of air between the spiral branches, with liquid films along them and extending up to each spiral end, see Figure 5.1b. At longer times ($t > 18\text{ s}$), the films depin from the spiral ends and start to recede in the system, see Figure 5.1c,d.

The evaporation rate, $E = -dV/dt$, where V is the liquid volume measured by image processing as described in Chapter 2 is shown in Figure 5.2. A quasi-constant evaporation rate period (CRP) is observed with $E \approx 4.5 \times 10^{-12} \mu\text{m}^3 \text{s}^{-1}$, from $t = 0$ to $t = 18\text{ s}$ (see Appendix D for simulations of vapor diffusion in the micromodel in that case). Once the films have depinned around $t = 18\text{ s}$, a sharp decrease of the evaporation rate is observed.

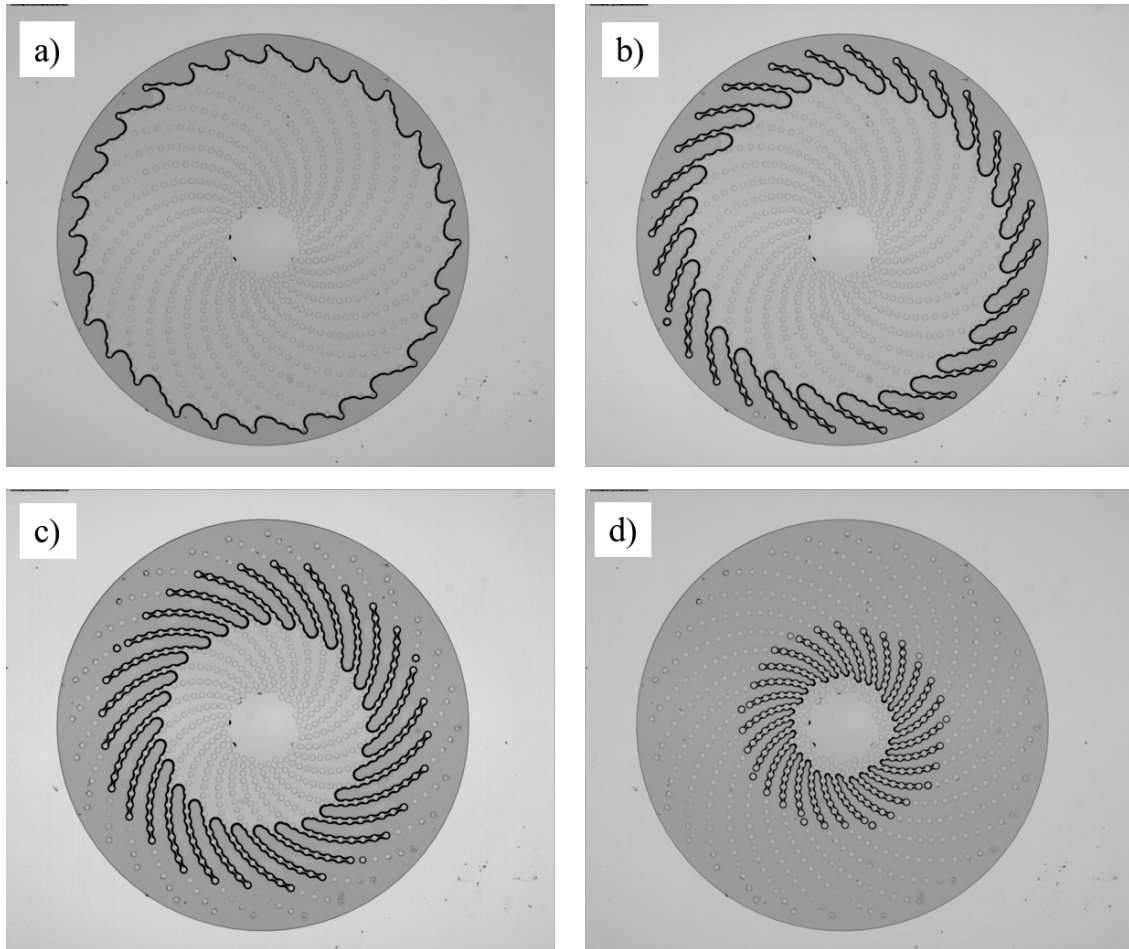


Figure 5.1: Evaporation of heptane in a $50 \mu\text{m}$ -thick micromodel: phase distribution at $t = 0$ s (a), $t = 18$ s (b), $t = 62$ s (c) and $t = 125$ s (d).

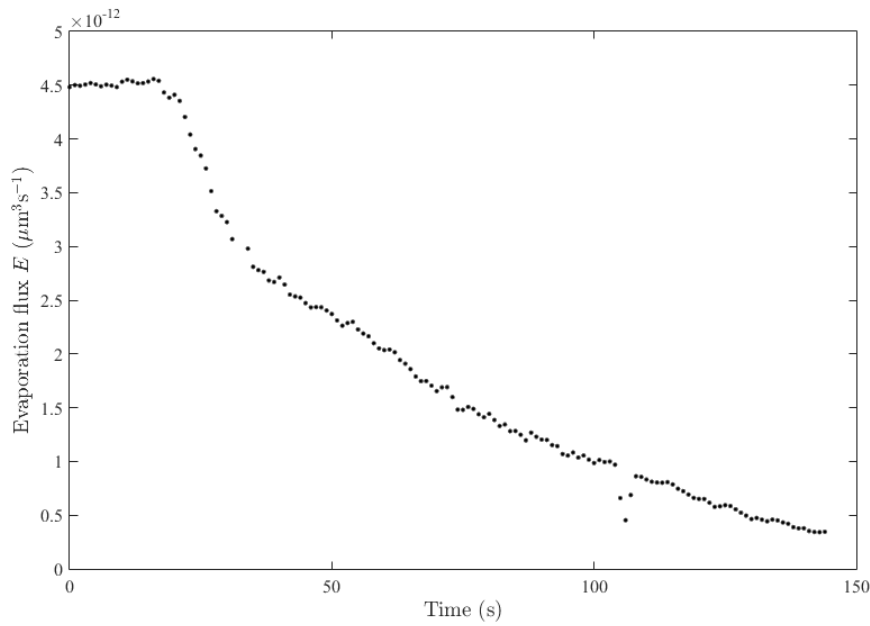


Figure 5.2: Evaporation of heptane in a $50\ \mu\text{m}$ -thick micromodel: evaporation rate E as a function of time.

5.1.2 Large micromodels ($500\ \mu\text{m}$ thickness)

Evaporation also takes place as explained just above in the largest of the two kinds of spiral micromodels used, see Figure 5.3. A typical evolution of the evaporation rate versus time is shown in Figure 5.4. However, during the CRP period, a strong dissymmetry is observed with main meniscus receding “faster” in some regions of the micromodel (this remains true for all fluids tested), see Figure 5.3b. This dissymmetry disappears progressively and typically, once depinning from the spiral end occurred for each of the liquid films, axisymmetry is recovered, see Figure 5.3c. We believe that this is due to defects in microfabrication, with the top (on Figure 5.3) part of the micromodel being thinner after positioning and bonding of the top plate, this latter stage resulting in a slight “crushing” of the micromodel top part. Figure 5.4 show the corresponding evaporation rate, with a CRP from $t \approx 750\ \text{s}$ to $t \approx 3500\ \text{s}$. Note the higher initial evaporation rates observed from $t = 0$ to $t \approx 750\ \text{s}$ correspond the phase during which the meniscus positions around the external end of the pattern, starting from a completely filled microsystem.

5.1.3 Fibonacci spirals as a model porous medium

The phenomenology discussed above is quite similar to the one observed in square cross-section capillary tube by Chauvet *et al.* [10] and discussed in Chapter 1. By analogy with Chauvet’s configuration, one can consider each space in between two neighbouring spirals as a unique pore (similar to a capillary tube), with two liquid films on each side, along the spirals. However, it is more relevant to consider the liquid films seen in the spiral system as a network of connected liquid brigdes

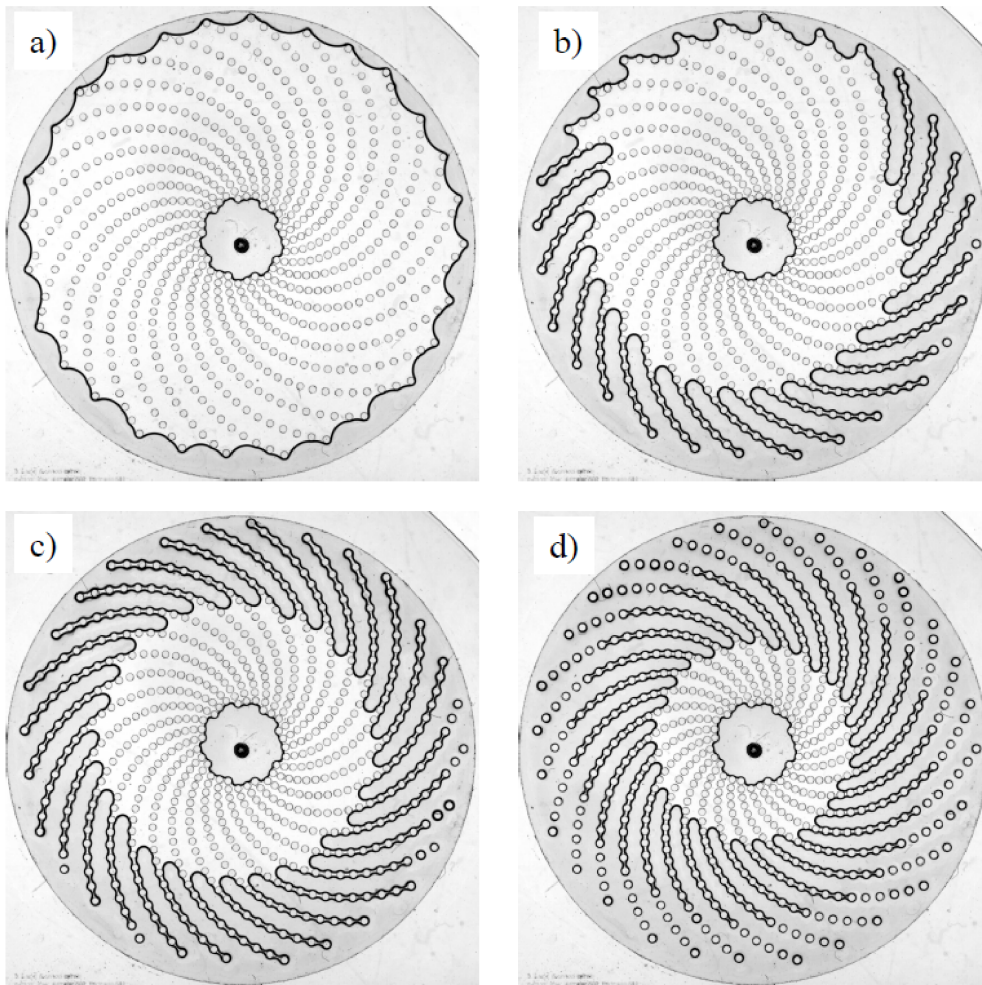


Figure 5.3: Evaporation of hexane in a $500\ \mu\text{m}$ -thick micromodel: phase distribution at $t = 750\ \text{s}$ (a), $t = 2250\ \text{s}$ (b), $t = 3250\ \text{s}$ (c) and $t = 4750\ \text{s}$ (d). For this experiments, the time $t = 0$ corresponds to the very beginning of the experiment, with a micromodel completely filled with liquid. Some of the liquid has to evaporate before reaching the situation displayed in (a), with the meniscus positioned around the external end of the cylinders pattern.

positionned between each pair of neighboring pillars. Then, the space between two spirals can also be seen as a succession of pores, each pore throat being defined in between pairs of neighboring pillar in adjacent spirals, see Figure 5.5. Therefore, in the following, the evaporation process will be described as the progressive invasion by air of a model porous medium rather than the invasion of a bunch of adjacent capillary tubes.

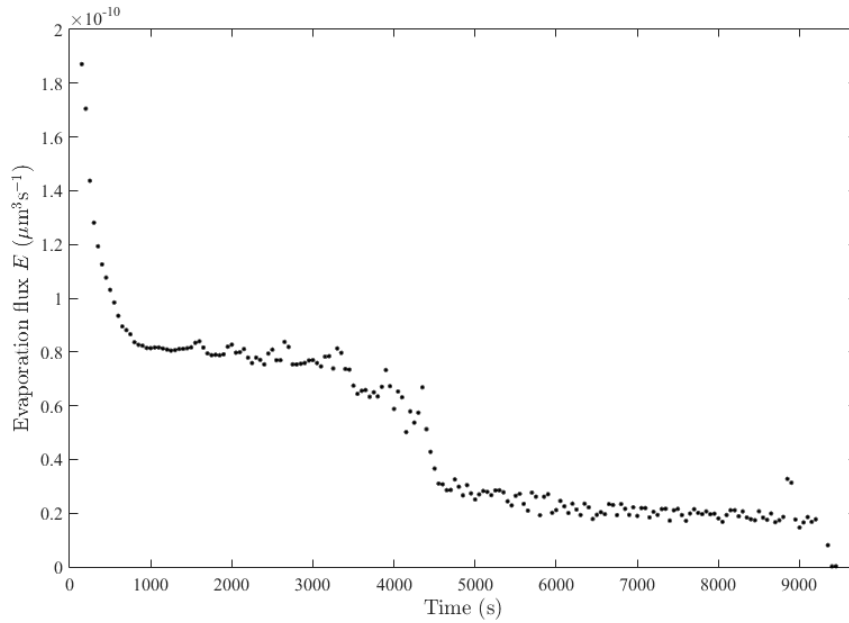


Figure 5.4: Evaporation of hexane in a $500 \mu\text{m}$ -thick micromodel: evaporation rate E as a function of time.

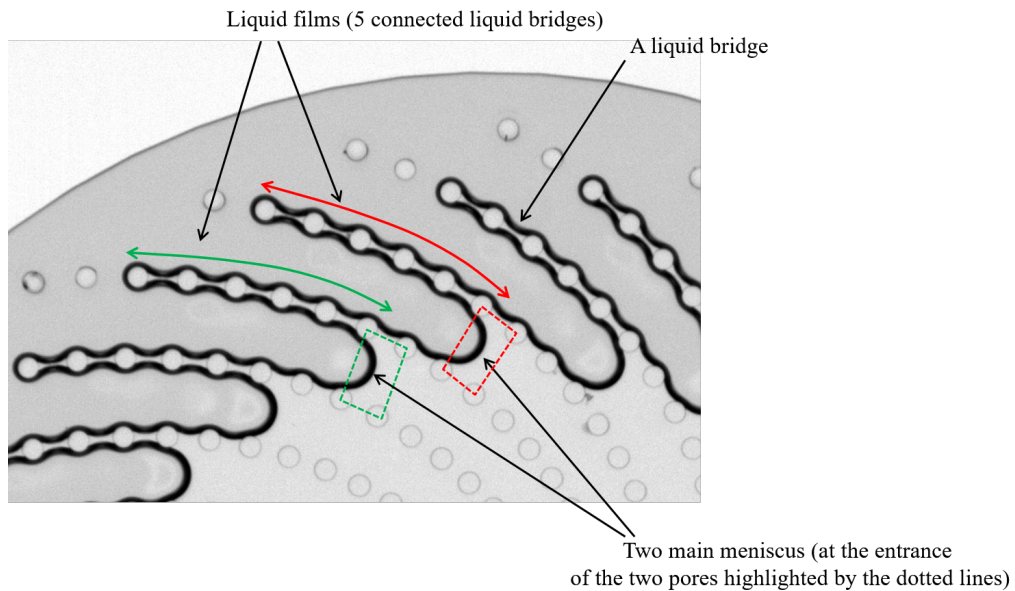


Figure 5.5: Micromodel as a porous medium: sketch showing the “definition” of liquid film, liquid bridge, main meniscus and pore in this particular geometry.

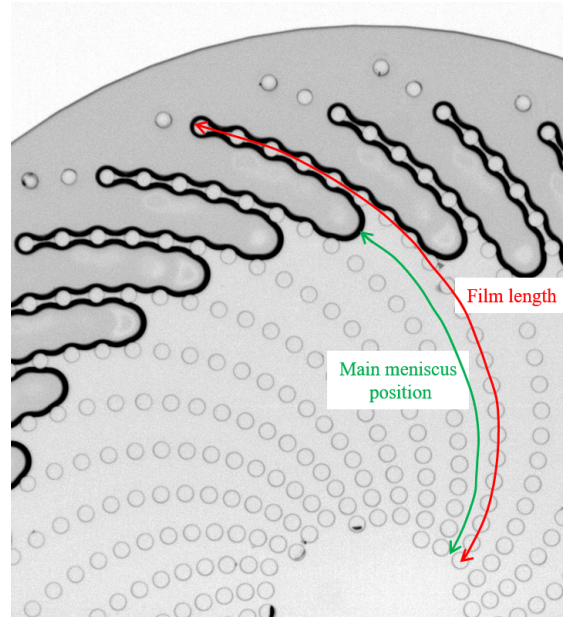


Figure 5.6: Micromodel as a porous medium: sketch showing the definition of the liquid film length and of the main meniscus position.

5.2 Quantitative description of a drying experiment

5.2.1 Description of the interfaces displacement

Figure 5.7 shows the evolution with time of the film length and main meniscus position, as defined in Figure 5.6, for a given “pair” liquid film-main meniscus (for evaporation of heptane in a $50\ \mu\text{m}$ -thick micromodel). It is important to note that both positions evolve in a discontinuous manner. In fact, the film extent is controlled by the total number of connected liquid bridges, as seen in Figure 5.5. As the liquid film progressively depins from the most external cylinders, its total length evolves discontinuously. Also, the main meniscus displacement is not continuous: it “jumps” from one meniscus entrance to the next. This motion, an extremely simplified version of the so-called Haynes jump observed in more realistic porous media, see e.g. Berg *et al.* [2], will be detailed in the following. Figure 5.8 shows the evolution with time of the liquid films length and of main menisci position, averaged over the 28 spirals of the micromodel, the error bars being the standard deviation to the mean. During the constant rate period, from $t = 0$ to $t = 18\ \text{s}$, it is clear that the liquid films stay connected to the each spiral end.

Plotting the film or main meniscus position as a function of time is not very convenient when one needs to compare experiments performed with different fluids, as the experiments duration changes a lot from one fluid to another, depending on the fluid volatility. Also, plotting physical lengths (i.e. expressed in μm or mm) does not allow to compare at a glance the situations obtained in the small and large microsystems. That’s why in the following, each liquid film length will be marked

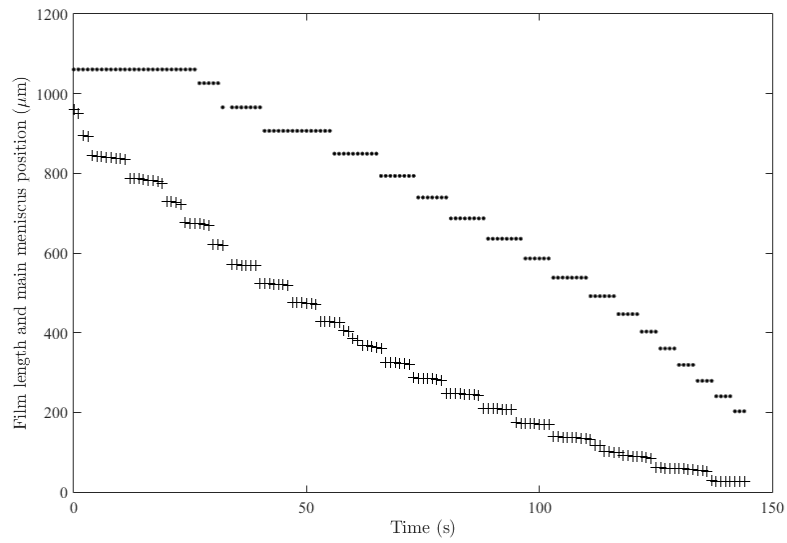


Figure 5.7: Liquid film length and main meniscus position (both in μm , see Figure 5.6 for definitions) as a function of time, for a given “pair” liquid film-main meniscus (heptane evaporating in a $50\ \mu\text{m}$ -thick micromodel).

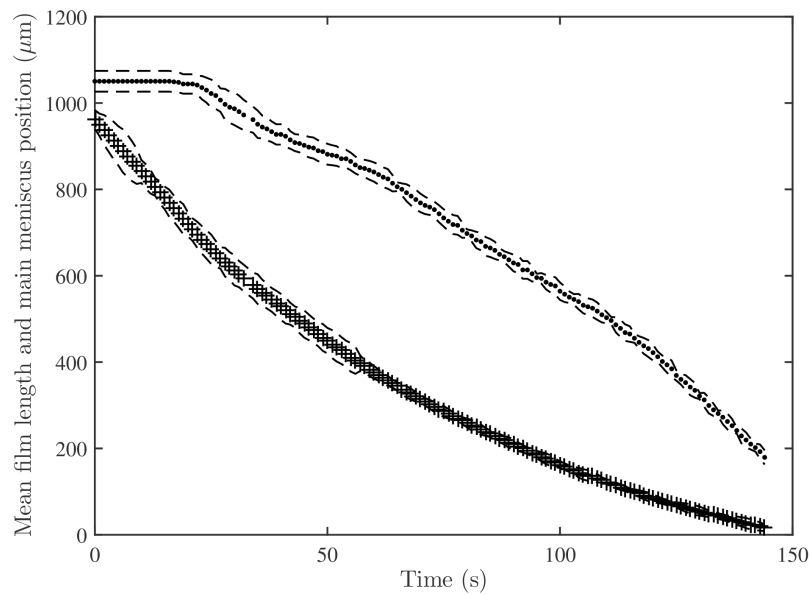


Figure 5.8: Liquid film length and main meniscus position averaged over the 28 spirals of the micromodel (heptane evaporating in a $50\ \mu\text{m}$ thick micromodel). The dotted lines show the standard deviation to the mean value.

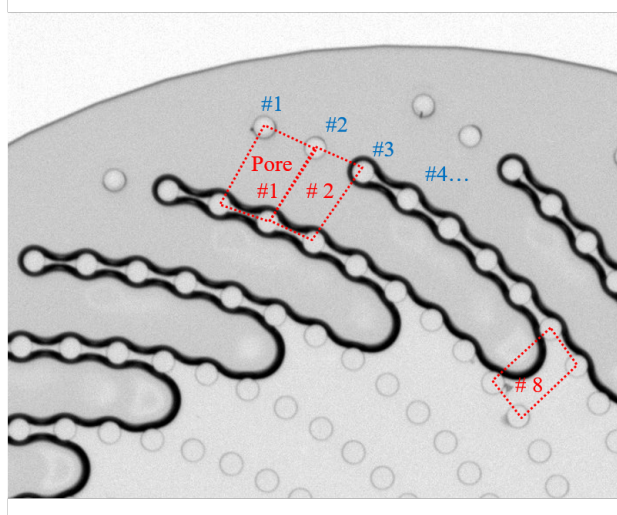


Figure 5.9: Sketch showing the way liquid film and main meniscus locations are marked out throughout this work. The liquid film with its end located at cylinder # 3 is associated with the main meniscus located at the entrance of pore # 8.

out using the number of the most external pillar wet by the fluid and connected to the main liquid cluster, i.e. using a number between 1 and 24. Similarly, each main meniscus position will be marked out by the number of the pore it occupies. A sketch detailing this important point is shown in Figure 5.9.

Figure 5.10 shows the liquid film location as a function of the main meniscus location using this convention for the same pair liquid film-main meniscus of Figure 5.7. Film and main meniscus locations only take integer values between 1 and 24. The dotted line shows the results after averaging over the 28 spirals (so 28 pairs liquid film-main meniscus), so that non-integer values are obtained. In the following, averaged values will be used mostly. In this representation, the data points corresponding to the beginning of the experiments are in the lower left corner of the graph. As both films' ends and main menisci recede towards the micromodel center with time, they are both marked out by increasing numbers.

5.2.2 Reproducibility

Using the representation introduced above, we first study the reproducibility of the experiments. Figure 5.11 shows the results for 6 experiments, using 3 different fluids (heptane, hexane and pentane). The reproducibility is very good: for a given fluid, one can hardly discern some differences from one experiment to another. This would of course remain true if more results for a given fluid were shown). The slight difference seen between, say, heptane and hexane on this graph is thus significative:

1. in average, depinning occurs earlier with hexane (black symbols) than with heptane (green symbols),
2. in average, the liquid films observed with hexane are typically one liquid bridge shorter than with heptane, during most of the experiment duration.

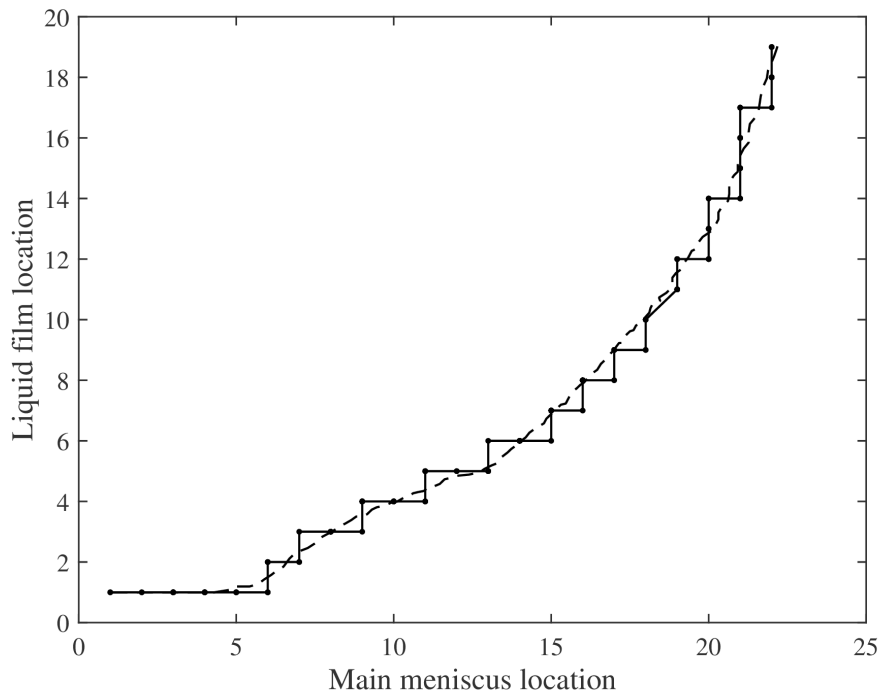


Figure 5.10: Liquid film location as a function of the main meniscus location (heptane evaporating in a $50\ \mu\text{m}$ -thick micromodel). Locations are marked out with integer values between 1 and 24, see Figure 5.9. Dot and solid line: result for a single pair liquid film-main meniscus. Dotted line: average over the 28 pairs liquid film-main meniscus of a micromodel.

Also, the liquid films observed with pentane (red symbols) are shorter and depin earlier than with hexane. An easier way to visualize these differences from one fluid to another will be proposed in the following.

5.3 Experimental results

For the small systems, experiments are quite short and were repeated several times (3 to 5 times) whereas one or two experiments only were done for the larger micromodels. To sum up the results, we focus on two quantities: the evaporation rate measured during the CRP and the films length for given main menisci positions. The emphasis in the following will be on the liquid films dynamics (i.e. length vs time) and their effects on evaporation. Thus, we will not present some results on the drying kinetics as done in the previous chapter. For instance, we will not try to relate the measured evaporation rate to the position of the drying front in the FRP. Such results can be extracted from the present experiments but we did not get them from image processing yet.

Table 5.1 shows the results concerning the evaporation rate measured during the CRP and gives the films length expressed as the number of connected liquid

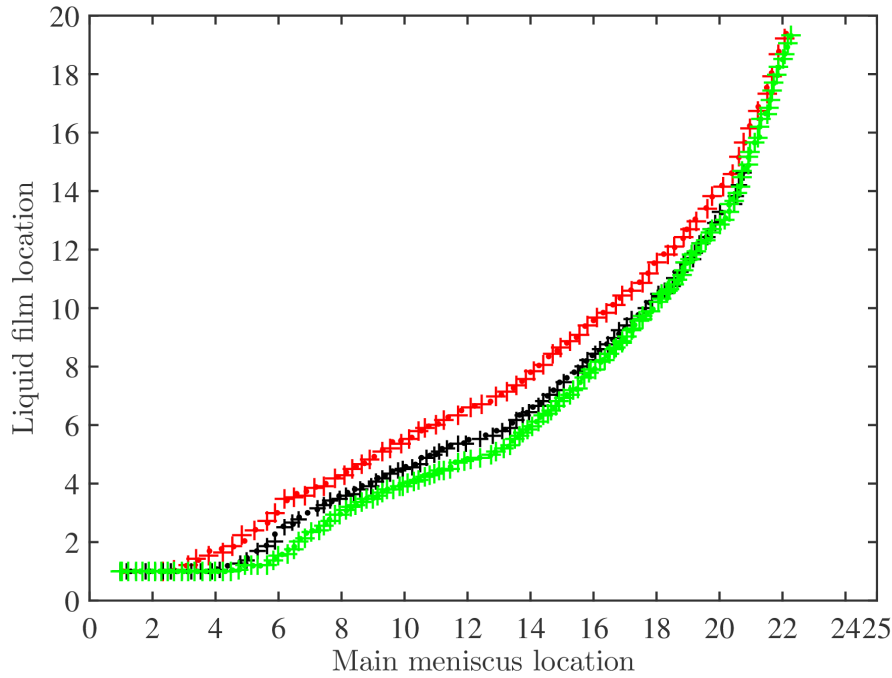


Figure 5.11: Liquid film location as a function of the main meniscus location. Experiments performed in a $50\ \mu\text{m}$ -thick micromodel. Red symbols (dots and crosses): 2 experiments performed with pentan; black symbols (dots and crosses): 2 experiments performed with hexane; green symbols (dots and crosses): 2 experiments performed with heptane.

bridges, L_{depin} , when the films depin from the most external cylinder. Such results are obtained for each pair liquid film-main meniscus and are then averaged. The uncertainty is taken as the standard deviation to the mean. One can then wonder if the difference between heptane and hexane is significant (which was maybe already the case by looking at Figure 5.11). To better illustrate the difference from one fluid to another, it is possible to compare the liquid film lengths obtained *along a given spiral*, with different fluids. Then, one can plot an histogram showing the distribution of the differences between the film lengths obtained with heptane and the film lengths obtained for another fluid. This allows to take into account the slight defects in microfabrication, that may alter the geometry from one part of the microsystem to another or perturb the depinning around a given cylinder. This is done for the first depinning, for heptane and hexane in Figure 5.12. The films are one liquid bridge longer with heptane for a large majority of spirals (18 out of 28) showing that we observe a significant effect (i.e. not within error bars). Table 5.1 also gives the film length when the films depin from cylinder # 4. This is because we believe that the geometrical defects due to microfabrication are located mostly on the external part of the system and thus may bias the results concerning the first depinning.

	Micromodel	E_{CRP} ($\mu\text{l s}^{-1}$)	L_{depin}	L_4
Propanol	Small	$2.7 \pm 0.1 \times 10^{-3}$	4.7 ± 0.9	8.2 ± 0.9
Heptane	Small	$6.5 \pm 0.3 \times 10^{-3}$	4.8 ± 0.6	7.1 ± 0.7
Hexane	Small	$13.2 \pm 0.6 \times 10^{-3}$	4.0 ± 0.5	5.5 ± 0.5
Pentane	Small	$86 \pm 7 \times 10^{-3}$	3.2 ± 0.4	4.1 ± 0.3
Heptane	Large	79×10^{-3}	10.6 ± 2.5	10.0 ± 0.0
Hexane	Large	248×10^{-3}	9.8 ± 2.4	9.9 ± 0.25
Pentane	Large	827×10^{-3}	8.1 ± 1.9	9.1 ± 0.7
HFE	Large	725×10^{-3}	6.7 ± 2.6	6.35 ± 0.5

Table 5.1: Table recapitulating the results obtained in small and large micromodels: evaporation rate during the CRP (E_{CRP}), mean film length at depinning from the most external cylinder (#1), L_{depin} , and mean film length when the films depin from cylinder # 4, L_4 , both expressed in number of connected liquid bridges.

5.4 Theoretical approach

The aim of this section is to study if we are able to predict the phase distribution within our micromodels, during a drying experiment. In the first subsection, we will study the situation where the capillary effects are supposed to be the sole responsible for the drying pattern observed. As will be seen, incorporating the

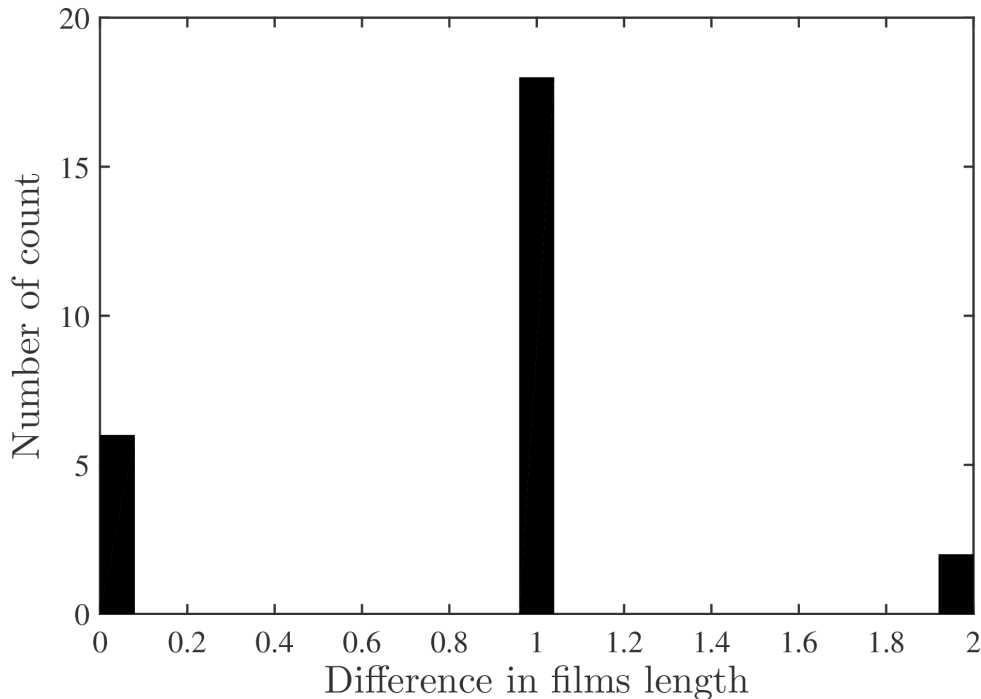


Figure 5.12: Histogram showing the difference between film lengths for heptane and hexane in a $50 \mu\text{m}$ -thick micromodel.

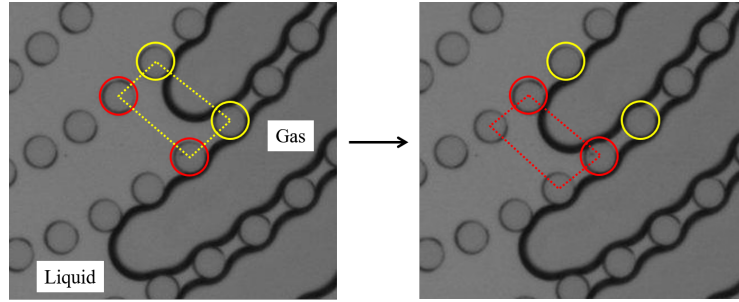


Figure 5.13: A scenario for capillary breakup of liquid bridges. Zoom on the main meniscus. Pore 1, respectively pore 2, is highlighted in yellow, respectively red.

viscous effects due to the evaporation-induced-flow within the liquid films should allow us to get a better agreement with the experiment. The development of a visco-capillary modelling will be dealt with in subsection 5.4.2. Note that the effect of gravity will be neglected. In fact, the Bond numbers are small for both the small and large micromodels. In our configuration, the Bond number may be defined as $\rho_l g h^2 / \gamma$. Taking $\gamma \approx 20 \times 10^{-3} \text{ N m}^{-1}$ and $\rho_l \approx 0.8 \text{ g} \cdot \text{cm}^{-3}$ for the fluids used (see Table 2.1, one obtain $Bo \approx O(0.1)$ for large micromodels ($h = 500 \mu\text{m}$) and $Bo \approx O(10^{-3})$ for the small ones ($h = 50 \mu\text{m}$). Also, we neglect any cooling effect induced by evaporation (which would change the physical properties of the fluid, depending on its position relative to the evaporative front). Experimental results and their discussion by Chauvet [10] have shown that this is a correct assumption for the fluids used in the present study, where the cooling effect is expected not to exceed a couple of degrees Celsius.

5.4.1 A capillary theory for the drying of spiral micromodel

A capillary effect to explain the liquid-bridge breakup

A crucial point to note is that the pores that are progressively invaded by the gas, as evaporation proceeds, are getting narrower and narrower. This is due to the fact that the spatial density of pillar increases from the edge to the center of the microsystem. As a result, a purely capillary mechanism may explain the reason why the liquid films progressively recedes along the spirals. It is explained below, with the help of Figures 5.13 and 5.14.

Let's consider the situation depicted in Figure 5.13, left and right focus on the main meniscus positionned in between the two cylinders highlighted in yellow, at the entrance of the pore highlighted by the dotted, yellow line. The capillary pressure, $P_c = P_{gas} - P_{liquid} = -\gamma C$ increases as evaporation proceeds (NB: C is negative). When it reaches the invasion pressure $P_{inv,1}$, the pore is invaded. The main meniscus positions at the entrance of the next pore, in between the two cylinders highlighted in red, see Figure 5.13, right. This pore will be invaded when P_c reaches the new value $P_{inv,2}$, with $P_{inv,1} < P_{inv,2}$. If one assumes that capillary equilibrium is reached in the liquid between these two invasions, the pressure in the liquid film along the spiral is equal to the pressure at the main meniscus. As the

capillary pressure has increased, the liquid bridges along the spiral must be thinner after pore 1 invasion, which is clearly seen on the images (see for instance the last liquid bridge highlighted by a green circle on Figure 5.14). Of course, the liquid bridges cannot thin indefinitely as there is a critical pressure for the liquid bridge break-up, P_{crit} , as already seen in Chapter 3. If P_{crit} (which is a function of the spacing between the two pillars of the liquid bridge considered) is smaller than $P_{inv,2}$, then the liquid bridge will break-up before the invasion of pore 2 ! Then, the film end will position to the next cylinder along the spiral and the new last liquid bridge of the liquid film will have a larger critical pressure (as the spacing between the cylinders has decreased). One has to compare $P_{inv,2}$ to a new value of P_{crit} to know what will happen next: liquid bridge break-up or invasion of pore 2.

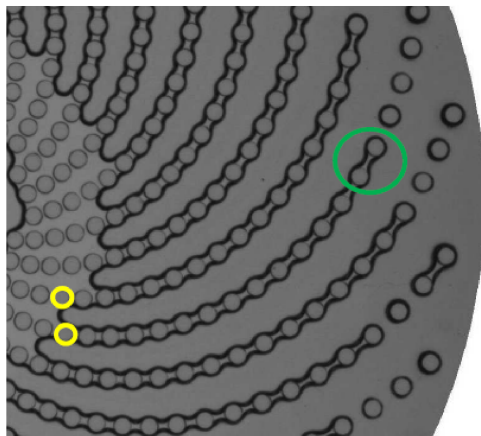
Thus, we have a purely capillary mechanism that could govern the phase distribution in the system during an experiment, involving a capillary control of the liquid films length. Of course, viscous effects due to the evaporation-induced flow within the liquid films may change the picture and this is an important point to clarify, which will be the subject of the next section. In the remaining of the present subsection, we show how to obtain quantitative predictions on the liquid phase distribution during drying, based on the above qualitative description.

Critical capillary pressure of a liquid bridge

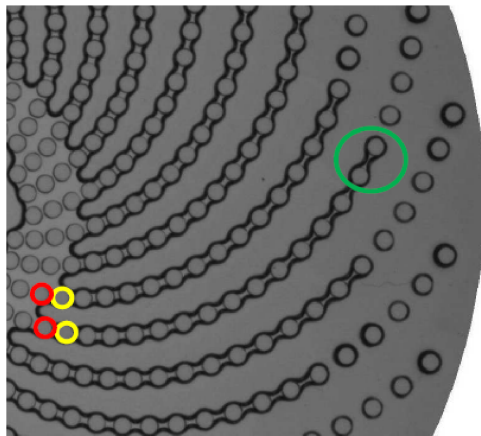
A key point of the above scenario is that there is a critical capillary pressure (or equivalently critical curvature) above which a liquid bridge cannot be sustained in between two neighboring cylinders. This point was studied using Surface Evolver, see §3.2.2. Figure 5.15 shows the evolution of the dimensionless critical curvature, $2d_c C_{crit}$ obtained in SE for a zero contact angle, as a function of the dimensionless spacing between the two cylinders $w_{//}/2d_c$: as might have been expected, the critical pressure increases when $w_{//}$ decreases. Results for different contact angles are given in Appendix C. The critical pressure is simply obtained as $-\gamma \times C_{crit}$, and increases as the spacing between cylinders decreases.

The Surface Evolver simulations were ran considering liquid bridges confined between two pillars only, whereas in the experiment we rather observe liquid films consisting of many connected liquid bridges, extending around several neighboring cylinders. Two questions arise : what is seen in the experiment as far as liquid-bridge breakup is concerned and how to make sure that the critical capillary pressure computed in SE, for liquid bridges between 2 cylinders is a good approximation of the real one, when only the liquid bridge at the end of a chain of liquid bridges breaks-up.

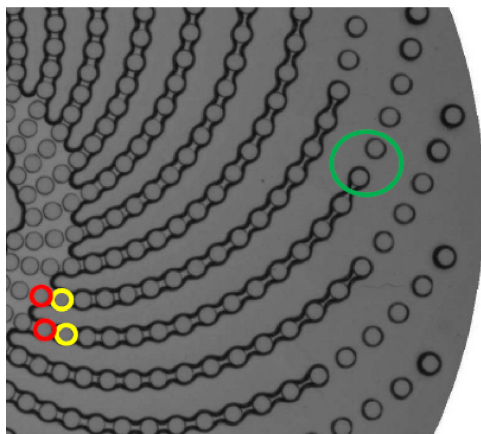
Let's consider the first question first. A typical experimental liquid bridge break-up is shown in Figure 5.16. After break-up, the presence of liquid rings around the most external pillar is demonstrated by the sharp black ring. Such an optical signature of the liquid films presence disappear as the liquid contained in the rings evaporates (see Figure 5.16d). For the range of pillar spacing encountered in the system, we always observe such an optical signature of the breakup. Note that we tried to image such a capillary breakup at a much higher frame acquisition rate, compared to the one used in a regular experiment (typically 1 Hz), but we did not



$$P_{inv,\#19}$$



$$P_{inv,\#19} < P_{inv,\#20}$$



$$P_{crit,\#5} \text{ vs } P_{inv,\#20}$$

Figure 5.14: A scenario for capillary breakup of liquid bridges. Next pore invasion *vs* thinning and capillary breakup of the most external liquid bridge on the spiral. Here, the liquid bridges thin when the capillary pressure changes after invasion of pore # 19, see e.g. the liquid bridge highlighted in green. Comparing $P_{inv,\#20}$ to $P_{crit,\#5}$ will determine what will happen next.

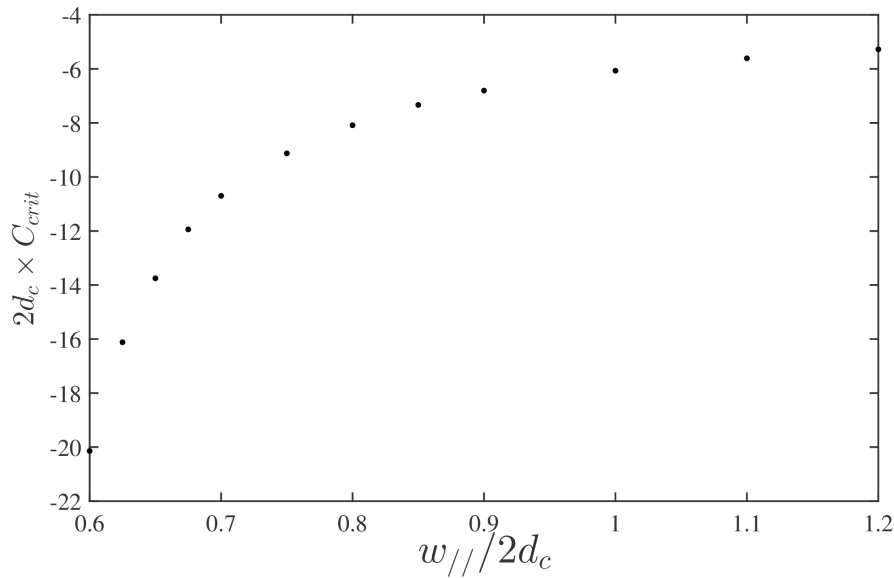


Figure 5.15: Dimensionless critical curvature $2d_c C_{crit}$ for a liquid bridge breakup, as a function of $w_{//} / 2d_c$, the dimensionless spacing between the two cylinders. The liquid is perfectly wetting on the cylinders and top/bottom plates.

succeed, even with a 100 Hz frame acquisition rate, in capturing the dynamical event at play during the breakup as it is really fast. Note that the exact distribution of the liquid around the most external cylinder is not important in the present approach. However, as already stated above, from SE simulations of isolated liquid rings around cylinders, we believe it consists of two isolated rings, on top and bottom of the cylinder.

Then, as far as the second question raised above is concerned, one need to check if the critical capillary pressure for break-up obtained in SE considering a liquid bridge between 2 isolated pillars is a fair approximation of the real critical pressure. To that end, we ran some SE simulations along a chain of cylinders with varying spacings between the cylinders, see §3.2.2. The varying spacings between the pillars corresponds to those imposed by the microfabrication design. The capillary shapes were obtained for successive, decreasing liquid volumes and, as expected, the liquid bridge breakup occurs in between the two most distant cylinders. In Figure 5.17, the critical pressure found when considering a chain of N cylinders (i.e. $N - 1$ liquid bridges), made dimensionless by its value for $N = 2$, is plotted as a function of N . The critical pressure is found to vary by less than 1%, whatever N is, compared to the reference case ($N = 2$).

To conclude, the points made above and the results shown are good arguments to state that studying thoroughly the case of liquid bridges confined in between two cylinders is enough to get a good description of what happens in the experiments.

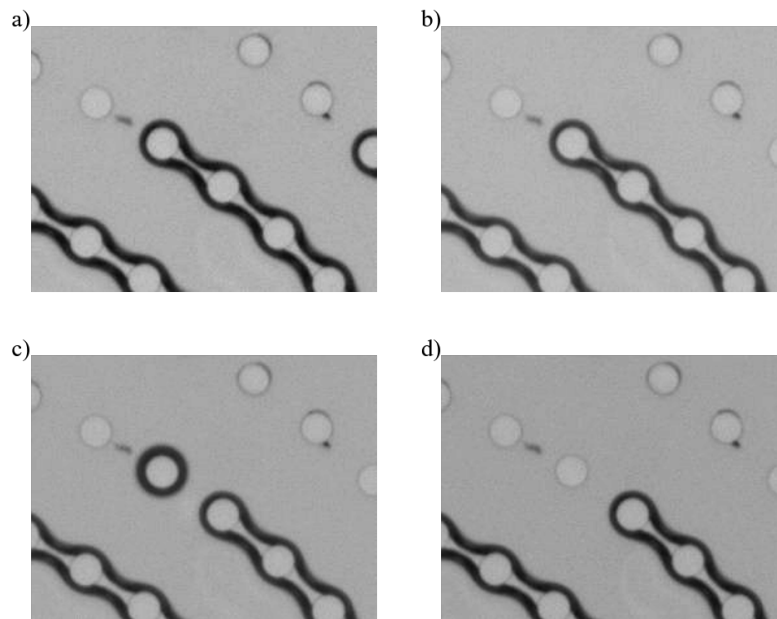


Figure 5.16: Four successive (a to d) images showing a capillary breakup event as observed experimentally.

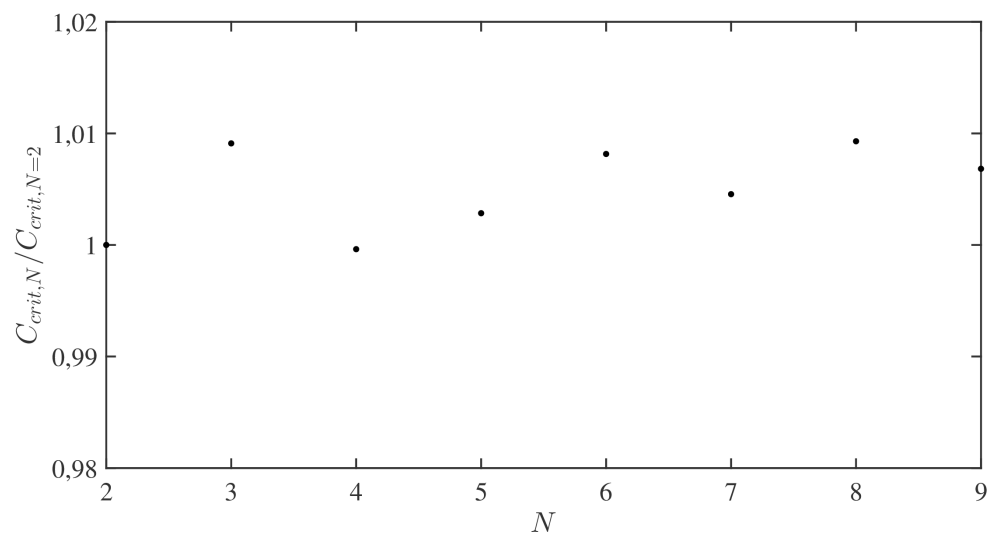


Figure 5.17: Critical curvature found when considering a chain of N cylinders, $C_{crit,N}$, divided by the value found for $N = 2$, as a function of N . The critical capillary pressure is simply $-\gamma C_{crit}$.

Invasion pressure

Another key element of the basic mechanism exposed in §5.4.1 is the knowledge of the invasion pressure for a given pore P_{inv} . Again, we use experimental evidence to advance on that point, focussing on some typical observations made regarding the displacement of a main meniscus within the micromodel.

We focus on a given main meniscus, see Figure 5.18a, and extract its curvilinear location along the line highlighted in red on a stack of images taken at high acquisition rate (100 Hz). This location is plotted as a function of time in Figure 5.19. It is clearly seen that the invasion proceeds by successive jumps, as already mentioned: a main meniscus positioned at the entrance of a given pore first slowly penetrates into the pore before a sudden jump occurs and drives the main meniscus to its next position, at the entrance of the next pore. In Figure 5.18b, we show an image taken at $t = 123$, just after a jump and in Figure 5.18c, an image taken at $t = 210$, just before the next jump. Highlighted in red is the circle inscribed in between the two pillars that mark the entrance of the pore about to be invaded. It is found that the liquid-gas interface closely matches the circle just before invasion. Consequently, as the liquid is perfectly wetting, the curvature of the interface in the observation plane, at invasion, is estimated as $-1/R_c$, the circle radius. Then, the invasion pressure is estimated as:

$$P_{inv} = \gamma \left(\frac{1}{R_c} + \frac{1}{h} \right) \quad (5.1)$$

where h is the micromodel thickness. Note that R_c is a function of the pore considered and decreases as one penetrates further in the micromodel.

Purely capillary invasion: model vs experiments

With the knowledge of the critical pressure for liquid bridge breakup and invasion pressure, it is quite easy to obtain a curve showing the capillary invasion predicted for our given micromodel design. The algorithm used to predict the capillary invasion is the following. Initially, the liquid film end is located at the spiral end so that the first liquid bridge critical value is concerned (position # 1, see Figure 5.9) and the main meniscus is located at position # 2 (i.e. the entrance of pore # 2). One compares the critical and invasion pressure and it is found that $P_{c,1} > P_{inv,2}$ so that as drying occurs and as the pressure decreases, the main meniscus is expected to jump to a new location, position # 3. Then, one compares $P_{c,1}$ and $P_{inv,3}$, and so on...The prediction for the liquid film location as a function of the main meniscus location is shown as dots+line on Figure 5.20.

Note first that we expect this results to be the same for any fluids, in large and small microsystems. In fact, the fluids have roughly the same contact angle (close to zero) and as both the critical pressure for breakup and the invasion pressure scale like $1/h$, the balance between these two values, which determines how the gas invasion occurs, is the same whatever h is.

Of course, this behavior for capillarity-controlled invasion of the drying micromodel is based on estimations of P_c and P_{inv} . Some deviations from this behavior

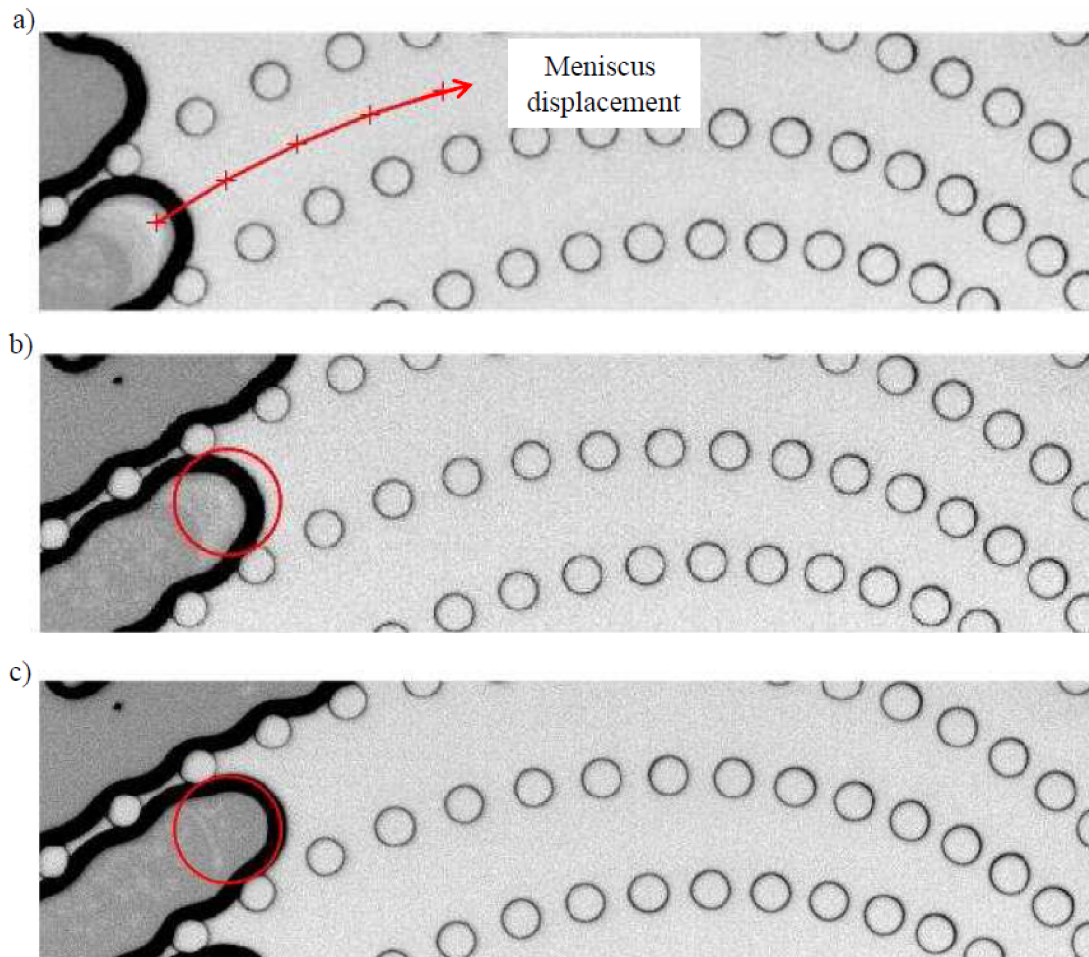


Figure 5.18: Displacement of a given main meniscus in between two spirals. a) Overview of the situation; b) Main meniscus location just after its jump at the pore entrance it is located; c) Main meniscus location just before its next jump. The circle in red is the circle inscribed in between the two pillars that mark the entrance of the pore about to be invaded.

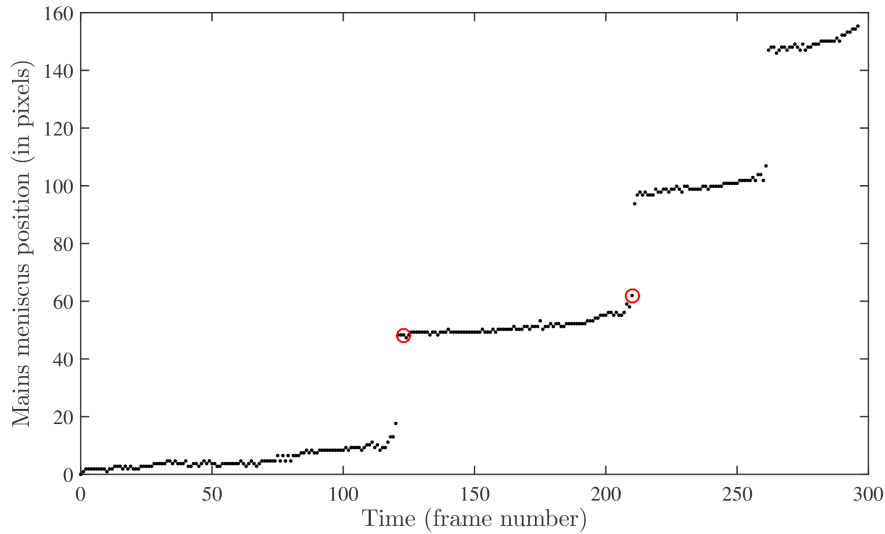


Figure 5.19: Main meniscus displacement as a function of time, along the red line sketched in Figure 5.18. The two data points highlighted with a red circle correspond to the situation depicted in Figure 5.18a, for $t = 123$ and Figure 5.18c, for $t = 210$.

may come from variations in the geometrical dimensions of the micromodel, due to the various defects induced during the microfabrication process and already discussed. In order to check the theoretical capillary predictions, some experiments were done performing a quasi-static drainage of a non-volatile, perfectly wetting, silicon oil initially filling the micromodel (with $\mu_{oil} = 10^{-2}$ Pa s). Such drainage experiments were performed in the largest of the two micromodels only, as it is equipped with a central hole from which drainage can be done. We use a Harvard PHD 2000 syringe pump with a refill rate of $Q = 0.1 \mu\text{l min}^{-1}$. The Capillary number Ca is $\mu_{oil}Q/\gamma_{oil}S$. Taking $\gamma_{oil} \approx 20 \times 10^{-3} \text{ Nm}^{-1}$ and S the cross section for the flow to be $\approx 2\pi hR$ with $R = 1 \text{ cm}$ a typical radius for the liquid cluster at the end of the drainage, one gets $Ca \approx 10^{-8}$ which validates the quasi-static drainage assumption.

The experimental data points for capillary invasion are shown as circles+dashed line on Figure 5.20. There is a large difference between the experiments and the theoretical predictions (dots+solid line). In particular, the films are much longer and depin from the most external pillar “later” (for a main meniscus at location # 15) in the drainage experiment. Also the invasion is far more “gradual” in the theoretical case, whereas in the experiment, 5 liquid bridges breakup at once. To understand these discrepancies, it would be very helpful to do a drainage experiment in the small systems (for which there are less geometrical defects induced by microfabrication, notably the top plate bonding) but such an experiment is hard to conceive due to the very small size of the micromodel. Also, one has to note that these results are very sensitive to the estimation of the critical capillary pressure and invasion pressure used. For instance, crosses on Figure 5.20 show the results ob-

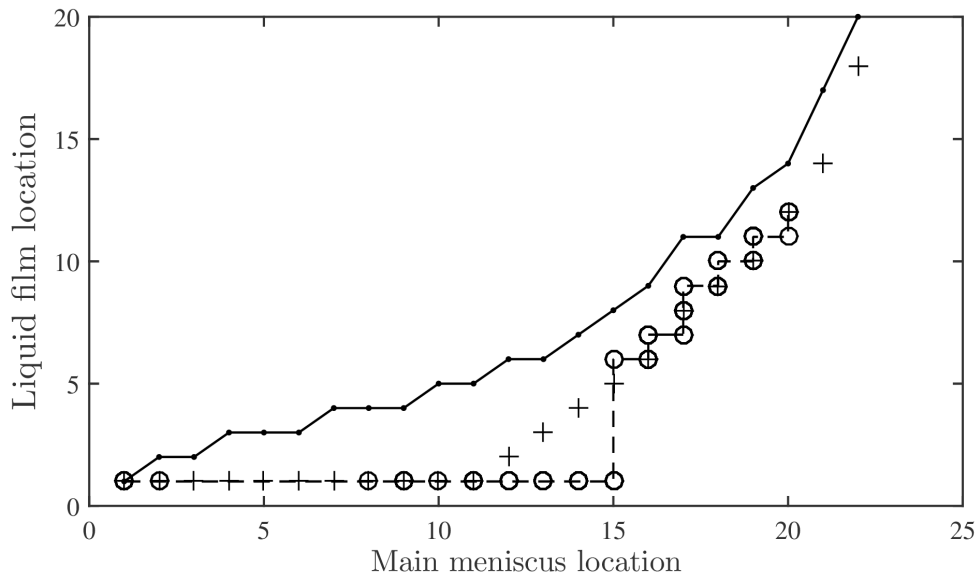


Figure 5.20: Capillary invasion of the large micromodel. Dots and solid line: theoretical prediction (also valid for the small micromodel); Crosses: theoretical prediction with a 5% increase in the critical pressure; Circles and dashed line: experimental results of a slow drainage experiment, in the large micromodel.

tained when “artificially” increasing the values found by SE for the critical pressure by 5% only, which are in much better agreement with the drainage experiment.

The results obtained in the large micromodel with heptane, hexane and pentane are shown in Figure 5.21, along with the results of the drainage experiment. There are almost no differences between the heptane, hexane and oil experiments. This shows that the drying pattern for heptane and hexane is controlled by capillary effects. However, liquid films with pentan (diamonds) depin earlier (when main meniscus is at position # 12) which may be the signature of viscous effects. Figure 5.22 compares the experimental data for heptane for the small and large micromodels. The invasion pattern is clearly different from one case to another. The liquid films depin earlier and are shorter in the small micromodel, at least until the main meniscus has sufficiently receded in the porous medium (location number # 15). Again, this may be the signature of viscous effects. This point is investigated in the next subsection.

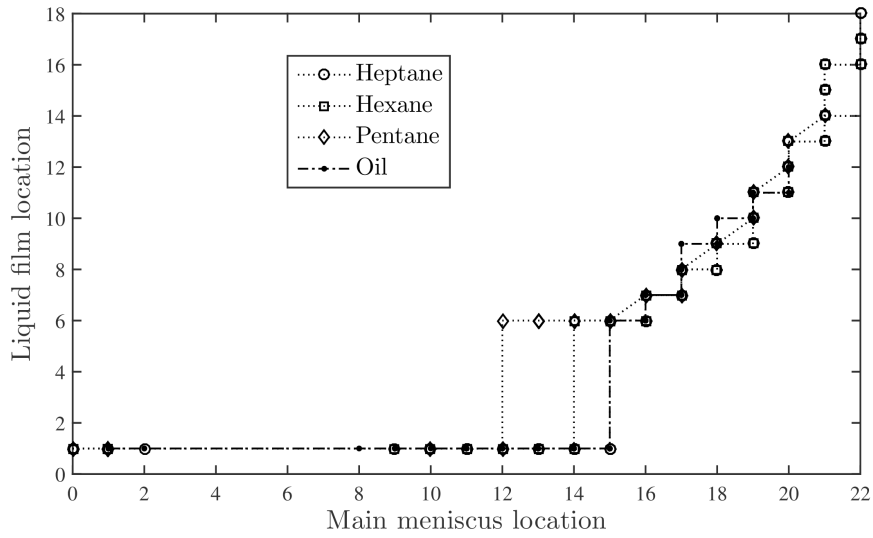


Figure 5.21: Experimental data for drying and drainage of the large micromodel. Dots and dash-dotted line: oil drainage; Circles and dotted line: heptane (drying) ; Squares and dotted line: hexane (drying) ; Diamonds and dotted line: pentane (drying).

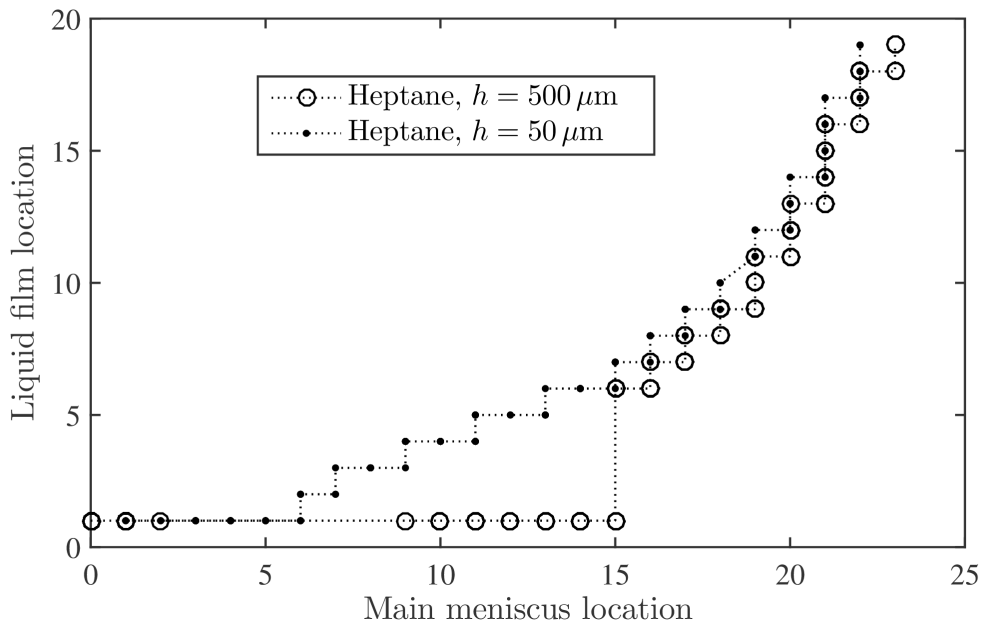


Figure 5.22: Drying of heptane in the small (dots) and large (circles) micromodels.

5.4.2 Viscous effects

As seen above, some differences in the drying pattern are seen, depending on the micromodel size for a given fluid, see Figure 5.22, and depending on the evaporating fluid for a same micromodel, see Figure 5.21 and Figure 5.11. In this subsection, we show how to characterize the viscous effects at play during drying and present hints to incorporate them into a visco-capillary theory for drying in our micromodels, in order to fully explain our experimental findings.

Scaling arguments

Let's recall the definition used for the viscous flow resistance in a liquid bridge used in the present study, inspired by Ransohoff & Radke (see §?? in Chapter 3):

$$\beta = \frac{R_{in}^2}{\mu_f \langle u \rangle} \times \frac{\Delta P}{w_{\parallel}}$$

We therefore define a viscous pressure drop as:

$$\Delta P_{\mu} = \beta \mu_f \langle u \rangle \frac{w_{\parallel}}{R_{in}^2}$$

with the mean velocity $\langle u \rangle = E/(28A_{in})$, where E is the evaporation rate and A_{in} is the total cross-section of the four liquid corners, at the liquid bridge inlet (see Figure 3.14). From Surface Evolver results, it is found that $A_{in} \approx 0.78(4 - \pi)R_{in}^2$, so that:

$$\Delta P_{\mu} = \beta(\theta, d, R_{in}) \mu_f \frac{E \times d}{0.67 \times 28 \times R_{in}^4}. \quad (5.2)$$

Then, as a first approximation and as confirmed by Surface Evolver results, $R_{in} \sim w_{\parallel}$. In fact, a smaller spacing between the 2 cylinders results in smaller liquid volumes that can “fit” in the liquid bridge which in turn leads to smaller R_{in} . Therefore, ΔP_{μ} scales as $\beta \mu_f E/w_{\parallel}^3$. Table 5.2 presents some values of the ratio $\mu_f E/w_{\parallel}^3$ for the different experimental cases considered in the present study. The experimental data shows that $E \sim h \sim w_{\parallel}$ so that ΔP_{μ} finally scales as w_{\parallel}^{-2} . Also, remember there is exactly a one order of magnitude difference in w_{\parallel} from the large to the small micromodels.

It is important to remember that one should rather compare this typical viscous pressure drop to a capillary pressure drop ΔP_c . The capillary pressure scales as h^{-1} i.e. w_{\parallel}^{-1} . So that a dimensionless number $\Delta P_{\mu}/\Delta P_c$ will scale as w_{\parallel}^{-1} . Deviations from a purely capillary behavior are seen in the small micromodels: results for different fluids (heptane, hexane and pentane) display some significative differences. This would mean that ΔP_{μ} values of $O(1)$ are enough to see viscous effects, see Table 5.2. Thus, one expects ΔP_{μ} values of $O(0.1)$ to be enough to see viscous effects in the large system, and such values are reached for pentane and HFE.

Fluid	Micromodel	$\mu_f E/d^3 \sim \Delta P_\mu(\text{Pa})$
Heptane	Large	0.03
Hexane	Large	0.07
HFE	Large	0.29
Pentane	Large	0.18
Propanol	Large	0.06
Heptane	Small	2.49
Hexane	Small	3.9
HFE	Small	19.1
Pentan	Small	18.1
Propanol	Small	5.45

Table 5.2: Pressure drop induced by viscosity effect in liquid bridge

Viscous effects vs time

After the basic scaling arguments above, one can wonder about the evolution of the viscous effects amplitude with time during a given drying experiment as the evaporation rate and the film length both change with time. During the CRP, E is roughly constant and the film length increases. After the films depinning, the evaporation decreases but the film length keeps on increasing. The viscous pressure drop is proportionnal to the number of liquid bridges forming the liquid film along a given spiral. Figure 5.23a shows the mean number of liquid bridges per liquid films, N_{lb} , and Figure 5.23b shows $N_{lb} \times E$ as a function of time, where the data used are those for an experiment performed with heptane in a small micromodel (for this particular experiment $E(t)$ is displayed in Figure 5.2). The amplitude of viscous effects at play is seen to increase in the beginning of the experiment and culminates around depinning. However, it then remains roughly constant until $t \approx 60$ s as the increase in N_{lb} compensates for the decrease in E .

A first estimate of ΔP_μ

Getting a value for ΔP_μ requires the knowledge of the viscous resistance β , a function of the contact angle and of the liquid bridge geometry. As explained in Chapter 3, β values were obtained through DNS computations based upon the solving of the Stokes equation in a unit cell obtained from the Surface Evolver-simulated liquid bridge geometry. Appendix C shows the results for $\beta(\theta, w_\parallel, R_{in})$ as Tables, for discrete sets of contact angles θ , distances between two cylinders w_\parallel and liquid volumes \mathcal{V} contained in the liquid bridge (for a given w_\parallel , there is a bijective relationship between \mathcal{V} and R_{in}).

Let's consider the situation depicted in Figure 5.24 and let's try to compute the viscous pressure drop for the flow in the liquid bridge chain. The liquid bridge chain consists of 5 liquid bridges and we will first compute the value of β for each of them. As mentioned above, the geometry of liquid bridge is needed to compute β . If w_\parallel

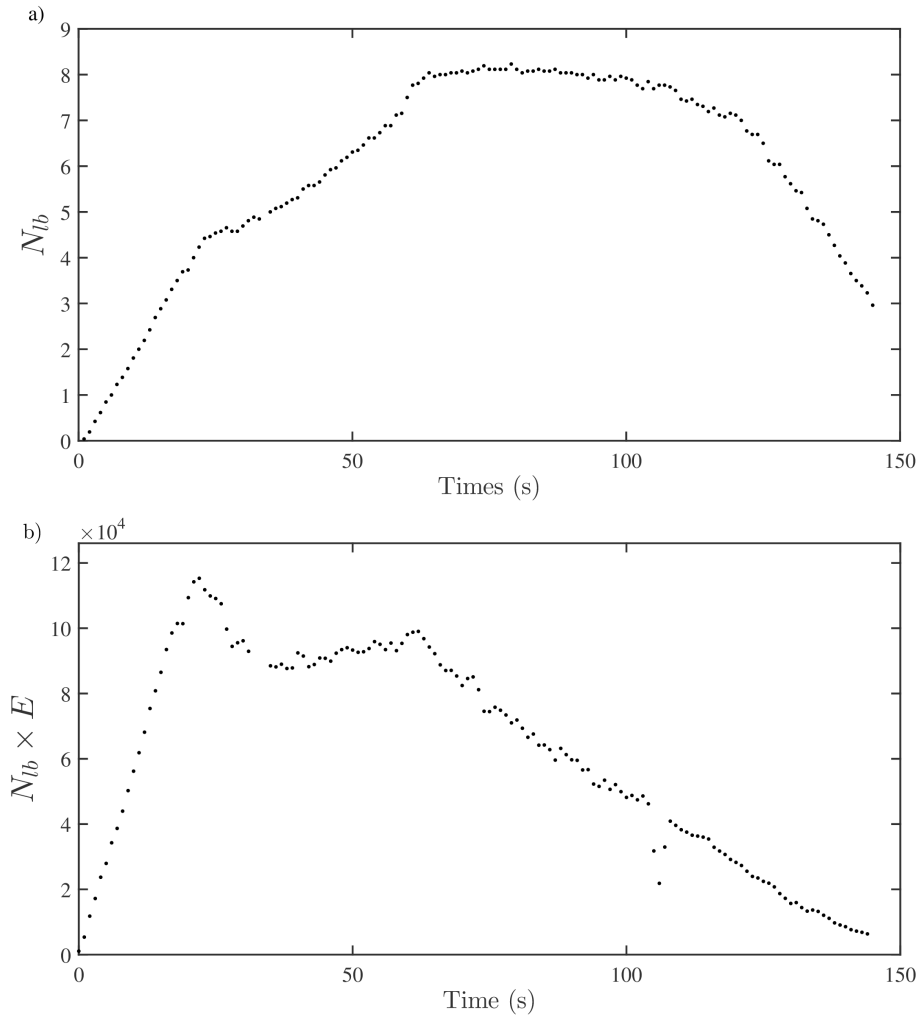


Figure 5.23: Drying experiment with heptane in a small micromodel. a) Mean number of liquid bridges per liquid film, N_{lb} , as a function of time. b) $N_{lb} \times E$ as a function of time.

is known from the micromodel design, one cannot obtain R_{in} easily from image processing. We rather focussed on the liquid bridge width w_1 . The width of a given liquid bridge is measured using a transverse intensity profile across the liquid bridge mid-plane, that is along the red lines highlighted in Figure 5.24. Such a width can be measured with an accuracy of 5 %. Then, one can use the relationship between R_{in} and w_1 , from Surface Evolver. Finally, we can use the Tables of Appendix C to express $\beta(\theta, w_{//}, w_1)$ and interpolate between these discrete sets of values to get β for any liquid bridge observed in the experiments.

Table 5.3 shows the results thus obtained for the liquid bridges of Figure 5.24. The evaporation rate considered to compute ΔP_μ from Equation 5.2 is $E = 3.725 \times 10^{-12} \mu\text{m}^3 \text{s}^{-1}$, see Figure 5.2. The viscous pressure drop ΔP_μ does not vary much from one liquid bridge to another and is of $O(22)$ Pa. The total viscous pressure drop is then $O(110)$ Pa. The same calculation of ΔP_μ was repeated for the case of heptane evaporating in a large micromodel. Considering a typical liquid bridge geometry,

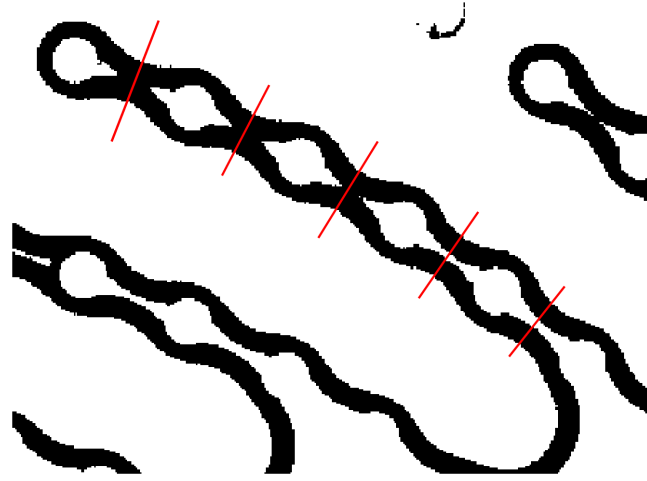


Figure 5.24: A liquid film consisting of 5 liquid bridges. Fluid is heptane, in a small micromodel and the evaporation rate is $E = 3.725 \times 10^{-12} \mu\text{m}^3 \text{s}^{-1}$ when this image is taken.

this led to $\Delta P_\mu = 0.4 \text{ Pa}$. As expected from the scaling arguments presented above, this value is two orders of magnitude smaller than the one obtained in the small micromodel.

This pressure drop has to be compared to the capillary pressures at play in the experiments. For small micromodels, the invasion pressures and critical pressure for liquid bridge are typically of $O(1000) \text{ Pa}$. At first glance, the typical $O(100) \text{ Pa}$ order of magnitude for ΔP_μ appears to be one order of magnitude smaller. However, one has to realize that the drying pattern is ruled by comparing invasion pressures to critical pressure for liquid bridge break-up, as explained above. Then, the order of magnitude for ΔP_μ has to be compared to *differences* between comparable invasion and/or critical pressures. If we consider a given location for the film end (for instance, pinned to the most external pillar of each spiral), it is interesting to compute the difference in invasion pressures between two main meniscus locations. For instance, using equation 5.1 and taking $\gamma = 20 \times 10^{-3} \text{ Nm}^{-1}$, one finds $P_{inv,\#4} - P_{inv,\#5} = O(10) \text{ Pa}$ for the small micromodel and $P_{inv,\#4} - P_{inv,\#5} = O(1) \text{ Pa}$ for the large one. Thus, it is clear that the viscous pressure drop in a single liquid bridge is larger than this value in the small micromodel whereas the contrary is true for the large one.

Towards a capillaro-viscous theory...

At that stage, we have all the ingredients to formulate a capillaro-viscous theory for the phase distribution observed during drying. Such a theory should allow us to

Liquid bridge #	1	2	3	4	5
$w_{\parallel}/2d_c$	1.12	1.09	1.06	1.03	1
w_1 (μm)	36.6 ± 1.8	36.5 ± 1.8	38 ± 1.9	41.5 ± 2.1	45.9 ± 2.3
R_{in} (μm)	11.7 ± 0.25	11.4 ± 0.25	11.3 ± 0.25	11.35 ± 0.25	11.6 ± 0.25
β	47.65 ± 1.5	49.5 ± 1.5	50.1 ± 1.5	48.5 ± 1.5	45.7 ± 1.5
ΔP_{μ} (Pa)	21.8 ± 1.85	24.5 ± 2.1	25 ± 2.1	23 ± 2	19.3 ± 1.6

Table 5.3: Viscous pressure drop calculations for each of the liquid bridge seen in Figure 5.24. The experimental uncertainty on w_1 leads to some uncertainties on R_{in} , β and finally a 8.5 % uncertainty on ΔP_{μ} .

estimate the liquid film lengths when the first depinning occurs (from each spiral most external cylinder). This is an important prediction as this first depinning marks the end of the constant evaporation rate period. Also, this would be very satisfying to be able to predict the film length evolution versus time, during the entire course of an experiment (and not only at the first depinning).

The basic idea will be to compute a cumulated viscous pressure drop along the succession of liquid bridges for each spiral and such an idea is now detailed:

1. One consider a given evaporation flux E .
2. One choose a main meniscus location (i.e. at the inlet of a given pore). The capillary pressure will be taken to be close to the capillary invasion pressure for the pore where the main meniscus is positionned.
3. One consider the first liquid bridge along the spiral. It is supposed to be a capillary equilibrium, at pressure P , and thus its capillary shape is known. From the knowledge of this shape and using the evaporation rate value E , the viscous pressure drop $\Delta P_{\mu,1}$ for the flow inside this liquid bridge will be computed.
4. One now consider the second liquid bridge along the spiral. It is supposed to be a capillary equilibrium, at pressure $P - \Delta P_{\mu,1}$. Again, a new viscous pressure drop $\Delta P_{\mu,2}$ can be computed.
5. And so on...At a given location along the spiral (i.e. at a given liquid bridge), the pressure is thus equal to the main meniscus pressure minus the viscous pressure drop cumulated over the liquid bridges preceding the one under study. At one point, this computed pressure will fall below the critical capillary pressure for a liquid bridge, meaning that the considered liquid bridge cannot be observed. One then has reached the maximal liquid film extension for the value of E considered.

This first approach is not fully satisfying : it recognizes the fact that the viscous effects are to be taken into account, however, it is based upon the fact that at the length-scale of a liquid bridge, the capillary shape is kept. Developping such

a method for computing the liquid film length is the subject of work currently in progress.

5.5 Conclusions

The phenomenology of the liquid films effect in the Fibonacci spiral micromodel is similar to the one encountered in Chauvet's work. The drying kinetic is controlled by the liquid films dynamic (film length vs time). However, it is far more complex to describe quantitatively because one has to cope with viscous effects that are strong enough to compete with capillary effects (in the small micromodel, gravity being negligible). Also, the liquid film shape is much more complex than in a straight corner and obtaining the viscous resistance to the evaporation-induced flow within the liquid films is quite involved. However, we believe that we are close to propose a visco-capillary drying model for such a situation. Then, we will be ready to deal with more realistic porous media, such as, for instance, regular 2D or 3D packings of spherical particles.

Chapter 6

Elasto-capillary devices

In previous chapters, the microsystem used were rigid. In this chapter, we propose several preliminary experimental investigations using experimental devices where elasto-capillary phenomena can take place. The idea is that the microsystem geometry can be deformed by elasto-capillary effects during drying of a wetting fluid, which has the potential to alter the drying kinetic.

6.1 Introduction to elasto-capillarity

Elasto-capillary effects occur when the capillary force is large enough to deform an elastic material. It involves the coupling between the interface surface energy and the elastic strain energy of solid structures wet by the liquid, involving strong nonlinear behaviors.

Figure 6.1 illustrates several examples of elasto-capillary effects. A common example of elasto-capillary effects occurs when wetted hairs assemble into bundles, see Figure 6.1a. In the microfabrication field, during the last step in wet-photolithography, the residual resist should be rinsed off by the developing solvent. During the dry out process, residual liquid will cluster around microstructures, and capillarity-induced forces will make the structures deform or collapse [49], see Figure 6.1c. It also happens when rinsing MEMS or NEMS devices: this phenomenon is then often called pattern collapse and it will limit the design of microdevices, such as pillar arrays, slender walls [3] and cantilevers [33], etc. Traditionally, people try to prevent such effects to happen, but in recent decades, some interesting devices benefiting on deformation induced by capillary forces have been designed, such as capillary origami [38], meniscus assembly of nano/micro-structures [27] and capillary actuators [4].

6.1.1 Mechanism of elasto-capillarity

Elasto-capillary length

Let's introduce a given typical length l for a given system. According to scaling laws, capillary force is proportional to l , pressure and elastic forces are proportional to l^2 and body forces (such as gravity) to l^3 . When scaling down to a smaller scale,

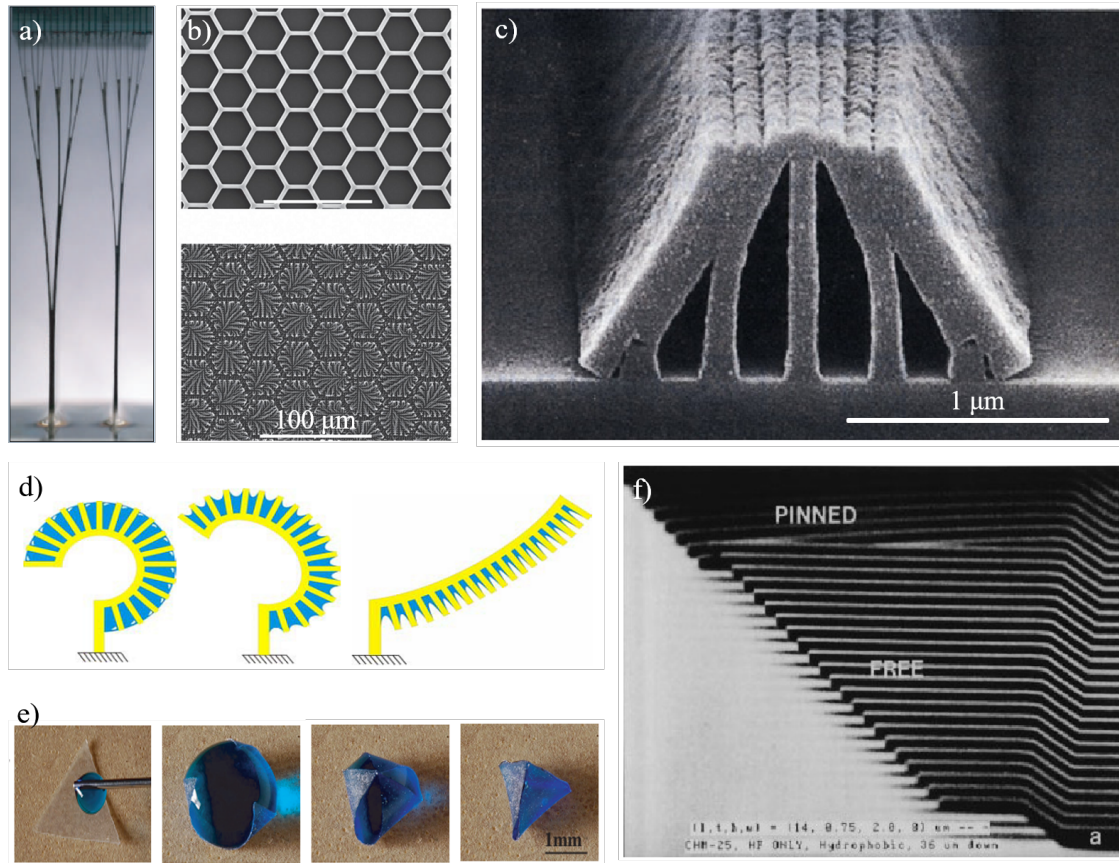


Figure 6.1: a) Parallel elastic lamellae bundled by wetting liquid, a model of wetting hair. b) Meniscus induced self-assembly of pillar array under a honeycomb mask [27]. c) Collapsed lamellae during development process of resist [49]. d) Polymer actuators driven by water surface tension inspired by hygroscopic spore dispersal mechanism [4]. e) Capillary origami, PDMS flexible sheet is self-wrapping with droplet, leading to 3D structure [38]. f) Micro cantilever beam stick to substrate when length exceed a critical limit [33].

the elastic or gravitational forces decrease faster than capillary force, so that the latter becomes the dominant one in the system. For example, a capillary length can be defined, under which capillary effects dominate over the gravity force. The capillary length is $l_c = \sqrt{\gamma/\rho g}$ and for water, $l_c = 2.7$ mm.

When it comes to consider the competition between a capillary force and an elastic force, a distinction has to be made between two situations: one is bulk elasto-capillarity, the other one is slender elasto-capillarity. The first situation is illustrated in Figure 6.2a. When the solid substrate on which a liquid droplet rest is not rigid, the vertical component of the surface tension ($\gamma \sin \theta$) will induce a deformation, marked as δ . The corresponding force is of order $\delta \times E$, leading to $\delta \approx \gamma \sin \theta / E$, where E is the Young's modulus of the solid substrate. Water ($\gamma \sim 70$ mN/m) on glass ($E \sim 70$ GPa) will induce a deformation of the order of 10^{-12} m, which is completely negligible.

The second situation occurs when a slender lamella is deformed by capillary

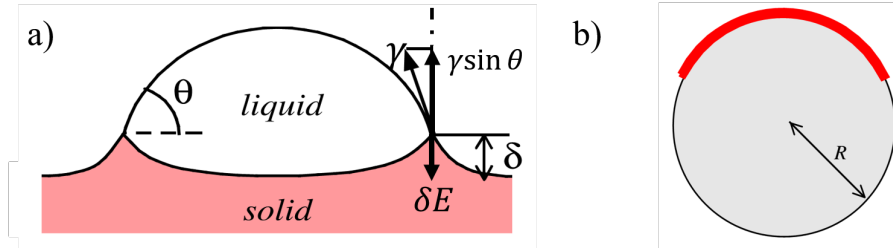


Figure 6.2: a) Droplet on deformable substrate, vertical component of surface tension is balanced by small deformation δE . b) Schematic illustration of slender lamella (color red) deformed by surface tension on a droplet (with radius of R).

force, as shown in Figure 6.2b. Roman proposed the concept of elasto-capillary length [3, 40] by considering a lamina (dimension $l \times w \times h$) in contact with a droplet (radius R). The surface energy in such a system is $E_\gamma \sim \gamma w l$, while the elastic energy of the lamina is $E_e \sim E h^3 w l / R^2$. At equilibrium, $E_s \approx E_e$, so that:

$$R \sim l_{ec} = \sqrt{\frac{E h^3}{\gamma}}. \quad (6.1)$$

The elasto-capillary length, l_{ec} , compares elasticity and surface tension for a slender structure. Similarly to the capillary length, only slender structure with a length over l_{ec} will display a significant deformation.

Forces in elasto-capillary situations

The capillary force is the only driving force in elasto-capillary device. There are some other terms reported in literatures, such as surface tension force [14], lateral capillary meniscus interaction force [8], but principally they are all capillary forces.

Let's consider a pair of parallel plates (each size $l \times w \times h$, spacing d) standing vertically on substrate, with a wetting droplet in between, contacting with the two plates and substrate, as shown in Figure 6.3. If we ignore the curvature on the wall direction, the capillary pressure is $\Delta P = 2\gamma \cos \theta / R$, with θ the contact angle and R the meniscus radius of curvature. When considering the deformation δ ,

$$\Delta P = 2\gamma \cos \theta / (d - 2\delta) + 8\gamma \sin \theta \delta / 3H(d - 2\delta). \quad (6.2)$$

Farshid [14] argued that the surface tension force (STF) acting on a triple line is important when studying pattern collapse. In the case of a droplet resting on a soft flat surface, he showed that the STF can deform the surface as shown in Figure 6.2a and with:

$$F_{STF} = \gamma \sin \theta l. \quad (6.3)$$

Lateral capillary meniscus interaction forces cause adjacent particles floating on free liquid surface to attract (when particles are both hydrophobic or both hydrophilic) or repulse one another. In recent studies, such an effect is also regarded as the major factor causing micro-pillar array clustering, Chandra & Yang 2009 [8]. In

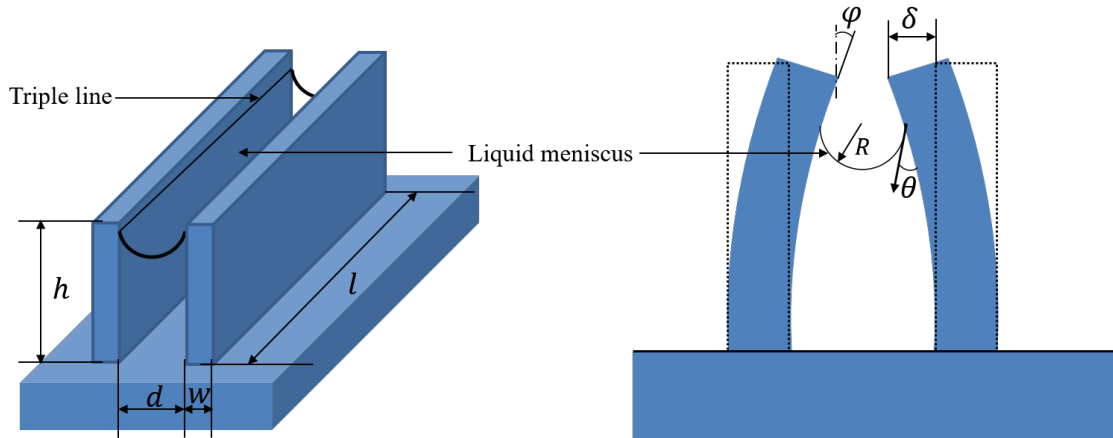


Figure 6.3: Elasto-capillary effect in between two parallel slender walls.

Chandra's studies, when consider a deflection δ , the capillary meniscus interaction force F_c acting on a micropillar array (d for diameter, p for pitch) is given by:

$$F_c = \frac{\pi\gamma d^2 \cos^2\theta}{2} \left(\sqrt{\frac{2}{(p-2\delta)^2 - d^2}} + \sqrt{\frac{1}{2(p-2\delta)^2 - d^2}} \right). \quad (6.4)$$

The rigidity of the pattern is considered as being the only restoring forces in the system. From Tanaka's research [49], in the bending beam model, for a given deformation noted as δ , the restoring force F can be written as

$$F = \frac{8EI\delta}{h^4}, \quad (6.5)$$

where E is the Young's modulus of the beam, I the inertia moment of the beam cross sectional area, given as $I = lw^3/12$. One can then calculate a critical aspect ratio for a given structure, A_c , above which the structures come into contact with one another at tips and collapses. For contact angle much smaller than 90° and assuming $w = d$:

$$A_c = \left(\frac{Ew}{24\gamma\cos\theta} \right)^{1/4}. \quad (6.6)$$

For a given elastic material and a given liquid, Young's modulus, contact angle and surface tension are fixed. When designing a deformable structure, the key element is to determine the size of structure using this critical aspect ratio. In our study, we used the elastomer PDMS (Polydimethylsiloxane, Young's modulus of Sylgard 184: $\sim 1.5 - 2$ MPa) as solid material, and ethanol ($\gamma = 22.3$ mN \cdot m at 20°C) as working liquid. Taking $w = 10$ μm leads to $A_c \approx 5$, indicating that structure height above 50 μm should collapse.

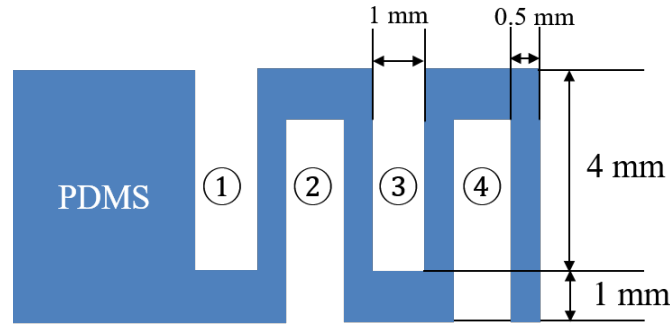


Figure 6.4: Geometry and dimensions of elasto-capillary spring device. The geometry is in periodical crenel shapes (labeled with circle numbers), with a thickness of 3 mm (in the direction perpendicular to the sketch plane). Bulk PDMS at the left supports the spring structure and is placed on a substrate, whereas the spring is suspended during an experiment.

6.1.2 Device design objectives

Two objectives are kept in mind. The first one is to design system with a simple geometry to investigate the pattern collapse mechanism. The second one is to design model porous media with a deformable pore space, to investigate the coupling between drying and elasto-capillary deformation of the pore space.

6.2 Elasto-capillary spring

In this section, we will introduce the design strategy and fabrication method to realize the elasto-capillary spring device. Inspired by Borno's rib-like micro-actuator driven by surface tension [4], as shown in Figure 6.1d, we designed crenel structure devices.

6.2.1 Device design and fabrication

Borno's micro-actuator mimics the geometry of fern sporangia, the reproductive vessel that can release spores into the air by means of surface tension forces. The micro-actuator is made of silicone polymer (PDMS), consisting of a slender spine which is decorated with ribs at one side, making cells that can hold water. These ribs act as levers upon which forces induced by surface tension enforce the spine deformation. We notice that this device introduce a rotational deformation by means of capillary force. Therefore, another question arise: will translational displacement be possible with such a geometry? We designed spring-like device based on same principle, to show that such translational displacement can be induced by elasto-capillary effects. The elasto-capillary spring device and its dimension are shown in Figure 6.4. As discussed above, the aspect ratio of the structure should be 5 at least to expect some deformation. Here, we designed a spring device with an aspect-ratio of 8. The pattern dimension is $7.5 \times 5 \times 3 \text{ mm}^3$. This is the smallest size that can be reached staying within the resolution of the 3D printer used in the protocol.

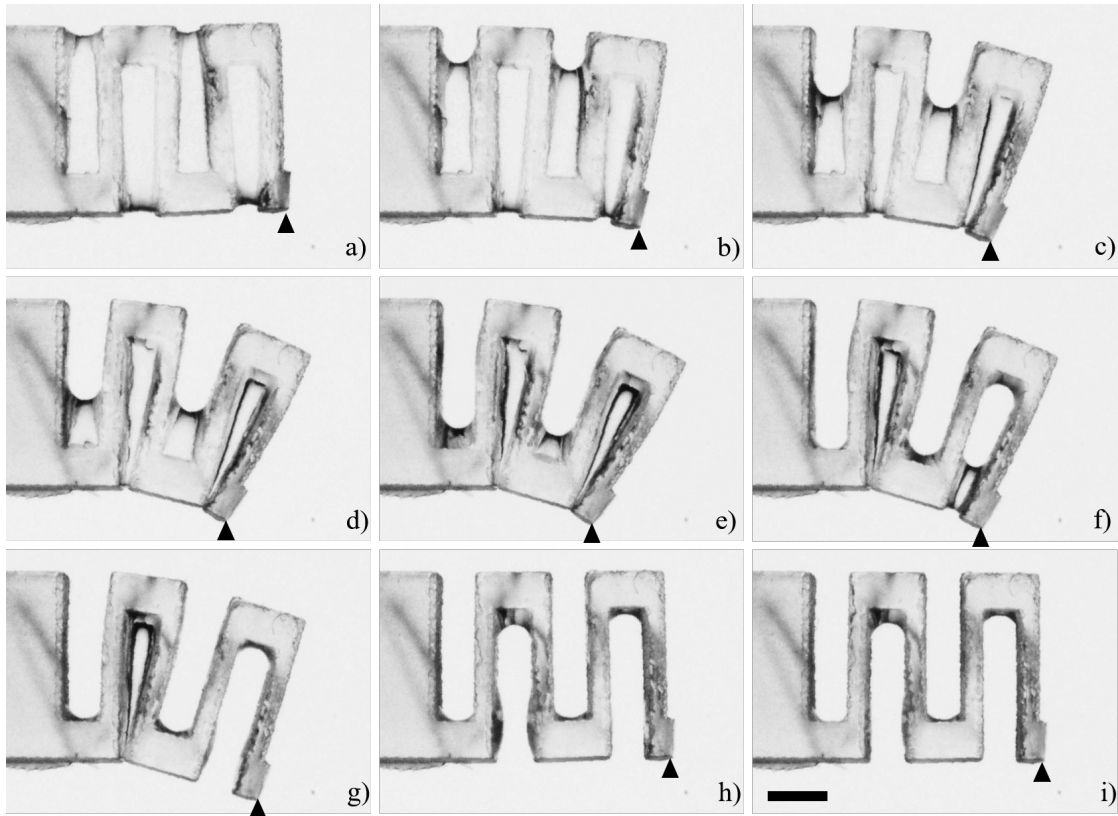


Figure 6.5: Top view images of an experiment with the elasto-capillary spring device, using ethanol as a working liquid and carried out at room temperature. From a) to i), the time step between two images is 5 second. Scale bar is 1.5 mm.

For the fabrication, we use a soft-lithography method, with 3D printing to fabricate the mold. The device geometry is designed by AutoCAD, and then exported to STL format for subsequent 3D printing. The 3D printer uses acrylic plastic as a material to build a mold. Before casting PDMS into the mold, we surface-treat the mold with a silanizing agent in order to facilitate the subsequent de-moulding process. PDMS base and curing agent (mass ratio 10:1) are mixed and degased in a vacuum chamber at room temperature. We cast the mixture into the mold and degas again. PDMS is then cured in a oven at 70 °C for 1.5 hours before a tricky de-moulding stage as the system is fragile.

6.2.2 Experiments and results

Typical experimental results are shown in Figure 6.5. On these top views, it is first seen that the device is initially slightly squeezed (compare images a and i), like a squeezed spring. As evaporation proceeds, menisci are clearly seen filling the space between the spring “turns” and an important deformation of the device is seen. To quantify this observation, we investigated by image processing the successive locations of the right-down tip of the capillary spring, indicated by a black triangle in Figure 6.5. The result is shown in Figure 6.6. The corresponding displacement of the tip is indicated with arrows. We can see that from the starting image a)

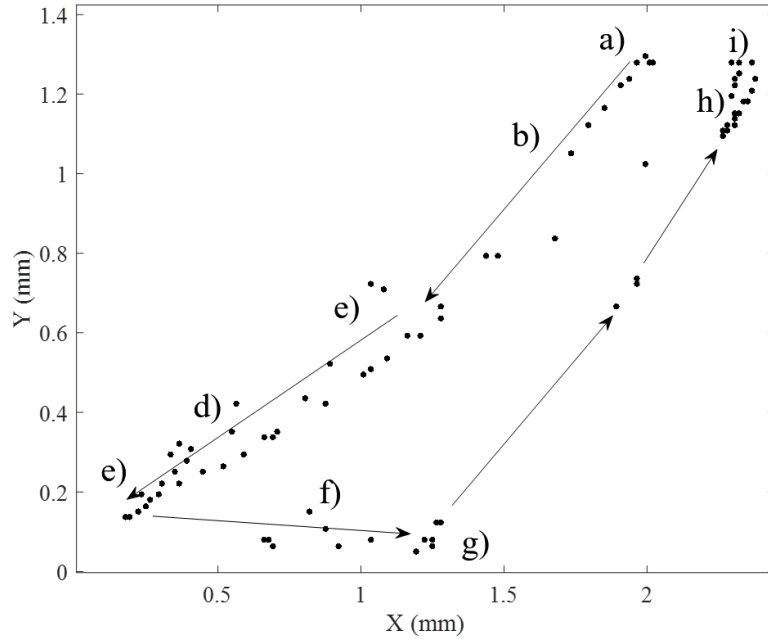


Figure 6.6: Trajectory of the right-down corner of the capillary spring (black triangle in Figure 6.5).

to the ending i), the right-down tip experiences a counter-clockwise rotation, and the collapses of the two capillary bridges at crenel #2 and #3 produce two periods with higher tip velocity, from e) to f) and from g) to h). Another point that is clearly quantified is the overall squeezing of the spring, see the tip location at a) (wet spring) and i) (dry spring).

6.2.3 Preliminary conclusion

The capillary spring presented clearly displays some elasto-capillary effects. If the free end of the spring device was attached to a stress sensor (piezoelectric chip for instance), one could measure the amplitude of the capillary force induced by elasto-capillarity and then relate this signal to the evaporation rate, thus building an evaporation sensor. Of course, such an application would require optimizing many geometrical parameters (crenels number, aspect ratio, etc.).

6.3 Drying in deformable cylinder array

In this section, two patterns of deformable cylinders are presented, with square and hexagonal spatial arrangement of the cylinders respectively. We first investigate the drying-induced pattern in this two devices, when the arrays are not confined, i.e. the cylinder array is opened and exposed to dry ambient air. Then, the pattern is covered with a glass plate and we obtain a situation quite similar to the micromodel used in the previous chapters.

6.3.1 Deformable cylinder array design and fabrication

As discussed above, structures with aspect ratio beyond 5 are likely to collapse, for $10\ \mu\text{m}$ thick structures. In order to observe significant cylinder deformations, we designed cylinders with a height of $50\ \mu\text{m}$ and with a diameter of $15\ \mu\text{m}$. Two types of cylinder spatial arrangement (square and hexagonal) were used, see Figure 6.7. The cylinder spacing (edge to edge) is fixed at $20\ \mu\text{m}$ for the two patterns. Such microsystems are fabricated using a soft-lithography method. The fabrication protocol is described below.

1. A mold wafer is fabricated at LAAS, using photolithography technology. A standard silicon wafer (4 inch, $525\ \mu\text{m}$ in thickness) is cleaned by oxygen plasma. SU-8 3050 is spin-coated to obtain a $50\ \mu\text{m}$ thickness (30 s at 500 rpm, then 30 s at 3200 rpm). Soft baking is realized on a hot plate (3 min at 65°C then 27 min at 95°C). Exposure (dose $210\ \text{mJ}/\text{cm}^2$) is realized on a mask aligner (MA6, Karl Suss, vacuum contact, filter at $365\ \text{nm}$, mode of constant pressure, exposure time 15.5 s). Post-exposure bake is done with the same condition as the soft bake. Then, standard development is performed under vacuum, with two steps for this high aspect ratio. Vacuum helps the developer to enter the small holes. Hard bake (10 min at 125°C) enables to remove fracture lines at the edges of the patterns.
2. An octadecyltrichlorosilane (OTS) treatment is realized on the mold wafer

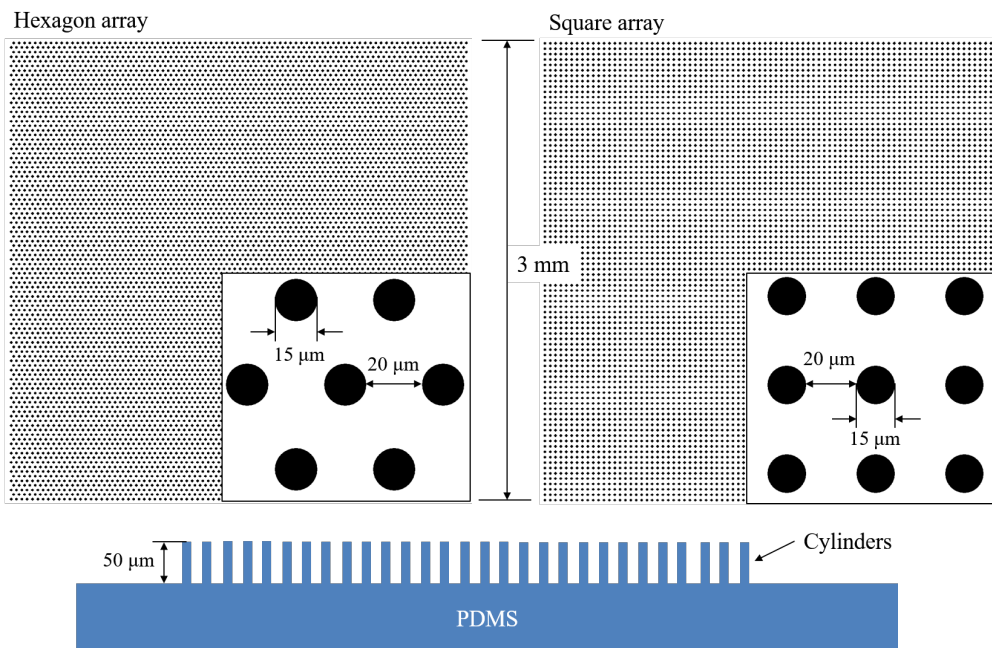


Figure 6.7: Geometry and dimensions of the arrays of deformable cylinders. The hexagonal cylinder array contains 18232 cylinders, the square one contains 7396 cylinders. Each cylinder has a $15\ \mu\text{m}$ diameter, a height of $50\ \mu\text{m}$ (side view at bottom), and the cylinder spacing (edge to edge) is $20\ \mu\text{m}$. Each array has a square shape, with a side size of about 3 mm.

as anti-adhesion process, in order to enable PDMS un-molding. The mold is exposed to an oxygen plasma for 2 min (1000 sccm, 60 W). Immediately after, OTS treatment is realized with OTS/Xylene solution (0.5 mL in 50 mL) under nitrogen environment to avoid moisture (solution prepared just before used). Reaction is done for 5 min, then rinsed with xylene, acetone and water successively, before a final drying stage with nitrogen.

3. Soft-lithography with PDMS. Protocol is the same as with the elasto-capillary spring device.

Post micro-fabrication with SEM (Hitachi S-3700) indicates that the cylinder height is equal to $53 \pm 1 \mu\text{m}$, which is close to the designed value.

6.3.2 Experimental results: drying of non-confined arrays

The cylinder array is placed on a desk with a LED back-light underneath. The camera is focussed on the cylinders tips. An ethanol droplet is directly deposited on the cylinder array with a pipette, before image acquisition starts.

Figure 6.8 illustrates the results on a square cylinder array. As evaporation proceeds, a clear deformation of the cylinders is seen, provoking a collapse of the cylinders leading to the formation of clusters. From Figure 6.8a to c, we think there is still liquid wetting the substrate surface in between the cylinders. Then, the liquid remains trapped around the clusters of cylinders only, see Figure 6.8d to g. Finally, once all the liquid has evaporated, we notice that the adhesive force between cylinders is able to maintain the contact between the cylinders tips. Interestingly, in such a square arrangement array, evaporation-induced deformation makes the cylinders to assemble by pairs or groups of four. Some researches investigating such clusters size and shape have already been reported, i.e. Chandra [9].

Figure 6.9 illustrates the experiment on the hexagonal array, with images showing the whole device. Again, elasto-capillary effects are displayed, but with more irregular cluster shapes. Interestingly, this pattern is in some way similar with crack patterns which form after desiccation of clay soil [56] and other complex system such as paint films or ceramic-coated metals. In [56], the authors build a network of triangular lattice nodes connected with springs, similar to our cylinder arrangement. Desiccation is reproduced by reinforcing the springs. At one point, this leads to the burst of the first spring and subsequently to the self-organized formation of a crack pattern. The underlying physical mechanism of crack formation, which must be related to pore scale hydrodynamic and capillary effects, is overlooked in their study. The deformation of the cylinder array seen in our experiment may have the potential to investigate the crack formation. A zoom on the crack pattern seen in Figure 6.9d is shown in Figure 6.10a, and the size distribution for the cylinder clusters is shown in figure 6.10b.

6.3.3 Experimental results : drying of confined arrays

We now turn to the results obtained by confining the cylinders pattern used in the previous subsection with a glass plate. The top glass plate is positioned after the

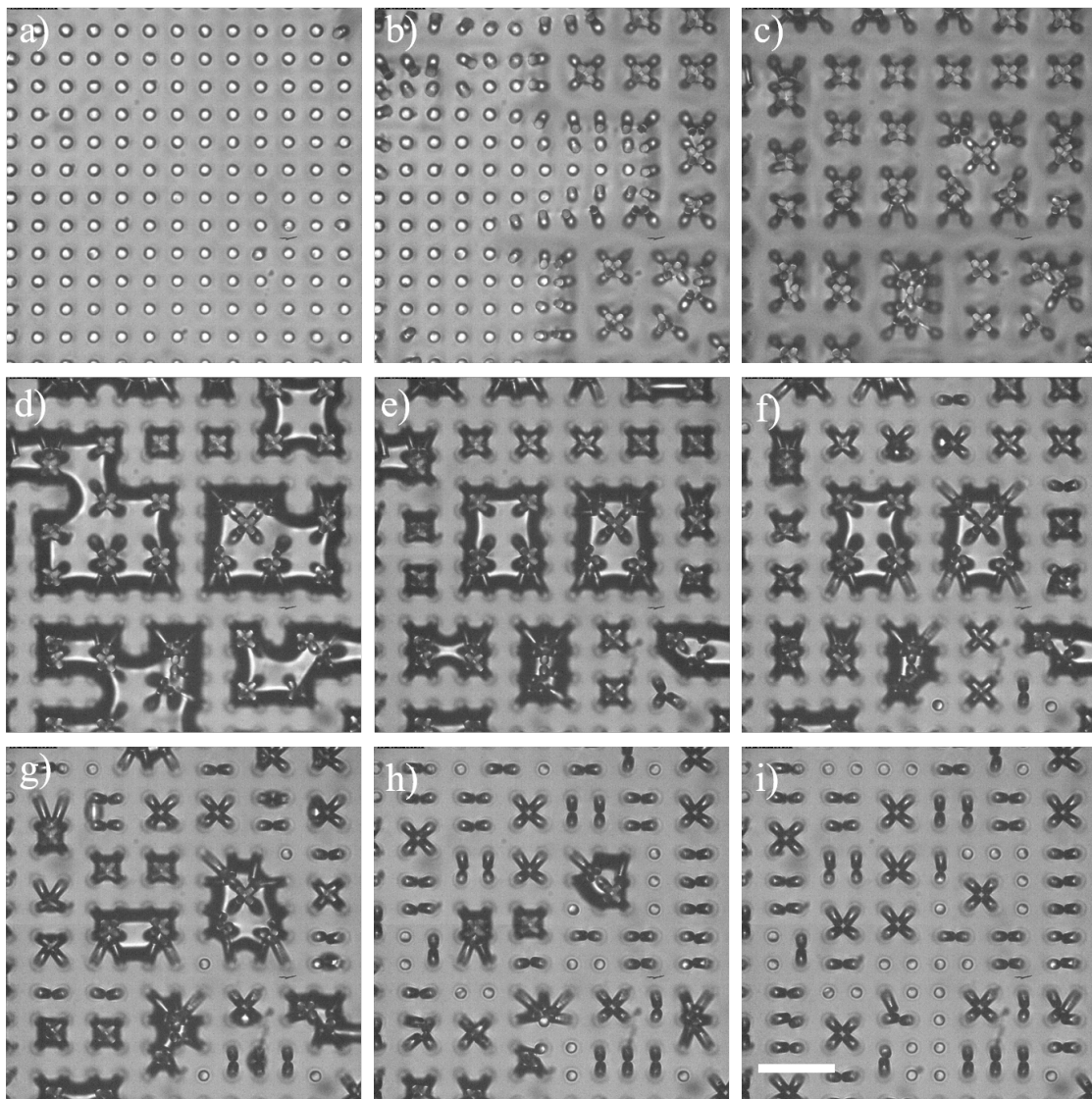


Figure 6.8: Drying of the square pattern, zoom on a small part of the full pattern. Time interval between two images is 8 seconds. Scale bar is $100\ \mu\text{m}$.

deposition of a volatile liquid droplet on the cylinders array. The drying process is followed by image acquisition as before. Figure 6.11 shows some images obtained with ethanol. At the beginning, a stable receding, drying front can be seen propagating from the edge towards the center, see Figure 6.11a. Subsequently, the drying front pins at a specific location, see Figure 6.11b to d, and the gas phase penetrates the array along well-defined “fracture” or fingers. Finally, the drying front starts penetrating again in the porous medium, from Figure 6.11d until isolated liquid clusters dry-out.

The fracturing pattern formed after Figure 6.11b) attracted our attention. Figure 6.13 is a zoom on the center of the array, taken between Figure 6.11f and Figure 6.11g. By image processing, we were able to measure the location of the cylinders (red dots) and this was repeated for an image obtained at the end of the experiment,

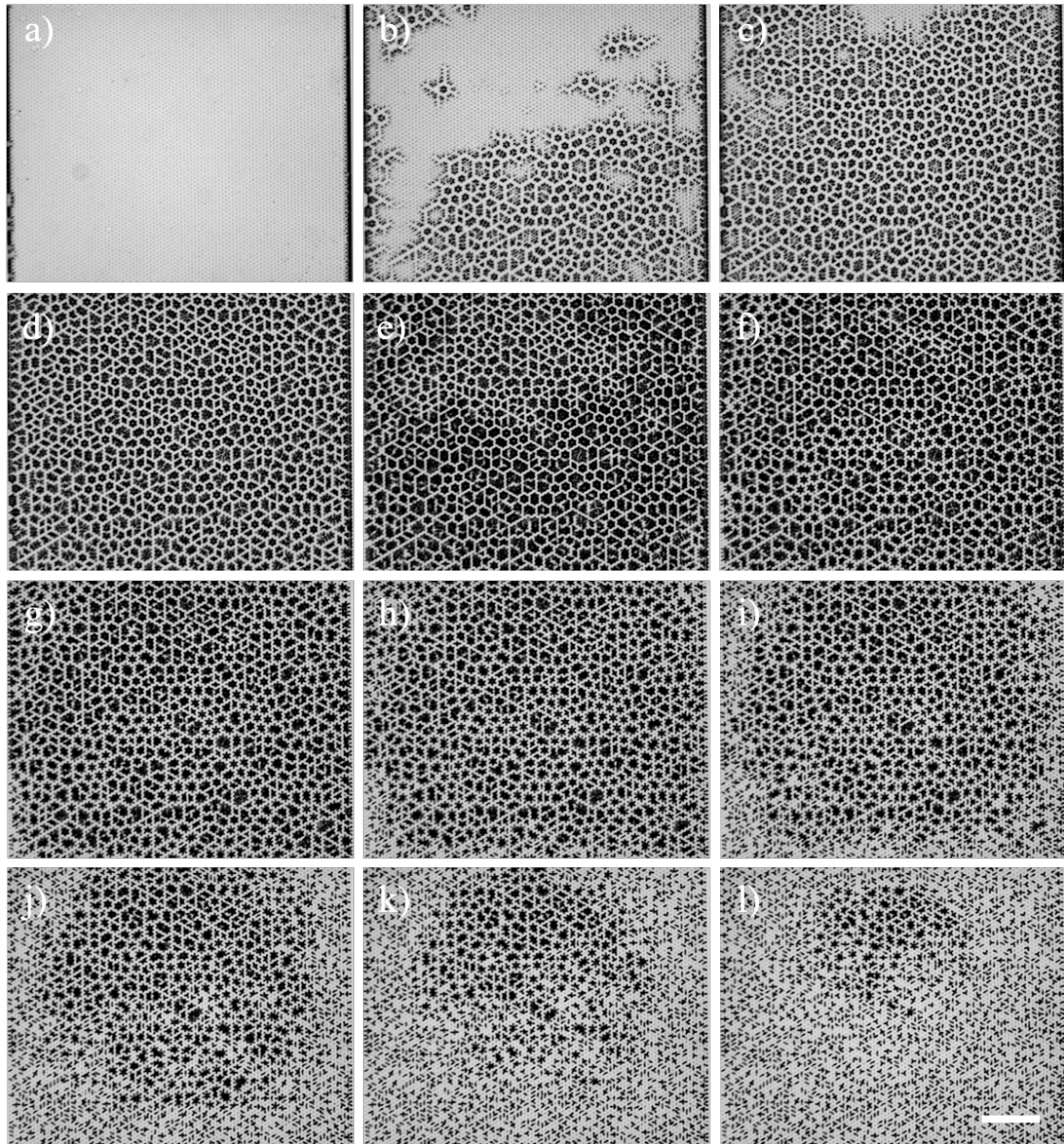


Figure 6.9: Drying of the hexagonal pattern, the full pattern is seen. Time interval between two images is 8 seconds. Scale bar is $500 \mu\text{m}$.

when the system is dry (yellow dots). The mismatch of the red and yellow dots indicates that a slight displacement of cylinders on which the meniscus rests can be measured. The displacement vector (from the yellow to the corresponding red dot) always points towards the liquid phase. The time evolution of the averaged displacement is shown in Figure 6.13. It remains roughly equal to $1.4 \mu\text{m}$ over the duration of the experiment, with an increasing number of cylinders being on a meniscus.

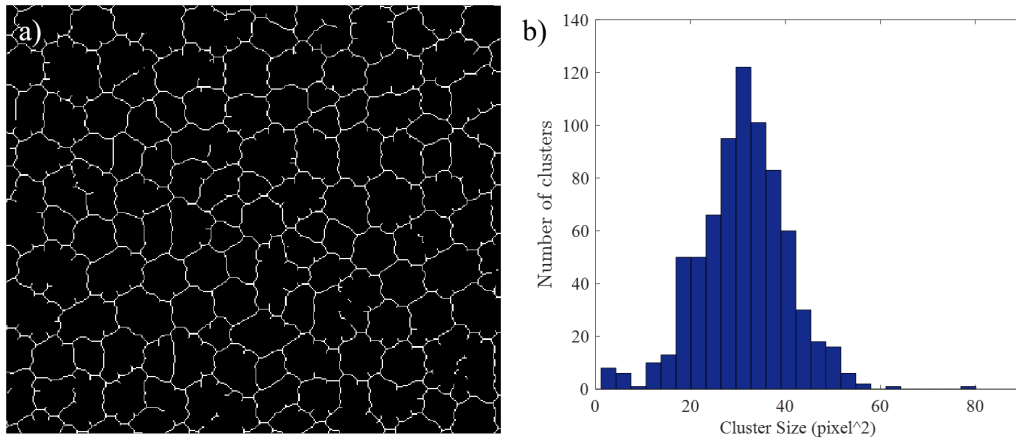


Figure 6.10: a) Zoom on the crack pattern formed in hexagonal pattern. b) Cylinder clusters size distribution.

6.4 Conclusion

In this chapter, we presented a coupled of preliminary experiments. An important achievement is that we can fabricate in the lab microsystems displaying measurable elasto-capillary effects (even if the microfabrication protocol can still be improved). The most interesting case, in the framework of this manuscript, is the last one, where elasto-capillary effects alter the pore space of a drying micromodel, with the appearance of a puzzling pattern due to the collapse of the cylinders. Now, we aim at comparing the drying kinetic in such a micromodel to the one obtained with a similar, non-deformable micromodel, to study the impact of the elasto-capillary deformation of the pore space. Such a work is currently in progress, as a part of Antoine Naillon's PhD work.

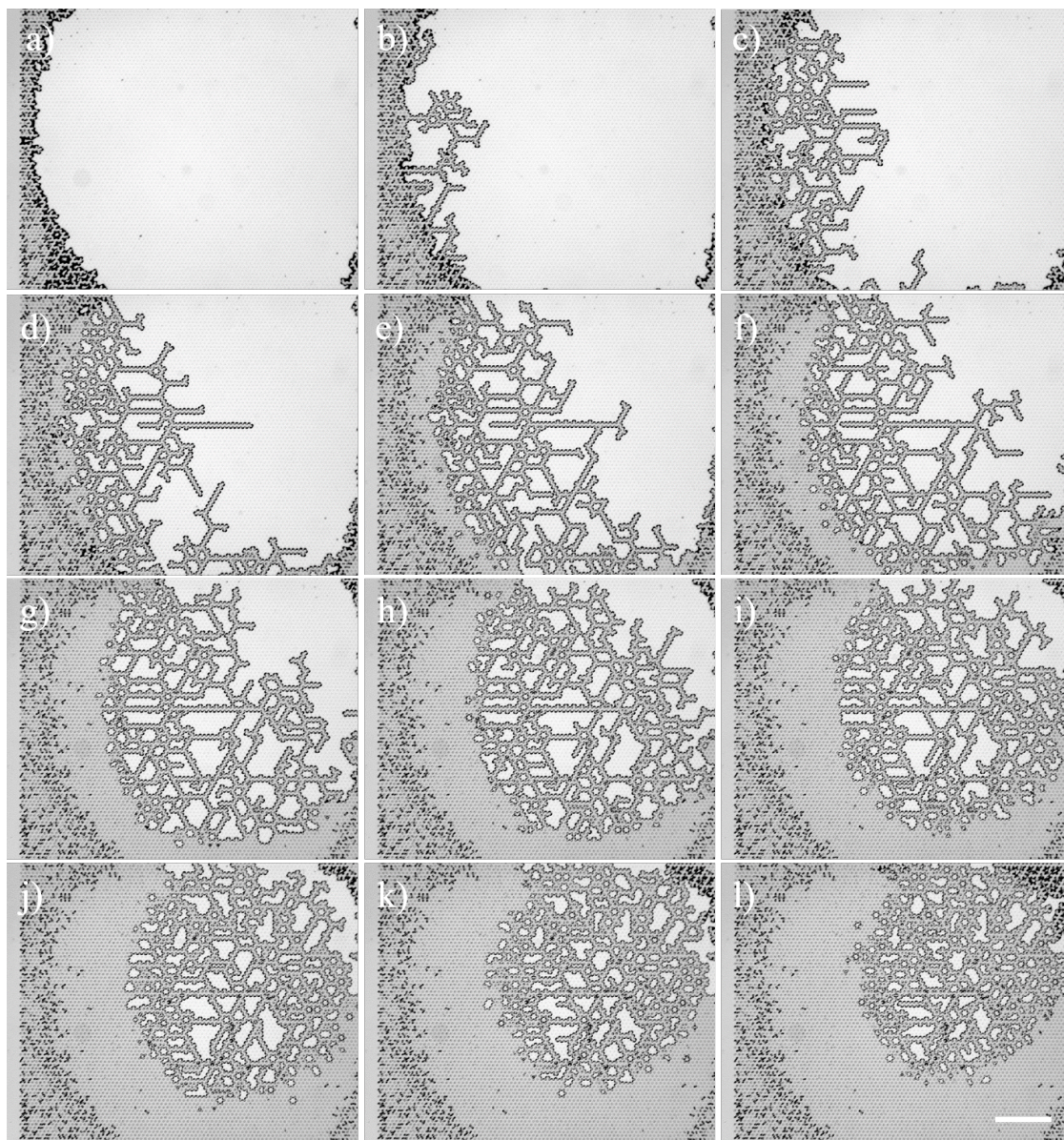


Figure 6.11: Images of drying in a deformable porous medium, obtained by covering the hexagonal pattern with a glass plate. Working liquid is ethanol, time interval between two images is 40 seconds. Scale bar is $500 \mu\text{m}$.

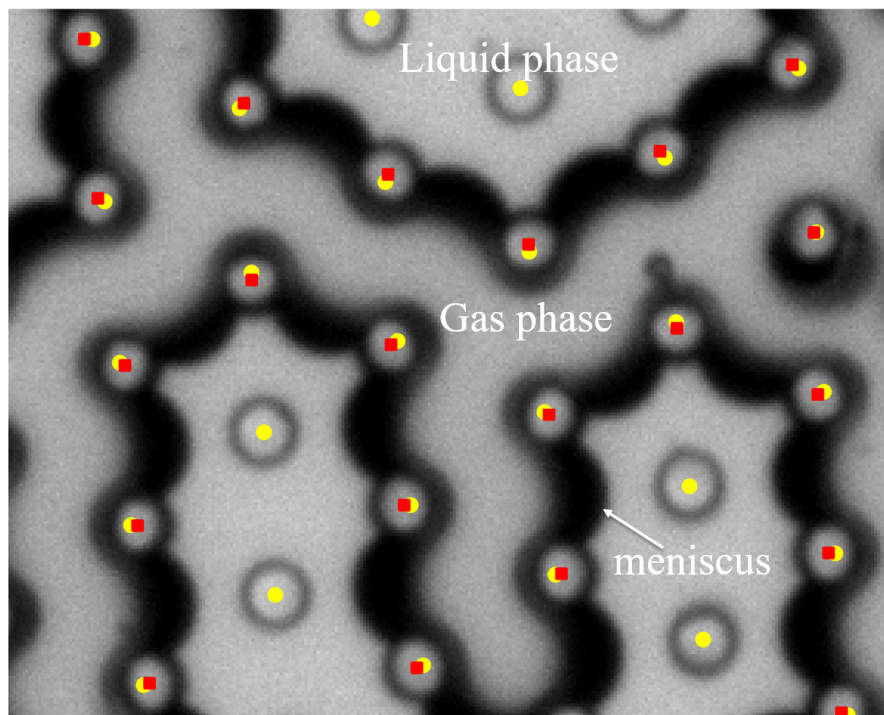


Figure 6.12: Schematic illustration of cylinder displacement on meniscus. Yellow circle dots represent for cylinder original position (obtained from binarized images), red square dots represent for cylinders new position after been deformed on meniscus. Displacement vectors (yellow to red) point to liquid phase.

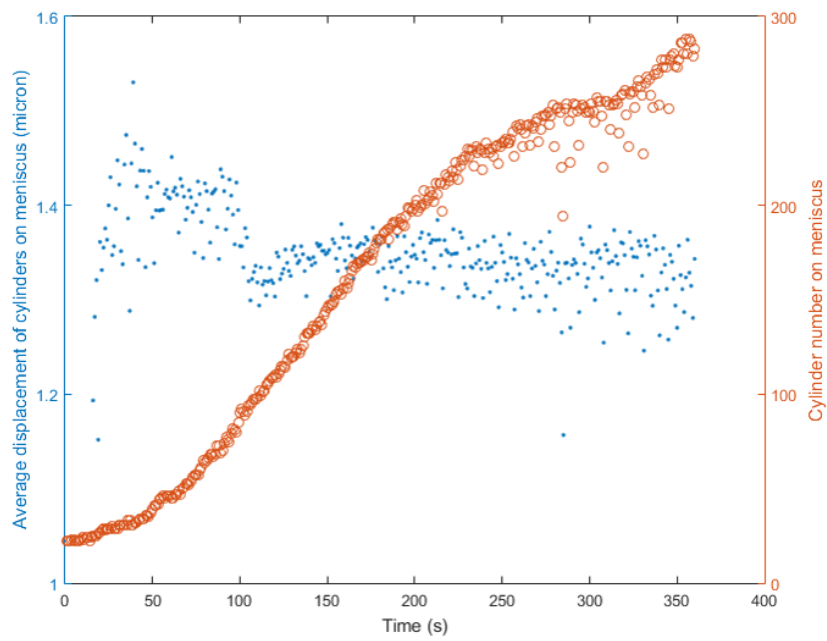


Figure 6.13: Averaged displacement of the cylinders and total number of cylinders on meniscus, as a function of time.

Chapter 7

Conclusion and perspectives

An important objective of the present work was to demonstrate how the evaporation of a pure fluid saturating a porous medium could be controlled by the geometry of the pore space. Such a goal was reached by using different micro-fabricated model porous media, consisting of arrays of cylinders arranged with a carefully designed pattern. In such micromodels, the position of the evaporation front can be controlled via the cylinders pattern.

One can distinguish two main control levels depending on which type of liquid-gas interface one is willing to control. The bulk interface can be controlled by playing with the gap gradient (Chapter 4) whereas the secondary capillary interface, corresponding to the liquid bridge chains considered in Chapter 5, is somewhat subtler to control. First, it requires a sufficient understanding of capillary invasion mechanisms so as to develop designs favouring the formation of thick capillary films or chains of liquid bridges (such as the Fibonacci pattern used in the present work). Second, taking into account the viscous dissipation in the liquid films, due to the evaporation-induced flow, is necessary to obtain quantitative predictions on the films dynamics.

As mentioned in Chapter 4, these results give a framework for the design of 3D systems with properties tailored to specific applications, e.g. microfluidic devices, porous materials, etc... Another possible application is the modelling of drying in porous media. In fact, the consideration of the relatively simple bridge chains discussed in this work can be also seen as a step toward the significantly more complex arrangements of liquid bridges existing in porous media. Following this idea, the present work could be extended in order to study the drying of porous media consisting of “crystalline” packings of monodisperse, spherical beads. A research strategy similar to the one followed in the present work, coupling Surface Evolver simulations to DNS, could be applied to such a case.

Finally, introducing the elasto-capillary effects, possibly in a controlled way in carefully designed micromodels, adds another layer of complexity, but together with a wider range of possible applications. This should be a fruitful topic for future research in the lab.

Bibliography

- [1] Shmuel Assouline, Kfir Narkis, Rivka Gherabli, Philippe Lefort, and Marc Prat. Analysis of the impact of surface layer properties on evaporation from porous systems using column experiments and modified definition of characteristic length. *Water Resources Research*, 50(5):3933–3955, 2014.
- [2] Steffen Berg, Holger Ott, Stephan A Klapp, Alex Schwing, Rob Neiteler, Niels Brussee, Axel Makurat, Leon Leu, Frieder Enzmann, Jens-Oliver Schwarz, et al. Real-time 3d imaging of haines jumps in porous media flow. *Proceedings of the National Academy of Sciences*, 110(10):3755–3759, 2013.
- [3] J. Bico, B. Roman, L. Moulin, and A. Boudaoud. Elastocapillary coalescence in wet hair. *Nature*, 432:690–690, 2004.
- [4] R. T. Borno, J. D. Steinmeyer, and M. M. Maharbiz. Transpiration actuation: the design, fabrication and characterization of biomimetic microactuators driven by the surface tension of water. *Journal of Micromechanics and Microengineering*, 16:2375–2383, 2006.
- [5] Kenneth A Brakke. The surface evolver. *Experimental mathematics*, 1:141–165, 1992.
- [6] Aaron T. Cannistra and Thomas J. Suleski. Characterization of hybrid molding and lithography for su-8 micro-optical components. *Journal of Micro/Nanolithography, MEMS, and MOEMS*, 9:013025–013025–7, 2010.
- [7] Cesare M Cejas, Lawrence A Hough, Christian Frétygny, and Rémi Dreyfus. Effect of granular packing geometry on evaporation. *arXiv preprint arXiv:1601.04584*, 2016.
- [8] D. Chandra and S. Yang. Capillary-force-induced clustering of micropillar arrays: Is it caused by isolated capillary bridges or by the lateral capillary meniscus interaction force? *Langmuir*, 25:10430–10434, 2009.
- [9] Dinesh Chandra and Shu Yang. Stability of high-aspect-ratio micropillar arrays against adhesive and capillary forces. *Accounts of chemical research*, 43(8):1080–1091, 2010.
- [10] F. Chauvet, P. Duru, S. Geoffroy, and M. Prat. Three periods of drying of a single square capillary tube. *Physical Review Letters*, 103:4, 2009.

- [11] F. Chauvet, P. Duru, and M. Prat. Depinning of evaporating liquid films in square capillary tubes influence of corners' roundedness. *Physics of Fluids*, 22, 2010.
- [12] Fabien Chauvet. *Effet des films liquides en vaporation*. Thesis, 2009.
- [13] P. Duru M. Prat P. Joseph S. Geoffroy Chen, C. Towards the computation of viscous flow resistance of a liquid bridge. In *Proceedings 8th International Conference on Computational and Experimental Methods in Multiphase and Complex Flow*, volume 89, 2015.
- [14] S. F. Chini and A. Amirfazli. Understanding pattern collapse in photolithography process due to capillary forces. *Langmuir*, 26:13707–13714, 2010.
- [15] Marek Cieplak and Mark O Robbins. Influence of contact angle on quasistatic fluid invasion of porous media. *Physical Review B*, 41(16):11508, 1990.
- [16] F Clément and J Leng. Evaporation of liquids and solutions in confined geometry. *Langmuir*, 20(16):6538–6541, 2004.
- [17] E. H. Conradie and D. F. Moore. Su-8 thick photoresist processing as a functional material for mems applications. *Journal of Micromechanics and Microengineering*, 12:368–374, 2002.
- [18] P. Coussot. Scaling approach of the convective drying of a porous medium. *European Physical Journal B*, 15:557–566, 2000.
- [19] John H Cushman and TR Ginn. Nonlocal dispersion in media with continuously evolving scales of heterogeneity. *Transport in Porous Media*, 13(1): 123–138, 1993.
- [20] Howard Ted Davis. *Statistical mechanics of phases, interfaces, and thin films*. Wiley-VCH, 1996.
- [21] Stephane Douady and Yves Couder. Phyllotaxis as a physical self-organized growth process. *Physical Review Letters*, 68(13):2098, 1992.
- [22] Amir Faghri. *Heat pipe science and technology*. Global Digital Press, 1995.
- [23] Andrea Ferrari and Ivan Lunati. Inertial effects during irreversible meniscus reconfiguration in angular pores. *Advances in Water Resources*, 74:1–13, 2014.
- [24] Mauri Fortes and Martin R Okos. Changes in physical properties of corn during drying. *Transactions of the ASAE*, 23:1004–1008, 1980.
- [25] Suresh V Garimella, Yogendra K Joshi, Avram Bar-Cohen, Ravi Mahajan, KC Toh, VP Carey, Martine Baelmans, J Lohan, B Sammakia, and F Andros. Thermal challenges in next generation electronic systems-summary of panel presentations and discussions. *Components and Packaging Technologies, IEEE Transactions on*, 25(4):569–575, 2002.

- [26] William B Haines. Studies in the physical properties of soil. v. the hysteresis effect in capillary properties, and the modes of moisture distribution associated therewith. *The Journal of Agricultural Science*, 20(01):97–116, 1930.
- [27] Sung H Kang, Ning Wu, Alison Grinthal, and Joanna Aizenberg. Meniscus lithography: Evaporation-induced self-organization of pillar arrays into moire patterns. *Physical review letters*, 107(17):177802, 2011.
- [28] J. B. Laurindo and M. Prat. Numerical and experimental network study of evaporation in capillary porous media. phase distributions. *Chemical Engineering Science*, 51:5171–5185, 1996.
- [29] J. B. Laurindo and M. Prat. Numerical and experimental network study of evaporation in capillary porous media. drying rates. *Chemical Engineering Science*, 53:2257–, 1998.
- [30] Jacques Leng, Barbara Lonetti, Patrick Tabeling, Mathieu Joanicot, and Armand Ajdari. Microevaporators for kinetic exploration of phase diagrams. *Physical review letters*, 96(8):084503, 2006.
- [31] Roland Lenormand and Cesar Zarcone. Invasion percolation in an etched network: measurement of a fractal dimension. *Physical review letters*, 54(20):2226, 1985.
- [32] N. Scott Lynn and David S. Dandy. Passive microfluidic pumping using coupled capillary/evaporation effects. *Lab on a Chip*, 9:3422–3429, 2009.
- [33] C. H. Mastrangelo and C. H. Hsu. Mechanical stability and adhesion of microstructures under capillary forces part 1: Basic theory. *Journal of microelectromechanical systems*, 2, 1993.
- [34] Dani Or, Peter Lehmann, Ebrahim Shahraeeni, and Nima Shokri. Advances in soil evaporation physics - a review. *Vadose Zone Journal*, 12, 2013.
- [35] M. Prat. Percolation model of drying under isothermal conditions in porous-media. *International Journal of Multiphase Flow*, 19:691–704, 1993.
- [36] M. Prat. Isothermal drying of nonhygroscopic capillary-porous materials as an invasion percolation process. *International Journal of Multiphase Flow*, 21: 875–892, 1995.
- [37] M. Prat. Pore network models of drying, contact angle, and film flows. *Chemical Engineering & Technology*, 34:1029–1038, 2011.
- [38] C. Py, P. Reverdy, L. Doppler, J. Bico, B. Roman, and C. N. Baroud. Capillary origami: Spontaneous wrapping of a droplet with an elastic sheet. *Physical Review Letters*, 98, 2007.
- [39] T. C. Ransohoff and C. J. Radke. Laminar-flow of a wetting liquid along the corners of a predominantly gas-occupied noncircular pore. *Journal of Colloid and Interface Science*, 121:392–401, 1988.

- [40] Benoit Roman and José Bico. Elasto-capillarity: deforming an elastic structure with a liquid droplet. *Journal of Physics: Condensed Matter*, 22(49):493101, 2010.
- [41] R Rutishauser and P Peisl. Phyllotaxy. encyclopedia of life sciences, 2001.
- [42] M. Scheel, R. Seemann, M. Brinkmann, M. Di Michiel, A. Sheppard, B. Breidenbach, and S. Herminghaus. Morphological clues to wet granular pile stability. *Nature Materials*, 7:189–193, 2008.
- [43] Mario Scheel, Ralf Seemann, Martin Brinkmann, M Di Michiel, Adrian Sheppard, and Stephan Herminghaus. Liquid distribution and cohesion in wet granular assemblies beyond the capillary bridge regime. *Journal of Physics: Condensed Matter*, 20(49):494236, 2008.
- [44] G. W. Scherer. Stress from crystallization of salt. *Cement and Concrete Research*, 34:1613–1624, 2004.
- [45] George W Scherer. Theory of drying. *Journal of the American Ceramic Society*, 73(1):3–14, 1990.
- [46] E-U Schlünder. On the mechanism of the constant drying rate period and its relevance to diffusion controlled catalytic gas phase reactions. *Chemical Engineering Science*, 43(10):2685–2688, 1988.
- [47] T. M. Shaw. Drying as an immiscible displacement process with fluid counterflow. *Physical Review Letters*, 59:1671–1674, 1987.
- [48] M. SUZUKI and S. MAEDA. On the mechanism of drying of granular beds. *Journal of chemical engineering of Japan*, 1(1):26–31, 1968.
- [49] T. Tanaka, M. Morigami, and N. Atoda. Mechanism of resist pattern collapse during development process. *Japanese journal of applied physics*, 32:6059–6064, 1993.
- [50] W. H. Teh, U. Durig, U. Drechsler, C. G. Smith, and H. J. Guntherodt. Effect of low numerical-aperture femtosecond two-photon absorption on (su-8) resist for ultrahigh-aspect-ratio microstereolithography. *Journal of Applied Physics*, 97, 2005.
- [51] Yuksel Temiz, Jelena Skorucak, and Emmanuel Delamarche. Capillary-driven microfluidic chips with evaporation-induced flow control and dielectrophoretic microbead trapping. *Journal of Micro/Nanolithography, MEMS, and MOEMS*, 13:033018–033018, 2014.
- [52] Jaap Van Brakel. Mass transfer in convective drying. 1980.
- [53] Orlin D Velev and Shalini Gupta. Materials fabricated by micro-and nanoparticle assembly—the challenging path from science to engineering. *Advanced Materials*, 21(19):1897–1905, 2009.

- [54] S. Veran-Tissoires, M. Marcoux, and M. Prat. Discrete salt crystallization at the surface of a porous medium. *Physical Review Letters*, 108:054502, 2012.
- [55] Olivier Vincent, David A Sessoms, Erik J Huber, Jules Guioth, and Abraham D Stroock. Drying by cavitation and poroelastic relaxations in porous media with macroscopic pores connected by nanoscale throats. *Physical review letters*, 113(13):134501, 2014.
- [56] H. J. Vogel, H. Hoffmann, A. Leopold, and K. Roth. Studies of crack dynamics in clay soil: II. a physically based model for crack formation. *Geoderma*, 125: 213–223, 2005.
- [57] N Vorhauer, YJ Wang, A Kharaghani, E Tsotsas, and M Prat. Drying with formation of capillary rings in a model porous medium. *Transport in Porous Media*, 110(2):197–223, 2015.
- [58] Stephen Whitaker. Role of the species momentum equation in the analysis of the stefan diffusion tube. *Industrial & Engineering Chemistry Research*, 30(5): 978–983, 1991.
- [59] David Wilkinson and Jorge F Willemsen. Invasion percolation: a new form of percolation theory. *Journal of Physics A: Mathematical and General*, 16:3365, 1983.
- [60] A. G. Yiotis, D. Salin, E. S. Tajar, and Y. C. Yortsos. Analytical solutions of drying in porous media for gravity-stabilized fronts. *Physical Review E*, 85, 2012.
- [61] Dengen Zhou, Martin Blunt, and FM Orr. Hydrocarbon drainage along corners of noncircular capillaries. *Journal of colloid and interface science*, 187:11–21, 1997.
- [62] M. Zimmermann, S. Bentley, H. Schmid, P. Hunziker, and E. Delamarche. Continuous flow in open microfluidics using controlled evaporation. *Lab on a Chip*, 5:1355–1359, 2005.

Appendix A

Algorithm used to generate the Fibonacci spiral pattern

The Matlab code used to generate the Fibonacci spiral pattern is listed below. By tuning the parameter dt (a deviation from the “golden ratio”), different Fibonacci spiral pattern can be obtained. For the specific design used for the micromodel used in the present work, $dt = 0.001485$ (see line 6 of the code).

```
1 StartNum = 140; % omit the overlapped pillar in center
2 EndNum = 800;
3 radius = 250; % radius of pillars
4 R = (StartNum:EndNum)*26; %increasement of radius
5 g = (1 + sqrt(5))/2; % golden ratio
6 dt = 0.001485; % deviation for spiral array
7 t = g + dt;
8 xx = a*(R).* cos(2*pi*t*R); % coordinates of cylinders
9 yy = a*(R).* sin(2*pi*t*R);
10 theta = 0:0.01:2*pi;
11 for i = 1:length(xx)
12     plot(radius*cos(theta)+xx(i), radius*sin(theta)+yy(i),'-b');
13     hold on;
14 end
```


Appendix B

Surface Evolver simulation of a receding front, in a Fibonacci spiral pattern

In this Appendix, we show preliminary results on the simulation of a receding front in between two branches of a Fibonacci spiral pattern. We first detail the geometry and then present some preliminary results on the capillary pressure evolution .

The geometry studied is similar to the one introduced in Figure 3.13 of Chapter 3. The Res-settle Volume Method (RVM), introduced in Chapter 3, is used to study the interface shape evolution with a volume step decrease of 0.025. The contact angle on the bottom and top plates is 10° and the fluid perfectly wets the cylinders. Figure B.1 shows the evolution of the capillary pressure as a function of the saturation in the space between the two branches (as defined in §3.2.3). The four insets display the interface shapes for saturation 0.98, 0.92, 0.79 and 0.61 respectively. In Figure B.2, we compare the SE-computed interface shape, for a 0.92 saturation, and the one observed experimentally (for evaporation of pentane in a small micromodel). The agreement is very good, showing the ability of SE to correctly simulate such complex interface shapes.

We now focus on the capillary pressure evolution, as displayed in Figure B.1. The capillary pressure globally increases when the saturation decreases. This is expected as the interface penetrates in a porous medium where the pore size progressively decreases. But the displayed oscillations are surprising. One question is to relate this capillary pressure evolution to the precise location of the main meniscus. In Figure B.3, we focus on the invasion of a single pore. It is seen that this invasion can be described as a succession of equilibrium shapes in SE, whereas in the experiments the main meniscus “jumps” from one pore to another (as discussed in Chapter 5). Highlighted by dashed lines in Figure B.3 are the circles inscribed in between the two pillars that mark the entrance of the pore about to be invaded (sub-image 1 in Figure B.3) and the entrance of the next pore where the interface is located, in sub-image 8. Interestingly, these two locations correspond to a maximum in capillary pressure, see Figure B.4. Thus, it would be very interesting to relate the interface shapes really observed in the experiment to the one computed in SE, which would allow to have an insight on the capillary pressure evolution during a pore invasion

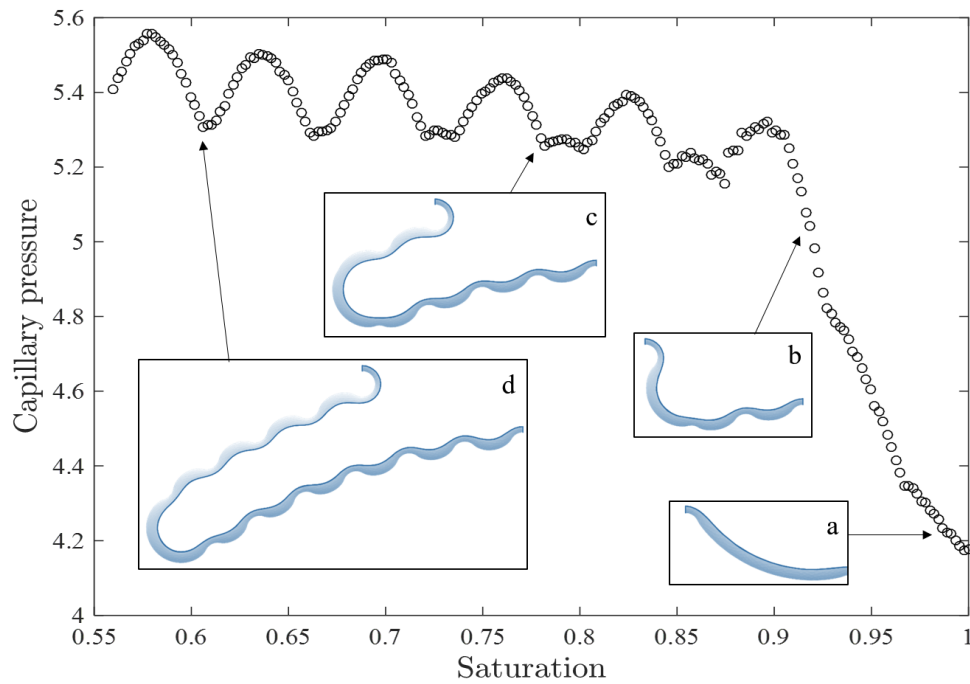


Figure B.1: Capillary pressure for a receding front. Four interface shapes, corresponding to saturation of 0.98, 0.92, 0.79 and 0.61 respectively, are shown as insets.

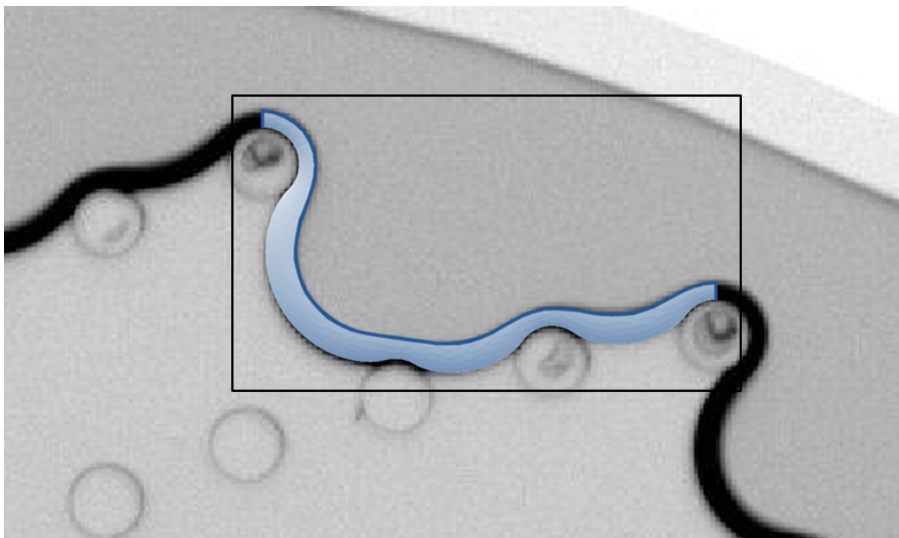


Figure B.2: Interface shape computed by SE, compared with an experimental image, for a 0.92 saturation, see Figure B.1.

event.

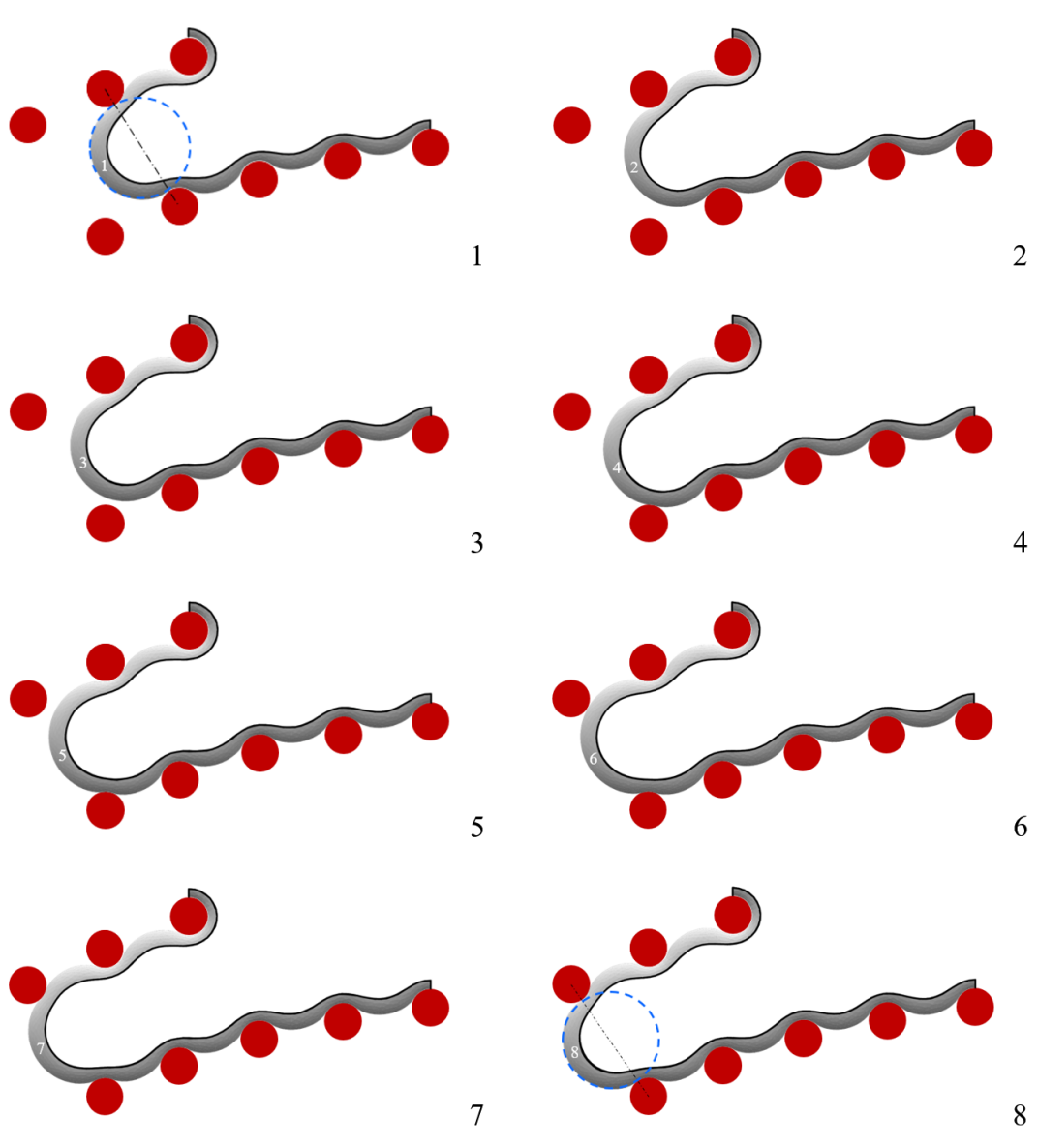


Figure B.3: Interface shapes for saturation 0.826, 0.817, 0.808, 0.800, 0.791, 0.782, 0.773 and 0.764 respectively.

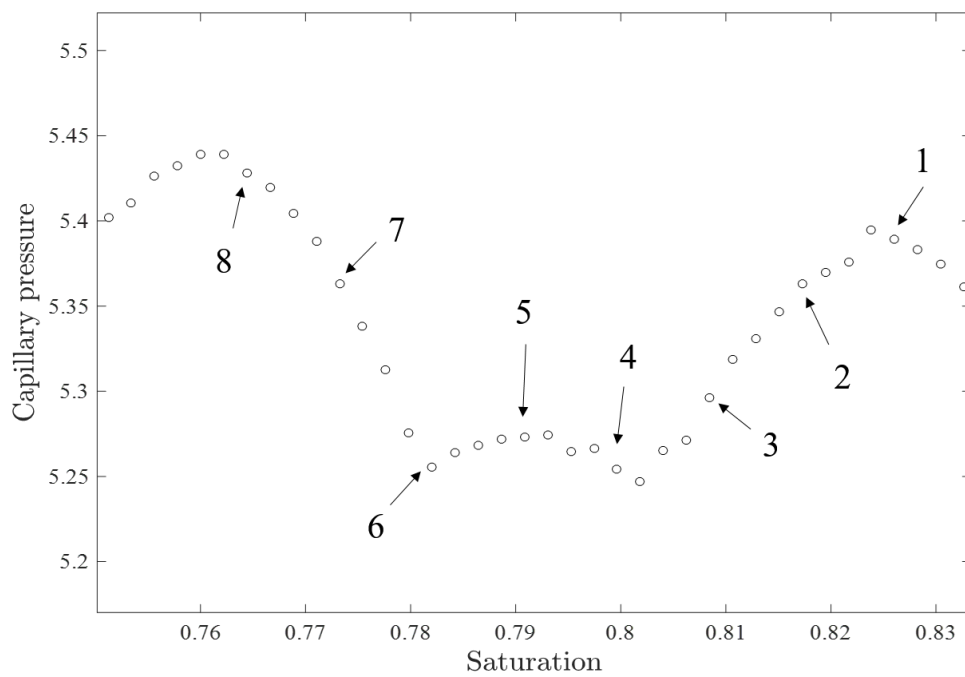


Figure B.4: Capillary pressure for saturation from 0.8349 to 0.7644. The capillary pressure values for the 8 interface shapes displayed in Figure B.3 are marked out by numbers (1 to 8).

Appendix C

Flow resistance of liquid bridge

This appendix first lists out the results for the flow resistance β , computed by Comsol using liquid bridge shapes combined with shapes obtained in Surface Evolver. The relevant pieces of information concerning the liquid bridge shape are also given: spacing $w_{//}$, mean curvature (C), liquid bridge width (BW_1 , BW_2), R_{in} and Volume of unite cell of liquid bridge (V) that used in Stoke flow simulation, which is dimensionless by volume of two pillars.

Then, results obtained for the critical pressure for liquid bridge breakup are given.

$w_{\parallel}/2d_c$	$V/(2d_c)^3$	BW1/ $2d_c$	BW2/ $2d_c$	$R_{in}/2d_c \times 10^{-3}$	C	β
1.1	0.2359	0.5066	0.1319	0.1292	-5.4083	37.2397
	0.2251	0.4921	0.1180	0.1285	-5.4742	38.7148
	0.2035	0.4630	0.0900	0.1247	-5.5882	40.0847
	0.1926	0.4493	0.0741	0.1271	-5.6207	42.6300
	0.1722	0.4213	0.0461	0.1214	-5.7424	41.8452
	0.1621	0.4076	0.0320	0.1209	-5.7945	43.4231
	0.1524	0.3936	0.0190	0.1228	-5.8452	46.6928
	0.1425	0.3798	0.0059	0.1202	-5.9046	46.1251
1.0	0.2045	0.5132	0.1461	0.1224	-5.7412	40.4182
	0.1943	0.4976	0.1308	0.1197	-5.8262	40.8151
	0.184	0.482	0.1152	0.1185	-5.9104	42.1511
	0.1738	0.4664	0.1001	0.1189	-5.9854	44.8333
	0.1639	0.4506	0.0859	0.1161	-6.0846	45.1189
	0.1542	0.4353	0.0708	0.1137	-6.165	45.007
	0.1447	0.4199	0.056	0.1144	-6.2481	48.0902
	0.1344	0.4057	0.0375	0.1132	-6.2825	48.7149
	0.1249	0.3908	0.0219	0.1149	-6.3441	51.9438
	0.1185	0.3809	0.0113	0.1119	-6.3762	50.7613
	0.1155	0.3756	0.0065	0.1117	-6.3982	51.1586
	0.1124	0.3706	0.0015	0.1105	-6.4335	50.5897
0.9	0.1677	0.5151	0.1545	0.1162	-6.2256	46.0908
	0.1578	0.4982	0.137	0.1117	-6.3381	45.3706
	0.148	0.4808	0.1197	0.1118	-6.4514	48.2288
	0.1386	0.4632	0.1028	0.1093	-6.5761	49.3517
	0.1291	0.4458	0.0856	0.1076	-6.698	51.1332
	0.1111	0.4111	0.0521	0.103	-6.9584	52.7125
	0.1014	0.3945	0.0332	0.1046	-7.0608	57.2206
	0.093	0.3771	0.0171	0.1016	-7.1952	57.6038
	0.0871	0.3656	0.0065	0.0995	-7.2812	57.1777
0.8	0.116	0.4836	0.1324	0.1026	-7.1676	53.3527
	0.0986	0.4429	0.0952	0.0959	-7.5955	55.6882
	0.09	0.4225	0.0754	0.0947	-7.8167	59.4507
	0.0814	0.4025	0.0552	0.094	-8.0267	62.8016
	0.0732	0.382	0.0363	0.0899	-8.2699	63.3769
	0.0649	0.362	0.0154	0.0889	-8.4937	66.2962
	0.0621	0.3547	0.0082	0.0881	-8.5453	67.8905
	0.75	0.1108	0.5114	0.1683	0.1008	-7.3687
0.1024		0.4895	0.1494	0.0962	-7.66	51.3827
0.0941		0.4675	0.1305	0.0939	-7.9764	57.6968
0.0852		0.4454	0.1069	0.0915	-8.2262	60.8248
0.0769		0.4231	0.0863	0.0893	-8.5477	65.1573
0.0686		0.4002	0.064	0.0872	-8.873	68.1305
0.0524		0.3538	0.0187	0.0821	-9.4778	74.2757
0.0498		0.3461	0.0117	0.0813	-9.5939	76.3857
0.0472		0.3385	0.0036	0.0775	-9.7138	71.653

Table C.1: DNS results of liquid bridge for $\theta = 0^\circ$.

$w_{//}/2d_c$	$V/(2d_c)^3$	BW1/ $2d_c$	BW2/ $2d_c$	$R_{in}/2d_c \times 10^{-3}$	C	β
0.7	0.0914	0.5074	0.1757	0.0941	-8.0645	57.134
	0.0833	0.4834	0.155	0.0901	-8.4752	60.6442
	0.075	0.4588	0.1323	0.0853	-8.9072	61.291
	0.0671	0.4334	0.1093	0.0838	-9.3284	68.2688
	0.0592	0.4073	0.0854	0.0783	-9.8326	69.6777
	0.0436	0.3547	0.0355	0.0741	-10.8258	79.7939
	0.041	0.3468	0.026	0.0723	-10.978	79.7392
	0.0385	0.3379	0.0178	0.0719	-11.1732	84.0282
0.0359	0.329	0.0097	0.0718	-11.3464	87.4623	
0.675	0.0536	0.408	0.0967	0.075	-10.4654	72.8867
	0.0383	0.3515	0.0427	0.0691	-11.7768	84.4969
	0.0332	0.3248	0.0232	0.0661	-12.2261	85.8792
	0.0308	0.3143	0.014	0.0655	-12.4507	89.885
	0.0283	0.3066	0.003	0.0641	-12.6792	89.7791
0.65	0.0704	0.495	0.182	0.0835	-9.1633	60.3142
	0.0397	0.3767	0.078	0.0663	-12.2153	79.608
	0.0323	0.3381	0.0483	0.0622	-13.0815	89.0231
	0.0273	0.318	0.0265	0.06	-13.7547	92.7794
	0.0248	0.3078	0.0153	0.0573	-14.0731	89.2009
	0.0225	0.2938	0.0047	0.0578	-14.4062	98.3172
0.625	0.0576	0.4782	0.1778	0.0787	-10.1525	68.6674
	0.0356	0.376	0.0969	0.0622	-13.2655	84.2508
	0.0284	0.339	0.0642	0.0567	-14.6057	91.8204
	0.0186	0.2838	0.0146	0.0512	-16.5082	101.7374
	0.0162	0.2716	0.0007	0.0499	-16.9808	104.111
0.6	0.0354	0.4035	0.1363	0.0606	-13.6105	80.8547
	0.0283	0.3624	0.1037	0.0551	-15.3194	90.0258
	0.0188	0.294	0.0525	0.0486	-18.0555	109.649
	0.014	0.2655	0.0215	0.0446	-19.7634	112.4888
	0.0117	0.2477	0.0049	0.043	-20.6038	120.5035

Table C.2: DNS results of liquid bridge for $\theta = 0^\circ$.

$w_{//}/2d_c$	$V/(2d_c)^3$	BW1/ $2d_c$	BW2/ $2d_c$	$R_{in}/2d_c \times 10^{-3}$	C	β
1.1	0.2363	0.5043	0.133	0.1295	-5.3877	39.8397
	0.2255	0.4899	0.1191	0.1289	-5.4538	40.9936
	0.2145	0.4752	0.105	0.1265	-5.5105	41.366
	0.2039	0.4606	0.0912	0.125	-5.5666	42.0746
	0.193	0.4467	0.0755	0.1264	-5.5999	44.8247
	0.1626	0.4051	0.0334	0.1225	-5.771	48.3653
1.0	0.2049	0.5112	0.1472	0.1227	-5.7195	42.268
	0.1946	0.4955	0.132	0.121	-5.7999	44.2463
	0.1843	0.4799	0.1164	0.1187	-5.8824	44.5208
	0.1742	0.4642	0.1014	0.119	-5.9585	48.3641
	0.1643	0.4485	0.0871	0.115	-6.0635	46.8121
0.9	0.1681	0.513	0.1558	0.1162	-6.2031	49.5262
	0.1581	0.4961	0.1382	0.1124	-6.3109	49.2028
	0.1483	0.4786	0.1208	0.1121	-6.4216	50.6296
	0.139	0.461	0.1041	0.1099	-6.5507	52.0242
	0.1294	0.4437	0.0866	0.108	-6.6663	53.5184
	0.1201	0.4264	0.0693	0.106	-6.7834	55.9416
	0.1017	0.3922	0.0343	0.1048	-7.0335	60.6063
	0.0932	0.3748	0.0182	0.1013	-7.1653	60.0514
0.85	0.1456	0.514	0.1503	0.1089	-6.5624	46.291
	0.1269	0.4753	0.1153	0.1044	-6.8797	49.3783
	0.1179	0.4556	0.097	0.1037	-7.0228	52.5791
	0.1087	0.437	0.0778	0.1014	-7.1688	53.5482
	0.1005	0.4184	0.0634	0.0986	-7.4021	54.7349
	0.0916	0.3987	0.045	0.0961	-7.5587	56.0138
	0.0831	0.3791	0.0264	0.0943	-7.7182	57.7155
0.8	0.1252	0.5014	0.1524	0.1056	-6.9345	54.4336
	0.1164	0.4813	0.1342	0.1027	-7.1401	56.2316
	0.1076	0.4608	0.1153	0.1007	-7.3238	58.2082
	0.0988	0.4408	0.0962	0.0958	-7.5625	58.6102
	0.0816	0.4001	0.0565	0.0938	-7.9979	65.468
	0.065	0.3598	0.0163	0.0893	-8.4556	71.8825
0.75	0.1095	0.513	0.1652	0.099	-7.4363	51.843
	0.1011	0.4904	0.1468	0.0948	-7.7393	54.4236
	0.0926	0.4675	0.1255	0.0927	-8.0065	56.6851
	0.0843	0.4447	0.1049	0.0907	-8.2941	60.0852
	0.0762	0.4215	0.0844	0.0876	-8.6306	62.5977
	0.0683	0.398	0.065	0.0834	-8.9993	64.1675
	0.06	0.373	0.0423	0.0815	-9.2944	67.7078
	0.0573	0.3658	0.0341	0.0805	-9.3865	67.9413
0.7	0.0836	0.4814	0.1564	0.09	-8.4427	62.9986
	0.0752	0.4567	0.1333	0.0855	-8.8651	65.3367
	0.0672	0.4312	0.1101	0.0834	-9.2842	70.5436
	0.0594	0.4053	0.0865	0.0785	-9.7863	74.2804

Table C.3: DNS results of liquid bridge for $\theta = 5^\circ$.

$w_{\parallel}/2d_c$	$V/(2d_c)^3$	BW1/ $2d_c$	BW2/ $2d_c$	$R_{in}/2d_c \times 10^{-3}$	C	β
0.7	0.0513	0.3786	0.0618	0.077	-10.2529	78.6643
	0.0437	0.3525	0.0365	0.074	-10.78	83.8725
	0.036	0.3267	0.0105	0.0727	-11.3095	95.2004
0.675	0.0766	0.4885	0.1679	0.0854	-8.892	59.1027
	0.0612	0.4305	0.1231	0.0763	-10.042	66.1452
	0.0536	0.403	0.0997	0.0722	-10.7194	70.2384
	0.0456	0.3693	0.0703	0.0706	-11.2149	76.3684
	0.0379	0.3388	0.0416	0.0678	-11.838	82.3758
	0.0354	0.3293	0.0316	0.0666	-12.0548	85.1401
0.65	0.0698	0.4934	0.1806	0.0826	-9.2812	60.5286
	0.0621	0.4636	0.1572	0.0783	-9.9287	64.9615
	0.0471	0.3993	0.1075	0.0694	-11.4444	74.9028
	0.0396	0.3661	0.0797	0.0659	-12.3486	82.0762
	0.0276	0.3067	0.0318	0.0573	-14.1478	90.0735
0.625	0.0501	0.4433	0.1526	0.0712	-11.1569	70.3191
	0.0425	0.4052	0.1248	0.0664	-12.128	76.3798
	0.0355	0.3693	0.0976	0.0601	-13.4604	80.4375
	0.0215	0.2857	0.0357	0.0483	-16.7882	95.8821
	0.0192	0.2712	0.0243	0.0462	-17.4518	100.7728
0.6	0.0498	0.477	0.1907	0.0738	-10.8377	72.4232
	0.0355	0.4013	0.137	0.0608	-13.5389	83.883
	0.0283	0.3608	0.1044	0.0556	-15.2555	94.1766
	0.0213	0.3079	0.0673	0.0503	-17.2254	107.6981
	0.0141	0.2639	0.0221	0.045	-19.6946	128.0155

Table C.4: DNS results of liquid bridge for $\theta = 5^\circ$.

$w_{//}/2d_c$	$V/(2d_c)^3$	BW1/ $2d_c$	BW2/ $2d_c$	$R_{in}/2d_c \times 10^{-3}$	C	β
1.1	0.2376	0.4977	0.137	0.131	-5.3185	40.6804
	0.2266	0.4832	0.1229	0.1289	-5.3836	41.5371
	0.2157	0.4687	0.1086	0.1279	-5.4398	42.5077
	0.1941	0.4401	0.0792	0.126	-5.5341	45.2889
	0.1838	0.4261	0.0651	0.125	-5.5939	45.2206
	0.1634	0.3985	0.0366	0.1246	-5.6913	49.7386
	0.1538	0.3845	0.0243	0.1227	-5.7601	49.7793
1.0	0.2059	0.5052	0.1507	0.1236	-5.6405	43.5655
	0.1853	0.4739	0.1199	0.1199	-5.8062	45.0946
	0.1751	0.4583	0.1048	0.122	-5.8843	51.3307
	0.1651	0.4427	0.0903	0.1168	-5.9856	48.4215
	0.1555	0.4274	0.0755	0.1139	-6.0727	48.5039
	0.146	0.4119	0.0608	0.1131	-6.1556	51.5866
	0.1357	0.3971	0.0428	0.1152	-6.1845	53.909
	0.126	0.3822	0.0265	0.1159	-6.2362	57.5363
	0.1167	0.367	0.0112	0.1135	-6.2936	56.0882
0.9	0.1492	0.4726	0.1241	0.1125	-6.3267	55.136
	0.1399	0.4548	0.1085	0.1113	-6.4703	53.9006
	0.1303	0.4376	0.0907	0.1085	-6.5783	54.8562
	0.1121	0.4028	0.0568	0.1037	-6.8453	57.2602
	0.1026	0.3858	0.0388	0.1048	-6.9588	62.586
	0.0939	0.3686	0.0215	0.1026	-7.075	62.6213
	0.85	0.1463	0.5055	0.1535	0.1108	-6.4366
0.1372		0.4869	0.1368	0.1076	-6.6106	49.2676
0.128		0.4673	0.1196	0.1052	-6.7856	50.6868
0.1187		0.4477	0.1007	0.1038	-6.9139	53.1669
0.1096		0.4286	0.0824	0.1023	-7.0647	55.2112
0.1008		0.4098	0.0644	0.1006	-7.224	57.8196
0.0926		0.3906	0.0492	0.0961	-7.4581	57.4255
0.8	0.1259	0.4956	0.1558	0.1061	-6.8291	54.6505
	0.1171	0.4756	0.1379	0.1042	-7.0338	58.2881
	0.1083	0.4552	0.1185	0.1015	-7.2188	59.4128
	0.0993	0.4351	0.0991	0.0968	-7.4429	59.7736
	0.0907	0.4146	0.0797	0.0955	-7.6612	64.3104
	0.0822	0.3942	0.0602	0.0943	-7.8823	67.157
	0.074	0.374	0.041	0.0911	-8.1258	67.4629
	0.0656	0.3538	0.0196	0.0898	-8.3196	73.4646
0.75	0.1102	0.5049	0.1687	0.1	-7.2948	52.8645
	0.1016	0.4818	0.1491	0.0971	-7.5673	56.0966
	0.0933	0.4598	0.1293	0.0939	-7.8611	58.5587
	0.085	0.4371	0.1094	0.0906	-8.1974	60.3663
	0.0767	0.4132	0.0874	0.0886	-8.4574	65.5587
	0.0688	0.3902	0.0684	0.0854	-8.8481	68.6313
	0.0607	0.3653	0.0459	0.0821	-9.1634	70.2445
	0.0579	0.3567	0.0377	0.0815	-9.2648	71.2208

Table C.5: DNS results of liquid bridge for $\theta = 10^\circ$.

$w_{\parallel}/2d_c$	$V/(2d_c)^3$	BW1/ $2d_c$	BW2/ $2d_c$	$R_{in}/2d_c \times 10^{-3}$	C	β
0.7	0.0921	0.5002	0.1797	0.0959	-7.8858	62.1637
	0.0841	0.4761	0.1595	0.0914	-8.3064	66.1494
	0.0757	0.4512	0.1363	0.0876	-8.7169	69.5885
	0.0677	0.4257	0.1133	0.084	-9.1443	72.7155
	0.0598	0.3997	0.0897	0.0812	-9.6377	79.292
	0.0518	0.3729	0.0649	0.0769	-10.1161	82.9137
	0.0441	0.3469	0.0396	0.0743	-10.6369	86.8721
	0.0363	0.3206	0.0127	0.0728	-11.1391	95.7018
0.675	0.054	0.3963	0.1019	0.0733	-10.5017	74.0524
	0.046	0.3636	0.0737	0.0715	-11.0311	81.1528
	0.0382	0.3326	0.0438	0.0693	-11.6061	87.1966
0.65	0.0703	0.4864	0.1834	0.0834	-9.0975	61.7997
	0.0626	0.4564	0.1606	0.0792	-9.7577	67.3245
	0.0552	0.4264	0.1376	0.0743	-10.5156	73.7931
	0.0471	0.3928	0.1078	0.071	-11.1716	77.1381
	0.0399	0.3598	0.0814	0.0672	-12.0776	85.891
	0.0326	0.3252	0.0536	0.0612	-13.1652	90.5231
	0.0277	0.3015	0.0331	0.0583	-13.857	94.2009
	0.625	0.0579	0.4683	0.1816	0.0758	-10.1344
0.0504		0.4361	0.1553	0.0723	-10.9452	73.3308
0.0428		0.3987	0.1263	0.0679	-11.8247	80.0409
0.0356		0.3637	0.098	0.0623	-13.0688	86.7696
0.0288		0.3238	0.0713	0.0543	-14.8578	91.5238
0.0193		0.2667	0.0258	0.0471	-17.1501	104.5545
0.6	0.0501	0.4715	0.1927	0.0748	-10.6427	74.9603
	0.0429	0.4375	0.1671	0.068	-11.8365	78.2925
	0.0357	0.3967	0.139	0.062	-13.2945	88.0088
	0.0214	0.3043	0.0691	0.0507	-16.9963	112.8413
	0.0142	0.2597	0.0239	0.045	-19.4567	125.3574

Table C.6: DNS results of liquid bridge for $\theta = 10^\circ$.

Appendix D

Vapor concentration field in a Fibonacci spiral micromodel, during the CRP

In this Appendix, we present some simulation results for the vapor concentration field in a Fibonacci spiral micromodel. The geometry of the simulation domain is shown in Figure D.1: it consists in the space in between two spirals. We will focus on a phase distribution similar to the one observed in the constant evaporation rate period (CRP), with liquid films reaching the most external cylinder of each spiral.

We will make the assumption that vapor diffusion in the gas phase is quasi-steady. Also, we will use some interface shapes obtained with Surface Evolver, at capillary equilibrium. Regarding vapor diffusion, a characteristic vapor diffusion time is

$$\tau_{diff} \approx \frac{\delta^2}{D},$$

where δ is the spacing between the top cover plate and the most external pillar of the pattern, see Figure 2.9 in Chapter 2. Taking $D \approx 10^{-5} \text{ m}^2\text{s}^{-1}$ for the fluids used and $\delta \sim O(1) \text{ mm}$ and $\delta \sim O(100) \mu\text{m}$ for the large and small micromodel respectively, one ends up with $\tau_{diff} \approx 10^{-1}$ and $\tau_{diff} \approx 10^{-3}$ for the large and small micromodels respectively. This characteristic time is much smaller than the typical drying time observed in the experiments (typically 10s for the small micromodels and 1000s for the large one), which is the characteristic time at which the interface recedes in the micromodel. Therefore, the assumption of quasi-steady vapor diffusion is a good one. We will also assume that the saturation vapor concentration is small so that convective effects in the gas phase can be neglected [58] and the situation is isothermal.

The numerical domain used is 2D, to avoid time-consuming 3D simulations. It is colored in blue in Figure D.1 whereas the liquid is in gray. The interface shape is the one obtained by SE on the plane containing the bottom plate, see Figure D.1. We have to solve the Laplace equation for the vapor concentration, $\Delta c = 0$, in this domain. The boundary conditions at liquid-gas interface is $c = c_e$, where c_e is the saturation vapor concentration. At the external edge, $c = c_\infty \approx 0$ since evaporation occurs in dry, ambient air. Note a symmetric boundary condition was set at the

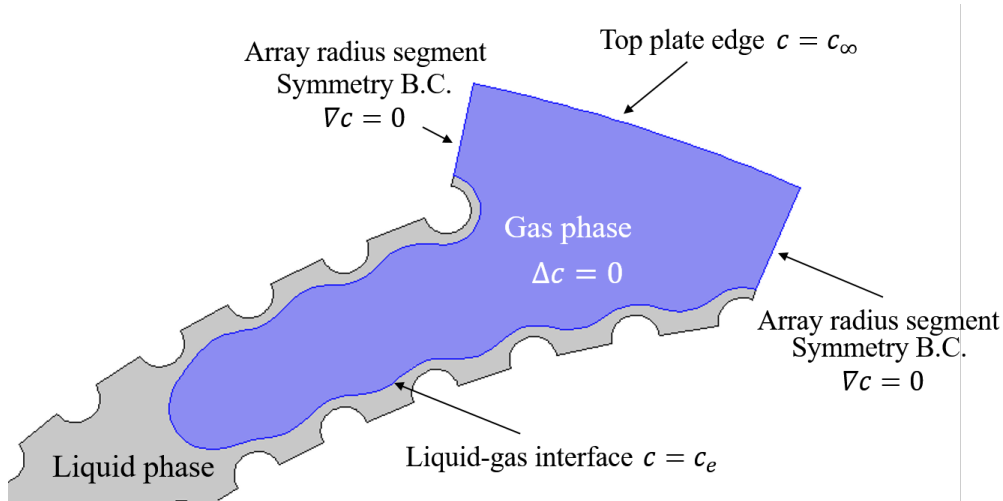


Figure D.1: Numerical domain for the computation of the vapor concentration. The gas phase is colored in blue. The saturation of the unit cell, as defined in §3.2.3, is 0.7.

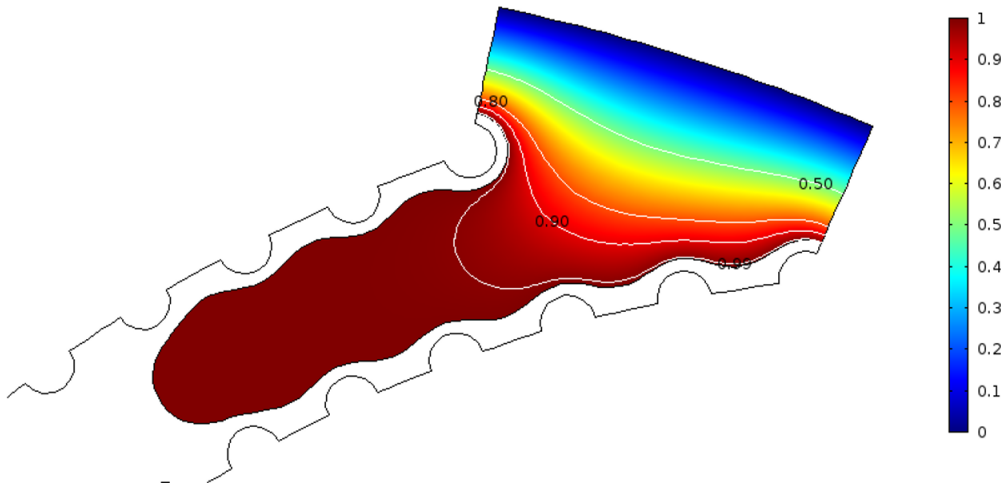


Figure D.2: Vapor concentration field in the gas phase. The vapor concentration is made dimensionless by dividing by c_e . The white contour lines correspond to relative concentration: 0.5, 0.8, 0.9, 0.99 respectively.

two segments delimitating the computational domain outside the pore space, see Figure D.1.

A typical result for the vapor concentration field is shown in figure D.2. It is found that the gas phase within the two spirals is almost saturated with vapor. Therefore, evaporation occurs at the external end of the liquid films only. Such a concentration field is also obtained at a smaller saturation, i.e. longer liquid films and a more advanced location of the main meniscus into the pore space, see Figure D.3 This result is very similar to those obtained by Chauvet [10], in a capillary tube with a square cross-section when liquid films are present in the tube corners. This is a key ingredient to explain the CRP: as long as the liquid films are connected

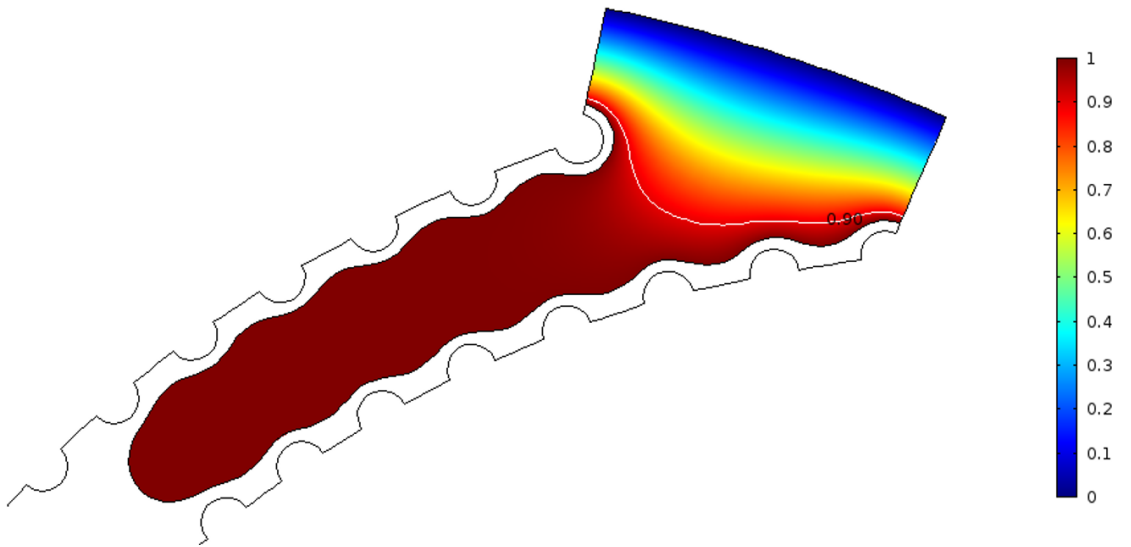


Figure D.3: Vapor concentration field in the gas phase for a phase distribution corresponding to a saturation equals to 0.58.

to the most external cylinders of each spiral, the fact that the gas phase invades the pore space has no influence on the drying kinetics and a Fibonacci micromodel behaves like a radial pattern with a decreasing spacing between the cylinders from center to periphery, the “unstable” case described in Chapter 4.

